Rational design of porous silica-based materials via multiscale colloidal assembly

Citation for published version (APA):
Fijneman, A. J. (2020). *Rational design of porous silica-based materials via multiscale colloidal assembly*. [Phd Thesis 1 (Research TU/e / Graduation TU/e), Chemical Engineering and Chemistry]. Technische Universiteit Eindhoven.

Document status and date:
Published: 05/11/2020

Document Version:
Publisher’s PDF, also known as Version of Record (includes final page, issue and volume numbers)

Please check the document version of this publication:

- A submitted manuscript is the version of the article upon submission and before peer-review. There can be important differences between the submitted version and the official published version of record. People interested in the research are advised to contact the author for the final version of the publication, or visit the DOI to the publisher's website.
- The final author version and the galley proof are versions of the publication after peer review.
- The final published version features the final layout of the paper including the volume, issue and page numbers.

Link to publication

General rights
Copyright and moral rights for the publications made accessible in the public portal are retained by the authors and/or other copyright owners and it is a condition of accessing publications that users recognise and abide by the legal requirements associated with these rights.

- Users may download and print one copy of any publication from the public portal for the purpose of private study or research.
- You may not further distribute the material or use it for any profit-making activity or commercial gain
- You may freely distribute the URL identifying the publication in the public portal.

If the publication is distributed under the terms of Article 25fa of the Dutch Copyright Act, indicated by the “Taverne” license above, please follow below link for the End User Agreement:

www.tue.nl/taverne

Take down policy
If you believe that this document breaches copyright please contact us at:

openaccess@tue.nl

providing details and we will investigate your claim.

Download date: 04. Oct. 2023

Rational Design of Porous Silica-Based Materials via Multiscale Colloidal Assembly

PROEFSCHRIFT

ter verkrijging van de graad van doctor aan de Technische Universiteit Eindhoven, op gezag van de rector magnificus prof.dr.ir. F.P.T. Baaijens, voor een commissie aangewezen door het College voor Promoties, in het openbaar te verdedigen op donderdag 5 november 2020 om 16:00 uur

door

Andreas Josephus Fijneman

geboren te Tilburg

Dit proefschrift is goedgekeurd door de promotoren en de samenstelling van de promotiecommissie is als volgt:

voorzitter: prof. dr. E.J.M. Hensen
1e promotor: prof. dr. G. de With
2e promotor: dr. A.C. de Carvalho Esteves
copromotor: dr. H. Friedrich
leden: dr. M. Persson (Chalmers University of Technology)
prof. dr. K. Holmberg (Chalmers University of Technology)
prof. dr. F. Gallucci
adviseur: dr. J. Högblom (Nouryon Pulp and Performance Chemicals AB)

Het onderzoek dat in dit proefschrift wordt beschreven is uitgevoerd in overeenstemming met de TU/e Gedragscode Wetenschapsbeoefening.

“What I cannot create, I do not understand.”

Richard Feynman

Rational Design of Porous Silica-Based Materials via Multiscale Colloidal Assembly

By Andreas J. Fijneman

Eindhoven University of Technology, 2020

A catalogue record is available from the Eindhoven University of Technology Library

ISBN: 978-90-386-5120-0

The research described in this thesis has been carried out at Nouryon Pulp and Performance Chemicals AB, Bohus, Sweden and at the Laboratory of Physical Chemistry (SPC) within the department of Chemical Engineering and Chemistry at Eindhoven University of Technology, the Netherlands. The research was supported by the European Union's Horizon 2020 research and innovation programme under the Marie Skłodowska-Curie grant agreement no. 676045 "MULTIMAT".

FSC
www.fsc.org
MIX
Paper from
responsible sources

Printed by: Gildeprint Drukkerijen, Enschede

Cover design: A.J. Fijneman

Cover graphics by Freepik (freepik.com)

Table of Contents

Nomenclature

Abbreviations

1D	one-dimensional
3D	three-dimensional
atm	atmosphere
BET	Brunauer-Emmett-Teller
BJH	Barrett-Joyner-Halenda
BP	boiling point
cryoTEM	cryogenic transmission electron microscopy
CSM	core-shell microsphere
DLCA	diffusion limited cluster aggregation
DLS	dynamic light scattering
DLVO	Derjaguin-Landau-Verwey-Overbeek
ES-DMA	electrospray differential mobility analysis
HAADF	high angle annular dark field
HM	hollow microsphere
HPC	hydroxypropyl cellulose
HPLC	high-performance liquid chromatography
IUPAC	International Union of Pure and Applied Chemistry
LC-STEM	low convergence angle scanning transmission electron microscopy
MSM	mesoporous silica microsphere
MST	mesitylene
O/W	oil-in-water
PD	pore diameter
PEA	phenethyl alcohol
PSD	pore size distribution
PV	pore volume
PVA	polyvinyl alcohol
RPM	rotations per minute
SAXS	small angle X-ray scattering
SD	standard deviation
SEM	scanning electron microscopy
SSA	specific surface area
STEM	scanning transmission electron microscopy
TEM	transmission electron microscopy
TEOS	tetraethyl orthosilicate
W/O	water-in-oil
XDLVO	extended DLVO

List of symbols

Symbol	Physical quantity	Unit
a	particle radius	m
A	regression coefficient	$\mathrm{J \cdot mol^{-1}}$
A_H	Hamaker constant	J
B	regression coefficient	-
C	concentration	M
Ca	capillary number	-
CV	coefficient of variation	%
d_0	equilibrium distance	m
d_f	fractal dimension	-
D	separation distance	m
$\mathscr{D}$	diffusion coefficient	$\mathrm{m^2 \cdot s^{-1}}$
D_P	particle diameter	m
$D_\mathrm{P}[1,0]$	number mean diameter	m
$D_\mathrm{P}[4,3]$	volume mean diameter	m
e	elementary charge	C
f	correction image	-
$f(\kappa a)$	Henry function	-
F_0	hydration force constant	$\mathrm{N \cdot m^{-2}}$
h	channel height	m
H	enthalpy	$\mathrm{J \cdot mol^{-1}}$
I	ionic strength	M
J	flux	$\mathrm{mol \cdot m^{-2} s^{-1}}$
k	aggregation rate constant	-
k^*	geometry factor	-
k_B	Boltzmann constant	$\mathrm{J \cdot K^{-1}}$
K	dissociation constant	-
L	thickness	m
M	molar mass	$\mathrm{g \cdot mol^{-1}}$
n	refractive index	-
$\hat{n}$	unit normal vector	-
N	number	-
N_A	Avogadro number	-
NA	numerical aperture	-
p	equilibrium pressure	Pa
p°	saturation pressure	Pa
P	absolute pressure	Pa
$\mathscr{P}$	parachor	$\mathrm{cm^3 \cdot g^{1/4} /(s^{1/2} \cdot mol)}$
$\mathbb{P}$	probability	-
q	scattering intensity	-

Symbol	Physical quantity	Unit
Q	volumetric flow rate	μl·min^{-1}
r	distance	m
R	universal gas constant	J·K^{-1}·mol^{-1}
$\mathscr{R}$	radius	m
R_g	radius of gyration	m
Re	Reynolds number	-
S	degree of aggregation	-
t	time	s
T	temperature	K
$\mathscr{T}$	thickness	m
u	dimensionless separation distance	-
U	interaction potential	$k_\mathrm{B}T$
V_m	molar volume	cm^3·mol^{-1}
V_p	particle volume	m^3
V_pore	pore volume per gram	cm^3·g^{-1}
w	width	m
W	stability ratio	-
We	Weber number	-
Y	mass fraction	wt%
z	valency	-
Z	channel distance	m

Symbol	Physical quantity	Unit
α	half-angle	°
β	collection angle	°
$\beta(u)$	hydrodynamic retardation function	-
δ	reflection coefficient	-
$\varepsilon\varepsilon_0$	dielectric constant	C^2·J^{-1}·m^{-1}
ζ	zeta-potential	J·C^{-1}
η	viscosity at a shear rate of zero	Pa·s
θ	angle	°
κ	inverse Debye length	m
λ	hydration diameter	m
λ	travel length	m
Λ	viscosity ratio	-
μ_e	electrophoretic mobility	μm·s^{-1}·V^{-1}·cm
ρ	density	g·cm^{-3}
σ	interfacial tension	mN·m^{-1}
σ_ζ	electrokinetic charge density	C·m^{-2}

Symbol	Physical quantity	Unit
τ	tortuosity	-
φ	volume fraction	-
ϕ	porosity	-
Φ	volumetric flow rate ratio	-
χ	evaporation coefficient	-
ψ_0	surface potential	$\mathrm{J{\cdot}C^{-1}}$

Subscripts

0	free
1	standard
2	reduced
a	acid
b	base
c	continuous phase
C	center
calc	calculated
charging	charge
d	dispersed phase
el	electrostatic
eff	effective
fast	diffusion-limited
gel	sol particle gelation
hyd	hydration
linearity	linearity
m	mass
max	maximum
mix	mixing
O	oil
or	orifice
outlet	outlet channel
R	reaction
salt	ammonium acetate
shrink	emulsion droplet shrinkage
slow	reaction-limited
solved	dissolved in continuous phase
SS	spherical-spherical
vdW	van der Waals
vap	vaporization
W	water

Chapter 1

Introduction

1.1 Silicates, silica and the sol-gel process

Silicate minerals are the most abundant class of minerals found in the earth's crust and upper mantle[1]. Silicate minerals can occur in many different forms and structures. Common examples include quartz, feldspar and mica but also as various precious gemstones are part of the silicate family. The basic structural unit of every silicate mineral is the SiO_4 tetrahedron[2,3]. These tetrahedral units can easily link together in a three-dimensional framework via shared O atoms. If the units are linked together in a dense periodic structure, the mineral is crystalline. If the units are linked randomly in a non-periodic structure, the mineral is amorphous[3]. A schematic representation is shown in **Figure 1.1**.

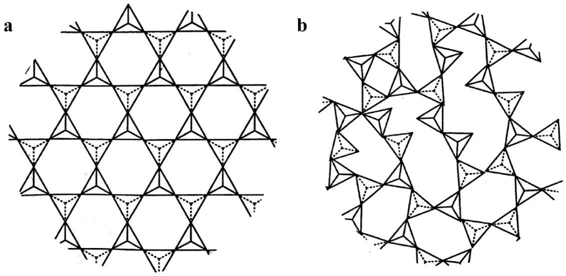

Figure 1.1: Schematic two-dimensional representation of (a) crystalline silicates and (b) amorphous silicates. Image adopted from Bergna[3].

Silica is another name for silicon dioxide (SiO_2). Some silicate minerals such as quartz are made up of pure silica but the vast majority contain one or more metal ions[1]. Synthetic silica, most notably in the form of amorphous silica nanoparticles, silica gels and zeolites, is industrially manufactured on an enormous scale. Due to its porous properties it has widespread applications in fields such as insulation[4], coatings[5], catalysis[6], photonics[7], aerospace[8] and pharmaceutics[9]. The global demand for synthetic silica is approximately 3 million tons per year and rising, which makes silica a technologically important material[10].

There are many different ways to manufacture porous silica-based materials but arguably the most important process is the sol-gel process[11–13]. The sol-gel process involves on the one hand the condensation and subsequent polymerization of monomers into a suspension of nanoparticles in a liquid, called a *sol*. On the other hand, it involves the formation of porous, interconnected, three-dimension rigid particle networks surrounding a liquid phase, called *gels*. The transition of a sol into a gel is called gelation, which is an irreversible process due to the formation of covalent bonds between the silica nanoparticles.

One of the best known methods to produce silica nanoparticles is the Stöber process[14], which is based on the hydrolysis of tetraethoxysilane (TEOS) in an alcohol in the presence of ammonia. Via the Stöber process it is possible to produce monodisperse nanoparticles in the range of 5 to 2000 nm[15]. The downside is, however, that Stöber silica particles are relatively expensive to produce. For the bulk manufacturing of silica nanoparticles the acidification of sodium silicate (water glass) is generally the preferred route because water glass is inexpensive, abundantly available and can still yield nanoparticles with a relatively narrow size-range[16]. Regardless of the method, the first step in the production of silica nanoparticles is usually the formation of monosilicic acid, $Si(OH)_4$, see equation (1.1) and equation (1.2), respectively[17,18]:

$$Si(OR)_4 + 4H_2O \rightarrow Si(OH)_4 + 4ROH \tag{1.1}$$

$$Na_2SiO_3 + H_2O + 2HCl \rightarrow Si(OH)_4 + 2NaCl \tag{1.2}$$

Silicic acid is a weak acid and has a low solubility limit of approximately 70 mg·l⁻¹ at 25 °C[2]. Above the solubility limit, silicic acid condenses into oligomers by water elimination. In time these oligomeric structures densify and form colloidally stable primary nanoparticles of approximately 2.3 nm in diameter. Then, above a critical concentration, these primary particles form silica nanoparticles via a so called synchronized association processes, see **Figure 1.2**[19]. Although Figure 1.2 specifically shows TEOS as the starting material, a similar mechanism takes place when water glass is used as the raw material.

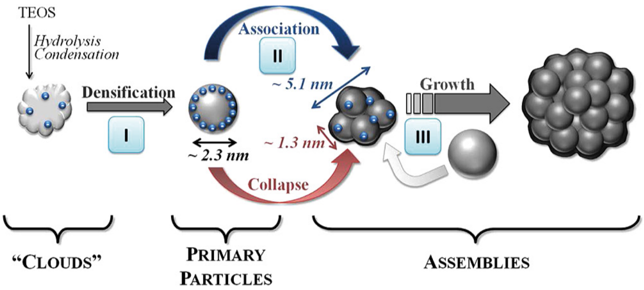

Figure 1.2: Schematic illustration of the formation mechanism of silica nanoparticles starting from TEOS. Image adopted from Carcouët et al.[19].

Silica nanoparticles can easily react and form gels via a polycondensation reaction upon change of pH, temperature and ionic strength. Under basic conditions, i.e., above the isoelectric point of silica (pH ≈ 2), the gelation mechanism involves the nucleophilic attack of a deprotonated silanol group on a neutral silica species, while under acidic conditions, i.e., under the isoelectric point, the mechanism involves the nucleophilic attack of a neutral silica species on a protonated silanol group[2], see equation (1.3) and (1.4), respectively:

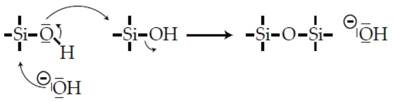

(1.3)

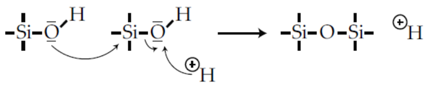

(1.4)

Gels formed under basic conditions are often branched and contain mesoporous pore structures (pore diameters 2 - 50 nm), whereas gels formed under acidic conditions are often more extended and weakly branched with microporous pore structures (pore diameters < 2 nm)[20].

Most gels formed in suspension have a very high total pore volume and surface area but suffer from a low mechanical strength[13]. Removal of the liquid from a gel under normal conditions results in the shrinkage or collapse of the gel network and the formation of dense materials, sometimes called *xerogels*. If the liquid is removed by hypercritical point drying, the gel network does not shrink and a very porous material is obtained, called an *aerogel*. If instead the liquid is removed via freeze-drying, the material is called a *cryogel*[2,3,11,21]. A schematic overview of the different routes is shown in **Figure 1.3**.

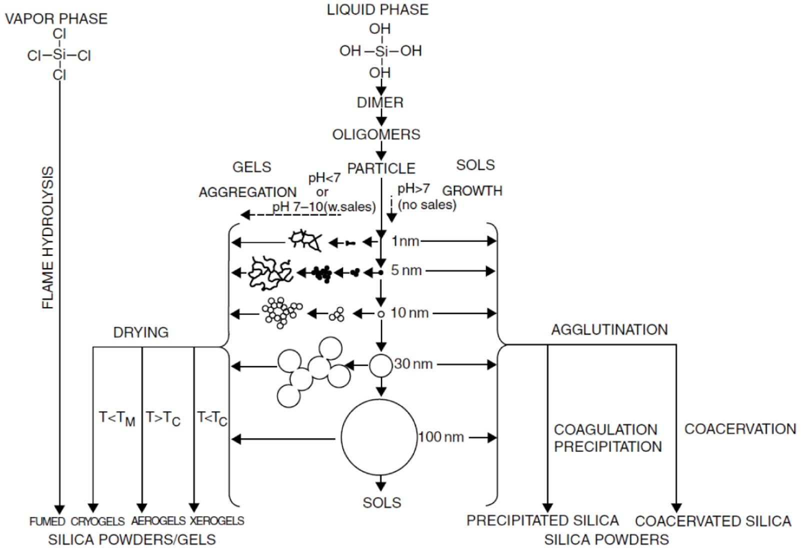

Figure 1.3: Schematic overview of the formation of silica sols and gels via condensation-polymerization of silicic acid. Image adopted from Bergna[3].

1.2 Nanoparticle assembly within spherical confinement

One of the foremost features of sol-gel chemistry is that it can be carried out in confined spaces to create porous materials of different shape, such as thin films[22], monolithic rods[23], foams[24] or micrometer-sized (hollow) spheres[25,26]. In this thesis, we focus specifically on the formation of porous micrometer-sized spheres, called mesoporous silica microspheres (MSMs), using water-in-oil (W/O) emulsion droplets as a template to confine the sol-gel reaction[27,28].

MSMs plays a key role in the pharmaceutical and life sciences industry, where they are used for the separation and purification of molecules[29]. Separation is commonly done using a technique called high-performance liquid chromatography (HPLC). The general principle of HPLC is simple: a fluid (the mobile phase or eluent) containing the analyte is passed through a fixed stationary bed (the stationary phase) consisting of MSMs and is separated into different fractions based on a difference in affinity between the molecules and the MSMs[30]. Different molecules require MSMs with different properties such as narrow pore sizes and high pore volumes. In most industrially relevant processes, however, generic MSMs are produced which have to undergo multiple time-consuming post-treatment steps to tune the microsphere properties[31–33]. Therefore, it is worthwhile to develop novel manufacturing processes to tailor-make MSMs that can be specifically tuned to the size and shape of the molecule of interest.

For the industrial production of spherical materials such as MSMs, emulsion templating is the standard approach due to scalability and ease of use[27]. The use of emulsions as templates can be roughly divided into methods that are dominated by: 1) the external confinement and process conditions, i.e., evaporation-driven or entropy-driven colloidal assembly[34–41], and 2) by the interaction forces between the nanoparticles, i.e., gelation-driven colloidal assembly[42–46]. The main difference between the two methods is that evaporation-driven assembly usually leads to more densely packed particles, whereas gelation-driven assembly usually leads to more porous particles. In most cases the emulsion templated formation of MSMs is a combination of the two extreme cases and separating their individual effects is difficult (**Figure 1.4**). This makes it challenging to get fundamental understanding of the respective contributions, a problem to be addressed in this thesis.

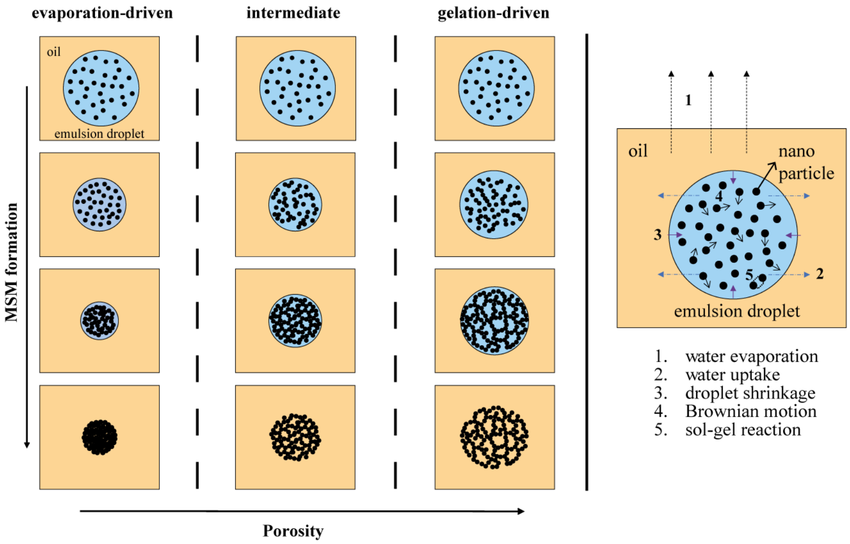

Figure 1.4: Schematic illustration of the different assembly routes and individual processes that occur during the formation of MSMs. Left-panel: the two extreme cases, i.e., evaporation-driven and gelation-driven, and intermediate case in MSM formation. Right-panel: different processes occurring during assembly.

To the best of our knowledge, nobody has studied MSM formation before as a combination of both evaporation-driven and gelation-driven assembly. In most fundamental studies only either one of the methods is used to assemble particles as detailed below.

Evaporation-driven colloidal assembly is generally used to manufacture particles with close-packed structural motifs, which are sometimes called supraparticles, supracolloids (colloids of colloids), or supraballs[39,41]. In this case a suspension of nanoparticles, e.g., a sol, is dispersed into another liquid to form emulsion droplets and subsequently the carrier liquid is removed to initiate colloidal assembly[47–49]. While the carrier liquid is evaporated, the droplets shrink, and the concentration of nanoparticles increases until there is no more free space between the nanoparticles, and they assemble into a sphere. If the nanoparticles are contained inside the emulsion droplets, particles with a high packing density can be formed when dried slowly[50,51]. If the nanoparticles adsorb exclusively at the droplet interface, hollow capsules can be formed[52,53]. The internal composition and properties of the formed particles is strongly dependent on the nature and size of the nanoparticles as well as the drying rate of the emulsion droplets[37].

In the case of gelation-driven assembly, assembly is initiated by a careful manipulation of the interaction forces between nanoparticle. By balancing the attractive and repulsive interactions between particles, the rate of gelation can be tuned and, hence, properties such as particle porosity can be controlled[39,44,45,54]. Unlike in evaporation-driven assembly, the carrier liquid is not removed but instead the nanoparticles themselves are interacting with each other. This can be done by strongly increasing the particle mobility and the particle "stickiness", i.e., by increasing the frequency that two particles collide and form irreversible bonds. To do so, salt can be added to screen the particle surface charges to increase the particle "stickiness" and the temperature can be increased to increase the particle mobility[55,56]. In the intermediate case aspects of both methods are combined, i.e., manipulation of the interaction forces between nanoparticles by salt addition in combination with controlled drying.

In summary, MSM formation is a complex process and a deep understanding of the entire process is required in order to design and synthesize microspheres with tunable properties on industrially relevant scales.

1.3 Multiscale characterization of MSM formation

The assembly of silica nanoparticles into MSMs spans multiple length scales. In order to understand and characterize MSMs from the bulk level down to the nanometer scale pore level, multiple imaging and analysis techniques are required. The main techniques used throughout this thesis will be briefly introduced below in relation to the MSM formation process.

Transmission Electron Microscopy is one of the most powerful tools available for characterization on the nanometer scale level[57–62]. Throughout this thesis TEM is used to acquire high resolution images of the colloidal silica nanoparticles used as building blocks to get a basic understanding of their size and shape. As the sols are suspended in a liquid, imaging in the native state required a special type of TEM called cryogenic TEM (cryoTEM), wherein the liquid sample is prepared and rapidly cooled by plunge vitrification in liquid ethane (**Figure 1.5a**)[63,64]. The imaging results are supplemented by scattering techniques such as electrospray differential mobility analysis (ES-DMA), dynamic light scattering (DLS) and zeta-potential measurements in order to obtain size distributions of the different sols and to assess their colloidal stability.

Unlike in TEM where two-dimensional projections of a three dimensional sample are obtained[65–67], in Scanning Electron Microscopy (SEM) images are obtained directly from the surface of the material[68–70]. This makes SEM a useful tool for the structural characterization, i.e., on the size, shape and morphology, of the different MSMs synthesized throughout this work (**Figure 1.5b**). Imaging results are supplemented by physical adsorption (physisorption) measurements in order to classify the different MSMs based on their surface area, pore volume, average pore sizes and pore size distributions[71,72]. A proper classification system is critical for the development of a scalable toolbox for MSMs with tunable properties.

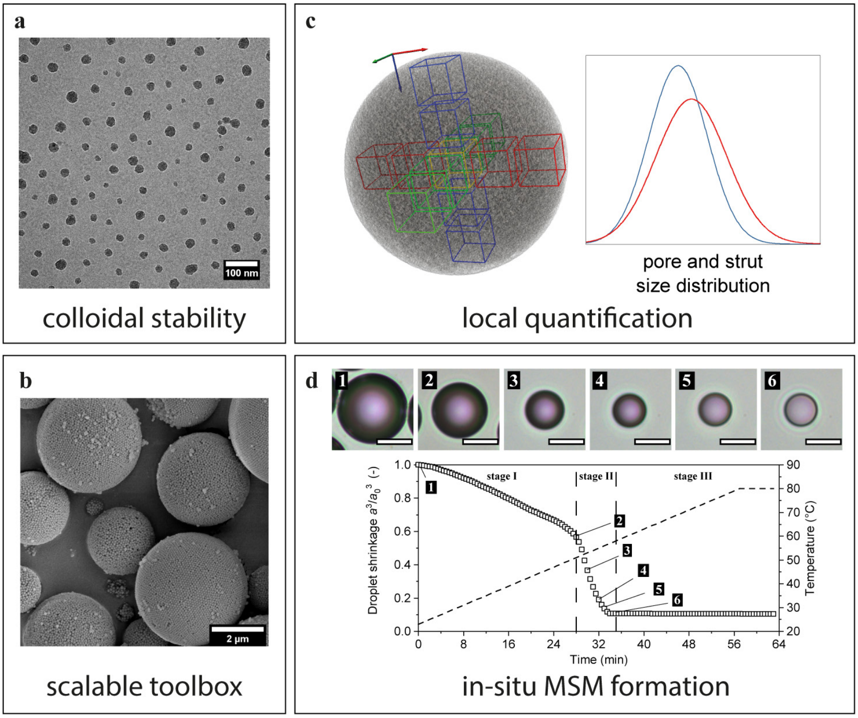

Figure 1.5: Schematic overview of some of the different characterization tools used throughout this work to study MSM formation: **(a)** TEM, **(b)** SEM, **(c)** tomography and **(d)** optical microscopy. Scale-bar in panel d: 20 µm.

To bridge the gap from bulk to the nanometer pore scale, quantitative electron tomography is combined with computer simulations. This combination makes it possible to obtain not only insight into the multiscale pore network of MSMs but also provides information on the mass transport properties through the porous structures (**Figure 1.5c**). Finally, to elucidate the actual MSM formation process, a microfluidic platform is combined with dynamic time-resolved optical imaging. This powerful combination enables the study of emulsion droplet shrinkage under specific experimental conditions and gives qualitative information on the gelation process and water transport in spherical confinement (**Figure 1.5d**).

1.4 Thesis outline

The aim of the work described in this thesis is to gain a fundamental understanding of the entire formation process and characterization of resulting MSMs, including: nanoparticle gelation, creating an emulsion model system, strategies for the development of a scalable toolbox of MSMs, a novel multiscale imaging and analysis to characterize MSMs and the introduction of a microfluidic platform for the synthesis of monodisperse MSMs and a fundamental understanding of water transport and gelation in confinement. We believe that the ideas described throughout this work are an important step towards the rational design of truly hierarchical materials for use in separation, catalysis and other applications.

In **Chapter 2** we introduce the colloidal silica building blocks used for the formation of MSMs and we use the extended version of the DLVO theory to quantitatively describe the stability of each silica building block and determine the critical salt concentrations to induce particle aggregation across multiple timescales. For this, a hydration repulsion potential is added to the classical DLVO theory, which is derived from experimental, macroscopic gelation experiments. In addition, electrokinetic charge densities are experimentally investigated as a function of nanoparticle size from zeta-potential measurements. A combination of cryo transmission electron microscopy, electrospray differential mobility analysis and dynamic light scattering are used to image and characterize the different colloidal silica sols.

In **Chapter 3** we describe a scalable process to synthesize MSMs with excellent reproducibility and independent control over pore size and overall porosity via the sol-gel emulsification of the different colloidal silica building blocks introduced in Chapter 2. By studying the independent manipulation of different assembly parameters during the sol-gel process, such as temperature, pressure, water uptake and the addition of salt, we demonstrate that we can precisely steer and control various porosity characteristics over a wider range than is shown so far in literature. In contrast with conventionally applied industrially relevant processes, the presented strategy does not require additional ageing or post-treatment steps and / or additional template molecules to guide the formation of the porous network.

In **Chapter 4** we demonstrate, for the first time, a method to obtain quantitative insight on the multiscale pore network of (commercial) MSMs similar to those synthesized in Chapter

3, using a combination of low convergence angle scanning transmission electron microscopy tomography with lattice Boltzmann simulations. We determine local variations in porosity, pore size distributions and intraparticle diffusion coefficient on the sub-particle scale that cannot be obtained otherwise, and show an excellent match between the single particle level and bulk. To overcome imaging artefacts inherent to imaging micrometer thick samples, i.e., local charging effects and the nonlinear relationship between image intensity and sample thickness, we developed a new correction algorithm in MATLAB based on the near perfect sphericity of the particles that can easily be expanded to other materials.

In **Chapter 5** we study the MSM formation process introduced in Chapter 3 in more detail using a microfluidic processing route in combination with time-resolved optical imaging. The effect of different parameters on the kinetics of colloidal assembly in confined spaces are explored in situ. In addition, a theoretical mass-transfer model is introduced to describe droplet shrinkage based on the local droplet density and solvent characteristics. The model is compared to experimental imaging results which were quantified by image analysis and show an excellent match.

In **Chapter 6** we extend the general principles laid out in Chapter 3 to fabricate MSMs with hierarchical structures, such as multilayered and hollow MSMs. We demonstrate the effect of fractal silica sols as building blocks on the porosity characteristics of MSMs and compare the results to conventional MSMs using standard bulk characterization techniques. In contrast with conventionally used spherical silica sols, MSMs constructed from fractal sols have a significantly higher microsphere porosity, whilst the perfect spherical shape remains intact.

In **Chapter 7** we give a summary of the main results presented in this thesis and conclude with an outlook. The work described in this thesis gives valuable insight in the underlying mechanisms of colloidal assembly in spherical confinement and provides the necessary tools for the microstructural design of tailor-made silica microspheres for use in separation applications and beyond.

1.5 References

1. Deer, W. A., Howie, R. A. & Zussman, J. *An Introduction to the Rock-Forming Minerals*. (Mineralogical Society of Great Britain and Ireland, 2013). doi:10.1180/DHZ.
2. Iler, R. K. *The Chemistry of Silica*. (John Wiley & Sons, Inc., 1979). ISBN: 047102404X.
3. Bergna, H. E. *The Colloid Chemistry of Silica*. *Advances* vol. 234 (American Chemical Society, 1994). doi: 10.1021/ba-1994-0234.
4. Reim, M. *et al.* Silica Aerogel Granulate Material for Thermal Insulation and Daylighting. *Sol. Energy* **79**, 131–139 (2005).
5. Guerrero-Martínez, A., Pérez-Juste, J. & Liz-Marzán, L. M. Recent Progress on Silica Coating of Nanoparticles and Related Nanomaterials. *Adv. Mater.* **22**, 1182–1195 (2010).

6. Polshettiwar, V. & Varma, R. S. Green Chemistry by Nano-Catalysis. *Green Chem.* **12**, 743–754 (2010).
7. Liu, B. *et al.* Switching Plastic Crystals of Colloidal Rods with Electric Fields. *Nat. Commun.* **5**, 1–8 (2014).
8. Randall, J. P., Meador, M. A. B. & Jana, S. C. Tailoring Mechanical Properties of Aerogels for Aerospace Applications. *ACS Appl. Mater. Interfaces* **3**, 613–626 (2011).
9. Slowing, I. I., Vivero-Escoto, J. L., Wu, C. W. & Lin, V. S. Y. Mesoporous Silica Nanoparticles as Controlled Release Drug Delivery and Gene Transfection Carriers. *Adv. Drug Deliv. Rev.* **60**, 1278–1288 (2008).
10. Hyde, E. D. E. R., Seyfaee, A., Neville, F. & Moreno-Atanasio, R. Colloidal Silica Particle Synthesis and Future Industrial Manufacturing Pathways: A Review. *Ind. Eng. Chem. Res.* **55**, 8891–8913 (2016).
11. Hench, L. L. & West, J. K. The Sol-Gel Process. *Chem. Rev.* **90**, 33–72 (1990).
12. Roy, R. Ceramics by the Solution-Sol-Gel Route. *Science (80-.).* **238**, 1664–1669 (1987).
13. Wright, J. D. & Sommerdijk, N. A. J. M. *Sol-Gel Materials Chemistry and Applications*. (CRC Press, 2001).
14. Stöber, W., Fink, A. & Bohn, E. Controlled Growth of Monodisperse Silica Spheres in the Micron Size Range. *J. Colloid Interface Sci.* **26**, 62–69 (1968).
15. Green, D. L. *et al.* Size, Volume fraction, and Nucleation of Stöber Silica Nanoparticles. *J. Colloid Interface Sci.* **266**, 346–358 (2003).
16. Drummond, C., McCann, R. & Patwardhan, S. V. A Feasibility Study of the Biologically Inspired Green Manufacturing of Precipitated Silica. *Chem. Eng. J.* **244**, 483–492 (2014).
17. Alexander, G. B. The Preparation of Monosilicic Acid. *J. Am. Chem. Soc.* **75**, 2887–2888 (1953).
18. Brinker, C. J. Hydrolysis and Condensation of Silicates: Effects on Structure. *J. Non. Cryst. Solids* **100**, 31–50 (1988).
19. Carcouët, C. C. M. C. *et al.* Nucleation and Growth of Monodisperse Silica Nanoparticles. *Nano Lett.* **14**, 1433–1438 (2014).
20. Qu, H., Bhattacharyya, S. & Ducheyne, P. Sol–Gel Processed Oxide Controlled Release Materials. in *Comprehensive Biomaterials* 475–495 (Elsevier, 2011). doi:10.1016/B978-0-08-055294-1.00138-0.
21. Ciriminna, R. *et al.* The Sol–Gel Route to Advanced Silica-Based Materials and Recent Applications. *Chem. Rev.* **113**, 6592–6620 (2013).
22. Lu, Y. *et al.* Continuous Formation of Supported Cubic and Hexagonal Mesoporous Films by Sol-Gel Dip-coating. *Nature* **389**, 364–368 (1997).
23. Siouffi, A. M. Silica Gel-based Monoliths Prepared by the Sol-Gel Method: Facts and Figures. *J. Chromatogr. A* **1000**, 801–818 (2003).
24. Shirtcliffe, N. J., McHale, G., Newton, M. I. & Perry, C. C. Intrinsically Superhydrophobic Organosilica Sol-Gel Foams. *Langmuir* **19**, 5626–5631 (2003).
25. Teng, Z., Han, Y., Li, J., Yan, F. & Yang, W. Preparation of Hollow Mesoporous Silica Spheres by a Sol-Gel/Emulsion Approach. *Microporous Mesoporous Mater.* **127**, 67–72 (2010).
26. Huo, Q. S., Feng, J. L., Schuth, F. & Stucky, G. D. Preparation of Hard Mesoporous Silica Spheres. *Chem. Mater.* **9**, 14–17 (1997).
27. Gustafsson, H. & Holmberg, K. Emulsion-based Synthesis of Porous Silica. *Adv.*

Colloid Interface Sci. **247**, 426–434 (2017).

28. Zhang, H. & Cooper, A. I. Emulsion-templated Hierarchically Porous Silica Beads using Silica Nanoparticles as Building Blocks. *Ind. Eng. Chem. Res.* **44**, 8707–8714 (2005).
29. Unger, K. K., Ditz, R., Machtejevas, E. & Skudas, R. Liquid Chromatography-its Development and Key Role in Life Science Applications. *Angew. Chemie* **49**, 2300–2312 (2010).
30. Snyder, L. R., Kirkland, J. J. & Dolan, J. W. *Introduction to Modern Liquid Chromatography. High-Performance Gradient Elution: The Practical Application of the Linear-Solvent-Strength Model* (John Wiley & Sons, Inc., 2009). doi:10.1002/9780470508183.
31. Nyström, M., Herrmann, W., Larsson, B. (EKA Nobel AB) US 5256386 (1993).
32. Balducci, L., Ungarelli, R. (Enichem S.p.A.; Eniricerche S.p.A.) US 6103209 (2000).
33. Zhiping, J., Fisk, R. P., O' Gara, J., Walter, T. H., Wyndham, K.D. (Waters Technologies Corporation) US 8778453 (2004).
34. Velev, O. D., Jede, T. A., Lobo, R. F. & Lenhoff, A. M. Porous Silica via Colloidal Crystallization. *Nature* **389**, 447–448 (1997).
35. Manoharan, V. N. Dense Packing and Symmetry in Small Clusters of Microspheres. *Science* **301**, 483–487 (2003).
36. Lee, S. Y., Gradon, L., Janeczko, S., Iskandar, F. & Okuyama, K. Formation of Highly Ordered Nanostructures by Drying Micrometer Colloidal Droplets. *ACS Nano* **4**, 4717–4724 (2010).
37. Lebedev-Stepanov, P. & Vlasov, K. Simulation of Self-Assembly in an Evaporating Droplet of Colloidal Solution by Dissipative Particle Dynamics. *Colloids Surfaces A Physicochem. Eng. Asp.* **432**, 132–138 (2013).
38. Wang, D. *et al.* Interplay Between Spherical Confinement and Particle Shape on the Self-Assembly of Rounded Cubes. *Nat. Commun.* **9**, 2228 (2018).
39. Wintzheimer, S. *et al.* Supraparticles: Functionality from Uniform Structural Motifs. *ACS Nano* **12**, 5093–5120 (2018).
40. Sacanna, S. & Pine, D. J. Shape-anisotropic Colloids: Building Blocks for Complex Assemblies. *Curr. Opin. Colloid Interface Sci.* **16**, 96–105 (2011).
41. Cho, Y.-S., Kim, S.-H., Yi, G.-R. & Yang, S.-M. Self-organization of Colloidal Nanospheres inside Emulsion Droplets: Higher-order Clusters, Supraparticles, and Supraballs. *Colloids Surfaces A Physicochem. Eng. Asp.* **345**, 237–245 (2009).
42. de Nijs, B. *et al.* Entropy-Driven Formation of Large Icosahedral Colloidal Clusters by Spherical Confinement. *Nat. Mater.* **14**, 56–60 (2015).
43. Yan, N., Liu, H., Zhu, Y., Jiang, W. & Dong, Z. Entropy-Driven Hierarchical Nanostructures from Cooperative Self-Assembly of Gold Nanoparticles/Block Copolymers under Three-Dimensional Confinement. *Macromolecules* **48**, 5980–5987 (2015).
44. Luo, D., Yan, C. & Wang, T. Interparticle Forces Underlying Nanoparticle Self-Assemblies. *Small* **11**, 5984–6008 (2015).
45. Piccinini, E., Pallarola, D., Battaglini, F. & Azzaroni, O. Self-limited Self-Assembly of Nanoparticles into Supraparticles: Towards Supramolecular Colloidal Materials by Design. *Mol. Syst. Des. Eng.* **1**, 155–162 (2016).
46. Wang, T., LaMontagne, D., Lynch, J., Zhuang, J. & Cao, Y. C. Colloidal Superparticles from Nanoparticle Assembly. *Chem. Soc. Rev.* **42**, 2804–2823 (2013).
47. Velev, O. D., Furusawa, K. & Nagayama, K. Assembly of Latex Particles by Using

Emulsion Droplets as Templates. 1. Microstructured Hollow Spheres. *Langmuir* **12**, 2374–2384 (1996).

48. Velev, O. D., Furusawa, K. & Nagayama, K. Assembly of Latex Particles by using Emulsion Droplets as Templates. 2. Ball-like and Composite Aggregates. *Langmuir* **12**, 2385–2391 (1996).
49. Velev, O. D. & Nagayama, K. Assembly of Latex Particles by using Emulsion Droplets. 3. Reverse (water in oil) System. *Langmuir* **13**, 1856–1859 (1997).
50. Bai, F. *et al.* A Versatile Bottom-up Assembly Approach to Colloidal Spheres from Nanocrystals. *Angew. Chemie - Int. Ed.* **46**, 6650–6653 (2007).
51. Andersson, N., Kronberg, B., Corkery, R. & Alberius, P. Combined Emulsion and Solvent Evaporation (ESE) Synthesis Route to Well-Ordered Mesoporous Materials. *Langmuir* **23**, 1459–1464 (2007).
52. Dinsmore, A. D. *et al.* Colloidosomes: Selectively Permeable Capsules Composed of Colloidal Particles. *Science* **298**, 1006–1009 (2002).
53. Bollhorst, T., Rezwan, K. & Maas, M. Colloidal capsules: Nano- and Microcapsules with Colloidal Particle Shells. *Chem. Soc. Rev.* **46**, 2091–2126 (2017).
54. Kotov, N. A. Practical Aspects of Self-Organization of Nanoparticles: Experimental Guide and Future Applications. *J. Mater. Chem.* **21**, 16673 (2011).
55. Kobayashi, M., Juillerat, F., Galletto, P., Bowen, P. & Borkovec, M. Aggregation and Charging of Colloidal Silica Particles: Effect of Particle Size. *Langmuir* **21**, 5761–5769 (2005).
56. Sögaard, C., Funehag, J. & Abbas, Z. Silica Sol as Grouting Material: a Physio-chemical Analysis. *Nano Converg.* **5**, 6 (2018).
57. Zhao, D. Triblock Copolymer Syntheses of Mesoporous Silica with Periodic 50 to 300 Ångstrom Pores. *Science* **279**, 548–552 (1998).
58. Kresge, C. T., Leonowicz, M. E., Roth, W. J., Vartuli, J. C. & Beck, J. S. Ordered Mesoporous Molecular Sieves Synthesized by a Liquid-Crystal Template Mechanism. *Nature* **359**, 710–712 (1992).
59. Anderson, M. W. *et al.* Modern Microscopy Methods for the Structural Study of Porous Materials. *Chem. Commun.* **4**, 907–916 (2004).
60. Kruk, M. *et al.* Determination of Pore Size and Pore Wall Structure of MCM-41 by Using Nitrogen Adsorption, Transmission Electron Microscopy, and X-ray Diffraction. *J. Phys. Chem. B* **104**, 292–301 (2000).
61. Meurig Thomas, J. & Midgley, P. A. High-Resolution Transmission Electron Microscopy: the Ultimate Nanoanalytical Technique. *Chem. Commun.* 1253–1267 (2004) doi:10.1039/B315513G.
62. Friedrich, H., de Jongh, P. E., Verkleij, A. J. & de Jong, K. P. Electron Tomography for Heterogeneous Catalysts and Related Nanostructured Materials. *Chem. Rev.* **109**, 1613–1629 (2009).
63. Dubochet, J., Chang, J.-J., Freeman, R., Lepault, J. & McDowall, A. W. Frozen Aqueous Suspensions. *Ultramicroscopy* **10**, 55–61 (1982).
64. Friedrich, H., Frederik, P. M., de With, G. & Sommerdijk, N. A. J. M. Imaging of Self-Assembled Structures: Interpretation of TEM and Cryo-TEM Images. *Angew. Chemie Int. Ed.* **49**, 7850–7858 (2010).
65. Williams, D. B. & Carter, C. B. *Transmission Electron Microscopy: A Textbook for Materials Science*. (Springer US, 2009). doi:10.1007/978-0-387-76501-3.
66. van Tendeloo, G., Van Dyck, D. & Pennycook, S. J. *Handbook of Nanoscopy*. (Wiley-VCH Verlag GmbH & Co. KGaA, 2012). doi:10.1002/9783527641864.

67. van Huis, M. A. & Friedrich, H. Electron Microscopy Techniques. in *Nanoparticles* 191–221 (Springer Berlin, 2014). doi:10.1007/978-3-662-44823-6_7.
68. Schulz-Ekloff, G., Rathouský, J. & Zukal, A. Mesoporous Silica with controlled Porous Structure and Regular Morphology. *Int. J. Inorg. Mater.* **1**, 97–102 (1999).
69. Che, S. *et al.* Direct Observation of 3D Mesoporous Structure by Scanning Electron Microscopy (SEM): SBA-15 Silica and CMK-5 Carbon. *Angew. Chemie Int. Ed.* **42**, 2182–2185 (2003).
70. Omer, L., Ruthstein, S., Goldfarb, D. & Talmon, Y. High-Resolution Cryogenic-Electron Microscopy Reveals Details of a Hexagonal-to-Bicontinuous Cubic Phase Transition in Mesoporous Silica Synthesis. *J. Am. Chem. Soc.* **131**, 12466–12473 (2009).
71. Lowell, S., Shields, J. E., Thomas, M. A. & Thommes, M. *Characterization of Porous Solids and Powders: Surface Area, Pore Size and Density*. vol. 16 (Springer Netherlands, 2004). doi: 10.1007/978-1-4020-2303-3
72. Thommes, M. *et al.* Physisorption of Gases, with Special Reference to the Evaluation of Surface Area and Pore Size Distribution (IUPAC Technical Report). *Pure Appl. Chem.* **87**, 1051–1069 (2015).

Chapter 2

Colloidal Silica Stability and Particle Aggregation

Abstract

Colloidal silica nanoparticles (silica sols) are essential building blocks for a wide variety of functional materials and relevant to many industries including commodity chemicals and pharma. Assembly of sols into often porous materials, such as the mesoporous silica microspheres (MSMs) studied in this thesis, proceeds via silica particle aggregation. As aggregation dynamics strongly depends on the choice of the silica sols, this directly influences the internal and external morphology of the MSMs that can be obtained. Therefore, a basic understanding of the size, shape and stability of the silica sols is vital in order to design and synthesize MSMs with tunable properties. In this chapter, a theoretical framework is outlined that provides a solid foundation for the sol-gel experiments described in the remainder of the thesis. Electron microscopy and scattering techniques are used to characterize in detail the different sols. The stability of the sols is assessed by an extended version of the DLVO theory and the chapter concludes with an in-depth discussion of particle aggregation dynamics as a function of salt concentration.

Part of this chapter is published in:

Fijneman, A. J. *et al.* Multiscale Colloidal Assembly of Silica Nanoparticles into Microspheres with Tunable Mesopores. *Adv. Funct. Mater.* **30**, 2002725 (2020).

2.1 General introduction

A colloidal system is typically defined as a heterogeneous mixture of microscopic particles in the order of 1 – 1000 nm called colloids (solid, liquid or gas), that are dispersed in a continuous medium[1]. Examples include foams (gas in liquid), emulsions (liquid in liquid), colloidal suspensions or sols (solid in liquid) and aerosols (solid in gas). Unlike solutions, which are homogeneous mixtures of two or more substances, colloidal systems display the Tyndall effect, i.e., the scattering of visible light by colloidal particles[2]. In this work the words colloidal suspension and (silica) sol are used interchangeably and all refer to a suspension of silica nanoparticles of variable but well-defined size in water. A sol is considered stable if the nanoparticles do not settle or aggregate for a certain period of time, typically a day or longer. Depending on the nature of the particles, a sol can be stable for many years[3,4].

The stability of sols can be described using the DLVO theory, named after Derjaguin, Landau, Verwey and Overbeek. The DLVO theory provides a theoretical framework that describes the interaction potential between two charged surfaces in a liquid medium[5]. The interaction potential is a combination of attractive van der Waals interactions and repulsive electrostatic interactions[6]. The combination of these interactions leads to a potential energy-distance profile with, at close separation, a deep minimum, called the primary minimum, followed by a maximum, called the energy barrier, and sometimes followed by another minimum, called the secondary minimum (**Figure 2.1**). The height of the energy barrier corresponds directly to the probability that a particle-particle collision will lead to particle aggregation and is determined by physicochemical parameters such as the Hamaker constant, surface potential, electrolyte concentration and the dielectric constant of the solvent[7].

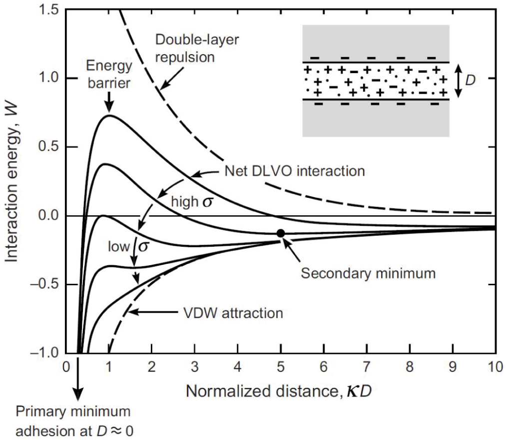

Figure 2.1: Schematic illustration of an energy-distance profile for the DLVO interaction between two planar surfaces. Image adopted from Israelachvili[8].

The terms aggregation, agglomeration, flocculation, coagulation and gelation are often used interchangeably but strictly speaking mean different things. Agglomeration and aggregation are generic terms for the formation of a contiguous cluster of primary particles that are held together by physical adhesion forces or chemical bonds. The difference is in the way the particles are held together. Agglomerates are held loosely together and can usually be broken up again by, e.g., strong mechanical interactions. Aggregates are held strongly together and cannot be broken up again. The term flocculation is often used for agglomeration induced by polymeric agents. Coagulation is agglomeration in liquid dispersions. In sol-gel chemistry, aggregation, coagulation and gelation are one and the same[2].

Most sols become unstable and coagulate when the particles are no longer charged, thus, are no longer able to repel each other effectively. Silica sols are an exception. Iler showed that a silica sol can be stable at the point of zero charge (pH 2), even though the nanoparticles don't repel each other[3]. Irreversible particle aggregation only occurs when two nanoparticles form siloxane bridges between the particles. For the base catalyzed route, which is the preferred route in this work due to stability reasons, the formation of siloxane bridges is catalyzed by the presence of hydroxyl ions, which are a function of the pH[9]. The higher the pH, the more hydroxyl ions are present and, therefore, the lower the particle stability. However, the surface charge also increases with increasing pH. At high pH the nanoparticles are highly charged, which prevents the particles from coming close enough together to actually form siloxane bridges[10]. At the point of zero charge the particles have no charge, but the concentration of hydroxyl ions is also very low, which explains why the nanoparticles can still be stable without any electrostatic repulsion. The minimum in stability is reached at pH 6, due to an increase in hydroxyl ions while the surface charge density is still relatively low. At higher pH, between 8 and 10.5, the nanoparticles become so highly charged that they effectively repel each other regardless of the hydroxyl ion concentration. Above pH 10.5 the silica starts to dissolve. A negatively charged stable silica sol therefore has, by definition, a pH between 8 and 10.5 (**Figure 2.2**).

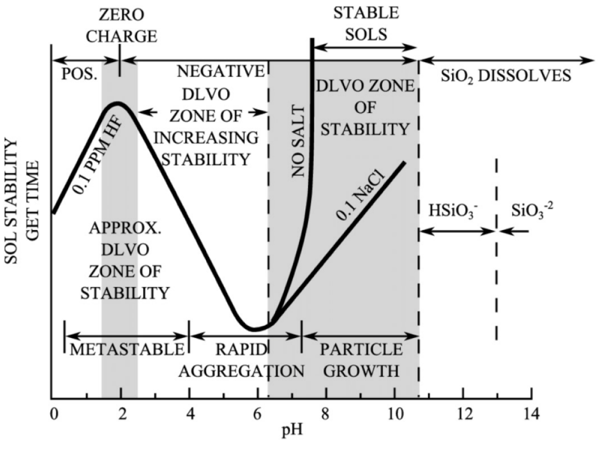

Figure 2.2: Effect of pH on the stability of a colloidal silica sol. Solid lines represent experimental results by Iler[4]. Below the point of zero charge (pH 2), the nanoparticles are positively charged. Above the point of zero charge, the nanoparticles are negatively charged. Between pH 2 and 4 and pH 8 and 10.5 the sols are stable. Shaded areas are predictions by the DLVO theory. The DLVO theory does not match the experimental results at low pH due to the role of hydroxyl ions that are not taken into consideration in the DLVO theory. Image adopted from Bergna[4].

In this chapter, a series of silica sol nanoparticles ranging from 4 nm up to 100 nm are characterized with microscopy and scattering techniques. Electrokinetic charge densities are experimentally investigated as a function of nanoparticle size from zeta-potential measurements. The stability of the silica sols is described quantitatively using an extended version of the DLVO theory. For this, a hydration repulsion potential is added to the classical DLVO theory, which is derived from macroscopic gelation experiments. The extended DLVO theory is then used to predict particle aggregation as a function of salt concentration for every silica sol and an explanation is given for the different rates of destabilization of each silica sol.

2.2 Characterization of silica nanoparticles

Before the stability of the sols can be described with the DLVO theory, several key properties must be characterized first. Most important is determining the size of the nanoparticles. There are several techniques to measure the size and size distribution of silica nanoparticles. Here, cryogenic transmission electron microscopy (cryoTEM) was used to image the nanoparticles in their native solution state at high resolution and to measure the size and size distribution of the five silica sols employed in this thesis. Electrospray-differential mobility analysis (ES-DMA) and dynamic light scattering (DLS) were also utilized to measure the size distribution on the bulk scale.

TEM is a powerful technique to image organic or inorganic materials with sub-nanometer resolution. Samples are generally dispersed on a metal grid covered with a thin carbon layer as a suspension and subsequently dried in air or by blotting. The sample has to be very thin (electron-transparent) in order for the electrons to travel through the sample[11,12]. Since drying can affect the material structure, it can be worthwhile to vitrify the sample in its native state under cryogenic conditions. In cryoTEM the sample is prepared by plunge freezing the specimen in liquid ethane, which rapidly cools down the sample. If done correctly, the sample will be vitrified in a thin, transparent film of amorphous water in the order of 100 - 200 nm in thickness[13,14].

The high resolution information provided by cryoTEM is particular useful when imaging silica nanoparticles that are only a few nanometers in size[15]. In our case, imaging was relatively straightforward. Samples were diluted to a silica concentration of approximately 1 wt% using Milli-Q water to prevent particles from overlapping along the sample thickness and were subsequently vitrified and imaged. The results are shown in **Figure 2.3**.

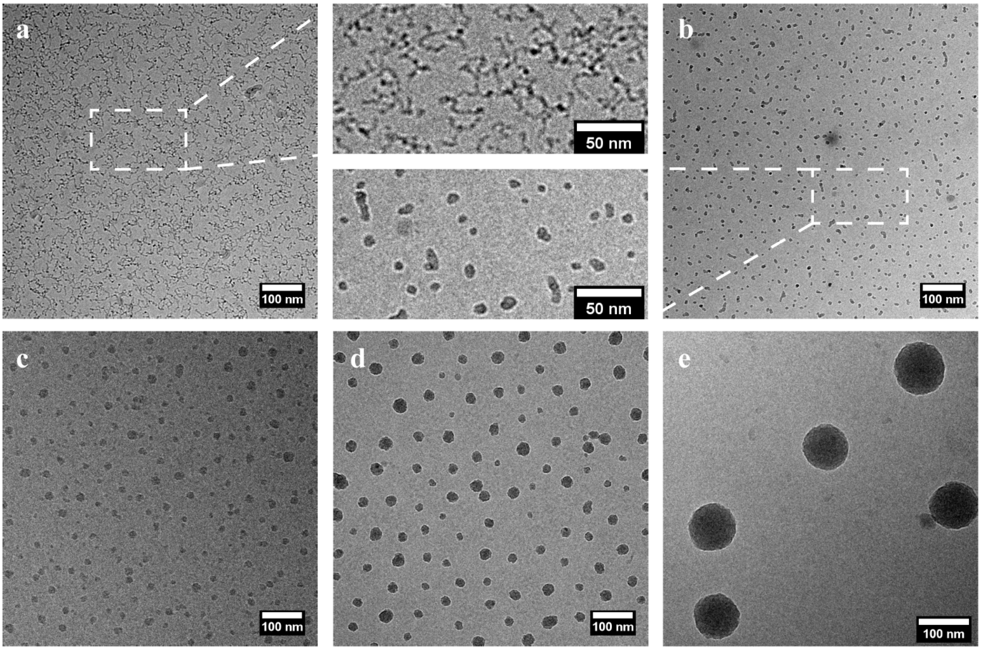

Figure 2.3: CryoTEM micrographs of dilute silica nanoparticles (1 wt%). **(a)** 4 nm (sol 1), **(b)** 8 nm (sol 2), **(c)** 18 nm (sol 3), **(d)** 25 nm (sol 4), **(e)** 100 nm (sol 5).

Aside from the obvious difference in size between the five silica sols, there are some notable differences in the shape of the nanoparticles as well. The largest nanoparticles are practically spherical, whereas the smallest nanoparticles have started to form aggregates. The reason for this is the low stability of this sol, which will be explained using the DLVO theory later in this chapter.

For size analysis approximately 300 particles of each sample were analyzed manually by measuring the longest and shortest axis using an in-house developed MATLAB script. Only individual distinguishable particles were measured. For the smallest nanoparticles, either discrete nanoparticles were imaged or particles that could easily be identified within the aggregates due to differences in contrast. The values of both axes were multiplied and the square root was taken to obtain a geometrical mean diameter and standard deviation (SD) of each nanoparticle. A number mean diameter $D_\mathrm{P}[1,0]$ and volume mean diameter $D_\mathrm{P}[4,3]$ of the whole population were calculated from:

$$D_\mathrm{P}[1,0] = \frac{\sum_{i=1}^{n} D_{\mathrm{P},i}}{n} \qquad (2.1)$$

$$D_\mathrm{P}[4,3] = \frac{\sum_{i=1}^{n} D_{\mathrm{P},i}^4}{\sum_{i=1}^{n} D_{\mathrm{P},i}^3} \tag{2.2}$$

Additionally, the aspect ratio was calculated by dividing the longest axis over the shortest axis. The results are summed up in **Table 2.1**. The number mean and volume mean particle size distributions are shown in **Figure 2.4**.

Table 2.1: Nanoparticle size and aspect ratio as determined via cryoTEM.

sol	number mean $D_\mathrm{P}[1,0] \pm$ SD (nm)	standard error	volume mean $D_\mathrm{P}[4,3] \pm$ SD (nm)	standard error	aspect ratio
1	4.2 ± 1.0	0.06	4.9 ± 1.2	0.07	1.36 ± 0.31
2	8.2 ± 2.5	0.13	10.6 ± 3.5	0.18	1.31 ± 0.33
3	17.5 ± 4.6	0.26	21.6 ± 6.1	0.34	1.20 ± 0.16
4	25.2 ± 5.8	0.32	28.8 ± 6.8	0.38	1.13 ± 0.10
5	95.4 ± 18.3	2.67	102.3 ± 19.6	2.85	1.05 ± 0.05

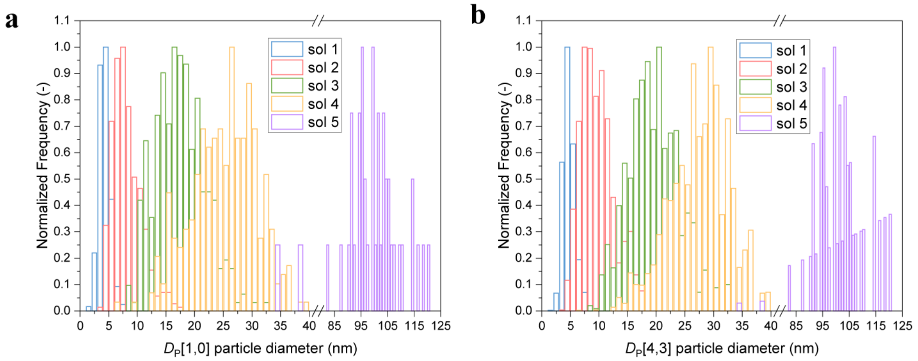

Figure 2.4: (a) Number mean $D_\mathrm{P}[1,0]$ particle size distribution and **(b)** Volume mean $D_\mathrm{P}[4,3]$ particle size distribution, determined via cryoTEM. Approximately 300 particles were measured manually per sample.

Measuring particles by hand is a tedious process and may be subject to operator bias. It is therefore worthwhile to compare the results to other techniques such as electrospray-differential mobility analysis (ES-DMA) or dynamic light scattering (DLS). In ES-DMA the colloidal nanoparticles are aerosolized via an electrospray, after which they are charged and classified based on their electrical mobility using an ion mobility spectrometer. The mobility of the nanoparticles depends on the particle size and their electrical charge. Two nanoparticles with the same charge but different sizes will have a different electrical mobility. For spherical particles the mobility diameter is equivalent to the volumetric particle diameter. For non-spherical particles, however, the mobility diameter can be a significant overestimation of the actual particle size[16]. Here, ES-DMA was used to measure the mobility particle size distribution of the sols 1-4 and the results were compared to the size distribution obtained via cryoTEM. The results are summed up in **Table 2.2** and shown in **Figure 2.5a**.

Table 2.2: Nanoparticle size as determined via ES-DMA and DLS, respectively.

sol	mobility diameter ± SD (nm)	standard error	Z-average (nm)	standard error
1	15.5 ± 5.1	0.20	-	-
2	11.6 ± 2.9	0.09	-	-
3	21.2 ± 4.8	0.11	-	-
4	30.6 ± 6.6	0.21	-	-
5	-	-	104.1 ± 1.6	0.71

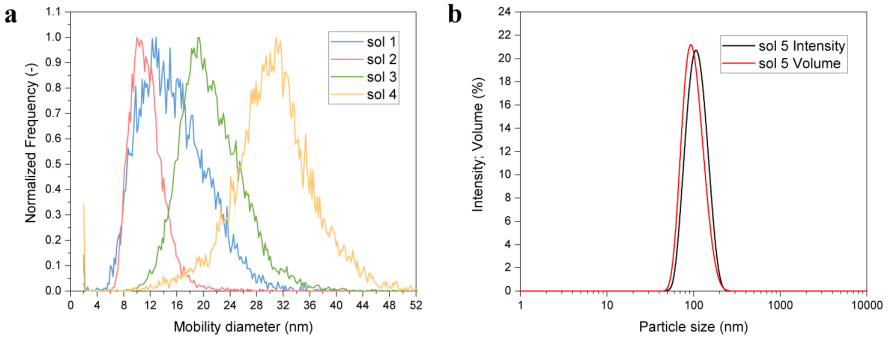

Figure 2.5: (a) Mobility or volume mean particle size distribution of sol 1 to 4, determined via ES-DMA. **(b)** Intensity and volume weighted size distribution of sol 5, determined via DLS.

Since ES-DMA is not suitable to measure large nanoparticles, DLS was used to measure the size distribution of the sol 5 with the largest nanoparticles. In DLS the intensity of scattered light is measured as a function of time using a high power, coherent laser. As the particles move in solution due to Brownian motion, the intensity of the scattered light will fluctuate due to interference of the light waves. From the intensity fluctuations a diffusion coefficient of the particles can be calculated, which is related to the hydrodynamic radius of the particles via the Stokes-Einstein relation[17]. An intensity and volume weighted size distribution is plotted in **Figure 2.5b** and the Z-average particle size is listed in Table 2.2.

The Z-average is calculated using the following equation[17]:

$$D_Z = \frac{\sum_{i=1}^{n} q_i}{\sum_{i=1}^{n} \left(q_i \big/ D_{P,i} \right)} \tag{2.3}$$

Here, q_i is the scattering intensity of particle i, and $D_{P,i}$ is the diameter of particle i.

Aside from sol 1 the results obtained via the two different techniques are quite similar. The particle size distributions measured via ES-DMA are slightly larger than those measured via cryoTEM but this can be explained due to the difference between a number weighted size distribution (via cryoTEM) and a volume weighted size distribution (via ES-DMA). The size distribution for sol 1 measured via ES-DMA is, however, significantly different. This can be attributed to the nanoaggregates that are present in this sample. Due to these aggregates the actual particle size is significantly overestimated by ES-DMA.

2.3 Bulk alkali concentration as a function of pH

All sols used in this work have been adjusted in pH to the stable regime, i.e., pH 8.0 – 10.5, by the addition of ammonia. The amount of ammonia that is added has a direct effect on the thickness of the electric double layer. It is therefore important to have an estimate of the number of ions present in each sol.

Ammonia in water acts as a weak base according to the following equilibrium:

$$\mathrm{NH_3 + H_2O \rightleftarrows NH_4^+ + OH^-} \tag{2.4}$$

Depending on the temperature and pH some of the ammonia is converted into ammonium ions. The ratio of ammonia and ammonium can be related to the pH using the Henderson-Hasselbalch equation[18]:

$$\mathrm{p}[\mathrm{OH}] = \mathrm{p}K_\mathrm{b} + \log\left(\frac{[\mathrm{NH_4^+}]}{[\mathrm{NH_3}]}\right) \tag{2.5}$$

in which the base dissociation constant K_b can be derived from the acid dissociation constant K_a and the ionization constant of water K_w:

$$\mathrm{p}K_\mathrm{b} = \mathrm{p}K_\mathrm{w} - \mathrm{p}K_\mathrm{a} \tag{2.6}$$

K_a can be calculated using the following equation[19]:

$$K_\mathrm{a} = 5.67\times10^{-10}\exp\left(-6286\left(\frac{1}{T}-\frac{1}{298.15}\right)\right) \tag{2.7}$$

At $T = 25$ °C, $K_\mathrm{a} = 5.67\times10^{-10}$ and subsequently $\mathrm{p}K_\mathrm{a} = 9.24$ and $\mathrm{p}K_\mathrm{b} = 4.75$.

The ratio of ammonia to ammonium can then be plotted as a function of the pH (**Figure 2.6**).

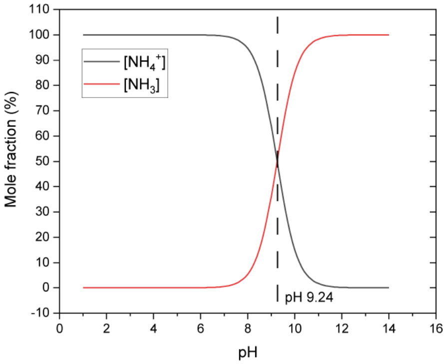

Figure 2.6: Ammonia and ammonium mole fraction as a function of pH at $T = 25$ °C.

Figure 2.6 clearly shows that at pH 9.24 the concentration of ammonia is equal to the concentration of ammonium. The ammonium ion concentration for each sol is shown in **Table 2.3**.

Table 2.3: Equilibrium ion concentration of the silica sols.

sol	pH	C_{ammonia} (M)	$[NH_3]_{eq}$	$[NH_4^+]_{eq}$
1	10.1	0.65	0.60	0.08
2	9.2	0.10	0.05	0.05
3	8.6	0.08	0.01	0.07
4	9.1	0.12	0.07	0.07
5	8.6	0.02	0.00	0.02

The alkali concentration of sol 1 is significantly higher in comparison to the concentration for the other sols, which is due to its high specific surface area. Therefore, a higher alkali concentration is required to bring the sol into the stable pH range. Regardless, all of these alkali concentrations are relatively low and are not large enough to destabilize the sol due to shielding of the surface charges[10]. In the next section the bulk ion concentration is used to calculate the thickness of the electric double layer for each sol.

2.4 Electrokinetic charge density as a function of particle size

Each nanoparticle has a certain number of ions near its surface that can interact with the particle: the electric double-layer. The ions closest to the particle surface are bound to the particle surface due to electrostatic interactions (Stern layer). Ions further away from the surface can move around freely (diffuse layer). The distribution of the ions in the diffuse layer can be described using the Gouy-Chapman theory, which is based on the Poisson–

Boltzmann equation[20,21]. The thickness of the electric double-layer (Debye length, $1/\kappa$) can be calculated from the bulk ion concentration[6]:

$$\kappa = \sqrt{2IN_{\mathrm{A}}e^2 / \varepsilon\varepsilon_0 k_{\mathrm{B}}T} \tag{2.8}$$

where I is the ionic strength of the solution given by:

$$I = \frac{1}{2}\sum_i z_i^2 C_i N_{\mathrm{A}} \tag{2.9}$$

where N_{A} is Avogadro's number, e the elementary charge, $\varepsilon\varepsilon_0$ the dielectric constant of the solvent, k_{B} the Boltzmann constant, T the temperature, z_i is the valency of ion i and C_i the molar concentration of ion i.

Equation (2.8) shows that the larger the bulk ion concentration, the shorter the Debye length. This is logical because the more ions are near a charged surface, the more surface charges are shielded and the more compact the diffuse double-layer becomes. The thickness of the double-layer for each sol are listed in **Table 2.4**.

The double-layer is coupled to the bulk liquid via a shear plane, which is at a potential referred to as the zeta-potential. The zeta-potential cannot be measured directly but it can be calculated from electrophoretic mobility measurements via the Henry equation[22]:

$$\mu_{\mathrm{e}} = \frac{2\varepsilon\varepsilon_0\zeta f(\kappa a)}{3\eta} \tag{2.10}$$

where μ_{e} is the electrophoretic mobility, ζ the zeta-potential, $f(\kappa a)$ the Henry function, wherein κ is the inverse Debye length, a the particle radius, and η the viscosity of the medium at zero shear rate. The other symbols have their usual meaning.

The Henry function depends on the thickness of the Debye length compared to the particle radius. A simple empirical relation for the Henry function with a relative error of less than 0.1% is given by Swan et al.[23]:

$$f(\kappa a) = \frac{16 + 18\kappa a + 3(\kappa a)^2}{16 + 18\kappa a + 2(\kappa a)^2} \tag{2.11}$$

For $\kappa a \gg 1$, which means a very thin double layer compared to the particle size, $f(\kappa a) \to 1.5$, referred to as the Smoluchowski approximation. For $\kappa a \ll 1$, a thick double layer, $f(\kappa a) \to 1$, referred to as the Hückel approximation[24].

For all sols the Henry function was calculated using equation (2.11) after which two sets of ten zeta-potential measurements each were obtained. The average values and corresponding coefficients of variation are listed in Table 2.4.

The zeta-potential can be related to the electrokinetic charge density for symmetrical electrolytes via the empirical relationship proposed by Loeb et al.[22,25]:

$$\sigma_\zeta = \frac{\varepsilon\varepsilon_0 k_\mathrm{B} T \kappa}{e}\left[2\sinh\left(\frac{\bar{\zeta}}{2}\right)+\frac{4}{\kappa a}\tanh\left(\frac{\bar{\zeta}}{4}\right)\right] \tag{2.12}$$

with $\bar{\zeta} = \frac{e\zeta}{k_\mathrm{B} T}$ the dimensionless zeta potential.

Note that the electrokinetic charge density is the charge density normalized to the shear plane, unlike the surface charge density which is the charge density at the actual particle surface[25]. The surface charge density, however, cannot be calculated from the zeta-potential directly because the zeta-potential is not equal to the surface potential. The electrokinetic charge density gives an indication of the amount of charges on a silica nanoparticle, which originates from the amount of deprotonated silanol functional groups. The charge density of each sample was calculated using equation (2.12) and the results are summed up in Table 2.4 and visualized in **Figure 2.7**.

Table 2.4: Calculated Debye length, zeta-potential and electrokinetic charge density of each sample.

sol	$1/\kappa$ (nm)	κa	$f(\kappa a)$	ζ-potential (mV)	CV (%)	σ_ζ (mC·m^{-2})
1	1.52	1.39	1.04	−54.0 ± 2.4	4.4	−45.7
2	1.84	2.22	1.07	−57.5 ± 1.5	2.6	−35.5
3	1.66	5.27	1.17	−39.1 ± 2.3	5.8	−20.9
4	1.65	7.63	1.22	−35.3 ± 1.5	4.3	−17.9
5	3.17	16.4	1.32	−36.9 ± 1.4	3.7	−9.3

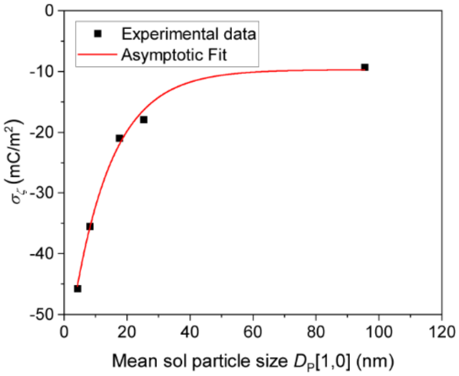

Figure 2.7: Electrokinetic charge density as a function of the particle size. Below a particle size of ~ 30 nm the charge density is strongly dependent on the particle size. Above ~ 30 nm the charge density becomes independent of the particle size.

Figure 2.7 clearly shows that the charge density depends on the particle size[26]. The larger the nanoparticle, the lower the charge density. Our results are in good agreement with a theoretical study by Barisik et al.[27] and an experimental study by Shi et al.[28], who showed that the charge density is constant for silica nanoparticles above 30 nm and goes down significantly, i.e., becomes more negative, for silica nanoparticles from 30 nm to 4 nm in size. This behavior can be attributed to a difference in the type of surface silanol groups depending on the nanoparticle size. Nanoparticles with a diameter less than 30 have a relatively high amount of isolated silanol groups that are far apart from each other due to the large particle curvature. In addition, the nanoparticles used in this work have corrugated surfaces, as seen in Figure 2.3. This implies that the silanol groups are most likely even further apart from each other. These isolated silanol groups can easily be deprotonated, corresponding to a more negative charge density. Nanoparticles with a diameter higher than 30 nm have relatively high amount of vicinal silanol groups, i.e., H-bridged silanol groups, which are not easily deprotonated[29].

2.5 DLVO theory and colloidal stability

With a good estimate of the size, electrolyte concentration and particle charge, the stability of the sols can be described using the DLVO theory. The classical expression for the interaction potential is given by[6]:

$$U_{\mathrm{SS}}(D) = U_{\mathrm{vdW}}(D) + U_{\mathrm{el}}(D) \tag{2.13}$$

where U_{ss} is the interaction potential for two spherical particles at a surface-to-surface separation distance D, U_{vdW} is the attractive van der Waals interaction potential and U_{el} is the repulsive electrostatic interaction potential caused by the electric double layer of the charged surface.

The electrostatic interaction potential between two spherical particles can be derived from the Poisson–Boltzmann equation[20,21]. Solving the full nonlinear Poisson-Boltzmann equation for spherical particles requires complex numerical analysis, which is beyond the scope of this work. The classical DLVO theory is based on the linearized Poisson-Boltzmann equation (Debye-Hückel approximation), for which an analytical solution exist[30,31]. An often used simplified solution for the electrostatic interaction potential between two identically charged spheres is given by[6]:

$$U_{\mathrm{el}}(D) = 32\pi a \varepsilon \varepsilon_0 \left(\frac{k_{\mathrm{B}} T}{ze} \right)^2 \gamma^2 \exp(-\kappa D) \tag{2.14}$$

with $\gamma = \tanh(\overline{\psi_0} / 4)$, and where $\overline{\psi_0} = \dfrac{e\psi_0}{k_{\mathrm{B}} T}$ is the dimensionless surface potential.

Equation (2.14) is, however, too simplified to describe the silica sols used in this work. The Debye-Hückel approximation is only valid for low potentials, $e|\psi| \ll k_{\mathrm{B}}T$, which is approximately 25 mV at room temperature. In addition, this analytical solution uses the Derjaguin approximation for two spherical particles[32], which is only valid when the particles are much larger than the electric double layer interaction (κa > 10) and the separation distances are small[30,33].

Since for most particles in this work κa is (much) smaller than 10 and the potentials are (much) larger than 25 mV, a more complex analytical solution is required. Sader et al.[34] modified equation (2.14) in order to calculate the electrostatic interaction potential between two identically charged spheres at constant surface potential for any distance regardless of the particle size, and this expression is valid for moderate to high surface potentials up to approximately 100 mV:

$$U_{\mathrm{el}}(D) = 64\pi\left(\frac{a^2}{2a+D}\right)\varepsilon\varepsilon_0\left(\frac{k_{\mathrm{B}}T}{ze}\right)^2 Y^2 \ln\left(1+\exp(-\kappa D)\right) \tag{2.15}$$

where $Y = \exp(\kappa D/2)\operatorname{arctanh}\left(\exp(-\kappa D/2)\tanh(\overline{\psi_0}/4)\right)$.

Equation (2.15) is a good approximation for the exact numerical results of the full Poisson-Boltzmann equation at constant surface potential[35].

It is important to mention that both equation (2.14) and equation (2.15) are derived for simple symmetrical monovalent electrolytes such as NaCl. The colloidal particles in this work are ammonia stabilized. Ammonia is not a simple, symmetrical monovalent electrolyte but for simplicity reasons we assume that ammonia in water takes the form of NH_4OH of which the ion concentration in the bulk solution is known (see previous section). Secondly, the electric double layer interactions in both equations are based on the surface potential. But since the surface potential cannot easily be determined experimentally, we assume that the surface potential is equal to the zeta potential, as is often done in literature[24].

The van der Waals interaction between two identical charged spheres at a separation distance D can be calculated via the Hamaker equation, which is valid at all separation distances regardless of the particle size[8]:

$$U_{vdW}(D) = -\frac{A_{\mathrm{H}}}{6}\left\{\frac{2a^2}{(4a+D)D} + \frac{2a^2}{(2a+D)^2} + \ln\left(\frac{(4a+D)D}{(2a+D)^2}\right)\right\} \tag{2.16}$$

where A_{H} is the Hamaker constant, which is 4.6×10^{-21} J for amorphous SiO_2 in water[36]. The other symbols have their usual meaning.

The particles cannot approach each other infinitesimally close due to short-range Born-repulsion[37]. Below a separation distance of $d_0 \approx 0.158$ nm, the Born repulsion potential is exceedingly strong, which prevents the particles from coming closer than $D = d_0$[38].

By combining equation (2.15) and equation (2.16) a potential energy-distance diagram can be drawn for each sol (**Figure 2.8**).

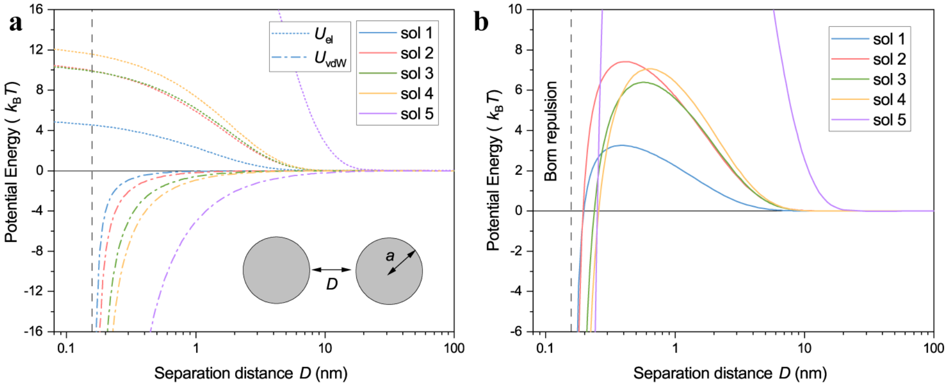

Figure 2.8: Calculated DLVO potential energy-distance diagrams for **(a)** the repulsive electric double layer interaction potential $U_{el}(D)$ and attractive van der Waals interaction potential $U_{vdW}(D)$ and **(b)** the total interaction potential $U_{SS}(D) = U_{el}(D) + U_{vdW}(D)$ of two silica nanoparticles of radius a at a separation distance D. $D \approx 0.158$ nm is the minimum equilibrium distance, below which the Born repulsion potential is exceedingly strong.

Sol 2 has an unusual high electric double layer repulsion for its particle size resulting from the comparatively high Debye length and high zeta-potential. Following equation (2.12) a high Debye length indicates a high surface potential and subsequently a high electrical repulsion between the nanoparticles.

Figure 2.8b shows that sol 1 has the lowest maximum energy barrier, sol 2, 3 and 4 have a similar barrier and sol 5 has the highest energy barrier (not shown due to scale). Aggregation of particles occurs when two particles can overcome the energy barrier through thermal agitation, i.e., an increase in Brownian motion and collide so that covalent bonds can be formed between particles. The probability that this happens decreases exponentially with an increasing barrier height. Therefore, the higher the energy barrier, the more stable the colloidal suspension.

The stability of the particles is not only a function of the height of the energy barrier but also of the viscous interaction between the particles. Stability is defined as the ratio of the fast (diffusion controlled) aggregation rate constant to the slow aggregation rate constant[39–43]:

$$W = \frac{k_{\text{fast}}}{k_{\text{slow}}} = \frac{2a\int_0^\infty \beta(u)\dfrac{\exp(U_{\text{ss}}(D))}{(2a+D)^2}\,\mathrm{d}D}{2a\int_0^\infty \beta(u)\dfrac{\exp(U_{\text{vdW}}(D))}{(2a+D)^2}\,\mathrm{d}D} \qquad (2.17)$$

where $\beta(u)$ is the hydrodynamic retardation function due to viscous forces:

$$\beta(u) = \frac{(6u+1)(u+2)}{2u(3u+2)} \tag{2.18}$$

and $u = D/a$ is the dimensionless distance between the particles.

The stability ratio is the inverse probability of two particles sticking together. The larger the value for the stability ratio, the lower the probability that two particles permanently stick together upon colliding and the more stable is the colloidal suspension. The stability ratio for the silica sols used in this work are listed in **Table 2.5**.

Table 2.5: Calculated energy barrier and stability ratio from the DLVO theory.

sol	U_{max} ($k_{\mathrm{B}}T$)	W_{DLVO}
1	3.3	9.9
2	7.4	3.7×10^{2}
3	6.4	1.0×10^{2}
4	7.1	1.6×10^{2}
5	37.2	7.6×10^{14}

These results show that for sol 1, 1 in 10 particle collisions will result in a permanent bond, indicating an extremely low particle stability. For sol 5 only 1 in 7.6×10^{14} collisions will result in a permanent bond, indicating a very high colloidal stability. Although the DLVO theory is based on a series of assumptions, it can describe the stability of most colloidal suspension well[5]. However, it was observed that, with the exception of sol 1, all sols are stable for several months at room temperature indicating that the DLVO theory does not accurately predict the stability of the colloidal sols used in this work. This means that the actual energy barriers of the sols should be significantly higher than predicted by the DLVO theory. One possible explanation is that the classical DLVO theory does not take into account so called hydration forces, which play a crucial role close to the particle surface[44,45]. Although these hydration forces are not fully understood, several attempts have been made to include this phenomena in the classical DLVO theory, which is then called the extended DLVO theory (XDLVO)[38,46,47].

2.6 Extended DLVO theory

The extended DLVO theory includes any particle-particle interactions that are not covered by the classical DLVO theory. Among these are structural forces (hydration forces, the hydrophobic effect), Lewis acid/base interactions and steric interactions[38,47]. Including every possible interaction is far too complex and beyond the scope of this work, therefore we limit ourselves to the hydration force that plays an important role at short particle-particle separation distances. The XDLVO interaction potential for our system can be written as:

$$U_{\mathrm{SS}}^{\mathrm{XDLVO}}(D)=U_{\mathrm{vdW}}(D)+U_{\mathrm{el}}(D)+U_{\mathrm{hyd}}(D) \tag{2.19}$$

where $U_{\mathrm{hyd}}(D)$ is the repulsion potential due to hydration forces[48,49]:

$$U_{\mathrm{hyd}}(D)=F_0 \pi a \lambda^2 \exp((-D/\lambda)) \tag{2.20}$$

where F_0 is the hydration force constant, a the particle radius and λ the hydration diameter or decay length of the counter ions.

The decay length λ is assumed constant at 0.662 nm, which is twice the radius of a hydrated NH_4^+ ion[50]. The hydration force constant F_0 depends on the level of hydration of the particle surface, the species of salt and the salt concentration and usually lies in the range from 10^6 to 5×10^8 $\mathrm{N{\cdot}m^{-2}}$ [48,49,51].

A value for F_0 can be estimated based on the gelation time of the different silica sols. The time it takes for a silica sol to gel corresponds to a certain stability ratio. The stability ratio corresponds to a certain height of the energy barrier, which is a function of the van der Waals forces, electrostatic forces and hydration forces. Since the van der Waals forces and electrostatic forces are known from the regular DLVO equation, a value for F_0 can be obtained by fitting the data.

The gelation time and stability ratio are related via the following relationship[48,52]:

$$t_{\mathrm{gel}}=\frac{3V_{\mathrm{p}}W\eta}{8\varphi k_{\mathrm{B}}T\left[(1+c)\varphi/2\right]^{d_{\mathrm{f}}/3}} \tag{2.21}$$

with $\varphi = 4\pi a^3 N_0 / 3$ and $c = (1-\varphi_{\mathrm{c}})/\varphi_{\mathrm{c}}$, and where t_{gel} is the gelation time, V_{p} the volume of one particle, W the stability ratio, η the viscosity at zero shear rate, φ the particle volume fraction, N_0 the initial number of particles, φ_{c} the critical volume fraction for spherical clusters, which is 0.64, and d_{f} the fractal dimension, which is 1.8 for diffusion limited aggregation (no salt) and 2.1 for reaction limited aggregation (with salt)[53,54]. Based on equation (2.21) the gelation time of the sols is plotted versus the stability ratio (**Figure 2.9)**.

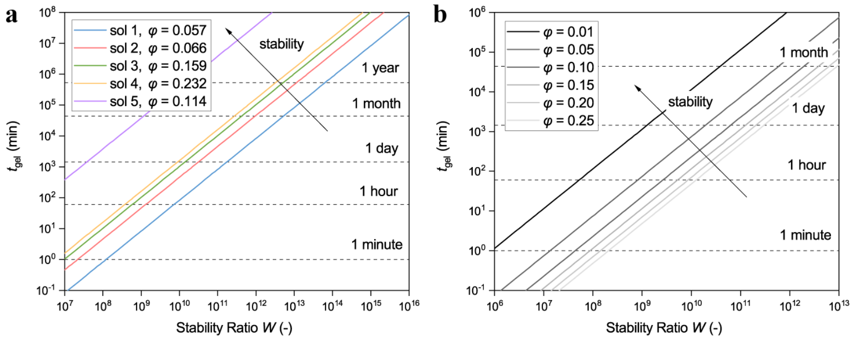

Figure 2.9: (a) Gelation time versus stability ratio for every sol. **(b)** Gelation time versus stability ratio for sol 2 at different volume fractions.

Figure 2.9a shows that sol 5 is significantly more stable than the other sols, most notably due to its large size compared to the other sols. Sol 2, 3 and 4 have roughly the same stability despite their size differences, which is due to large differences in their particle volume fraction. A diluted sol is more stable than a concentrated sol, simply because a diluted sol has less particles that can collide. To illustrate, the stability of sol 2 was plotted at different volume fractions (Figure 2.9b). From this plot it will be clear that the colloidal stability of a sol can be greatly increased by dilution.

Experimentally, we have observed that every sol except sol 1 is stable for at least six months at room temperature, i.e., t_{gel} = 6 months. Based on this observation, a stability ratio can be calculated and subsequently the minimum required height of the energy barrier that corresponds to this gel time and a value for F_0 by fitting the data. The results of this procedure for sol 1 to 5 are given in **Table 2.6**. The height of the energy barrier of sol 5 calculated via the classical DLVO theory was already sufficiently high to correspond to a gel time of ≥ 6 months. For the other sols, the hydration force constant falls well within the range given in the literature and are of the same order of magnitude as the numbers reported by van der Linden et al.[48] for Ludox colloidal silica.

Table 2.6: Calculated energy barriers to correspond with a gel time of ≥ 6 months.

sol	φ	W_{calc}	$U_{\max}$ (k_BT)	F_0 ($\mathrm{N{\cdot}m^{-2}}$)
1	0.057	3.2×10^{13}	34.1	5.02×10^{7}
2	0.066	5.7×10^{12}	32.4	2.24×10^{7}
3	0.159	2.5×10^{12}	32.5	1.20×10^{7}
4	0.232	1.6×10^{12}	32.2	0.85×10^{7}
5	0.114	6.9×10^{9}	-	-

To obtain a more exact value for F_0 the experimental gelation time was measured for each sol at different salt concentrations and extrapolated to a value for F_0 at zero added salt from a simple asymptotic fit through the data points. Ammonium acetate was chosen as salt in this work because ammonium ions are already present in the system and acetate can easily be removed from the particles by calcination. Gelation can, however, be induced with any salt species.

Experimental gelation times were measured by filling sample vials with a certain amount of sol and salt to a total volume of 1 ml. Gelation of the sol was then determined by gently inverting the vials and observing if the sol still flowed or not. A sample was considered fully gelled once it completely stopped flowing. Experimental conditions and gelation times are listed in **Table 2.9** in the Materials and methods section. Values for F_0 were then determined numerically by matching the known gelation time and corresponding stability ratio (from equation (2.21)) to the height of the energy barrier in the XDLVO theory, and plotted against the known salt concentration (**Figure 2.10**). During this procedure the surface potential (zeta potential) in the XDLVO theory was kept constant for every salt concentration. Formally, the surface potential changes as a function of salt, however, this greatly increases the complexity of the electrostatic potential equation[55]. Furthermore, as experimental data are leading the fitted F_0 value will necessarily include any deviation in surface potential and therefore accurately describe the system.

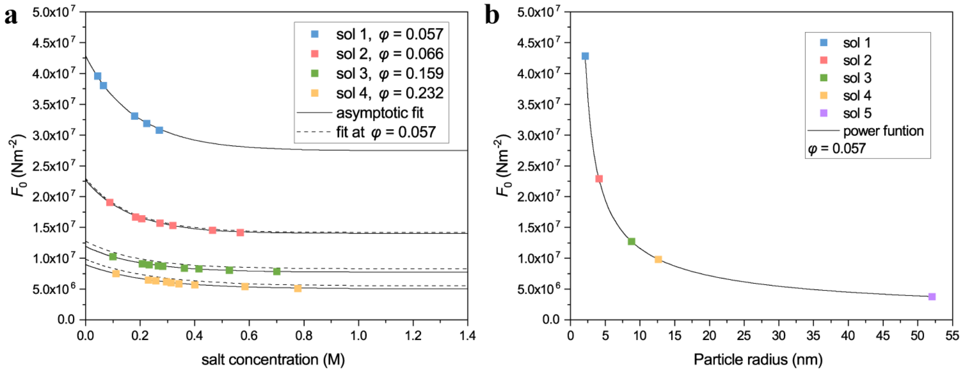

Figure 2.10: (a) Hydration force constant F_0 versus salt concentration for sol 1 to 4. F_0 decreases with increasing salt concentration and is only weakly dependent on the particle volume fraction (dashed lines). **(b)** F_0 versus particle size at zero salt concentration and $\varphi = 0.057$. F_0 decreases with increasing particle size.

For each sol F_0 decreases with increasing salt concentration and can be approximated via a simple asymptotic fit. Since each sol has a different particle size and different volume fraction, see also Table 2.1 and Table 2.6, additional lines were plotted for each sol at the volume fraction of sol 1 ($\varphi = 0.057$). This shows that F_0 is only weakly dependent on the volume fraction and is strongly dependent on the particle size[48]. A possible explanation for this is that the smaller the nanoparticle, the larger the nanoparticle curvature, i.e., more isolated silanol groups that can easily be deprotonated, which means a higher surface charge density and stronger interaction with counter ions near the particle surface. Sol 5 is not shown in this plot, simply because it does not gel under these conditions. However, a value for F_0 at zero salt concentration can be assumed by extrapolating the data from the other sols. To do so, F_0 was plotted for $\varphi = 0.057$ at zero salt versus the particle radius (Figure 2.10b). The data points can be fitted via a power function. At large particle size F_0 becomes more or less independent of the particle size, which is most likely due to the increasing amount of vicinal silanol groups on large silica colloids, similar to the electrokinetic charge density plot in Figure 2.7[29].

With a clear relationship between F_0 and the salt concentration, the full XDLVO equation was applied for every sol, resulting in the potential energy-distance diagrams shown in **Figure 2.11**. The corresponding parameters are listed in **Table 2.7.**

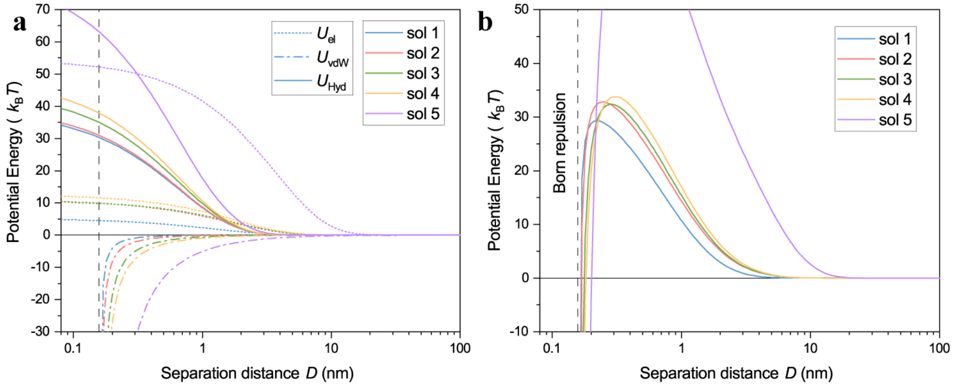

Figure 2.11: Calculated XDLVO potential energy-distance diagrams for: **(a)** the repulsive electric double layer interaction potential $U_{el}(D)$, attractive van der Waals interaction potential $U_{vdW}(D)$ and hydration repulsion potential $U_{hyd}(D)$; and **(b)** the total interaction potential $U_{SS}(D) = U_{el}(D) + U_{vdW}(D) + U_{hyd}(D)$ of two silica nanoparticles of radius a at a separation distance D. $D \approx 0.158$ nm is the minimum equilibrium distance, below which the Born repulsion potential is exceedingly strong.

Table 2.7: Calculated energy barrier and stability ratio from the XDLVO theory.

sol	F_0 (N·m^{-2})	U_{max} ($k_B T$)	W_{XDLVO}	t_{gel} (days)
1	4.28×10^{7}	29.3	3.10×10^{11}	2
2	2.27×10^{7}	32.8	8.75×10^{12}	280
3	1.19×10^{7}	32.4	4.60×10^{12}	330
4	8.98×10^{7}	33.8	1.72×10^{13}	1928
5	3.62×10^{6}	73.6	2.05×10^{30}	5.4×10^{22}

From Figure 2.11 it becomes clear that the hydration potential has a significant contribution to the total interaction potential at separation distances below 3 nm and scales with the particle size. With this additional interaction potential, the height of the energy barrier for each sol is significantly higher compared to the classical DLVO theory and now accurately describes the stability of the colloidal silica sols. Despite the similar height of the energy barriers, there are significant differences in the stability of each sol. Sol 1 is least stable at room temperature and will easily start to form aggregates, as seen before in the cryoTEM micrographs in Figure 2.3. The other sols are stable for several months and sol 5 is predicted to be stable indefinitely. Sol 5 has such a high stability because the particles behave like pseudo-hard spheres. The particles have a high electrostatic repulsion in combination with very few isolated silanol groups that can easily deprotonate in, which means that two particles cannot come close enough together to form covalent bonds upon collission[29].

2.7 Particle aggregation as a function of salt concentration

Salt concentration is the experimental parameter (including temperature) that can be easiest changed during MSM formation. An in-depth understanding of the effect of salt on particle aggregation is therefore essential for the following experimental chapters of this thesis.

With the full XDLVO equation the particle gelation time can be plotted versus the salt concentration and the results can be compared to experimental data points. Since the gelation time scales inversely with the particle volume fraction, two plots were constructed. One for each sol at its original volume fraction and one for each sol at a volume fraction of $\varphi = 0.057$ (**Figure 2.12**). Sol 5 is not visible in either of these plots because it is too stable under these conditions.

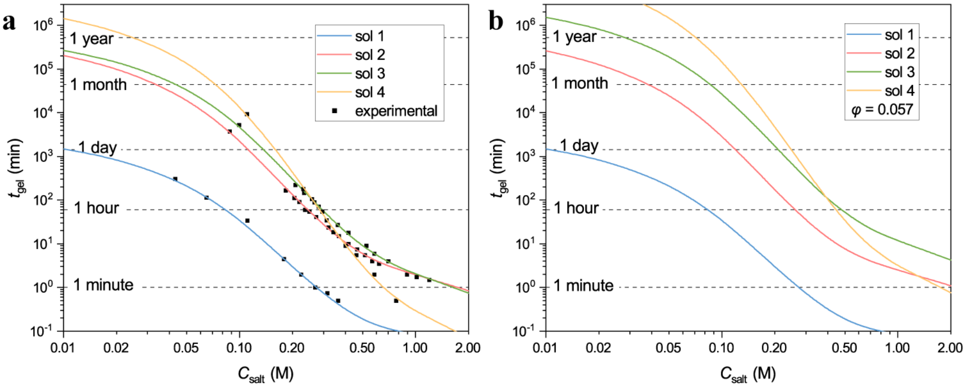

Figure 2.12: (a) Gelation time versus salt concentration for sol 1 to 4, calculated from the XDLVO equation described in the text. **(b)** Gelation time versus salt concentration at fixed particle volume fraction. t_{gel} increases with decreasing volume fraction.

There is a power law dependence of the gelation time on the salt concentration with exponents ranging from −2 to −5 (see **Table 2.8**). The power law exponent becomes more negative as the nanoparticle size increases (from sol 1 to sol 4) and when the particle volume fraction decreases. The dependence on the volume fraction is consistent with results reported by van der Linden et al. for Ludox colloidal silica[48]. However, the dependence on the particle size has not been previously addressed but has important implications on the stability of the sol. Importantly, sol 4 becomes less stable than sol 2 and sol 3 at high salt concentrations, even though it is significantly more stable than both sols at low salt concentrations. The same behavior is found when all sols have the same volume fraction (Figure 2.12b). This implies that the amount of salt required to induce gelation does not scale linearly with the particle size and that one should be careful not to add too much salt during the synthesis of MSMs.

We hypothesize that the observed power law dependence is related to the ratio of protonated/deprotonated silanols on the surface of the nanoparticles, which in turn is related to the particle curvature. The larger the nanoparticle, the fewer isolated silanol groups are present on the nanoparticle surface, which means that there are fewer silanol groups that need to be shielded at high salt concentrations. Similar behavior was observed while measuring the electrokinetic charge density, which is based on the same principle. Besides the type of silanol, the surface silanol density is also expected to be of significant importance on the gelation behavior of the sols[9,56,57]. However, a detailed investigation of the exact role of the surface silanol group under different salt concentrations is beyond the scope of this work.

Table 2.8: Power law exponents for the gelation time versus salt concentration.

sol	φ	Power law exponent
1	0.057	−1.46 ± 0.10
2	0.066	−3.34 ± 0.02
2	0.057	−3.45 ± 0.01
3	0.159	−3.67 ± 0.01
3	0.057	−4.44 ± 0.01
4	0.232	−4.13 ± 0.01
4	0.057	−5.17 ± 0.01

2.8 Conclusions

In summary, an extended version of the DLVO theory is used as a theoretical framework to quantitatively describe the stability of colloidal silica sols with particle sizes ranging from 4 to 100 nm in diameter. It is shown that the electrokinetic charge density strongly depends on the particle size but only for particles with a diameter of less than 30 nm. Particle aggregation is described as a function of salt concentration and it is shown that the rate of destabilization is related to the particle size and particle volume fraction. With increasing average size of the nanoparticles, they destabilize faster with increasing salt concentration. We believe that this behavior shares the same theoretical basis as the electrokinetic charge density dependence on the particle size, which is based on the ratio of protonated/deprotonated silanol groups on the surface of the nanoparticles. The theoretical framework outlined in this chapter provides a solid foundation for the sol-gel experiments performed in the rest of the thesis. Predicting particle aggregation behavior for silica sols of various sizes over a wide range of experimental conditions is one of the most important aspects of the synthesis of MSMs with tunable properties.

2.9 Materials and methods

Materials

The colloidal silica sols used in this work were provided by Nouryon Pulp and Performance Chemicals AB, Sweden and consist of colloidal silica nanoparticles of different sizes and concentrations in water. All sols are ammonium stabilized, which means they have been brought to a pH of 8.0 – 10.5 by the addition of ammonia (25% w/w Scharlau). A 5 M stock solution of salt was prepared of ammonium acetate (Merck). All chemicals were used as received without further purification. Unless otherwise stated all water used in this work was deionized by a Milli-Q Advantage A10 system (Merck Millipore) and had an electrical resistivity of 18.2 MΩ·cm at 25 °C.

Nanoparticle characterization

The particle volume fraction of the sols was determined using X-ray fluorescence spectroscopy (Philips MagiX PW2424), the size distribution was determined via electrospray differential mobility analysis (TSI macroIMS 3982) and dynamic light scattering (Malvern Zetasizer Nano ZS), the pH of the sols was measured using a calibrated pH electrode (Jenway 3510 pH meter) and the bulk ammonia concentration of each sol was determined via titration.

Electrophoretic mobilities were measured using a Malvern Zetasizer Nano ZS equipped with a 4 mW, 633 nm He–Ne laser. Measurements were performed using disposable polycarbonate folded capillary cells (Malvern DTS1070). The cells were rinsed with Milli-Q water prior to use. All measurements were performed at 25 °C and the samples were equilibrated for 120 s. The measurements were performed with automatically optimized conditions by the equipment while the voltage was fixed at 25 V. Electrophoretic mobilities were converted into zeta potentials post-measurement using the Henry equation.

CryoTEM micrographs were recorded with the TU/e CryoTitan electron microscope (Thermo Fisher Scientific) operating at 300 kV in bright-field TEM mode with an image sampling of 2048 × 2048 pixels (pixel size 0.387 $\mathrm{nm{\cdot}px^{-1}}$). The silica sols were diluted to approximately 1 wt% with Milli-Q water and applied on copper TEM grids (QUANTIFOIL® R 2/2, Cu 200 mesh - Quantifoil Micro Tools). The grids were surface plasma treated for 40 s using a Cressington 208 carbon coater prior to use. The samples were then vitrified by plunging them into liquid ethane using an automated vitrification robot (FEI Vitrobot Mark III).

Particle size analysis was performed in MATLAB R2016 using an in-house developed Matlab script. The script requires the long and short axes of particles to be defined by manually clicking at the corresponding edge of the particle in the image. Subsequently, the pixel positions are converted into distances using the magnification calibration of the corresponding Digital Micrograph image file. Approximately 300 particles were analyzed per sample. The reported values are the geometrical mean between the longest and shortest axes.

Gelation experiments

Nanoparticle gelation was determined macroscopically. Sample vials were filled with silica sol and salt to a volume of 1 ml. The salt solution was always added last and all vials were shaken vigorously by hand for 10 s after the addition of salt. The gelation time was then determined by repeatedly gently inverting the sample vials to observe if the sol still flowed or not. A sample was considered fully gelled once it completely stopped flowing. No correlation was observed between the number of times a sample was inverted and its impact on the gelation time. Experimentally observed gelation times versus salt concentrations for each sol are listed in **Table 2.9**.

Table 2.9: Experimental gelation time versus salt concentration for sol 1 to 4.

sol 1		sol 2		sol 3		sol 4	
C (M)	t_{gel} (min)	C (M)	t_{gel} (min)	C (M)	t_{gel} (min)	C (M)	t_{gel} (min)
0.44	0.5	1.25	1.5	1.08	1.75	0.84	0.5
0.39	0.75	0.95	2	0.77	4	0.65	2
0.35	1	0.67	3.5	0.65	6	0.53	5.5
0.30	2	0.62	4	0.59	9	0.47	9
0.26	4.5	0.57	5.5	0.48	18	0.41	18.5
0.19	34	0.52	7.5	0.43	27	0.38	35
0.14	115	0.47	10	0.35	71	0.36	55
0.12	308	0.42	15	0.33	90	0.32	107
		0.37	24	0.30	148	0.30	182
		0.33	41	0.27	226	0.18	9210
		0.30	55	0.17	5280		
		0.29	60				
		0.27	92				
		0.26	112				
		0.24	168				
		0.14	3717				

2.10 References

1. Everett, D. H. Manual of Symbols and Terminology for Physicochemical Quantities and Units, Appendix II: Definitions, Terminology and Symbols in Colloid and Surface Chemistry. *Pure Appl. Chem.* **31**, 577–638 (1972).
2. Babick, F. *Suspensions of Colloidal Particles and Aggregates*. (Springer International Publishing, 2016). doi:10.1007/978-3-319-30663-6.
3. Iler, R. K. *The Chemistry of Silica*. (John Wiley & Sons, Inc., 1979). ISBN: 047102404X.

4. Bergna, H. E. *The Colloid Chemistry of Silica*. *Advances* vol. 234 (American Chemical Society, 1994). doi: 10.1021/ba-1994-0234.
5. Derjaguin, B. V., Churaev, N. V. & Muller, V. M. The Derjaguin—Landau—Verwey—Overbeek (DLVO) Theory of Stability of Lyophobic Colloids. in *Surface Forces* (ed. Churaev, N. V.) 293–310 (Springer US, 1987). doi:10.1007/978-1-4757-6639-4_8.
6. Israelachvili, J. N. Electrostatic Forces between Surfaces in Liquids. in *Intermolecular and Surface Forces* 291–340 (Elsevier, 2011). doi:10.1016/B978-0-12-375182-9.10014-4.
7. Birdi, K. S. Introduction to Surface and Colloid Chemistry. in *Handbook of Surface and Colloid Chemistry* 110–123 (CRC Press, 2016). doi: 10.1201/b18633-5.
8. Israelachvili, J. N. Van der Waals Forces between Particles and Surfaces. in *Intermolecular and Surface Forces* 253–289 (Elsevier, 2011). doi:10.1016/B978-0-12-375182-9.10013-2.
9. Heston, W. M., Iler, R. K. & Sears, G. W. The Adsorption of Hydroxyl Ions From Aqueous Solution on the Surface of Amorphous Silica. *J. Phys. Chem.* **64**, 147–150 (1960).
10. Otterstedt, J.-E. & Brandreth, D. A. Surfaces of Small Particles. in *Small Particles Technology* 235–326 (Springer US, 1998). doi:10.1007/978-1-4757-6523-6.
11. Williams, D. B. & Carter, C. B. *The Transmission Electron Microscope*. *Transmission Electron Microscopy: A Textbook for Materials Science* (Springer US, 2009). doi:10.1007/978-0-387-76501-3_1.
12. van Tendeloo, G., Van Dyck, D. & Pennycook, S. J. *Handbook of Nanoscopy*. (Wiley-VCH Verlag GmbH & Co. KGaA, 2012). doi:10.1002/9783527641864.
13. Vos, M. R., Bomans, P. H. H., Frederik, P. M. & Sommerdijk, N. The Development of a Glove-Box/Vitrobot combination: Air-Water Interface Events Visualized by Cryo-TEM. *Ultramicroscopy* **108**, 1478–1483 (2008).
14. van Huis, M. A. & Friedrich, H. Electron Microscopy Techniques. in *Nanoparticles* 191–221 (Springer Berlin, 2014). doi:10.1007/978-3-662-44823-6_7.
15. Carcouët, C. C. M. C. *et al.* Nucleation and Growth of Monodisperse Silica Nanoparticles. *Nano Lett.* **14**, 1433–1438 (2014).
16. Guha, S., Li, M., Tarlov, M. J. & Zachariah, M. R. Electrospray-Differential Mobility Analysis of Bionanoparticles. *Trends Biotechnol.* **30**, 291–300 (2012).
17. Schärtl, W. *Light Scattering from Polymer Solutions and Nanoparticle Dispersions*. (Springer Berlin, 2007). doi:10.1007/978-3-540-71951-9.
18. de Levie, R. The Henderson-Hasselbalch Equation: Its History and Limitations. *J. Chem. Educ.* **80**, 146 (2009).
19. Bates, R. G. & Pinching, G. D. Dissociation Constant of Aqueous Ammonia at 0 to 50° from E. m. f. Studies of the Ammonium Salt of a Weak Acid. *J. Am. Chem. Soc.* **72**, 1393–1396 (1950).
20. Sögaard, C., Funehag, J. & Abbas, Z. Silica Sol as Grouting Material: a Physio-chemical Analysis. *Nano Converg.* **5**, 6 (2018).
21. Zhang, H., Hassanali, A. A., Shin, Y. K., Knight, C. & Singer, S. J. The Water-Amorphous Silica Interface: Analysis of the Stern Layer and Surface Conduction. *J. Chem. Phys.* **134**, 024705 (2011).
22. Hunter, R. J. The Calculation of Zeta Potential. in *Zeta Potential in Colloid Science* (ed. Hunter, R. J.) 59–124 (Elsevier, 1981). doi:10.1016/B978-0-12-361961-7.50007-9.

23. Swan, J. W. & Furst, E. M. A Simpler Expression for Henry's Function Describing the Electrophoretic Mobility of Spherical Colloids. *J. Colloid Interface Sci.* **388**, 92–94 (2012).
24. Makino, K. & Ohshima, H. Electrophoretic Mobility of a Colloidal Particle with Constant Surface Charge Density. *Langmuir* **26**, 18016–18019 (2010).
25. Jalil, A. H. & Pyell, U. Quantification of Zeta-Potential and Electrokinetic Surface Charge Density for Colloidal Silica Nanoparticles Dependent on Type and Concentration of the Counterion: Probing the Outer Helmholtz Plane. *J. Phys. Chem. C* **122**, 4437–4453 (2018).
26. Abbas, Z., Labbez, C., Nordholm, S. & Ahlberg, E. Size-Dependent Surface Charging of Nanoparticles. *J. Phys. Chem. C* **112**, 5715–5723 (2008).
27. Barisik, M., Atalay, S., Beskok, A. & Qian, S. Size-Dependent Surface Charge Properties of Silica Nanoparticles. *J. Phys. Chem. C* **118**, 1836–1842 (2014).
28. Shi, Y. R., Ye, M. P., Du, L. C. & Weng, Y. X. Experimental Determination of Particle Size-Dependent Surface Charge Density for Silica Nanospheres. *J. Phys. Chem. C* **122**, 23764–23771 (2018).
29. Kamiya, H., Mitsui, M., Takano, H. & Miyazawa, S. Influence of Particle Diameter on Surface Silanol Structure, Hydration Forces, and Aggregation Behavior of Alkoxide-Derived Silica Particles. *J. Am. Ceram. Soc.* **83**, 287–293 (2000).
30. Bell, G. M., Levine, S. & McCartney, L. N. Approximate Methods of Determining the Double-Layer Free Energy of Interaction between Two Charged Colloidal Spheres. *J. Colloid Interface Sci.* **33**, 335–359 (1970).
31. Russel, W. B., Saville, D. A. & Schowalter, W. R. Electrostatics. in *Colloidal Dispersions* 88–126 (Cambridge University Press, 1999).
32. Derjaguin, B. Untersuchungen über die Reibung und Adhäsion, IV. *Kolloid-Zeitschrift* **69**, 155–164 (1934).
33. McCartney, L. N. & Levine, S. An Improvement on Derjaguin's Expression at Small Potentials for the Double-Layer Interaction Energy of Two Spherical Colloidal Particles. *J. Colloid Interface Sci.* **30**, 345–354 (1969).
34. Sader, J. E., Carnie, S. L. & Chan, D. Y. C. Accurate Analytic Formulas for the Double-Layer Interaction between Spheres. *J. Colloid Interface Sci.* **171**, 46–54 (1995).
35. Nguyen, A. V., Evans, G. M. & Jameson, G. J. Electrical Double-Layer Interaction between Spherical Particles. in *Encyclopedia of Surface and Colloid Science* 630–641 (CRC Press, 2012).
36. Bergström, L. Hamaker Constants of Inorganic Materials. *Adv. Colloid Interface Sci.* **70**, 125–169 (1997).
37. Feke, D. L., Prabhu, N. D., Mann, J. A. & Mann, J. A. A Formulation of the Short-Range Repulsion Between Spherical Colloidal Particles. *J. Phys. Chem.* **88**, 5735–5739 (1984).
38. van Oss, C. J. The Extended DLVO Theory. in *Interface Science and Technology* vol. 16 31–48 (2008).
39. Reerink, H. & Overbeek, J. T. G. The Rate of Coagulation as a Measure of the Stability of Silver Iodide Sols. *Discuss. Faraday Soc.* **18**, 74 (1954).
40. McGown, D. N. L. Improved Theoretical Calculation of the Stability Ratio for Colloidal Systems. *J. Phys. Chem.* **71**, 449–450 (1967).
41. Spielman, L. A. Viscous Interactions in Brownian Coagulation. *J. Colloid Interface Sci.* **33**, 562–571 (1970).

42. Honig, E. P., Roebersen, G. J. & Wiersema, P. H. Effect of Hydrodynamic Interaction on the Coagulation Rate of Hydrophobic Colloids. *J. Colloid Interface Sci.* **36**, 97–109 (1971).
43. Ohshima, H. Approximate Analytic Expression for the Stability Ratio of Colloidal Dispersions. *Colloid Polym. Sci.* **292**, 2269–2274 (2014).
44. Marčelja, S. & Radić, N. Repulsion of Interfaces due to Boundary Water. *Chem. Phys. Lett.* **42**, 129–130 (1976).
45. Israelachvili, J. & Wennerström, H. Role of Hydration and Water Structure in Biological and Colloidal Interactions. *Nature* **379**, 219–225 (1996).
46. Yotsumoto, H. & Yoon, R.-H. Application of Extended DLVO Theory. *J. Colloid Interface Sci.* **157**, 434–441 (1993).
47. Grasso, D., Subramaniam, K., Butkus, M., Strevett, K. & Bergendahl, J. A Review of non-DLVO Interactions in Environmental Colloidal Systems. *Rev. Environ. Sci. Bio/Technology* **1**, 17–38 (2002).
48. van der Linden, M. *et al.* Microscopic Origin of the Hofmeister Effect in Gelation Kinetics of Colloidal Silica. *J. Phys. Chem. Lett.* **6**, 2881–2887 (2015).
49. Trompette, J. L. & Clifton, M. J. Influence of Ionic Specificity on the Microstructure and the Strength of Gelled Colloidal Silica Suspensions. *J. Colloid Interface Sci.* **276**, 475–482 (2004).
50. Volkov, A. G., Paula, S. & Deamer, D. W. Two Mechanisms of Permeation of Small Neutral Molecules and Hydrated Ions Across Phospholipid Bilayers. *Bioelectrochemistry Bioenerg.* **42**, 153–160 (1997).
51. Jia, Z. *et al.* A Generalized Model for the Stability of Polymer Colloids. *J. Colloid Interface Sci.* **302**, 187–202 (2006).
52. Zaccone, A., Crassous, J. J. & Ballauff, M. Colloidal Gelation with Variable Attraction Energy. *J. Chem. Phys.* **138**, 104908 (2013).
53. Lin, M. Y. *et al.* Universal Diffusion-Limited Colloid Aggregation. *J. Phys. Condens. Matter* **2**, 3093–3113 (1990).
54. Lin, M. Y. *et al.* Universal Reaction-Limited Colloid Aggregation. *Phys. Rev. A* **41**, 2005–2020 (1990).
55. Ninham, B. W. & Parsegian, V. A. Electrostatic Potential between Surfaces Bearing Ionizable Groups in Ionic Equilibrium with Physiologic Saline Solution. *J. Theor. Biol.* **31**, 405–428 (1971).
56. Branda, M. M., Montani, R. A. & Castellani, N. J. The Distribution of Silanols on the Amorphous Silica Surface: a Monte Carlo Simulation. *Surf. Sci.* **446**, L89–L94 (2000).
57. Zhuravlev, L. T. The Surface Chemistry of Amorphous Silica. Zhuravlev Model. *Colloids Surfaces A Physicochem. Eng. Asp.* **173**, 1–38 (2000).

Chapter 3

Multiscale Colloidal Assembly of Silica Nanoparticles into Microspheres with Tunable Mesopores

Abstract

Colloidal assembly of silica (nano)particles is a powerful method to design functional materials across multiple length scales. Although this method has enabled the fabrication of a wide range of silica-based materials, attempts to design and synthesize porous materials with a high level of tuneability and control over pore dimensions have remained relatively unsuccessful. Here, the colloidal assembly of silica nanoparticles into mesoporous silica microspheres (MSMs) is reported using a discrete set of silica sols within the confinement of a water-in-oil emulsion system. By studying the independent manipulation of different assembly parameters during the sol–gel process, a design strategy is outlined to synthesize MSMs with excellent reproducibility and independent control over pore size and overall porosity, which does not require additional ageing or post-treatment steps to reach pore sizes as large as 50 nm. The strategy as presented here can provide the necessary tools for the microstructural design of the next generation of tailor-made silica microspheres for use in separation applications and beyond.

This chapter is based on published work:

- Fijneman, A. J. *et al.* Multiscale Colloidal Assembly of Silica Nanoparticles into Microspheres with Tunable Mesopores. *Adv. Funct. Mater.* **30**, 2002725 (2020).
- Fijneman, A. J. *et al.*, Porous Silica Particles (Nouryon Chemicals International B.V.) filed EP 19177278.9 (2019).

3.1 General introduction

Mesoporous silica microspheres (MSMs) have long been used as the stationary phase in high performance liquid chromatography (HPLC) for the separation and purification of molecules due to their versatile and tunable properties[1,2]. Silica microspheres have good mechanical strength, high thermal and chemical stability and they can easily be modified with many different surface-active groups[3]. However, not all types of molecules can be separated efficiently with the MSMs that are commercially available today. An important yet notoriously difficult class of molecules to separate are biomacromolecules such as peptides and antibodies, mainly due to their large size and diverse properties[4,5]. Separation of this class of molecules depends upon the availability of MSMs that can be specifically tuned to the size and shape of the macromolecule of interest, thus, requiring new technologically scalable approaches for manufacturing.

To this end, we focus on creating MSMs with highly tunable porosity characteristics, i.e., pore size, pore volume and surface area, by sol-gel emulsion chemistry that is both versatile, easily reproducible and scalable. The sol-gel reaction, i.e., the transformation of a suspension of silica nanoparticles (sols) into gels, can easily be trigged upon change of pH, temperature or ionic strength[6,7]. Typical precursor solutions include tetraethyl orthosilicate (TEOS)[8–13] or sodium silicate (waterglass)[14,15], but in this work discrete silica nanoparticles are used as building blocks to form the gel. There are several benefits of using well-defined nanoparticles to form a gel. Gels made from particles do not need additional template molecules to guide the formation of a porous network, have great flexibility in terms of microstructural design and process scalability and most importantly, allow a high level of control over the reaction.

To attain MSMs, the sol-gel reaction is confined within emulsion droplets. Emulsions are ideal systems to synthesize particles with a well-defined shape and an internal composition defined by the confined nanoparticle building blocks. There are various approaches to use emulsions to create higher order assemblies which can be roughly divided into methods that are dominated by: 1) the external confinement and process conditions, i.e., evaporation-driven colloidal assembly[16–24], and 2) by the interaction forces between the nanoparticles, i.e., entropy-driven or gelation-driven colloidal assembly[25–29]. In evaporation-driven assembly the nanoparticles are forced into close contact by gradually removing the carrier liquid until the (nano)particles assemble into larger assemblies, which are sometimes called supraparticles, supracolloids or supraballs[22,24]. In gelation-driven assembly the nanoparticles are assembled into supraparticles by screening of the nanoparticle surface charges and by increasing the frequency of nanoparticle-nanoparticle collisions. The main difference between the two methods is that evaporation-driven assembly usually leads to densely packed supraparticles, whereas gelation-driven assembly usually leads to porous supraparticles such as MSMs.

Due to current limitations in tuning the porosity characteristics during MSM synthesis, in many conventionally applied industrially relevant processes the as-gelled silica microspheres have to undergo one or multiple ageing or post-treatment steps[30,31]. A common ageing step that is frequently used is Ostwald ripening. In Ostwald ripening the gelled microspheres are immersed in a liquid in which they are soluble and are heated to high temperatures for prolonged times in a sealed reactor. Material on the surface is then slowly dissolved and precipitated into regions of negative curvature, i.e., in between the necks between the nanoparticles and inside small pores. The result is a decrease in surface area and an increase in average pore size[32,33]. This is a time-consuming process and although successful, it also leads to significantly wider pore size distributions as compared to MSMs that have been directly synthesized[34].

In this work, we describe how to create MSMs with a highly tunable porosity characteristics using a limited set of discrete silica sol particles as building blocks confined within water-in-oil (W/O) emulsion droplets. We show that, by the choice of silica sol and mixtures thereof, careful manipulation of the gelation rate of the sol nanoparticles and the processing conditions, we can vary the surface area, pore volume and average pore diameter of the MSMs over a much wider range than has been shown so far in literature. The presented approach does not require additional post-treatment steps such as ageing and is expected to ensure availability of MSMs for efficient separation of a wide variety of biomacromolecules in future.

3.2 General mechanisms of microsphere formation

Perfectly spherical MSMs were synthesized via a protocol inspired by literature[10,35–37]. In general, a W/O emulsion was prepared by adding a colloidal silica sol to an external oil phase containing emulsifier under rapid stirring. After emulsification the gelation of the sol particles into MSMs was induced by either shrinking the emulsion droplets (dewatering) under vacuum conditions (evaporation-driven assembly) or by minimizing the water uptake of the oil phase and greatly increasing the reaction temperature in combination with high concentrations of salt (gelation-driven assembly). In this work water uptake is defined as the increase in storage capacity of the oil phase as a function of temperature above its saturation point at room temperature. After gelation the microspheres were removed from the oil phase via filtration and were subsequently dried and calcined to remove any organic residue still present in the MSMs. More detailed information can be found in the materials and methods section and Appendix section 3.1.

We hypothesize that MSM formation is dependent on two main parameters: (1) the rate of sol particle gelation r_{gel} modulated by the sol particles used as building blocks and by the reaction conditions and (2) the rate of emulsion droplet shrinkage r_{shrink} due to dewatering of the droplets. A proposed mechanism is shown in **Figure 3.1**.

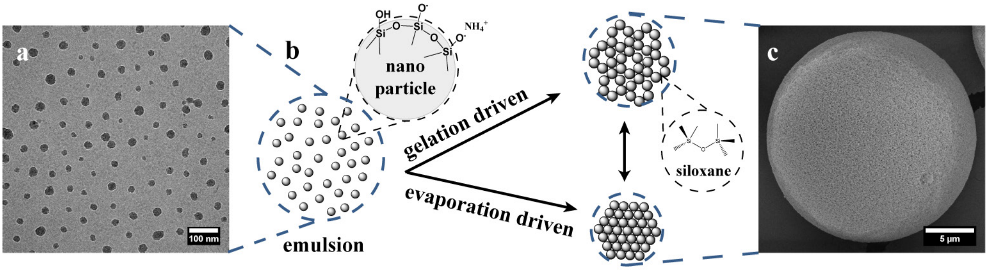

Figure 3.1: Proposed mechanism for the formation of MSMs. **(a)** cryoTEM image of an aqueous colloidal silica sol. **(b)** Schematic representation of the pore structure that is formed inside the emulsion droplet during the gelation process. The microsphere porosity can be modulated by the gelation rate of the particles r_{gel} and the shrinkage rate of the droplets r_{shrink}. **(c)** SEM image of an MSM after calcination.

At the start of the process, the colloidal silica particles are randomly distributed throughout the emulsion droplets. Then, depending on how quickly the sol particles within these droplets gel and how quickly water is transported out of the droplets, the resulting microspheres can either become very porous, very dense or anywhere in between. If the gelation of the sol particles occurs significantly faster than the shrinking of the droplets ($r_{\text{gel}} >> r_{\text{shrink}}$), i.e., when there is no shrinkage of the droplets and the assembly process is completely gelation-driven, the resulting microspheres can be very porous with a porosity as high as high as $\phi = 0.70$ and in theory as high as the total fraction of water in the sol. If the droplet shrinkage rate is significantly faster than the gelation rate ($r_{\text{gel}} << r_{\text{shrink}}$), i.e., evaporation-driven assembly, the sol particles are compressed into dense spheres, with a porosity as low as $\phi = 0.30$. Microsphere porosities in-between these two values are achieved by a careful balance between the gelation rate and droplet shrinkage rate. Regardless of the chosen pathway, all microspheres are perfectly spherical. SEM images of the surface of the microspheres reveal that the microspheres are completely assembled of smaller sol particles (**Figure A3.1**). A representative size distribution of the spheres is shown in **Figure A3.2**.

3.3 Synthesis of MSMs

Our design strategy is based on three parameters that will be addressed below: (1) choice of the silica building blocks, (2) control over the water uptake of the oil phase, and (3) control over the sol particle mobility and stickiness. Full control over all three parameters is key to tailor the porosity characteristics of the resulting MSMs for different applications (e.g., separation of macromolecules).

3.3.1 Choice of the colloidal silica building blocks

The first design principle obtained in this work, which will be employed throughout the following sections, is the choice of the colloidal silica sol as building blocks. The choice of the sol has a direct influence on the internal morphology (size of the pores and struts) as well as the external morphology (specific surface area) of the microspheres. To build a large variety of microspheres, five colloidal silica sols with different particle sizes varying from 4 nm up to 100 nm were used (see also Chapter 2 section 2.2). With these five sols microspheres were synthesized with specific surface areas (SSA) varying from 38 $m^2 \cdot g^{-1}$ up to 560 $m^2 \cdot g^{-1}$, and, most notably, independent of the size or the porosity of the microspheres (**Figure A3.3**). This infers that the struts in between the microspheres pores are approximately one nanoparticle in diameter.

All sols used in this work are negatively charged and, except for sol 1, are highly stable, i.e., they do not settle or aggregate spontaneously for up to several months[6,7]. The stability of a sol can be described using the DLVO theory. The DLVO theory provides a theoretical framework that describes the interaction potential between two charged surfaces in a liquid medium[38] (see also Chapter 2 section 2.5-2.6).

On first sight it appears that the smaller the size of the sol particles that are used as building blocks, the higher the porosity of the synthesized microspheres (**Figure 3.2a**). Smaller sol particles have a higher mobility due to Brownian motion. The frequency that two particles will collide and rapidly form a loose gel network (high porosity) is therefore higher for smaller particles. Moreover, smaller sol particles have a higher areal density of isolated silanol groups on the nanoparticle surface that can easily be deprotonated and react to form siloxane bridges[6,39]. The number of deprotonated silanol groups is directly related to the number of charges per nanoparticle[40]. To quantify the charge density of the different sols, the electrokinetic charge density versus the average sol particle size is shown in **Figure 3.2b**. The electrokinetic charge density is the charge density normalized at the shear plane, which can be derived from the zeta-potential (see also Chapter 2 section 2.4)[41,42].

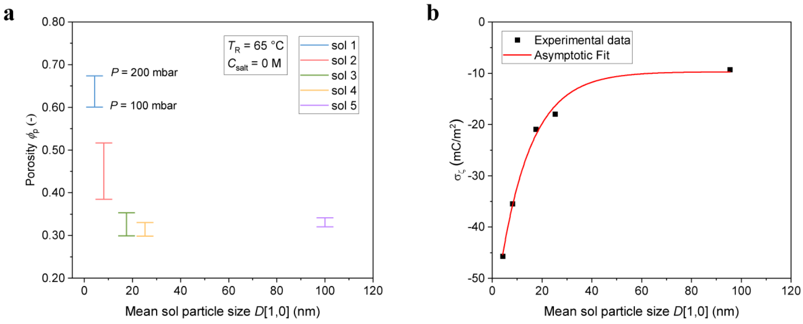

Figure 3.2: (a) Effect of sol particle size and reaction pressure on porosity. **(b)** Electrokinetic charge density as a function of the particle size. Below a particle size of ~ 30 nm the charge density is strongly dependent on the particle size. Above ~ 30 nm the charge density becomes independent of the particle size.

Figure 3.2b shows that the charge density depends on the particle size[40]. The larger the nanoparticle, the lower the charge density. This behavior can be attributed to the type of surface silanol groups that are present on the surface of the nanoparticles. The smallest nanoparticles used in this work, i.e., nanoparticles with a diameter less than 30 nm, have a relatively large particle curvature and somewhat corrugated surfaces. Because of this there are many isolated silanol groups that can easily be deprotonated, resulting in a negative surface charge density. Nanoparticles with a diameter larger than 30 nm have a relatively high amount of vicinal silanol groups, i.e., H-bridged silanol groups, which are not easily deprotonated and therefore have a less negative surface charge density[39]. Our results are in good agreement with a theoretical study by Barisik et al.[43] and an experimental study by Shi et al.[44], who showed that the charge density goes down significantly, i.e., becomes more negative, for silica nanoparticles from 4 to 30 nm in size and remains nearly constant for nanoparticles above 30 nm.

3.3.2 Evaporation-driven assembly

One way of manipulating the microsphere porosity is by controlled shrinkage of the emulsion droplets at elevated temperature and reduced pressure, i.e., evaporation-driven assembly. To illustrate this point, the porosity was compared for microspheres synthesized from the different sols at two different reaction pressures at a constant reaction temperature of T_R = 65 °C (Figure 3.2a). Here, one can clearly see that the lower the reaction pressure during the evaporation step, the lower the microsphere porosity.

Following the classical Clausius-Clapeyron equation:

$$\ln\left(\frac{P_1}{P_2}\right) = -\frac{\Delta_{\text{vap}}H}{R}\left(\frac{1}{T_1}-\frac{1}{T_2}\right) \tag{3.1}$$

a lower absolute pressure equals a lower boiling point of water[45]. Here P_1 is the atmospheric pressure (1013 mbar), P_2 the reduced pressure, T_1 the standard boiling point of water, T_2 the boiling point of water at reduced pressure, R the universal gas constant, and ΔH_{vap} the enthalpy of vaporization, which can be calculated from[46]:

$$\Delta_{\text{vap}}H = A\left(1-\frac{T_2}{T_c}\right)^B \tag{3.2}$$

in which A, B and T_c are regression coefficients depending on the chemical compound[46]. For water, A = 54 kJ·mol^{-1}, B = 0.34 and T_c = 647.13 K.

At P_2 = 200 mbar, T_2 = 60 °C. At P_2 = 100 mbar, T_2 = 45 °C. Therefore, at a lower absolute pressure and at constant reaction temperature T_R, more thermal energy $\Delta T = T_R - T_2$ is available for the evaporation process. The result is that the larger evaporation rate, the faster droplet shrinkage and, hence, more densely packed microspheres are obtained. To confirm, the amount of evaporated water over time was measured at both pressures and at a constant reaction temperature T_R = 65 °C (**Figure A3.4**). It can be seen that at P = 100 mbar (ΔT = 20 °C), the evaporation rate is roughly two times as large than at P = 200 mbar (ΔT = 5 °C).

3.3.3 Gelation-driven assembly

While it is easy to synthesize microspheres with a low porosity by simply shrinking the emulsion droplets, it is not as straightforward to synthesize microspheres with a high porosity, especially if the sol particles are larger than 20 nm. Therefore, in the next section, we do not shrink the droplets, but instead control the microsphere porosity via the reaction temperature and addition of salt. To illustrate this point, the resulting porosity for sol 3 is plotted at different reaction temperatures at atmospheric pressure and at a salt concentration of C_{salt} = 0.19 ± 0.02 M (**Figure 3.3a**). It can be seen that the porosity of the MSMs increases with an increasing temperature, which can be explained by an increased particle mobility. However, above T_R = 65 °C the porosity no longer increases even though the mobility of the sol particles still increases. The reason for this is that water uptake in the oil phase, phenethyl alcohol (PEA), also increases with increasing temperature (**Figure 3.3b** – inset)[47]. This causes a shrinkage of the emulsion droplets during the gelation process and subsequently leads to more densely packed microspheres than one would expect based solely on the increased particle mobility.

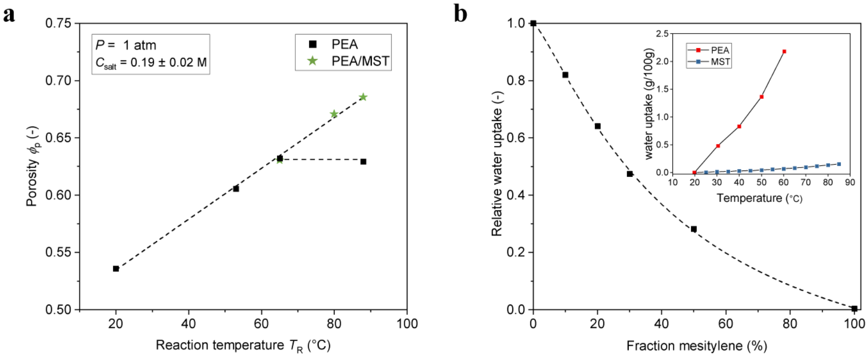

Figure 3.3: (a) Effect of the reaction temperature on the microsphere porosity. Black squares: porosity for the PEA system. Green stars: porosity when 50% MST is added. **(b)** Effect of MST on the relative water uptake in the mixed organic phase. Inset: water uptake for PEA and MST as function of temperature.

To minimize the effect of water uptake, i.e., to minimize the droplet shrinkage during the gelation process, a mixed organic phase was used containing a non-polar organic compound that has no affinity to water, i.e., mesitylene (MST). By adding a non-polar organic compound to the oil phase, the uptake of water becomes adjustable (Figure 3.3b). Note that if the concentration of MST is too high, i.e., ≥ 75% of the total mixture, the emulsifier precipitates and no stable emulsion can be formed. The addition of a non-polar organic compound, reducing water uptake and minimizing shrinkage of the aqueous droplets during gelling, allows the synthesis of MSM with significantly higher levels of porosity and pore sizes.

A high reaction temperature by itself is, however, not enough to access the whole range of microsphere porosities, especially if the particles are not forced into close contract due to shrinkage of the droplets. If the electric double layer around each sol particle is too large, i.e., the particles are too negatively charged, the particles will not stick together and instead repel each other upon collision. A small amount of salt is required to reduce repulsion of the sol particles and to induce spontaneous gelation over time[48,49]. Higher concentrations of salt lead to a more compressed double layer (shorter Debye screening length) and therefore faster gelation of the sol particles (more stickiness). To illustrate this effect, the concentration of added salt was plotted versus the porosity of microspheres synthesized from sol 4 (**Figure 3.4a**).

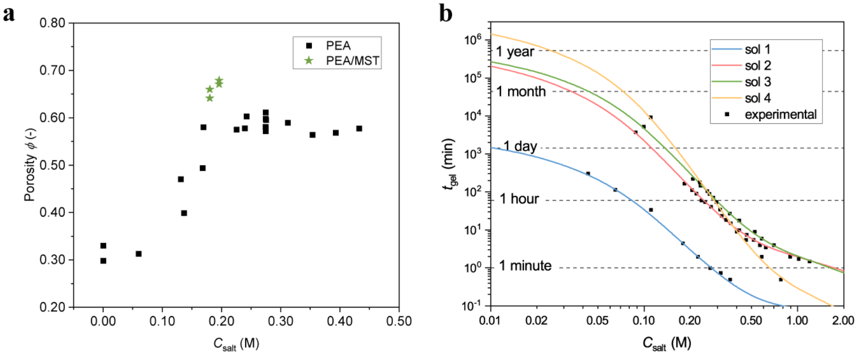

Figure 3.4: (a) Effect of the salt concentration on the microsphere porosity at elevated temperature T_R = 65-85 °C. Black squares: porosity for the PEA system. Green stars: porosity when 50% MST is added. **(b)** Macroscopic gelation experiments of the sols at room temperature. The optimal salt concentration can be estimated by matching the macroscopic gelation time with the duration of the experimental procedure. The solid lines are calculated using XDLVO theory.

Figure 3.4 shows that the microsphere porosity initially increases rapidly with an increasing salt concentration. Above a certain salt concentration, in this case $C_{salt} > 0.20$ M, the microsphere porosity no longer increases significantly even though the probability that particles will successfully stick together upon particle-particle collision will still increase with increasing salt concentration. Moreover, above $C_{salt} > 0.40$ M the emulsion itself will become unstable and particles start to precipitate out of solution and form large aggregated structures[50]. It appears that once the majority of the electrical charges are shielded, additional salt does more harm, i.e., cause large aggregates, than good, i.e., increase the microsphere porosity. The optimum salt concentration is dependent on the sol used as building blocks and requires some experimental optimization. The order of magnitude can, however, be estimated from, macroscopic gelation experiments of the sols at room temperature or calculated using XDLVO theory (**Figure 3.4b**). The best results, i.e., no aggregated structures, are obtained when the macroscopic gelation time of the sol particles is roughly equal to the duration of the experimental procedure, which is typically a few hours.

3.4. Evaluation of the pore network

The specific surface area of the MSMs together with the porosity determines the average pore diameter of the microspheres and, therefore, the potential application of the synthesized MSMs. In **Figure 3.5a** the average pore diameter of all synthesized MSMs from the five silica sols versus the microsphere porosity are shown. It can be clearly seen that the higher the porosity, the larger the average pore diameter. In addition, the larger the size of the sol nanoparticles used as building block, the larger is also the average pore diameter of the microspheres. From an application point of view the width of the pore size distribution is, however, just as important as the average pore diameter. For example, in chromatography, the narrower the spread of the pore size distribution, the higher the peak resolution that can be obtained[51]. The obtained width of the pore size distribution always had a coefficient of variation of CV = σ/μ = 0.4, regardless of the total porosity or the silica sol used (**Figure A3.5**), indicating good reproducibility and control during synthesis. We expect that the width of the pore distribution can be reduced if more monodisperse sols are used.

To evaluate the gas adsorption behavior between samples, microspheres with the same porosity ($\phi = 0.67$) but constructed from different sols were compared. The results are shown in **Figure 3.5b**. Every sample displayed IUPAC type IVa isotherms, which is characteristic for adsorption behavior inside mesoporous adsorbents[52]. At low pressure $p/p°$ there is a region of mono-multilayer adsorption on the mesopore walls, followed by pore condensation and finally a horizontal saturation plateau, indicating completely filled mesopores. The onset of the condensation increases, and the length of the saturation plateau decreases, for microspheres synthesized from sol 1 to sol 4. This is logical because the average pore diameter of the microspheres of sol 1 is smaller than that of sol 4, resulting in earlier and faster saturation of the complete pore network. The pore condensation regions of samples 2 to 4 have a partially common pressure range ($p/p° = 0.85\text{-}0.90$) and partially overlapping pore size distributions (5-15 nm). This is because pores of the same size have the same condensation pressure[53]. Pore condensation is followed by a hysteresis loop where the desorption branch becomes parallel to the adsorption branch. The hysteresis loops become narrower and steeper going from sol 1 to sol 4. In general, the steeper the loop, the faster nitrogen can evaporate from the pore network. Interpretation of the shape of a hysteresis loop is, however, not straightforward because the desorption branch is dependent on various network effects and pore blocking[52].

The pore size distributions of the compared samples show some overlap at the base of the profiles because the silica nanoparticles used as building blocks are not monodisperse and share partially similar size fractions (**Figure 3.5c**). Each sample, however, displays a narrow pore size distribution, which is significantly smaller than pore size distributions that can be obtained when additional ageing steps such as Ostwald ripening are used[34]. SEM shows that microspheres that were treated with an Ostwald ripening process have a much more uneven distribution of pores over the surface (**Figure A3.6**). MSMs that have been formed via direct nanoparticle assembly have an even distribution of pores across the surface.

These results clearly show that microspheres obtained via the presented method have better defined porosity characteristics and that the process in general is significantly more controllable than comparable process that require post-treatment steps, e.g., to tune pore sizes.

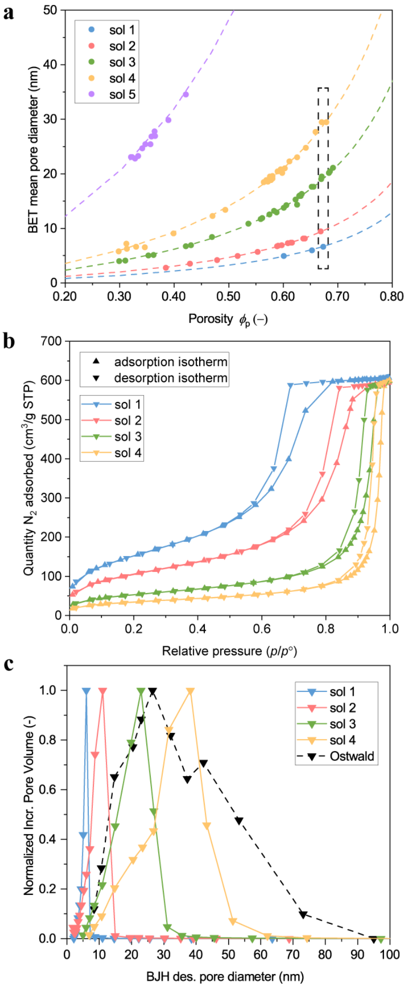

Figure 3.5: (a) Relationship between the average BET pore diameter and porosity of MSMs for the different silica sols. **(b)** Representative N_2 adsorption/desorption isotherms for MSMs from sols 1-4 with a porosity of $\phi = 0.67$. The isotherms display IUPAC type IVa behavior. **(c)** Corresponding pore size distributions calculated from the desorption branch of the isotherm shown in panel b. Overlap in the PSD's result from polydispersity of the sol particle sizes. A comparable sample obtained from an Ostwald ripening process is added for comparison.

3.5 Fine tuning via sol particle mixing

In above sections the general principles of tuning pore size and surface area of MSMs have been discussed. Above methodology can be further extended using mixtures of silica sols to very precisely tune the microsphere properties. By mixing two sols with different particle sizes, the resulting microspheres will have an average surface area based on the ratio of the mixture. By tuning the surface area, the pore size distribution of the microspheres can be shifted without changing the total porosity. Morphologically, this means that the average distance between the silica struts changes, i.e., the average pore diameter, which is reflected in the surface area per volume ratio. As an example, microspheres from a 1:2 mixture of sol 2 and sol 3 were synthesized. The resulting pore size distribution of the mixture is located precisely in between the two original sols (**Figure 3.6a**). The distribution profile overlaps at the base with the two original sols because the microspheres are build-up from both particle size fractions. However, the majority of the pores clearly have a pore diameter in-between that of the two original sols.

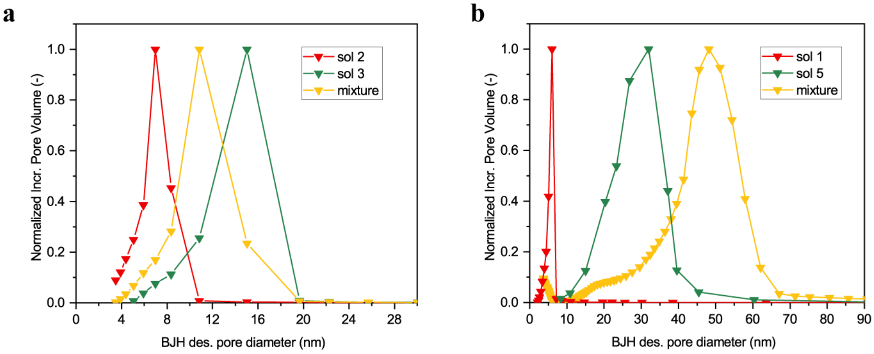

Figure 3.6: Effect of mixing two sol species. Based on the choice of the sols and the ratio of the mixture, MSMs with properties that fall in-between microspheres synthesized from the individual sol species or with properties beyond what is otherwise possible. **(a)** Pore size distribution of a mixture of sol 2+3, with a SSA of 252 $m^2{\cdot}g^{-1}$ and a particle porosity of $\phi = 0.62$. The SSA for sol 2 is 392 $m^2{\cdot}g^{-1}$ and for sol 3 is 197 $m^2{\cdot}g^{-1}$. **(b)** Pore size distribution obtained via mercury porosimetry of a mixture of sol 1+5, with a SSA of 49 $m^2{\cdot}g^{-1}$ and a particle porosity of $\phi =$ 0.52.

Furthermore, in select cases mixing two sols can yield MSMs with properties that are otherwise unobtainable. The largest average pore diameter that was obtained from one building block, i.e., sol 5, was 35 nm with a microsphere porosity of $\phi = 0.42$. Attempts to increase the average pore diameter further have not been successful because the larger the nanoparticle building block, the more difficult it becomes to obtain high porosities. By adding a small portion of another sol, microspheres can be obtained with higher porosities and subsequently larger pore sizes. To illustrate this point, 2 wt% of sol 1 was mixed with sol 5. The resulting microspheres have a porosity of $\phi = 0.52$ and an average pore diameter of 50 nm, which is significantly larger than what could be obtained from just one sol (**Figure 3.6b**).

The microspheres are still perfectly spherical but are not as densely packed as without the addition of sol 1 (**Figure A3.7**). This shows that, with a limited set of silica nanoparticles, a large variety of MSMs can be synthesized with precise control over pore size, porosity and specific surface area as needed for a specific application.

3.6 Conclusions

We have shown that the colloidal assembly of silica nanoparticles into MSMs can be precisely manipulated by actively and passively controlling the reaction conditions and environment in which the sol-gel reaction takes place. With these insights in the underlying mechanisms of colloidal assembly in hand, we introduced a strategy to the design of perfectly spherical MSMs with precisely tunable porosity characteristics across multiple length scales that are highly reproducible and scalable using only a limited set of discrete colloidal silica sols as building blocks. In contrast with conventionally applied industrially relevant processes, we demonstrated that we can synthesize MSMs with highly tunable porosity characteristics without the need for additional ageing or post-treatment steps and / or additional template molecules to guide the formation of the porous network. The results shown here are expected to have a significant impact and ensure availability of MSMs for use in different applications in future, e.g., for the separation of a wide variety of biomacromolecules[54].

3.7 Materials and methods

Materials

The colloidal silica sols used in this work were provided by Nouryon Pulp and Performance Chemicals AB, Sweden and consist of colloidal silica nanoparticles (sol) of different sizes and concentrations in water (**Table 3.1**). All sols are ammonium stabilized, which means they have been brought to a pH of 8.0 – 10.5 by the addition of ammonia (25% w/w, Scharlau). The sols 3A, 4A, 4B and 5A were diluted with deionized water that contained sufficient ammonia in order to ensure the concentration of ammonium ions was the same as the pre-diluted sol. The particle volume fraction of the sols was determined using X-ray fluorescence spectroscopy and the number mean particle diameter $D_P[1,0]$ and standard deviation (SD) were determined by cryoTEM (see Chapter 2 for details on the characterization procedure).

Phenethyl alcohol (PEA, 99%) and mesitylene (MST, 97%) as the oil phase and hydroxypropyl cellulose (HPC, average M 100.000 g·mol^{-1}) as a stabilizer and emulsifier were purchased from Acros Organics. A 5 M stock solution of salt was prepared of ammonium acetate (Merck). All chemicals were used as received without further purification. The water used in this work was deionized by a Milli-Q Advantage A10 system (Merck Millipore) and had an electrical resistivity of 18.2 MΩ·cm at 25 °C.

Table 3.1: Colloidal silica sols used to synthesize MSMs.

sol	SiO_2 wt%	number mean $D_P[1,0]$ ± SD (nm)	pH
1	12	4.2 ± 1.0	10.1
2	14	8.2 ± 2.5	9.2
3	30	17.5 ± 4.6	8.6
3A	14	-	-
4	40	25.2 ± 5.8	9.1
4A	25	-	-
4B	14	-	-
5	22	95.4 ± 18.3	8.6
5A	14	-	-

Water uptake

The water content in the saturated mixed organic phase was determined by means of the Karl-Fischer volumetric method using a Mettler-Toledo DL38 Karl Fischer titrator. Milli-Q water and organic phase (PEA and MST) were vigorously stirred in a 100 ml glass vial for 12 hours and subsequently settled at room temperature for at least 24 hours. Then the saturated solution was decanted in a separatory funnel and samples were taken for analysis.

Synthesis route

Three different experimental protocols were carried out to produce silica microspheres. A detailed description of the protocols, amounts of materials used, and properties of the resulting microspheres are listed in Appendix section 3.1.

Microsphere characterization

Specific surface areas, pore volumes and pore size distributions of the synthesized samples were determined from nitrogen sorption isotherms (Micromeritics TriStar 3000). The isotherms were measured at −196 °C. The specific surface area was calculated from the monolayer adsorbed gas quantity in the pressure interval $p/p° = 0.05\text{-}0.22$ using the Brunauer-Emmett-Teller (BET) equation[55]. The pore volume and pore size distribution were calculated from the desorption isotherm using the Barrett–Joyner–Halenda (BJH) model[52,56]. Every sample displayed IUPAC type IVa isotherms, indicating adsorption behavior inside mesoporous adsorbents[52]. The microsphere porosity was calculated from the pore volume per gram microspheres and the density of amorphous silicon dioxide[57]:

$$\phi = \frac{V_{\text{pore}}}{\frac{1}{\rho_{\text{SiO}_2}} + V_{\text{pore}}} \qquad (3.3)$$

where V_{pore} is the pore volume per gram microspheres and ρ_{SiO2} is the density of amorphous SiO_2, which we assume as 2.2 g·cm^{-3}.[6] While this value can be disputed, the effect of changing ρ_{SiO2} within reasonable boundaries is limited.

SEM images of select microspheres were obtained at 5 kV acceleration voltage using a Quanta3D scanning electron microscope (Thermo Fisher Scientific) equipped with a field emission electron gun. The particles were deposited on a SEM-stub and sputter-coated with a 20 nm layer of gold (Emitech K550) to prevent charging.

3.8 References

1. Gallis, K. W., Araujo, J. T., Duff, K. J., Moore, J. G. & Landry, C. C. The Use of Mesoporous Silica in Liquid Chromatography. *Adv. Mater.* **11**, 1452–1455 (1999).
2. Berthod, A. Silica: Backbone Material of Liquid Chromatographic Column Packings. *J. Chromatogr. A* **549**, 1–28 (1991).
3. Nawrocki, J. The Silanol Group and its Role in Liquid Chromatography. *J. Chromatogr. A* **779**, 29–71 (1997).
4. Unger, K. K., Ditz, R., Machtejevas, E. & Skudas, R. Liquid Chromatography-its Development and Key Role in Life Science Applications. *Angew. Chemie* **49**, 2300–2312 (2010).
5. Bobály, B., Sipkó, E. & Fekete, J. Challenges in Liquid Chromatographic Characterization of Proteins. *J. Chromatogr. B* **1032**, 3–22 (2016).
6. Iler, R. K. *The Chemistry of Silica*. (John Wiley & Sons, Inc., 1979). ISBN: 047102404X.
7. Bergna, H. E. *The Colloid Chemistry of Silica*. *Advances* vol. 234 (American Chemical Society, 1994). doi: 10.1021/ba-1994-0234.
8. Oh, C., Lee, Y. G., Park, J. H. & Oh, S. G. Synthesis of Silica Microspheroids for Templates in W/O Reverse Emulsion. *Colloids Surfaces A Physicochem. Eng. Asp.* **269**, 112–118 (2005).
9. Yang, L. M., Wang, Y. J., Sun, Y. W., Luo, G. S. & Dai, Y. Y. Synthesis of Micrometer-Sized Hard Silica Spheres with Uniform Mesopore Size and Textural Pores. *J. Colloid Interface Sci.* **299**, 823–830 (2006).
10. Andersson, N., Kronberg, B., Corkery, R. & Alberius, P. Combined Emulsion and Solvent Evaporation (ESE) Synthesis Route to Well-Ordered Mesoporous Materials. *Langmuir* **23**, 1459–1464 (2007).
11. Ahmed, A. *et al.* Synthesis of Uniform Porous Silica Microspheres with Hydrophilic Polymer as Stabilizing Agent. *Ind. Eng. Chem. Res.* **49**, 602–608 (2010).
12. Ernawati, L., Balgis, R., Ogi, T. & Okuyama, K. Tunable Synthesis of Mesoporous Silica Particles with unique Radially Oriented Pore Structures from Tetramethyl Orthosilicate via Oil-Water Emulsion Process. *Langmuir* **33**, 783–790 (2017).
13. Egly, S. *et al.* Bottom-Up Assembly of Silica and Bioactive Glass Supraparticles with

Tunable Hierarchical Porosity. *Langmuir* **34**, 2063–2072 (2018).

14. Sierra, L. & Guth, J.-L. Synthesis of Mesoporous Silica with Tunable Pore Size from Sodium Silicate Solutions and a Polyethylene Oxide Surfactant. *Microporous Mesoporous Mater.* **27**, 243–253 (1999).
15. Kosuge, K., Kikukawa, N. & Takemori, M. One-Step Preparation of Porous Silica Spheres from Sodium Silicate using Triblock Copolymer Templating. *Chem. Mater.* **16**, 4181–4186 (2004).
16. Velev, O. D., Jede, T. A., Lobo, R. F. & Lenhoff, A. M. Porous Silica via Colloidal Crystallization. *Nature* **389**, 447–448 (1997).
17. Manoharan, V. N. Dense Packing and Symmetry in Small Clusters of Microspheres. *Science* **301**, 483–487 (2003).
18. Lee, S. Y., Gradon, L., Janeczko, S., Iskandar, F. & Okuyama, K. Formation of Highly Ordered Nanostructures by Drying Micrometer Colloidal Droplets. *ACS Nano* **4**, 4717–4724 (2010).
19. Lebedev-Stepanov, P. & Vlasov, K. Simulation of Self-Assembly in an Evaporating Droplet of Colloidal Solution by Dissipative Particle Dynamics. *Colloids Surfaces A Physicochem. Eng. Asp.* **432**, 132–138 (2013).
20. Gustafsson, H. & Holmberg, K. Emulsion-Based Synthesis of Porous Silica. *Adv. Colloid Interface Sci.* **247**, 426–434 (2017).
21. Wang, D. *et al.* Interplay Between Spherical Confinement and Particle Shape on the Self-Assembly of Rounded Cubes. *Nat. Commun.* **9**, 2228 (2018).
22. Wintzheimer, S. *et al.* Supraparticles: Functionality from Uniform Structural Motifs. *ACS Nano* **12**, 5093–5120 (2018).
23. Sacanna, S. & Pine, D. J. Shape-Anisotropic Colloids: Building Blocks for Complex Assemblies. *Curr. Opin. Colloid Interface Sci.* **16**, 96–105 (2011).
24. Cho, Y.-S., Kim, S.-H., Yi, G.-R. & Yang, S.-M. Self-Organization of Colloidal Nanospheres inside Emulsion Droplets: Higher-Order Clusters, Supraparticles, and Supraballs. *Colloids Surfaces A Physicochem. Eng. Asp.* **345**, 237–245 (2009).
25. de Nijs, B. *et al.* Entropy-Driven Formation of Large Icosahedral Colloidal Clusters by Spherical Confinement. *Nat. Mater.* **14**, 56–60 (2015).
26. Yan, N., Liu, H., Zhu, Y., Jiang, W. & Dong, Z. Entropy-Driven Hierarchical Nanostructures from Cooperative Self-Assembly of Gold Nanoparticles/Block Copolymers under Three-Dimensional Confinement. *Macromolecules* **48**, 5980–5987 (2015).
27. Luo, D., Yan, C. & Wang, T. Interparticle Forces Underlying Nanoparticle Self-Assemblies. *Small* **11**, 5984–6008 (2015).
28. Piccinini, E., Pallarola, D., Battaglini, F. & Azzaroni, O. Self-Limited Self-Assembly of Nanoparticles into Supraparticles: Towards Supramolecular Colloidal Materials by Design. *Mol. Syst. Des. Eng.* **1**, 155–162 (2016).
29. Wang, T., LaMontagne, D., Lynch, J., Zhuang, J. & Cao, Y. C. Colloidal Superparticles from Nanoparticle Assembly. *Chem. Soc. Rev.* **42**, 2804–2823 (2013).
30. Balducci, L., Ungarelli, R. (Enichem S.p.A.; Eniricerche S.p.A.) US 6103209 (2000).
31. Zhiping, J., Fisk, R. P., O’ Gara, J., Walter, T. H., Wyndham, K.D. (Waters Technologies Corporation) US 8778453 (2004).
32. Unger, K. K. Pore Structure of Silica. in *Porous Silica* 15–55 (Elsevier, 1979). doi:10.1016/S0301-4770(08)60806-4.
33. Voorhees, P. W. The Theory of Ostwald Ripening. *J. Stat. Phys.* **38**, 231–252 (1985).
34. Hench, L. L. & West, J. K. The Sol-Gel Process. *Chem. Rev.* **90**, 33–72 (1990).

35. Nyström, M., Herrmann, W., Larsson, B. (EKA Nobel AB) US 5256386 (1993).
36. Park, J. H., Oh, C., Shin, S. Il, Moon, S. K. & Oh, S. G. Preparation of Hollow Silica Microspheres in W/O Emulsions with Polymers. *J. Colloid Interface Sci.* **266**, 107–114 (2003).
37. Lee, Y.-G., Oh, C., Yoo, S.-K., Koo, S.-M. & Oh, S.-G. New Approach for the Control of Size and Surface Characteristics of Mesoporous Silica Particles by using Mixed Surfactants in W/O Emulsion. *Microporous Mesoporous Mater.* **86**, 134–144 (2005).
38. Derjaguin, B. V., Churaev, N. V. & Muller, V. M. The Derjaguin—Landau—Verwey—Overbeek (DLVO) Theory of Stability of Lyophobic Colloids. in *Surface Forces* 293–310 (Springer US, 1987). doi:10.1007/978-1-4757-6639-4_8.
39. Kamiya, H., Mitsui, M., Takano, H. & Miyazawa, S. Influence of Particle Diameter on Surface Silanol Structure, Hydration Forces, and Aggregation Behavior of Alkoxide-Derived Silica Particles. *J. Am. Ceram. Soc.* **83**, 287–293 (2000).
40. Abbas, Z., Labbez, C., Nordholm, S. & Ahlberg, E. Size-Dependent Surface Charging of Nanoparticles. *J. Phys. Chem. C* **112**, 5715–5723 (2008).
41. Hunter, R. J. The Calculation of Zeta Potential. in *Zeta Potential in Colloid Science* 59–124 (Elsevier, 1981). doi:10.1016/B978-0-12-361961-7.50007-9.
42. Jalil, A. H. & Pyell, U. Quantification of Zeta-Potential and Electrokinetic Surface Charge Density for Colloidal Silica Nanoparticles Dependent on Type and Concentration of the Counterion: Probing the Outer Helmholtz Plane. *J. Phys. Chem. C* **122**, 4437–4453 (2018).
43. Barisik, M., Atalay, S., Beskok, A. & Qian, S. Size-Dependent Surface Charge Properties of Silica Nanoparticles. *J. Phys. Chem. C* **118**, 1836–1842 (2014).
44. Shi, Y. R., Ye, M. P., Du, L. C. & Weng, Y. X. Experimental Determination of Particle Size-Dependent Surface Charge Density for Silica Nanospheres. *J. Phys. Chem. C* **122**, 23764–23771 (2018).
45. Ansermet, J.-P. & Brechet, S. D. *Principles of Thermodynamics*. (Cambridge University Press, 2018). doi:10.1017/9781108620932.
46. Yaws, C. L. & Satyro, M. A. Enthalpy of Vaporization—Organic Compounds. in *Thermophysical Properties of Chemicals and Hydrocarbons* 309–400 (Elsevier, 2009). doi:10.1016/B978-081551596-8.50012-2.
47. Goral, M. & Wisniewska-Goclowska, B. IUPAC-NIST Solubility Data Series. 82. Alcohols with Water–Revised and Updated: Part 5. C8–C17 Alcohols with Water. *J. Phys. Chem. Ref. Data* **36**, 685–731 (2007).
48. Kobayashi, M., Juillerat, F., Galletto, P., Bowen, P. & Borkovec, M. Aggregation and Charging of Colloidal Silica Particles: Effect of Particle size. *Langmuir* **21**, 5761–5769 (2005).
49. Sögaard, C., Funehag, J. & Abbas, Z. Silica Sol as Grouting Material: a Physio-chemical Analysis. *Nano Converg.* **5**, 6 (2018).
50. Tadros, T. F. Emulsion Formation, Stability, and Rheology. in *Emulsion Formation and Stability* 1–76 (Wiley-VCH Verlag GmbH & Co. KGaA, 2013). doi:10.1002/9783527647941.
51. Snyder, L. R., Kirkland, J. J. & Dolan, J. W. *Introduction to Modern Liquid Chromatography. High-Performance Gradient Elution: The Practical Application of the Linear-Solvent-Strength Model* (John Wiley & Sons, Inc., 2009). doi:10.1002/9780470508183.
52. Thommes, M. *et al.* Physisorption of Gases, with Special Reference to the Evaluation

of Surface Area and Pore Size Distribution (IUPAC Technical Report). *Pure Appl. Chem.* **87**, 1051–1069 (2015).

53. Grosman, A. & Ortega, C. Capillary Condensation in Porous Materials. Hysteresis and Interaction Mechanism without Pore Blocking/Percolation Process. *Langmuir* **24**, 3977–3986 (2008).
54. Fijneman, A.J., Högblom, J., Sommerdijk, N.A.J.M., Friedrich, H. (Nouryon Chemicals International B.V.) filed EP 19177278.9 (2019).
55. Brunauer, S., Emmett, P. H. & Teller, E. Adsorption of Gases in Multimolecular Layers. *J. Am. Chem. Soc.* **60**, 309–319 (1938).
56. Barrett, E. P., Joyner, L. G. & Halenda, P. P. The Determination of Pore Volume and Area Distributions in Porous Substances. I. Computations from Nitrogen Isotherms. *J. Am. Chem. Soc.* **73**, 373–380 (1951).
57. Lowell, S., Shields, J. E., Thomas, M. A. & Thommes, M. Other Surface Area Methods. in *Characterization of Porous Solids and Powders: Surface Area, Pore Size and Density* 82–93 (Springer, 2004). doi:10.1007/978-1-4020-2303-3_6.

Appendices

Appendix 3.1 Sample preparation

3.1.1 Experimental protocol

Three different experimental protocols were carried out which are detailed below. Amounts of materials used are provided in **Table A3.1**, synthesis conditions in **Table A3.2** and properties of the resulting MSMs are provided in **Table A3.3**. For each procedure, a 5 wt% aqueous solution of hydroxypropyl cellulose (HPC) was used as emulsifier and stabilizing agent. It was prepared by dispersing HPC (5 g) in Milli-Q water (95 g) at 60 °C. The mixture was stirred continuously, and allowed to cool to room temperature after one hour. Stirring was continued for 24 h. It was then filtered twice over 5 µm pore size filter paper (Munktell), and stored in a plastic container until further use.

Procedure 1: evaporation-driven assembly

An oil phase was prepared by mixing phenethyl alcohol (PEA) and 5 wt% HPC solution in a beaker at room temperature and stirring at 300 RPM for one hour with an overhead mixer (IKA Yellow line OST Basic), after which the mixture was fully transparent.

Colloidal silica (and where applicable – see Table A3.1 - 5 M aqueous ammonium acetate solution) were then added to above mixture under constant stirring (350 RPM) to form a water-in-oil emulsion which had a white/milky appearance. After 60 minutes of stirring, the emulsion was poured in a round bottom flask that was subsequently attached to a rotary evaporator fitted with a water bath (Buchi R-200) and exposed to the temperature and reduced pressure specified in Table A3.2.

Rotary evaporation was continued for 90 minutes, at which point almost all the water had been removed from the emulsion, resulting in an almost completely clear/transparent mixture. The temperature was then increased to 85 °C for a further 30 minutes, before being allowed to cool to room temperature. The resulting MSMs were separated by filtration over a Pyrex glass filter and dried at 90 °C for 16 hours. Finally, MSMs were calcined in air at 650 °C for 4 hours.

Procedure 2: gelation-driven assembly

Identical to procedure 1, except the flask was rotated in the water bath at atmospheric pressure and heated for the time specified in Table A3.2. After the time specified in Table A3.2, after which gelling had occurred, a reduced post-gelling pressure according to Table A3.2 was applied for a period of approximately 30 minutes. The temperature of the water bath was then raised to 85 °C and stirring continued for a further 30 minutes at the same pressure.

Procedure 3: gelation-driven assembly

Identical to procedure 2, except mesitylene (MST) was mixed with PEA prior to emulsification.

Procedure 4: Ostwald ripening

A silica prepared via procedure 1 was subjected to Ostwald ripening to increase the average pore diameter. This was done by adding 31 g of silica to a 1 L steel autoclave, together with 619 g water and 73 g of 25 wt% aqueous ammonia solution. The autoclave was sealed and heated to 120 °C for 116 hours. After cooling to 30 °C, 105 g of 63 wt% nitric acid was added. The silica was then filtered off, washed with 300 g water, followed by 158 g acetone. The silica was then dried in an oven at 90 °C for 16 hours.

3.1.2 List of samples

Tables A3.1 to A3.3 are arranged so that the samples are grouped according to the silica sol that was used as building blocks.

Table A3.1: Quantities of materials used

Example	Sol	PEA (g)	MST (g)	HPC (g) [a]	Silica (g) [b]	NH_4Ac (µl) [c]
1	1	50	0	0.13	1.15	0
2	1	50	0	0.13	1.14	0
3	1	50	0	0.13	1.15	0

Example	Sol	PEA (g)	MST (g)	HPC (g) [a]	Silica (g) [b]	NH_4Ac (µl) [c]
4	2	50	0	0.04	1.33	0
5	2	50	0	0.13	1.32	0
6	2	50	0	0.13	1.32	100
7	2	50	0	0.13	1.33	0
8	2	50	0	0.13	1.33	100
9	2	50	0	0.13	1.32	200
10	2	50	0	0.13	1.33	200
11	2	50	0	0.04	1.33	200
12	2	50	0	0.13	1.33	100
13	2	50	0	0.04	1.32	250
14	2	50	0	0.13	4.02	750
15	2	50	0	0.13	1.33	200
16	2	50	0	0.13	1.33	250
17	2	50	0	0.04	1.32	200
18	2	50	0	0.21	1.33	200
19	3A	50	0	0.13	1.35	0
20	3	50	0	0.13	2.88	0
21	3A	50	0	0.13	1.35	0
22	3	50	0	0.13	2.88	0
23	3A	50	0	0.12	1.35	200
24	3A	50	0	0.13	1.34	100
25	3A	100	0	0.42	2.88	200
26	3	100	0	0.25	2.89	200
27	3	50	0	0.13	2.88	200
28	3	50	0	0.13	2.88	200
29	3A	50	0	0.13	1.35	200
30	3A	100	0	0.25	1.38	122
31	3A	100	0	0.42	2.89	750
32	3	50	0	0.13	2.89	200
33	3	100	0	0.25	2.89	200
34	3	100	0	0.25	2.88	200
35	3A	100	0	0.42	2.89	575
36	3	100	0	0.25	2.90	200
37	3A	50	50	0.21	2.89	650
38	3	100	0	0.25	2.89	200
39	3A	100	0	0.42	2.90	825
40	3	100	0	0.25	2.89	200
41	3	100	0	0.25	2.88	300
42	3A	100	0	0.25	1.38	200
43	3A	100	100	0.42	2.85	650
44	3A	100	100	0.42	2.90	650
45	3A	100	100	0.42	2.84	650
46	3	56	56	0.23	2.89	200
47	3A	100	100	0.42	2.84	650
48	4B	50	0	0.13	1.36	0

Example	Sol	PEA (g)	MST (g)	HPC (g) [a]	Silica (g) [b]	NH$_4$Ac (μl) [c]
49	4B	50	0	0.13	1.36	70
50	4B	50	0	0.13	1.36	0
51	4B	50	0	0.13	1.36	200
52	4	50	0	0.13	2.94	150
53	4	50	0	0.13	2.94	200
54	4B	100	0	0.42	2.93	1050
55	4B	100	0	0.42	2.94	1200
56	4B	100	0	0.42	2.93	900
57	4A	100	0	0.25	2.46	300
58	4B	100	0	0.42	2.94	1350
59	4	50	0	0.13	2.96	300
60	4B	50	50	0.21	2.93	900
61	4	100	0	0.25	2.94	200
62	4B	50	50	0.21	2.94	900
63	4A	100	0	0.42	1.50	250
64	4B	100	0	0.42	2.94	900
65	4B	50	50	0.21	2.94	900
66	4	100	0	0.25	2.94	300
67	4B	100	0	0.42	2.94	900
68	4B	100	0	0.25	1.38	200
69	4B	500	501	2.09	14.78	3000
70	4B	501	501	2.09	14.77	3000
71	4B	100	100	0.42	2.93	600
72	4B	100	100	0.42	2.94	600
73	5A	50	0	0.13	1.08	0
74	5A	50	0	0.21	1.08	0
75	5	50	50	0.11	2.16	0
76	5	50	50	0.11	2.17	0
77	5A	50	50	0.11	2.16	0
78	5	100	0	0.42	1.33	60
79	5	100	0	0.25	2.17	50
80	5A	100	0	0.25	1.33	50
81	5	100	0	0.25	2.17	50

[a] Amount of HPC expressed on a dry basis.

[b] Amount of silica added on a dry basis (i.e., not including water from the sol).

[c] Volume of 5 M ammonium acetate solution used.

Table A3.2: Synthesis conditions.

Example	Synthetic Procedure	Heating Temp (°C)	Heating Pressure (mbar)	Heating Time (min)	Final Pressure (mbar)
1	1	65	100	90	100
2	1	65	160	90	160
3	1	65	200	90	200
4	1	65	100	90	100
5	1	65	160	90	160
6	1	65	100	90	100
7	1	65	200	90	200
8	1	65	160	90	160
9	1	65	100	90	100
10	1	65	100	90	100
11	1	65	100	90	100
12	1	65	200	90	200
13	1	65	124	90	124
14	1	65	124	90	124
15	1	65	180	90	180
16	1	65	160	90	160
17	1	65	160	90	160
18	1	65	200	90	200
19	1	65	100	90	100
20	1	65	100	90	100
21	1	65	200	90	200
22	1	65	200	90	200
23	1	65	100	90	100
24	1	65	100	90	100
25	2	53	atm	90	100
26	2	65	atm	90	atm
27	1	65	100	90	100
28	1	65	100	90	100
29	1	65	200	90	200
30	2	53	atm	90	100
31	2	53	atm	45	100
32	1	65	200	90	200
33	2	53	atm	90	100
34	1	88	500	90	500
35	2	53	atm	90	100
36	2	88	atm	90	500
37	3	65	atm	90	200
38	2	65	atm	90	100
39	2	53	atm	60	200
40	2	65	atm	90	200
41	2	65	atm	90	200
42	1	88	500	90	500

Example	Synthetic Procedure	Heating Temp (°C)	Heating Pressure (mbar)	Heating Time (min)	Final Pressure (mbar)
43	3	65	atm	90	400
43	3	80	atm	90	400
44	3	80	atm	90	400
45	3	88	atm	90	500
47	3	75	atm	90	400
48	1	65	100	90	100
49	1	65	100	90	100
50	1	65	200	90	200
51	1	65	100	90	100
52	1	65	100	90	100
53	1	65	100	90	100
54	2	53	atm	45	100
55	2	53	atm	45	100
56	2	53	atm	90	100
57	2	65	atm	90	200
58	2	53	atm	45	100
59	1	65	200	90	200
60	3	65	atm	60	200
61	1	88	500	90	500
62	3	65	atm	60	200
63	2	65	atm	90	200
64	2	65	atm	30	200
65	3	65	atm	90	200
66	1	88	500	90	500
67	2	65	atm	60	200
68	1	88	500	90	500
69	3	90	atm	90	200
70	3	88	atm	90	550
71	3	88	atm	90	500
72	3	88	atm	90	500
73	1	65	100	90	100
74	1	65	50	90	50
75	1	65	atm	90	200
76	1	65	atm	90	200
77	1	65	atm	90	200
78	2	65	atm	90	200
79	1	88	500	90	500
80	2	88	atm	90	500
81	2	88	atm	90	500

Table A3.3: MSM properties.

Example	SSA ($m^2 \cdot g^{-1}$)	PV ($cm^3 \cdot g^{-1}$)	Porosity (-)	μ_{BET} PD (Å)	μ_{BJH} PD (Å)	σ_{BJH} PD (Å)	CV
1	550	0.68	0.60	50	41	12	0.29
2	570	0.85	0.65	60	48	13	0.27
3	563	0.94	0.67	67	53	14	0.26
4	401	0.28	0.38	28	28	9	0.31
5	390	0.34	0.43	35	31	9	0.29
6	396	0.42	0.48	42	37	10	0.28
7	391	0.49	0.52	50	40	11	0.28
8	397	0.56	0.55	57	48	15	0.30
9	384	0.65	0.59	68	60	20	0.33
10	382	0.66	0.59	69	60	20	0.34
11	390	0.67	0.60	69	59	19	0.32
12	385	0.71	0.61	73	61	18	0.29
13	392	0.72	0.61	74	64	23	0.36
14	397	0.73	0.62	74	63	20	0.32
15	398	0.80	0.64	82	69	23	0.33
16	391	0.80	0.64	81	72	25	0.35
17	398	0.81	0.64	81	71	23	0.33
18	388	0.92	0.67	95	82	32	0.39
19	194	0.19	0.30	40	33	10	0.30
20	198	0.20	0.31	41	33	9	0.27
21	197	0.25	0.35	50	40	11	0.27
22	202	0.26	0.36	51	41	11	0.26
23	197	0.33	0.42	67	57	17	0.31
24	199	0.34	0.43	69	58	18	0.31
25	191	0.40	0.47	85	71	22	0.31
26	193	0.52	0.54	108	95	27	0.28
27	196	0.58	0.56	117	102	39	0.38
28	196	0.58	0.56	119	104	40	0.38
29	196	0.61	0.57	125	113	37	0.32
30	193	0.64	0.58	132	115	42	0.36
31	200	0.65	0.59	130	115	42	0.37
32	198	0.68	0.60	138	122	38	0.31
33	197	0.70	0.61	142	125	36	0.29
34	196	0.75	0.62	153	132	33	0.25
35	212	0.76	0.62	143	125	45	0.36
36	194	0.77	0.63	159	133	31	0.23
37	194	0.78	0.63	160	157	50	0.32
38	196	0.78	0.63	159	137	28	0.21
39	196	0.78	0.63	160	165	58	0.35
40	193	0.79	0.63	163	137	29	0.21
41	193	0.85	0.65	177	177	38	0.21
42	197	0.87	0.66	176	176	53	0.30
43	194	0.92	0.67	190	199	63	0.32
44	190	0.93	0.67	195	196	56	0.28

Example	SSA ($m^2 \cdot g^{-1}$)	PV ($cm^3 \cdot g^{-1}$)	Porosity (-)	μ_{BET} PD (Å)	μ_{BJH} PD (Å)	σ_{BJH} PD (Å)	CV
45	195	0.98	0.68	201	208	70	0.34
46	195	0.99	0.69	204	204	51	0.25
47	194	1.02	0.69	211	216	64	0.30
48	133	0.19	0.30	58	49	14	0.28
49	132	0.21	0.31	63	53	14	0.27
50	135	0.22	0.33	66	56	15	0.28
51	133	0.30	0.40	91	80	25	0.32
52	132	0.40	0.47	123	112	36	0.32
53	132	0.44	0.49	134	123	34	0.27
54	127	0.59	0.56	185	199	61	0.30
55	128	0.60	0.57	188	200	61	0.31
56	131	0.61	0.57	186	201	63	0.31
57	126	0.62	0.58	195	210	71	0.34
58	130	0.62	0.58	191	210	66	0.31
59	132	0.62	0.58	188	204	56	0.27
60	129	0.63	0.58	195	208	55	0.26
61	132	0.63	0.58	191	198	48	0.24
62	129	0.63	0.58	195	216	59	0.27
63	128	0.65	0.59	204	216	58	0.27
64	128	0.67	0.60	208	222	71	0.32
65	134	0.68	0.60	202	216	59	0.27
66	132	0.69	0.60	210	221	53	0.24
67	128	0.72	0.61	223	246	92	0.37
68	132	0.76	0.63	230	243	80	0.33
69	131	0.81	0.64	248	264	82	0.31
70	127	0.88	0.66	277	292	90	0.31
71	126	0.93	0.67	295	312	98	0.31
72	130	0.96	0.68	295	317	102	0.32
73	37	0.21	0.32	231	236	59	0.25
74	38	0.22	0.32	231	241	71	0.29
75	39	0.22	0.33	228	233	43	0.18
76	39	0.23	0.33	233	242	51	0.21
77	38	0.24	0.34	247	256	63	0.25
78	38	0.24	0.35	255	270	60	0.22
79	40	0.25	0.36	255	278	66	0.24
80	38	0.26	0.36	278	284	70	0.25
81	39	0.26	0.36	270	281	73	0.26

Appendix 3.2 Microsphere characterization

3.2.1 Microsphere morphology

Zoomed-in SEM images of the surface of the microspheres reveal that the microspheres are completely assembled of smaller sol particles (**Figure A3.1**).

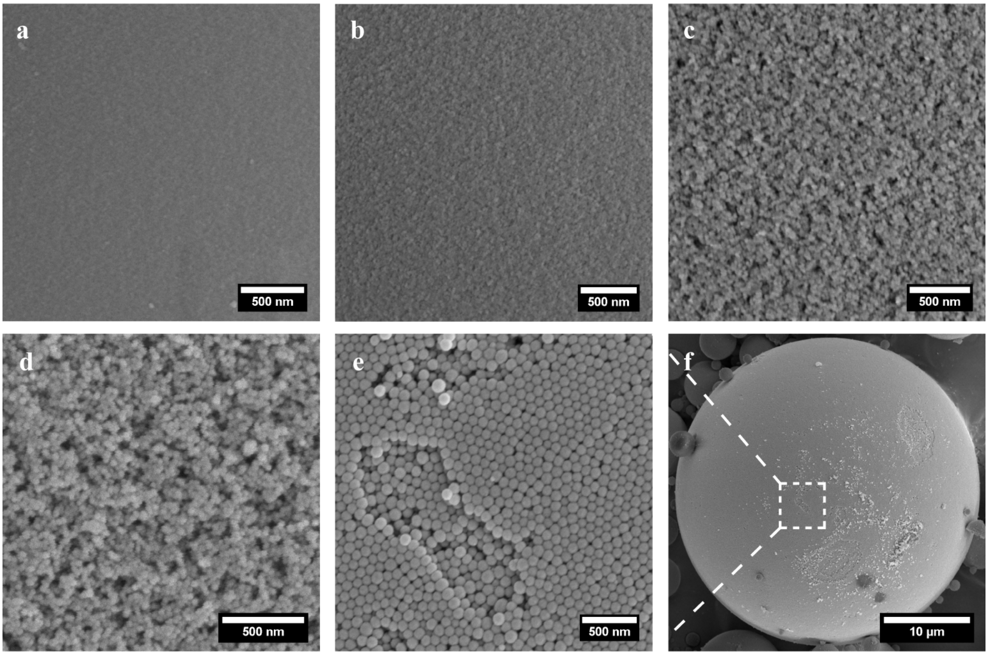

Figure A3.1: Zoomed-in SEM images of the surface of the synthesized microspheres, revealing that the microspheres are assembled form different sol particle building blocks: **(a)** sol 1 – 4 nm particles, **(b)** sol 2 – 8 nm particles, **(c)** sol 3 – 18 nm particles, **(d)** sol 4 – 25 nm particles, **(e)** sol 5 – 100 nm particles. **(f)** Macroscopic image of the microsphere corresponding to zoomed-in image e.

3.2.2 Microsphere size distribution

Particle size distributions of select synthesized microspheres were obtained via laser diffraction (Malvern Mastersizer Micro) following the Mie scattering theory with a refractive index of 1.456 and an absorption coefficient of 0.01. A representative distribution is shown in **Figure A3.2**.

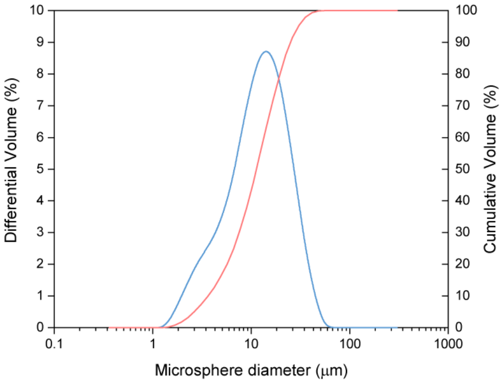

Figure A3.2: Particle size distribution of a representative sample, obtained via laser diffraction.

3.2.3 Microsphere surface area

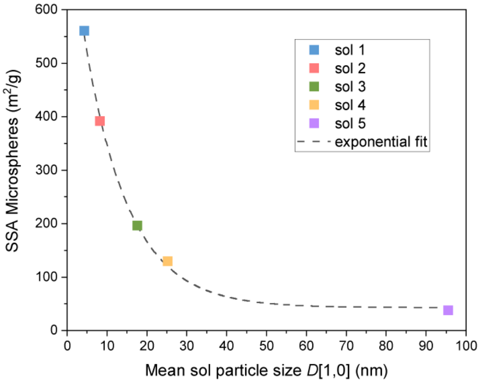

Figure A3.3: SSA of the synthesized microspheres versus the mean sol particle size. The SSA of the microspheres is completely independent of the microsphere size or porosity.

3.2.4 Effect of reaction pressure on the water evaporation rate

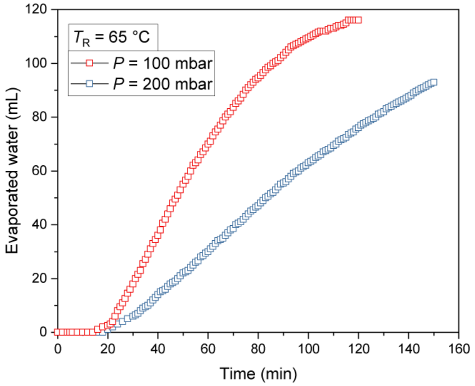

Figure A3.4: Effect of the absolute pressure on the evaporation rate at a constant reaction temperature T_R = 65 °C. The evaporation rate increases with decreasing absolute pressure.

3.2.5 Microsphere pore size distribution

Pore size distributions were calculated from the desorption isotherm using the Barrett–Joyner–Halenda (BJH) model[1,2]. The width of the distributions are independent of the silica sol that was used to synthesize the microsphere and independent of the microsphere porosity (**Figure A3.5**).

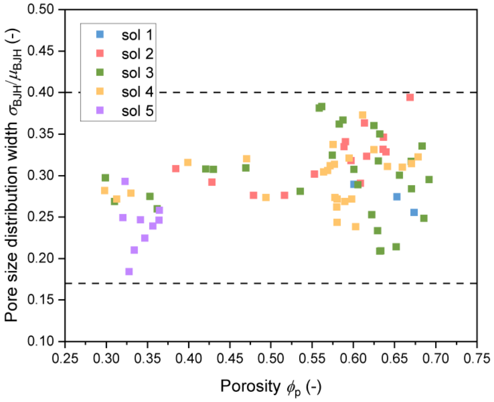

Figure A3.5: Width of the pore size distribution. There is no correlation between the spread of the PSD and the microsphere porosity or the silica sol used as building block. The σ_{BJH}/μ_{BJH} is always below 0.4, indicating a relatively narrow pore size distribution.

3.2.5 Direct assembly versus Ostwald ripening

SEM images of microspheres synthesized via direct assembly versus microspheres obtained via Ostwald ripening have distinct differences (**Figure A3.6**). Microspheres obtained via Ostwald ripening have an uneven and less homogeneous surface compared to microspheres obtained via direct nanoparticle assembly. This has negative implications for the pore size distribution and subsequently the potential separation efficiency.

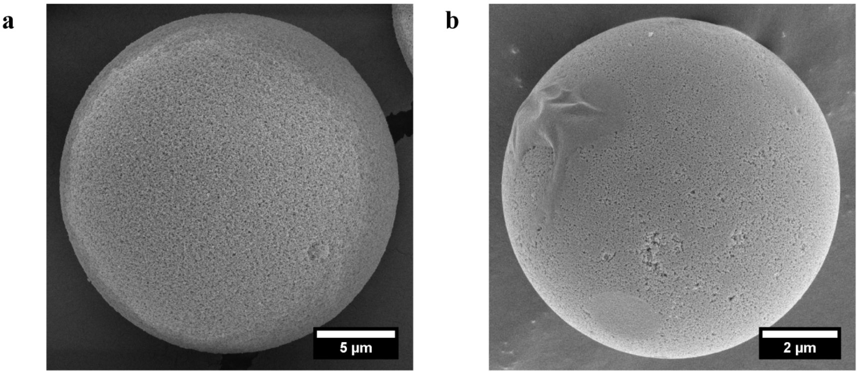

Figure A3.6: Representative SEM images of **(a)** a microsphere synthesized via direct assembly of sol 4 and **(b)** a microsphere synthesized via an Ostwald ripening procedure.

3.2.6 Effect of silica sol mixing

SEM reveals that microspheres synthesized from a mixture of silica sols are still perfectly spherical (**Figure A3.7**). Due to the addition of a fraction of smaller silica sol nanoparticles, the overall porosity of the microspheres increases as well as the average pore diameter. This can be seen by a slightly rougher surface of the microspheres, which indicate a less dense packing fraction.

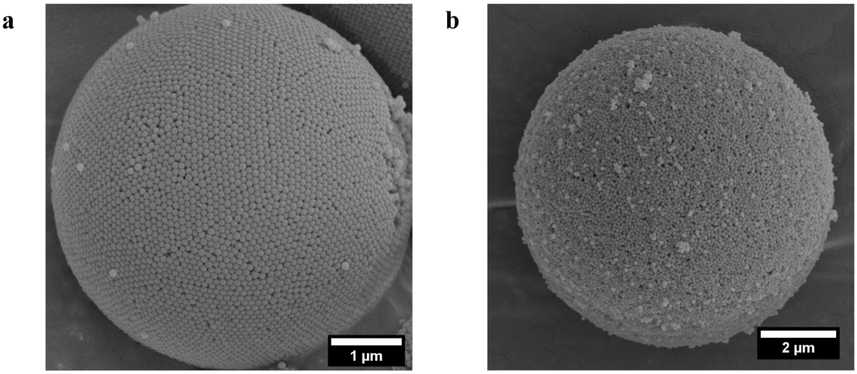

Figure A3.7: Representative SEM images of **(a)** a microsphere synthesized from sol 5 and **(b)** a microsphere synthesized from sol 5 + 2 wt% sol 1.

Appendix 3.3 Experimental optimization

3.3.1 Choice of organic solvent

Several solvents were tested to find a suitable continuous phase of the W/O emulsion. The solvent has to be liquid at room temperature and atmospheric pressure, have a relatively high boiling point, has to be compatible with an emulsifier and it should have a moderate water uptake. The moderate water uptake allows transport of water out of the emulsion droplets during solvent evaporation, whereas the high boiling point prevents the oil phase from boiling and evaporating during heat-up.

Polar solvents such as alcohols and esters generally have moderate to high miscibility with water. Here, a selection of alcohols and esters were evaluated of different lengths and chemical properties, see **Table A3.4**[3–7]. The solvents were selected based on the aforementioned requirements. All six solvents were able to form stable W/O emulsions with one of the silica sols, i.e., sol 2, and at least one of the evaluated emulsifiers (see Appendix section 3.3.2). However, not every solvent gave spherical particles, see **Figure A3.8**.

Table A3.4: Evaluated solvents to form the external oil phase.

Solvent	**Formula**	**Class**	**Density @ 20 ˚C (g/ml)**	**B.P. (˚C)**	**water uptake @ 20 ˚C (g/100 g)**
2-methyl-1-butanol	$C_5H_{12}O$	primary alc.	0.814	129	7.83
ethyl acetoacetate	$C_6H_{10}O_3$	ester	1.021	181	2.86
4-methyl-2-pentanol	$C_6H_{14}O$	secondary alc.	0.805	132	6.25
benzylalcohol	C_7H_8O	aromatic alc.	1.041	205	8.31
phenethyl alcohol	$C_8H_{10}O$	aromatic alc.	1.021	225	8.06
1-octanol	$C_8H_{18}O$	primary alc.	0.823	195	4.62

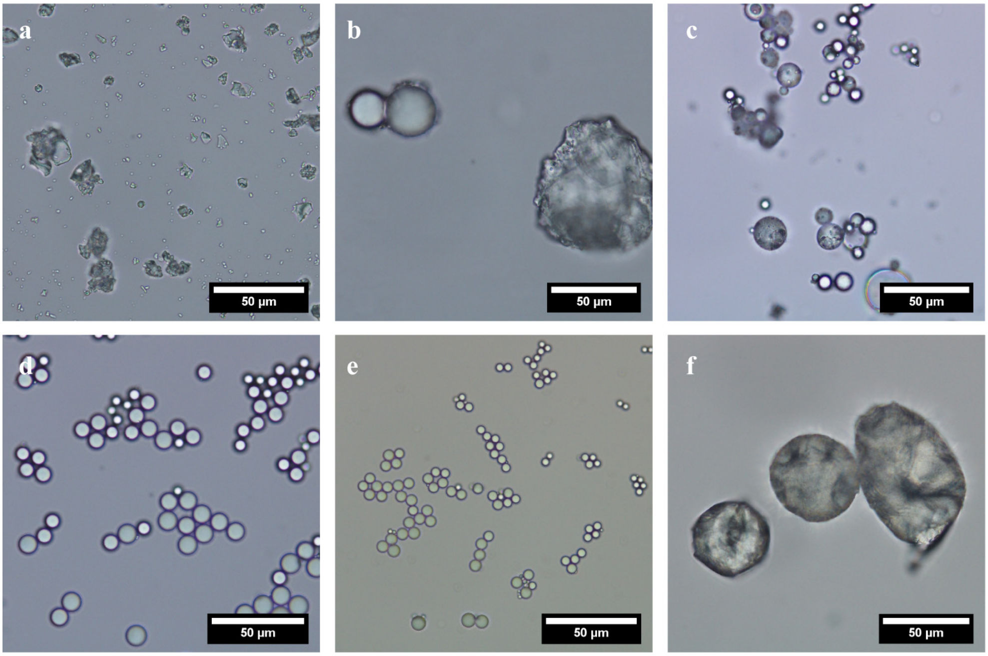

Figure A3.8: Effect of different solvents on the formation of silica microspheres: **(a)** 2-methyl-1-butanol, **(b)** ethyl acetoacetate, **(c)** 4-methyl-2-pentanol, **(d)** benzylalcohol, **(e)** phenethyl alcohol and **(f)** 1-octanol.

The two aromatic solvents, i.e., benzyl alcohol and phenethyl alcohol, gave by far the best results. It is likely that other combinations of solvents and emulsifiers can give similar results. However, no other solvents were tested. Phenethyl alcohol was preferred over benzyl alcohol because it had a smaller increase in water-uptake at elevated temperatures.

3.3.2 Choice of emulsifier

The choice of emulsifier was determined by two factors: the emulsifier should be compatible with the organic solvent; and the emulsifier should not dissociate during the gelation process. Several classes of emulsifiers were evaluated with mixed results. An overview is given in **Table A3.5**.

Table A3.5: Evaluated emulsifiers to be dispersed in the external oil phase.

Emulsifier	**Class**	**Emulsion**	**Particles**
Span/Tween	Nonionic surfactant	Yes	No
Cetyl trimethylammonium bromide	Anionic surfactant	No	No
Sodium dodecyl sulfate	Anionic surfactant	No	No
Polyvinyl alcohol	Polymer	Yes	Yes

Emulsifier	Class	Emulsion	Particles
Polyacrylate (Pemulen)	Polymer	No	No
Polyethylene glycol	Polymer	Yes	No
Ethyl hydroxyethyl cellulose	Cellulose	Yes	Yes
Microfibrillated cellulose	Cellulose	No	No
Hydroxypropyl cellulose	Cellulose	Yes	Yes

From the surfactants only select blends of Span80 (sorbitan monooleate) and Tween80 (polyethoxylated sorbitan monooleate) were able to form stable emulsion droplets. Various blends of Span and Tween with a wide range of hydrophilic-lipophilic balance (HLB) levels (HLB 4 to 12) were tested. Emulsifiers with a high HLB levels tend to be more hydrophilic/polar and are generally used to produce O/W emulsions. Emulsifiers with a low HLB level tend to be more lipophilic/non-polar and are generally used to produce W/O emulsions[8.] In our case only blends with a HLB level between 11 and 12 were able to form stable W/O emulsions. Although the emulsions were stable for several hours, all of them phase separated upon heating and water removal.

Polyvinyl alcohol (PVA) was by far the most interesting of the polymeric emulsifiers that were tested. PVA is a synthetic, atactic water-soluble polymer that is formed by the hydrolyzation of poly(vinyl acetate). PVA is typically produced in different hydrolyzation grades, ranging from 80% hydrolyzed to ≥99% hydrolyzed. The higher the level of hydrolyzation, the more hydroxyl groups are present in the polymer and the higher its surface tension[9]. The total concentration of PVA in the system was varied between 1.00 wt% and 0.01 wt% of the total volume of the system. Emulsions with a PVA concentration below 0.01 wt% were inherently unstable. An example of a representative microsphere formed using PVA is given in **Figure A3.9**.

The microspheres are spherical but also have a significant number of craters on the particle surface. These craters could have either formed due to particle-particle collisions with smaller microspheres or the particle surface was once covered with smaller microspheres that have broken-off at a certain point during the process. Based on the occasional presence of small particles that are still attached to a larger sphere and the spherical shape of the craters, the latter seems more likely. It does not, however, explain why the microspheres would be covered with smaller microspheres in the first place. We speculate that the polyvinyl alcohol and silica particles undergo a kind of coacervation process during the heating and solvent evaporation[10]. PVA can bond to the particle surface via hydrogen bonds and make them more hydrophobic. It is possible that this results into microspheres with a number of weakly bonded smaller spheres attached to their surface that simply break-off in time due to mechanical agitation. A reduction of the total concentration of PVA typically results in more numerous and smaller crates on the particle surface.

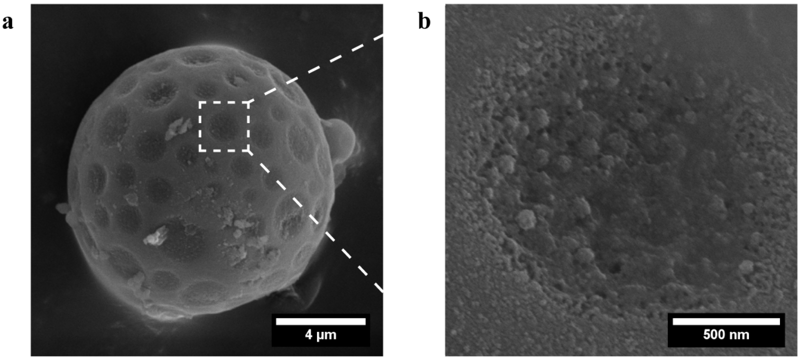

Figure A3.9: **(a)** SEM image of a silica particle synthesized with PVA as emulsifier. The surface is covered in craters. **(b)** Zoomed-in region of a crater.

Cellulosic emulsifiers behave similar to polymeric emulsifiers. They form a barrier around the emulsion droplets and keep them separated during the gelation process. Cellulosic emulsifiers are often added to formulations as a thickening and stabilizing agent rather than an emulsifier. They increase the viscosity of the external oil phase, lowering the chance that the emulsion droplets can coalesce. However, they can also function as an emulsifier as they can anchor to the emulsion droplets and lower the interfacial tension[11–13]. Not all types of cellulose were compatible with the evaluated organic solvents. Microfibrillated cellulose did not form stable emulsions, regardless of the solvent used. Ethyl hydroxyethyl cellulose and hydroxypropyl cellulose both formed stable emulsions with the organic solvents and did not precipitate during the gelation process.

Cellulosic emulsifiers have a cloud point above which they precipitate out of solution. The cloud point is strongly dependent on the presence of other surfactants and electrolytes, the solvent, molecular weight of the cellulose molecule, its structure and the concentration[14–16]. Park et al. showed that HPC can assist in the formation of spherical, mesoporous silica microspheres, although they only used it as a stabilizing agent in combination with other surfactants[17,18]. We chose HPC because it is compatible with polar organic solvents and is stable over a large range of process conditions and, unlike PVA, forms particles with a smooth surface. Although HPC can produce very stable emulsion droplets, it will precipitate out of solution at temperatures in excess of 90 °C, when a large concentration of salt is added to the solution or when the solvent is too apolar. When this happens, the emulsion droplets coalesce, and the particles aggregate together into large assemblies of individual microspheres.

3.3.3 References

1. Thommes, M. *et al.* Physisorption of Gases, with Special Reference to the Evaluation of Surface Area and Pore Size Distribution (IUPAC Technical Report). *Pure Appl. Chem.* **87**, 1051–1069 (2015).

2. Barrett, E. P., Joyner, L. G. & Halenda, P. P. The Determination of Pore Volume and Area Distributions in Porous Substances. I. Computations from Nitrogen Isotherms. *J. Am. Chem. Soc.* **73**, 373–380 (1951).
3. Goral, M. & Wisniewska-Goclowska, B. IUPAC-NIST Solubility Data Series. 82: Alcohols with Water—Revised and Updated: Part 2. C5 Alcohols with Water. *J. Phys. Chem. Ref. Data* **36**, 133–190 (2007).
4. Goral, M. & Wisniewska-Goclowska, B. IUPAC-NIST Solubility Data Series. 82. Alcohols with Water—Revised and Updated: Part 3. C6 Alcohols with Water. *J. Phys. Chem. Ref. Data* **36**, 399–443 (2007).
5. Goral, M. & Wisniewska-Goclowska, B. IUPAC-NIST Solubility Data Series. 82. Alcohols with Water—Revised and Updated: Part 4. C7 Alcohols with Water. *J. Phys. Chem. Ref. Data* **36**, 445–484 (2007).
6. Goral, M. & Wisniewska-Goclowska, B. IUPAC-NIST Solubility Data Series. 82. Alcohols with Water–Revised and Updated: Part 5. C8–C17 Alcohols with Water. *J. Phys. Chem. Ref. Data* **36**, 685–731 (2007).
7. Stephenson, R. & Stuart, J. Mutual Binary Solubilities: Water-Alcohols and Water-Esters. *J. Chem. Eng. Data* **31**, 56–70 (1986).
8. ICI. *The HLB System - a Time-Saving Guide to Emulsifier Selection*. (1980).
9. Tadros, T. F. Adsorption of Polyvinyl Alcohol on Silica at Various pH Values and its Effect on the Floculation of the Dispersion *J. Colloid Interface Sci.* **64**, 36–47 (1978).
10. Iler, R. K. Coacervates of Polyvinyl Alcohol and Colloidal Silica. *J. Colloid Interface Sci.* **51**, 388–393 (1975).
11. Wüstenberg, T. Hydroxypropylcellulose. in *Cellulose and Cellulose Derivatives in the Food Industry* 319–342 (Wiley-VCH Verlag GmbH & Co. KGaA, 2014). doi:10.1002/9783527682935.ch07.
12. Mezdour, S., Lepine, A., Erazo-Majewicz, P., Ducept, F. & Michon, C. Oil/water Surface Rheological Properties of Hydroxypropyl Cellulose (HPC) Alone and Mixed with Lecithin: Contribution to Emulsion Stability. *Colloids Surfaces A Physicochem. Eng. Asp.* **331**, 76–83 (2008).
13. Dickinson, E. Hydrocolloids as Emulsifiers and Emulsion Stabilizers. *Food Hydrocoll.* **23**, 1473–1482 (2009).
14. Khuman, P., Singh, W. B. K., Devi, S. D. & Naorem, H. Viscosityerature Behavior of Hydroxypropyl Cellulose Solution in Presence of an Electrolyte or a Surfactant: A Convenient Method to Determine the Cloud Point of Polymer Solutions. *J. Macromol. Sci. Part A Pure Appl. Chem.* **51**, 924–930 (2014).
15. Drummond, C. J., Albers, S. & Furlong, D. N. Polymer-Surfactant Interactions: (Hydroxypropyl)cellulose with Ionic and Ion-Ionic Surfactants. *Colloids and Surfaces* **62**, 75–85 (1992).
16. Nishio, Y. *et al.* Salt Addition Effects on Mesophase Structure and Optical Properties of Aqueous Hydroxypropyl Cellulose Solutions. *Polym. J.* **34**, 149–157 (2002).
17. Park, J. H., Oh, C., Shin, S. Il, Moon, S. K. & Oh, S. G. Preparation of Hollow Silica Microspheres in W/O emulsions with Polymers. *J. Colloid Interface Sci.* **266**, 107–114 (2003).
18. Lee, Y.-G., Oh, C., Yoo, S.-K., Koo, S.-M. & Oh, S.-G. New Approach for the Control of Size and Surface Characteristics of Mesoporous Silica Particles by using Mixed Surfactants in W/O Emulsion. *Microporous Mesoporous Mater.* **86**, 134–144 (2005)

Chapter 4

Local Quantification of Mesoporous Silica Microspheres using Multiscale Electron Tomography and Lattice Boltzmann Simulations

Abstract

The multiscale pore structure of mesoporous silica microspheres plays an important role for tuning mass transfer kinetics in technological applications such as liquid chromatography. While local analysis of a pore network in such materials has been previously achieved, multiscale quantification of microspheres down to the nanometer scale pore level is still lacking. Here, we demonstrate for the first time, by combining low convergence angle scanning transmission electron microscopy tomography (LC-STEM tomography) with image analysis and lattice Boltzmann simulations, that the multiscale pore network of commercial mesoporous silica microspheres can be quantified. This includes comparing the local tortuosity and intraparticle diffusion coefficients between different regions within the same microsphere. The results, spanning more than two orders of magnitude between nanostructures and entire object, are in good agreement with bulk characterization techniques such as nitrogen gas physisorption and add valuable local information for tuning mass transfer behavior (in liquid chromatography or catalysis) on the single microsphere level.

Parts of this chapter is published in:

Fijneman, A. J. *et al.* Local Quantification of Mesoporous Silica Microspheres using Multiscale Electron Tomography and Lattice Boltzmann Simulations. *Microporous Mesoporous Mater.* **302**, 110243 (2020).

4.1 General introduction

Electron tomography is a powerful technique to image the three-dimensional (3D) structure of an object with nanometer resolution using a series of two-dimensional (2D) electron micrographs. It is frequently used in the biological, chemical and physical sciences to study the 3D morphology of materials[1–7]. Materials with nanoscale porosity in particular have received a great deal of attention over the past years, mainly because of their (potential) application in catalysis or separation processes[8–25]. One example is provided by mesoporous silica microspheres that are used as packing material in high performance liquid chromatography (HPLC)[26]. These particles play an important role in the separation and analysis of a large variety of molecules based on differences in mass transfer properties[27,28]. They are often highly porous and have complex pore networks that extend over multiple length scales, making them difficult to study by (Scanning) Transmission Electron Microscopy ((S)TEM) based 3D imaging approaches. This is on account that particles are often in the micrometer range (2-25 µm), which necessitates cutting of the particles with, e.g., focused-ion beam microscopy or an ultramicrotome, thus not yielding information on the single particle level[29]. Non-destructive characterization of micrometer-sized particles has been done with X-ray microcomputed tomography, but this technique does not have the required resolution to resolve pores which are mostly nanometer-sized[30,31]. A recent approach utilizing low convergence angle (LC) STEM tomography has shown great promise for imaging micrometer thick samples with nanometer resolution[32–35].

When imaging micrometer thick samples by (S)TEM tomography, artifacts may occur as image intensity does not scale linearly with respect to the thickness of the sample[36,37]. This nonlinearity will cause gradients in image intensity in the tomographic reconstruction because standard reconstruction algorithms are based on linear models (**Figure A4.1**)[38]. Corrections for this nonlinearity are possible for objects consisting of different chemical composition[37,39] or by correlative approaches[40]. As the mesoporous silica particles consist only of one phase (silicon dioxide) and due to limited capability of correlative approaches, we correct instead for the nonlinearity using the near perfect sphericity of the particles.

Relating the 3D imaging results directly to material performance and material properties on the sub particle scale can provide valuable insight on the relationship between structure and performance and can lead to better models to simulate, e.g., mass transfer behavior[10,19–23,41,42]. A good way to quantify mass transfer is by computing the intraparticle diffusivity of the material using computer simulations. There are several ways of doing so[19,41,43] but the approach chosen here is to solve the diffusion equation via the lattice Boltzmann method[44]. This method is frequently used to simulate flow in complex structures but can also be used for diffusion simulations under various boundary conditions[45–47].

Extending on previous work where local analysis of a pore network was achieved[19–25], we present here an imaging and analysis workflow for the quantitative multiscale characterization of an entire 2-µm sized porous silica microsphere with 10 nm pores via LC-

STEM tomography. The obtained 3D data is used to investigate for the first time variations in pore size distribution, porosity as well as the intraparticle diffusivity and tortuosity between different regions within the same microsphere via lattice Boltzmann simulations. The results are compared to standard bulk characterization techniques such as nitrogen physisorption and show an excellent match between properties on bulk and single particle level. With this multiscale imaging and quantification workflow in hand, materials that expose hierarchical ordering or a graded porosity can now be investigated.

4.2 Imaging and analysis workflow

To image the 3D pore structure of the mesoporous silica microsphere, a specially designed data processing workflow was implemented that is summarized in **Scheme 4.1**. The workflow consists of several steps that will be briefly introduced below. For detailed information on the design rationale and detailed explanantions of each specific step we refer to the Appendix section 4.1 and supporting **Figures A4.2-A4.10**.

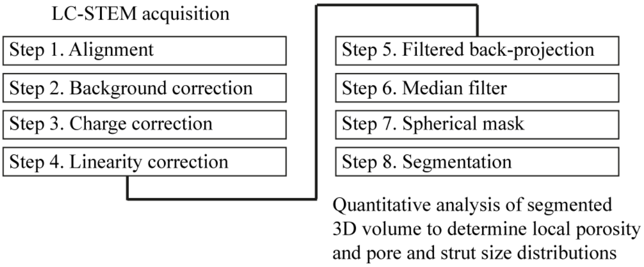

Scheme 4.1: Workflow for the quantitative electron tomography of a commercial mesoporous silica particle (steps explained in the main text).

The first important step towards quantification of an electron tomogram is the alignment of the tilt-series of 2D STEM images (step 1 in Scheme 4.1 and Appendix section 4.1.2). Tilt-series alignment is conventionally performed by manual or automatic tracking of the position of several gold fiducial markers on the sample or the support film over each projection angle[48]. However, since the investigated silica particle was close to a perfect sphere, the center of the sphere could be used for tilt-series alignment instead. By tracking the position of the center, the corresponding *xy*-shifts between images during tilting are obtained. These *xy*-shifts were subsequently used to align the tilt-series automatically and without the need for any gold fiducial markers.

The intensity of the background with tilt was then corrected (step 2 in Scheme 4.1 and Appendix section 4.1.3), followed by the local charging of the particle (step 3 in Scheme 4.1 and Appendix section 4.1.4). The silica particle is not interacting uniformly with the electron beam, which causes local charging[49]. Due to this there are two different thickness-intensity relations present in the particle: one for the charged side (left side) and one for the uncharged side (right side) **(Figure 4.1a)**. To correct for charging, a mean experimental projection image of the microsphere was calculated. This image was obtained by averaging over all 137 STEM projections using the center 90% percentiles of each pixel. Then, a radial symmetric image of the particle was computed that is based only on the thickness-intensity relation of the non-charged side. By dividing this radial symmetric image by the mean projection image, a correction factor image for the charging effect is obtained. Since the correction factor image is based on the mean projection image, local variations in the projected porosity of the particle are preserved. After applying the charge correction to the tilt-series, the maximum intensity is observed (as expected for a sphere) in the center of the particle throughout the tilt-series.

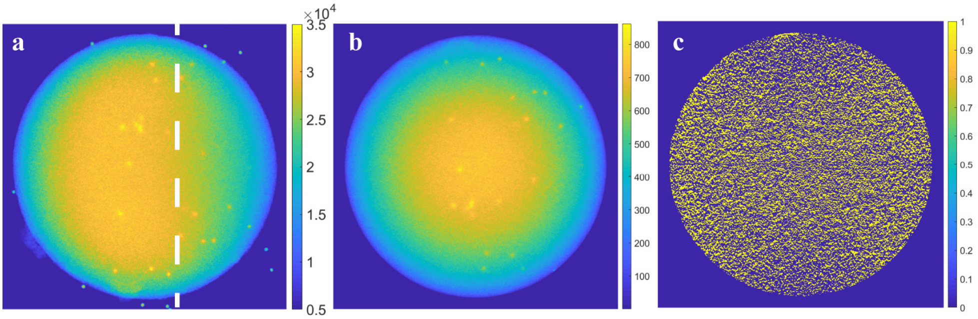

Figure 4.1: (a) STEM micrograph at 0° tilt rendered in false color for better visibility of nonlinear thickness and residual charging artifacts. **(b)** STEM micrograph at 0° tilt after correcting for the background, charge and nonlinearity. The intensity now scales linearly with the thickness. **(c)** Central numerical cross section after segmentation. The vaguely visible horizontal line through the center is an artefact appearing along the rotation axis.

To correct for nonlinearity between image intensity and projected thickness (step 4 in Scheme 4.1 and Appendix section 4.1.5), a projection of a perfect sphere was created with the same dimensions as the investigated particle. By dividing the projection of a perfect sphere by the mean experimental projection image, a correction factor image for nonlinearity was obtained. Multiplying this correction factor image with the charging corrected images of the tilt-series finally provides a tilt-series of the particle which is linearized in intensity with preserved local variations in porosity (**Figure 4.1b**).

The intensity linearized tilt-series was then reconstructed (step 5 and 6 in Scheme 1 and Appendix section 4.1.6) by a standard weighted back projection algorithm with linear density scaling[50], a low-pass weighting filter (0.2 px^{-1} cut off with 0.05 px^{-1} fall off) and followed by an edge preserving median filter (5 × 5 × 5) for further denoising[51]. The reconstruction has a total size of 1601 × 1601 × 1601 voxels and a final pixel size of 1.432 $\text{nm}\cdot\text{px}^{-1}$. After reconstruction, the 3D data inside a spherical mask corresponding to the particle (step 7 in Scheme 4.1 and Appendix section 4.1.7), was segmented using a global intensity threshold (step 8 in Scheme 4.1 and Appendix section 4.1.8). This threshold corresponds to a particle porosity of 65%, as determined by N_2 physisorption for the bulk material. Segmentation assigns all pixels with intensities below the threshold to a value of 0 which is considered a pore, while every pixel value above the threshold is set to 1 and considered to be silica. An example of a numerical cross section through the 3D reconstruction is shown in **Figure 4.1c**.

4.3 Quantification of porosity, strut and pore size distributions

Quantification of the segmented reconstruction enables us to calculate globally and locally the porosity, strut and pore size distribution (PSD), which cannot be done by any other means. The segmentation approach that was used to calculate the size distributions is reasonable, because the assumption of a segmentation threshold based on global porosity and the analysis of the local PSDs are not directly related properties.

To quantify the data in different regions of the particle 13 sub-volumes of 250 × 250 × 250 voxels in size each were extracted, which are located along the x-axis from left to right (in red), along the y-axis from back to front (in green) and along the z-axis from top to bottom (in blue), respectively (**Figure 4.2a**). Size distributions of the pores and silica struts of respectively the whole particle and of each of the sub-volumes were calculated using the following procedure (**Figure A4.9**). First, a Euclidean distance transform is calculated from the segmented data (inverse logical for pores) to obtain a distance map which, for each point making up the pores, gives the shortest distance between this point to the pore boundary, i.e., the nearest silica surface[52]. Next, the centerlines of the pore network are obtained by skeletonization[53]. By multiplying the distance map with the skeleton of the pore network only values along the centerlines of the pore network are selected and considered for calculation of the pore diameter distribution. Since the values given in the distance map effectively represent the locally observed pore radius, multiplying them by two times the pixel size gives the pore diameter. Due to resolution constraints (reconstruction, noise removal, etc.) values larger than 5 pixels (7.2 nm) are considered reliable. All remaining values are sorted in a histogram with a bin size of 1 pixel (1.4 nm) and normalized with respect to the total pore volume. The same is done for the silica strut network using the original binarized data without logical inversion.

Globally, the PSD obtained from the tomography of the whole particle match excellently with the PSD obtained from nitrogen physisorption data of the bulk material (**Figure 4.2b**). This indicates an extraordinary homogeneity of the product (from particle to particle). There is a slight difference between the PSD obtained from the adsorption isotherm compared to the desorption isotherm because there is a physical difference in the way the pores are filled (capillary condensation) and emptied (capillary evaporation)[54].

Locally, the PSDs in the middle of the particle are slightly narrower than the PSD over the whole particle and the PSDs on the edge of the particle are slightly broader (**Figure A4.10**). Along the x-axis the pores are somewhat smaller at the center (9.6 ± 1.3 nm) than at the edge of the particle (11.6 ± 2.5 nm), whereas the size of the silica struts network remains constant throughout the particle (8.9 ± 0.9 nm) (**Figure 4.2c**). A similar trend can be seen along the z-

axis, except here the size of the silica struts is also slightly larger at the edge of the particle (9.6 ± 1.4 nm) than at the center **(Figure 4.2d)**. The sub-volumes along the *y*-axis show a different trend. Here, the pores are slightly larger at one edge of the particle (10.7 ± 2.0 nm) than at the other edge of the particle (10.0 ± 1.5 nm) (**Figure 4.2e**).

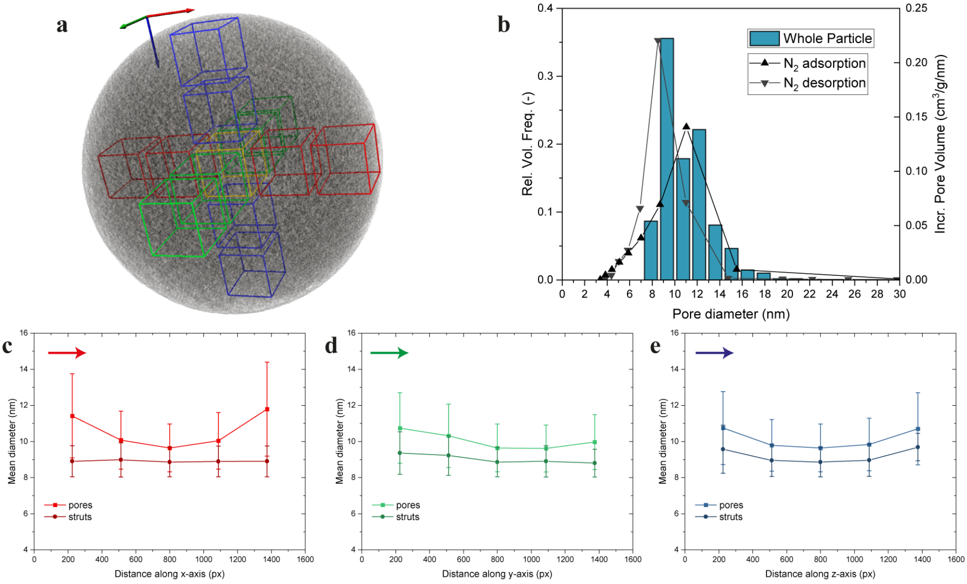

Figure 4.2: **(a)** Schematic representation of the segmented reconstruction in which 13 sub-volumes of 250 × 250 × 250 voxels are highlighted along the *x*-axis (in red), *y*-axis (in green), and *z*-axis (in blue), respectively. **(b)** Comparison of the PSD of the whole particle as determined via tomography versus the PSD determined via N_2 gas physisorption. The close match indicates an extraordinary particle-to-particle homogeneity. **(c-e)** Local variations in the mean pore diameter and mean strut diameter along the *x*-axis, *y*-axis, and *z*-axis, respectively.

The local porosity, defined as the number of pore pixels times the pixel size and divided over the total size of the sub-volume, also varies slightly throughout the particle. Along the *x*-axis the porosity is clearly higher at the edge of the particle (ϕ = 0.74) compared to the center (ϕ = 0.62), whereas it remains relatively constant (ϕ = 0.62 ± 0.02) along the *y*-axis and *z*-axis, respectively (**Figure 4.3a-c**). The trend in porosity follows the average pore and strut size variations along the major axis.

Since the pore network of the investigated particle is governed only by the size of the silica sol nanoparticles, and the size of the silica struts network remains constant throughout the particle, the observed inhomogeneity in porosity and pore size must be a result of the formation mechanism. We hypothesize that, due to evaporation of water, the emulsion droplet initially decreases in diameter accompanied by an increase in solid concentration near the droplet interface. This results in gelation starting from the droplet surface with further water evaporation being then somewhat hindered, which could explain a slight difference in particle volume fraction throughout the particle. Similar effects have been observed in, e.g., spray drying of droplets containing solid nanoparticles[55].

These local intraparticle differences indicate subtle but unmistaken local inhomogeneity throughout the particle, which could have a profound impact on the mass transport behavior throughout the particle[56]. This is important because the particle is used in chromatography applications where mass transport plays an important role in the separation efficiency. Insight in the behavior of mass transport through multiscale porous structures can ultimately lead to better computer models and the design of more efficient particles[57].

4.4 Lattice Boltzmann diffusion simulations

The segmented 3D tomography data can also be used to simulate locally the effective diffusion[10,19,20,22–25]. Here we do so for all 13 sub-volumes within the same sphere using the lattice Boltzmann method to solve the diffusion equation (Appendix section 4.2.1)[46]. This gives a value for the effective intraparticle diffusion coefficient $\mathcal{D}_{\text{eff}}$ over the free diffusion constant $\mathcal{D}_0$, which depend on the geometry of the structure (porosity and tortuosity) but not on the length scale of the pores (**Figure 4.3a-c**)[58,59]:

$$\mathcal{D}_{\text{eff}} = k^{*}\mathcal{D}_0 \tag{4.1}$$

where $\mathcal{D}_{\text{eff}}$ is the effective diffusion coefficient in the pore network, $\mathcal{D}_0$ is the free diffusion coefficient (2.3×10^{-9} $\text{m}^2\cdot\text{s}^{-1}$) and k^* is a dimensionless proportionality factor called the ‘geometry factor’.

The results in Figure 4.3a-c show that the diffusion constant is almost proportional to the porosity in the sub-volume for each of the three major axis. The higher the local porosity, the higher the local diffusion constant. The diffusion constant was computed in three directions for each individual sub-volume. Although the diffusion coefficient should be more or less constant in each direction because there is no obvious distinct anisotropy in the particle, there is a clear distinction between the diffusion values in the *x*-, *y*-, and *z*-direction in each individual sub-volume (**Figure A4.11**). This is unrelated to the particle morphology but is rather a result of the so called ‘missing wedge of data’ from the tomography due to the limited angular range of projections[60]. To account for the anisotropic resolution, tomography data was simulated from a perfectly isotropic cube with the same dimensions and porosity as the investigated particle (Appendix section 4.2.2). Projections were computed over the experimental angular range (± 68°) as well as over the full angular range (± 90°). Simulated reconstructions were then calculated with and without the same processing steps that were applied to the experimental tomogram of the investigated particle (**Table A4.1**).

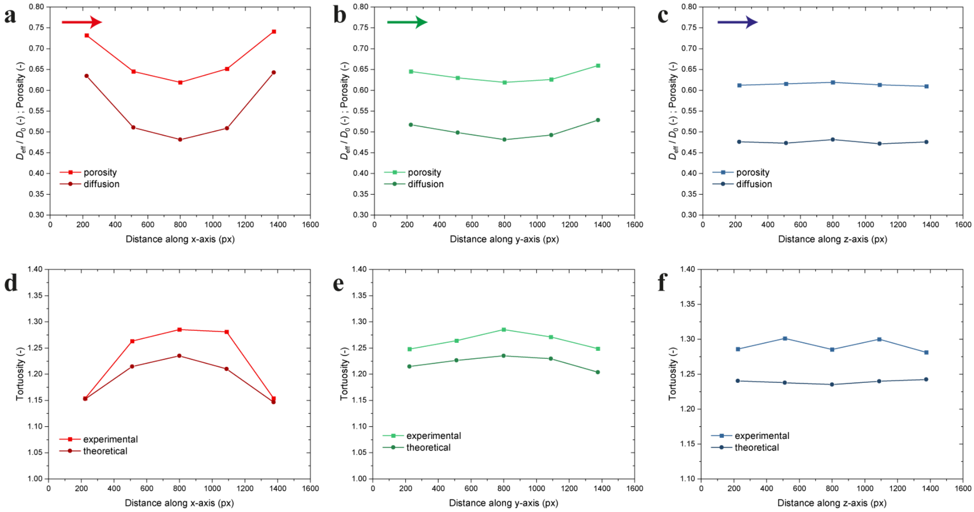

Figure 4.3: **(a-c)** Local variations in the porosity and intraparticle diffusion coefficient along the *x*-axis, *y*-axis, and *z*-axis, respectively. **(d-f)** Local variations in the intraparticle tortuosity coefficient along the *x*-axis, *y*-axis, and *z*-axis, respectively.

The results show that there is no difference in the values for $\mathcal{D}_{\text{eff}}/\mathcal{D}_0$ with or without processing, indicating that the processing steps that were applied do not shift the location of the pore boundaries. In addition, there is no variation for $\mathcal{D}_{\text{eff}}/\mathcal{D}_0$ in the *x*-, *y*-, and *z*-direction in each sub-volume when projections were computed over the full angular range. This indicates that anisotropy in the direction of the missing wedge artefact (*z*-direction) is a limitation of the imaging approach and is unrelated to the observed local inhomogeneity of the investigated particle.

4.5 Intraparticle tortuosity

The relationship between the intraparticle porosity and intraparticle tortuosity, defined as the length of the traveled distance through the medium to the straight-line length across the medium, has significant implications for mass transfer behavior through porous media and has been the subject of many studies over the past decades[61–65]. Barrande et al.[63] derived the following equation for the intraparticle tortuosity from particle conductivity experiments on spherical glass beads:

$$\tau = 1 - 0.49 \ln \phi \tag{4.2}$$

where τ is the intraparticle tortuosity and ϕ is the intraparticle porosity.

Barrande et al. state that tortuosity is a topological characteristic of the material and therefore depends only on porosity for a random system of spheres. As a consequence, they argue that the equation is also valid for any particle that itself is made of a random distribution of dense spheres if the porosity is homogeneously distributed through the particles. Applying equation (4.2) on our data and averaging over each of the 13 sub-volumes yields an intraparticle tortuosity of 1.21 ± 0.03 (**Figure 4.3d-f**), which is in good agreement with results reported in literature[63,66]. An intraparticle tortuosity close to 1 indicates that there is little to no hindrance to diffusion, which is important in separation applications[62].

The tortuosity can also be derived from the lattice Boltzmann diffusion simulations[67]:

$$\mathscr{D}_{\mathrm{eff}} = \frac{\phi}{\tau}\mathscr{D}_0 \tag{4.3}$$

where ϕ is the intraparticle porosity and τ is the tortuosity of the structure, $\mathscr{D}_{\mathrm{eff}}$ is the effective diffusion constant and $\mathscr{D}_0$ is the free diffusion constant.

Applying equation (4.3) on our data and averaging over each of the 13 sub-volumes yields an intraparticle tortuosity of 1.26 ± 0.05 (Figure 4.3d-f), which is in very good agreement with the intraparticle tortuosity derived from equation (4.2). This indicates that equation (4.2) is a simple yet surprisingly accurate way to get an indication for the intraparticle tortuosity for these types of materials.

The diffusion simulations and tortuosity calculations confirm that there are local intraparticle differences that will have an impact on the diffusion path across the particle. With these new insights into the intraparticle morphology, steps can be taken towards elucidating the mass transfer behavior inside the studied commercial mesoporous silica microspheres or other materials in the future.

4.6 Conclusions

We present a method to obtain quantitative insight into pore and strut size distributions throughout mesoporous silica spheres and, hence, mass transport through multiscale porous structures using LC-STEM tomography in combination with lattice Boltzmann simulations. We show for the first time on the example of commercially available mesoporous silica an excellent match between the single microsphere level and the bulk material. Furthermore, quantifying differences in the pore distribution, intraparticle diffusivity and tortuosity between different regions that cannot be obtained otherwise highlight the benefits of using multiscale electron tomography in combination with image analysis. Expanding the technique to other materials can lead to new approaches to tune particle porosity and/or graded porosity and to optimize mass transfer kinetics on the single microsphere level.

4.7 Materials and methods

Materials

Mesoporous silica microspheres were provided by Nouryon Pulp and Performance Chemicals (Bohus, Sweden) and are commercially available under the brand name Kromasil® Classic – 100 Å SIL 1.8 µm. The material was characterized using nitrogen physisorption (Micromeritics TriStar 3000). The results are shown in **Figure 4.4**. The sample displays IUPAC type IVa behavior, which is characteristic for adsorption behavior inside mesoporous solids. The hysteresis loop indicates a disordered mesostructure. The particles have an average particle size of 2 µm, a BET specific surface area of 317 $m^2 \cdot g^{-1}$, a pore volume per gram of 0.86 $cm^3 \cdot g^{-1}$, and an average pore diameter of 10.9 nm. The average porosity of the particles was calculated from the pore volume per gram particles and the density of amorphous silicon dioxide[68]:

$$\phi = \frac{V_{\text{pore}}}{\frac{1}{\rho_{\text{SiO}_2}} + V_{\text{pore}}} = 0.65 \tag{4.4}$$

where V_{pore} is the pore volume per gram particles and ρ_{SiO2} is the density of amorphous SiO_2, which we assume as 2.2 $g \cdot cm^{-3}$.[69] While this value can be disputed, the effect of changing ρ_{SiO2} within reasonable boundaries is limited.

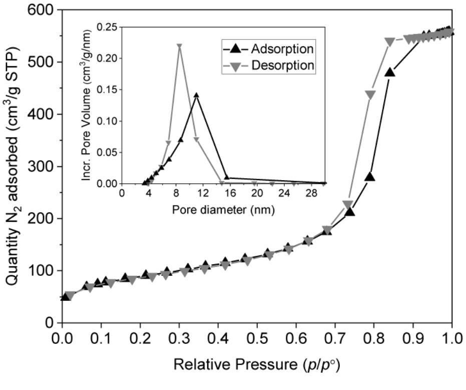

Figure 4.4: Representative N_2 adsorption/desorption isotherms of the porous silica microspheres used in this study. The isotherms display IUPAC type IVa behavior and the hysteresis loop indicates a disordered mesostructure. Inset: pore size distribution, as obtained from the adsorption and desorption isotherm, respectively.

The mesoporous silica microspheres were synthesized according to a method described in detail elsewhere[70]. In brief, the starting material is a basic aqueous silica sol, with a particle size corresponding to an area within the range of from about 50 to about 500 $m^2 \cdot g^{-1}$. The sol is emulsified in a polar, organic solvent that has a limited miscibility or solubility with water, such as, e.g., benzyl alcohol. The emulsification is carried out in the presence of a non-ionic emulsifier, such as cellulose ether. Water from the emulsion droplets is subsequently removed by distillation under an elevated temperature and reduced pressure, causing the silica nanoparticles inside the emulsion droplets to form a gel network. After washing with ethanol and water the silica microspheres are calcined at 600 °C to ensure no organic material is left inside the material. The pore dimensions are governed only by the size of the silica sol nanoparticles and reaction conditions[71]. No templating additives are added to guide or otherwise alter the pore structure.

TEM sample preparation and STEM tilt-series acquisition

A spatula of dry silica particles was suspended in ethanol and 3 μl drops of the suspension were applied on 200 mesh copper TEM grids with a continuous carbon film (Electron Microscopy Sciences) and left to dry in air. The grids were surface plasma treated for 40 s using a Cressington 208 carbon coater and loaded with 20 nm gold fiducial markers prior to use.

LC-STEM micrographs were recorded with the TU/e CryoTitan electron microscope (Thermo Fisher Scientific) operating at 300 kV in microprobe STEM mode at a spot size 9 with an image sampling of 4096 × 4096 pixels. Image magnification was set at 38000x (pixel size 0.716 $\mathrm{nm{\cdot}px^{-1}}$), such that only one particle was located in the field of view. The convergence semi-angle was set at 2 mrad and the camera length was set to 240 mm with images being recorded on a Fischione high-angle annular dark-field detector (HAADF) STEM detector. The convergence angle and camera length were experimentally optimized to get a large depth of field as well as to capture as many scattered electrons as possible, while retaining a high enough spatial resolution to resolve the individual pores. A tilt-series was recorded from a tilt angle of −68° to +68°, every 1° with a total frame time of 20 s.

A representative image of the analyzed particles is shown in **Figure A4.1a**. It can clearly be seen that the particle is nearly perfectly spherical.

Image processing

Most image processing steps were done in MATLAB R2016b using an in-house developed script and the DIPlib scientific image processing library V2.8.1. The workflow is shown in Scheme 4.1 and is further described in the main text. Detailed information regarding each step can be found in the Appendix section 4.1 and in Figures A4.2-A4.10.

The tomography data was reconstructed in IMOD 4.9 using a weighted back projection algorithm with a linear density scaling of 1 and a low-pass radial filter (0.2 $\mathrm{px^{-1}}$ cut off with 0.05 $\mathrm{px^{-1}}$ fall off).[48] A median filter (5 × 5 × 5) was applied to remove shot noise. Both filters set the resolution cut-off at 5 pixels.

3D visualization of the reconstruction was done in Avizo 8.1 (Thermo Fisher Scientific).

Lattice Boltzmann Simulations

In order to transform the tomographic reconstruction into a 3D surface suitable for diffusion simulations, the segmented reconstruction was converted into a triangulated isosurface using VoxSurface 1.2 (VINN Excellence SuMo Biomaterials Center). Lattice Boltzmann simulations were then performed using Gesualdo 1.4 (VINN Excellence SuMo Biomaterials Center). The lattice Boltzmann method was used to solve the diffusion equation using zero flux boundary conditions on the material surface[45]. After the diffusion equation was solved to steady state, the effective diffusion coefficient was computed from the average flux in the direction of the concentration gradient. Additional information can be found in the Appendix section 4.2.

4.8 References

1. Anderson, M. W. *et al.* Modern Microscopy Methods for the Structural Study of Porous Materials. *Chem. Commun.* **4**, 907–916 (2004).
2. McEwen, B. F. & Marko, M. The Emergence of Electron Tomography as an Important Tool for Investigating Cellular Ultrastructure. *J. Histochem. Cytochem.* **49**, 553–564 (2001).
3. Kübel, C. *et al.* Recent Advances in Electron Tomography: TEM and HAADF-STEM Tomography for Materials Science and Semiconductor Applications. *Microsc. Microanal.* **11**, 378–400 (2005).
4. Midgley, P. A., Ward, E. P. W., Hungría, A. B. & Thomas, J. M. Nanotomography in the Chemical, Biological and Materials Sciences. *Chem. Soc. Rev.* **36**, 1477–94 (2007).
5. Batenburg, K. J. *et al.* 3D Imaging of Nanomaterials by Discrete Tomography. *Ultramicroscopy* **109**, 730–740 (2009).
6. Saghi, Z. & Midgley, P. A. Electron Tomography in the (S)TEM: From Nanoscale Morphological Analysis to 3D Atomic Imaging. *Annu. Rev. Mater. Res.* **42**, 59–79 (2012).
7. Evans, J. E. & Friedrich, H. Advanced Tomography Techniques for Inorganic, Organic, and Biological Materials. *MRS Bull.* **41**, 516–521 (2016).
8. Friedrich, H., de Jongh, P. E., Verkleij, A. J. & de Jong, K. P. Electron Tomography for Heterogeneous Catalysts and Related Nanostructured Materials. *Chem. Rev.* **109**, 1613–1629 (2009).
9. Biermans, E., Molina, L., Batenburg, K. J., Bals, S. & Van Tendeloo, G. Measuring Porosity at the Nanoscale by Quantitative Electron Tomography. *Nano Lett.* **10**, 5014–5019 (2010).
10. Yao, Y., Czymmek, K. J., Pazhianur, R. & Lenhoff, A. M. Three-Dimensional Pore Structure of Chromatographic Adsorbents from Electron Tomography. *Langmuir* **22**, 11148–11157 (2006).
11. Zečević, J., De Jong, K. P. & De Jongh, P. E. Progress in Electron Tomography to Assess the 3D Nanostructure of Catalysts. *Curr. Opin. Solid State Mater. Sci.* **17**, 115–125 (2013).
12. Sakamoto, Y. *et al.* Direct Imaging of the Pores and Cages of Three-Dimensional

Mesoporous Materials. *Nature* **408**, 449–453 (2000).

13. Kruk, M. *et al.* Determination of Pore Size and Pore Wall Structure of MCM-41 by Using Nitrogen Adsorption, Transmission Electron Microscopy, and X-ray Diffraction. *J. Phys. Chem. B* **104**, 292–301 (2000).
14. Janssen, A. H., Koster, A. J. & de Jong, K. P. Three-Dimensional Transmission Electron Microscopic Observations of Mesopores in Dealuminated Zeolite Y. *Angew. Chemie Int. Ed.* **40**, 1102–1104 (2001).
15. Janssen, A. H., Koster, A. J. & de Jong, K. P. On the Shape of the Mesopores in Zeolite Y: A Three-Dimensional Transmission Electron Microscopy Study Combined with Texture Analysis. *J. Phys. Chem. B* **106**, 11905–11909 (2002).
16. Midgley, P. A., Weyland, M., Thomas, J. M. & Johnson, B. F. G. Z-Contrast Tomography: a Technique in Three-Dimensional Nanostructural Analysis based on Rutherford Scattering. *Chem. Commun.* 907–908 (2001).
17. Midgley, P. A. & Weyland, M. 3D Electron Microscopy in the Physical Sciences: the Development of Z-contrast and EFTEM Tomography. *Ultramicroscopy* **96**, 413–431 (2003).
18. Martines, M. U. *et al.* Hexagonal Mesoporous Silica Nanoparticles with Large Pores and a Hierarchical Porosity tested for HPLC. *Comptes Rendus Chim.* **8**, 627–634 (2005).
19. Langford, J. F., Schure, M. R., Yao, Y., Maloney, S. F. & Lenhoff, A. M. Effects of Pore Structure and Molecular Size on Diffusion in Chromatographic Adsorbents. *J. Chromatogr. A* **1126**, 95–106 (2006).
20. Stoeckel, D. *et al.* Morphological Analysis of Disordered Macroporous–Mesoporous Solids Based on Physical Reconstruction by Nanoscale Tomography. *Langmuir* **30**, 9022–9027 (2014).
21. Hamngren Blomqvist, C. *et al.* Pore Size Effects on Convective Flow and Diffusion through Nanoporous Silica Gels. *Colloids Surfaces A Physicochem. Eng. Asp.* **484**, 288–296 (2015).
22. Reich, S. J. *et al.* Hindered Diffusion in Ordered Mesoporous Silicas: Insights from Pore-Scale Simulations in Physical Reconstructions of SBA-15 and KIT-6 Silica. *J. Phys. Chem. C* **122**, 12350–12361 (2018).
23. Reich, S. J. *et al.* Hindrance Factor Expression for Diffusion in Random Mesoporous Adsorbents Obtained from Pore-Scale Simulations in Physical Reconstructions. *Ind. Eng. Chem. Res.* **57**, 3031–3042 (2018).
24. Reich, S.-J. *et al.* Transport under Confinement: Hindrance Factors for Diffusion in Core-Shell and Fully Porous Particles with Different Mesopore Space Morphologies. *Microporous Mesoporous Mater.* **282**, 188–196 (2019).
25. Wang, W. *et al.* Quantifying Morphology and Diffusion Properties of Mesoporous Carbon From High-Fidelity 3D Reconstructions. *Microsc. Microanal.* **25**, 891–902 (2019).
26. Snyder, L. R., Kirkland, J. J. & Dolan, J. W. *Introduction to Modern Liquid Chromatography. High-Performance Gradient Elution: The Practical Application of the Linear-Solvent-Strength Model* (John Wiley & Sons, Inc., 2009). doi:10.1002/9780470508183.
27. Gritti, F. & Guiochon, G. Importance of Sample Intraparticle Diffusivity in Investigations of the Mass Transfer Mechanism in Liquid Chromatography. *AIChE J.* **57**, 346–358 (2011).
28. Gritti, F., Horvath, K. & Guiochon, G. How Changing the Particle Structure can

speed up Protein Mass Transfer Kinetics in Liquid Chromatography. *J. Chromatogr. A* **1263**, 84–98 (2012).

29. Mayer, J., Giannuzzi, L. A., Kamino, T. & Michael, J. TEM Sample Preparation and Damage. *MRS Bull.* **32**, 400–407 (2007).
30. Johnson, T. F. *et al.* Three Dimensional Characterisation of Chromatography Bead Internal Structure using X-ray Computed Tomography and Focused Ion Beam Microscopy. *J. Chromatogr. A* **1566**, 79–88 (2018).
31. Maire, E. *et al.* On the Application of X-ray Microtomography in the Field of Materials Science. *Adv. Eng. Mater.* **3**, 539 (2001).
32. Loos, J. *et al.* Electron Tomography on Micrometer-Thick Specimens with Nanometer Resolution. *Nano Lett.* **9**, 1704–1708 (2009).
33. Biskupek, J., Leschner, J., Walther, P. & Kaiser, U. Optimization of STEM Tomography Acquisition - A Comparison of Convergent Beam and Parallel Beam STEM Tomography. *Ultramicroscopy* **110**, 1231–1237 (2010).
34. Segal-Peretz, T. *et al.* Characterizing the Three-Dimensional Structure of Block Copolymers via Sequential Infiltration Synthesis and Scanning Transmission Electron Tomography. *ACS Nano* **9**, 5333–5347 (2015).
35. Gnanasekaran, K., Snel, R., de With, G. & Friedrich, H. Quantitative Nanoscopy: Tackling Sampling Limitations in (S)TEM Imaging of Polymers and Composites. *Ultramicroscopy* **160**, 130–139 (2016).
36. Bals, S., Kilaas, R. & Kisielowski, C. Nonlinear Imaging using Annular Dark Field TEM. *Ultramicroscopy* **104**, 281–289 (2005).
37. van den Broek, W. *et al.* Correction of Non-Linear Thickness Effects in HAADF STEM Electron Tomography. *Ultramicroscopy* **116**, 8–12 (2012).
38. Gordon, R., Bender, R. & Herman, G. T. Algebraic Reconstruction Techniques (ART) for Three-Dimensional Electron Microscopy and X-ray Photography. *J. Theor. Biol.* **29**, 471–481 (1970).
39. Zhong, Z. *et al.* Automatic Correction of Nonlinear Damping Effects in HAADF–STEM Tomography for Nanomaterials of Discrete Compositions. *Ultramicroscopy* **184**, 57–65 (2018).
40. Wolf, D. *et al.* Three-Dimensional Composition and Electric Potential Mapping of III-V Core-Multishell Nanowires by Correlative STEM and Holographic Tomography. *Nano Lett.* **18**, 4777–4784 (2018).
41. Hlushkou, D., Svidrytski, A. & Tallarek, U. Tracer-Size-Dependent Pore Space Accessibility and Long-Time Diffusion Coefficient in Amorphous, Mesoporous Silica. *J. Phys. Chem. C* **121**, 8416–8426 (2017).
42. Tallarek, U., Hlushkou, D., Rybka, J. & Höltzel, A. Multiscale Simulation of Diffusion in Porous Media: From Interfacial Dynamics to Hierarchical Porosity. *J. Phys. Chem. C* **123**, 15099–15112 (2019).
43. Svidrytski, A. *et al.* Morphology of Fluids Confined in Physically Reconstructed Mesoporous Silica: Experiment and Mean Field Density Functional Theory. *Langmuir* **34**, 9936–9945 (2018).
44. Krüger, T. *et al. The Lattice Boltzmann Method.* (Springer International Publishing, 2017). doi:10.1007/978-3-319-44649-3.
45. Ginzburg, I. Equilibrium-Type and Link-Type Lattice Boltzmann Models for Generic Advection and Anisotropic-Dispersion Equation. *Adv. Water Resour.* **28**, 1171–1195 (2005).
46. Gebäck, T., Marucci, M., Boissier, C., Arnehed, J. & Heintz, A. Investigation of the

Effect of the Tortuous Pore Structure on Water Diffusion through a Polymer Film Using Lattice Boltzmann Simulations. *J. Phys. Chem. B* **119**, 5220–5227 (2015).

47. Gebäck, T. & Heintz, A. A Lattice Boltzmann Method for the Advection-Diffusion Equation with Neumann Boundary Conditions. *Commun. Comput. Phys.* **15**, 487–505 (2014).
48. Kremer, J. R., Mastronarde, D. N. & McIntosh, J. R. Computer Visualization of Three-Dimensional Image Data Using IMOD. *J. Struct. Biol.* **116**, 71–76 (1996).
49. Egerton, R. F. Radiation Damage to Organic and Inorganic Specimens in the TEM. *Micron* **119**, 72–87 (2019).
50. Weyland, M. & Midgley, P. Electron Tomography. in *Transmission Electron Microscopy* 343–376 (Springer, 2016). doi:10.1007/978-3-319-26651-0_12.
51. van der Heide, P., Xu, X. P., Marsh, B. J., Hanein, D. & Volkmann, N. Efficient Automatic Noise Reduction of Electron Tomographic Reconstructions based on Iterative Median Filtering. *J. Struct. Biol.* **158**, 196–204 (2007).
52. Danielsson, P. Euclidean Distance Mapping. *Comput. Graph. Image Process.* **14**, 227–248 (1980).
53. Malandain, G. & Fernández-Vidal, S. Euclidean Skeletons. *Image Vis. Comput.* **16**, 317–327 (1998).
54. Thommes, M. *et al.* Physisorption of Gases, with Special Reference to the Evaluation of Surface Area and Pore Size Distribution (IUPAC Technical Report). *Pure Appl. Chem.* **87**, 1051–1069 (2015).
55. Mezhericher, M., Levy, A. & Borde, I. Theoretical Models of Single Droplet Drying Kinetics: A Review. *Dry. Technol.* **28**, 278–293 (2010).
56. Gritti, F. & Guiochon, G. New Insights on Mass Transfer Kinetics in Chromatography. *AIChE J.* **57**, 333–345 (2011).
57. Sie, S. T. & Krishna, R. Fundamentals and Selection of Advanced Fischer–Tropsch Reactors. *Appl. Catal. A Gen.* **186**, 55–70 (1999).
58. Shen, L. & Chen, Z. Critical Review of the Impact of Tortuosity on Diffusion. *Chem. Eng. Sci.* **62**, 3748–3755 (2007).
59. Ghanbarian, B., Hunt, A. G., Ewing, R. P. & Sahimi, M. Tortuosity in Porous Media: A Critical Review. *Soil Sci. Soc. Am. J.* **77**, 1461–1477 (2013).
60. Arslan, I., Tong, J. R. & Midgley, P. A. Reducing the Missing Wedge: High-Resolution Dual Axis Tomography of Inorganic Materials. *Ultramicroscopy* **106**, 994–1000 (2006).
61. Comiti, J. & Renaud, M. A New Model for Determining Mean Structure Parameters of Fixed Beds from Pressure Drop Measurements: Application to Beds Packed with Parallelepipedal Particles. *Chem. Eng. Sci.* **44**, 1539–1545 (1989).
62. Boudreau, B. P. The Diffusive Tortuosity of Fine-Grained Unlithified Sediments. *Geochim. Cosmochim. Acta* **60**, 3139–3142 (1996).
63. Barrande, M., Bouchet, R. & Denoyel, R. Tortuosity of Porous Particles. *Anal. Chem.* **79**, 9115–9121 (2007).
64. Matyka, M., Khalili, A. & Koza, Z. Tortuosity-Porosity Relation in Porous Media Flow. *Phys. Rev. E* **78**, 026306 (2008).
65. Sun, Z., Tang, X. & Cheng, G. Numerical Simulation for Tortuosity of Porous Media. *Microporous Mesoporous Mater.* **173**, 37–42 (2013).
66. Gritti, F. & Guiochon, G. Effect of the Surface Coverage of C18-bonded Silica Particles on the Obstructive Factor and Intraparticle Diffusion Mechanism. *Chem. Eng. Sci.* **61**, 7636–7650 (2006).

67. Iwai, H. *et al.* Quantification of SOFC Anode Microstructure based on Dual Beam FIB-SEM Technique. *J. Power Sources* **195**, 955–961 (2010).
68. Lowell, S., Shields, J. E., Thomas, M. A. & Thommes, M. Other Surface Area Methods. in *Characterization of Porous Solids and Powders: Surface Area, Pore Size and Density* (ed. Lowell, S.) 82–93 (Springer, 2004). doi:10.1007/978-1-4020-2303-3_6.
69. Iler, R. K. *The Chemistry of Silica*. (John Wiley & Sons, Inc., 1979). ISBN: 047102404X.
70. Nyström, Herrmann, W., Larsson, B. (EKA Nobel AB) US 5256386 (1993).
71. Gustafsson, H. & Holmberg, K. Emulsion-Based Synthesis of Porous Silica. *Adv. Colloid Interface Sci.* **247**, 426–434 (2017).

Appendices

Appendix 4.1 Detailed description of the workflow

4.1.1 Image intensity in STEM mode

The image intensity in STEM mode is based on the number of scattered electrons. The number of electrons that are scattered depends on the chemical composition of the material and the position of the annular ring detector. The annular ring detector can collect electrons within the collection angles β_{in} to β_{out}, which is determined by the camera length. Electrons scattered under high angles can be captured by a low camera length, whereas electrons scattered under low angles can be captured by a high camera length[1]. The image intensity scales more or less linearly with respect to the thickness of the sample. However, at high sample thickness the image intensity becomes damped due to some electrons being scattered outside of the annular ring detector[2-4]. This nonlinear damping of the image intensity causes artifacts in the tomographic reconstruction: the interior of the sample becomes underestimated while the exterior is overestimated (**Figure A4.1b**). In addition, electrostatic interaction of the particle with the electron beam can cause local increased intensity values[5-6]. These artefacts makes it difficult to calculate a global threshold for image segmentation, especially in homogeneous samples. Very thick samples with very small features such as the particles in this study cannot easily be segmented based on a difference in intensity and thus requires a different approach, as outlined below.

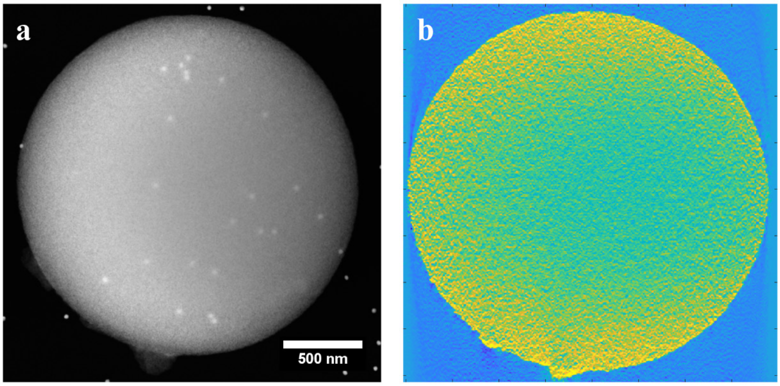

Figure A4.1: **(a)** LC-STEM image of a Kromasil® Classic – 100 Å SIL 1.8 μm. **(b)** Central numerical cross-section of the reconstruction after segmentation using a standard weighting back projection algorithm and without correcting for any imaging artefacts. An intensity gradient is clearly visible due to nonlinearity between the signal intensity and the particle thickness.

4.1.2 Alignment of the particle

During the measurement of the sample, the projection of the particle shifts in the image. These shifts are caused by movements of the sample under the microscope. However, for a good reconstruction steady images that are rotated around one single point are required. In this particular case there are two ways to align the particle: 1) alignment by tracking gold fiducial markers and 2) alignment based on the sphericity of the particle.

Because the particle is spherical, a clear circular object is visible in every projection. A threshold is applied to split the object from the background and an outline is determined. The radius and center of this object are then fitted using the least-squares method and the image is cropped, so that the center of the particle is always in the center of the image (**Figure A4.2**). A profile of the center and radius of the particle along the rotation angles is shown Figure A4.2b. It is clear that the series is tilted around the *x*-axis because the *x*-coordinate of the center of the particle in the projections remains constant. A minor decrease in the radius is visible from 744 pixels at −68° to 735 pixels at +68°. This shrinkage is the result of beam damage during image acquisition. After the alignment step the projections have a size of 1601 by 1601 pixels.

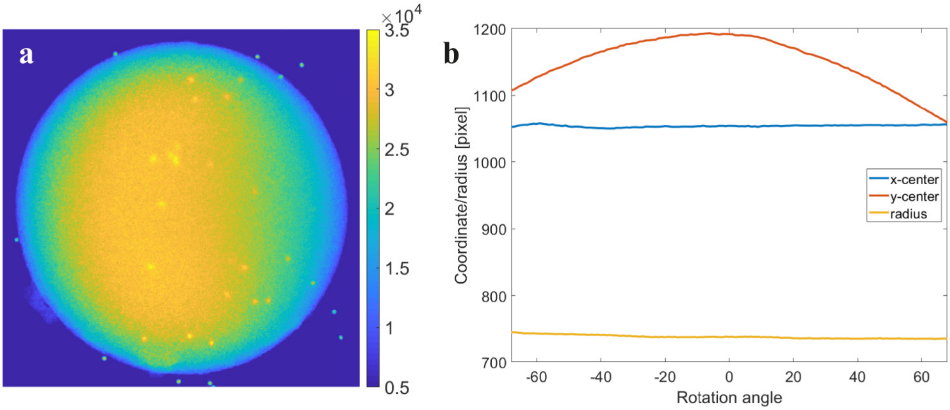

Figure A4.2: (a) STEM micrograph at 0° tilt rendered in false color for better visibility of nonlinear thickness and residual charging artifacts. **(b)** Profile of the fitted *x*- and *y*-center coordinates and radius of the outline in pixels along the rotation angles. A small decrease is visible from 744 pixels at −68º to 735 pixels at +68º due to beam damage.

4.1.3 Background correction

During image acquisition the particle is positioned on top of a carbon layer. This increases the intensity that is measured. Only the particle should be reconstructed in the filtered back-projection and therefore the background intensity of the carbon layer should be subtracted. However, the planar travel length of the beam is affected by the angle of plane and due to the carbon layer it is different for every rotation angle (**Figure A4.3**).

The variation of the background intensity caused by the carbon layer is measured in two steps. In the first step a rough background is selected for each individual angle by using an intensity threshold of 6000. All values below the threshold are considered background values. For each tilt angle the mean value and standard deviation are calculated. The mean background intensity and the mean background intensity minus one standard deviation are shown Figure A4.3c. In each projection an intensity is subtracted equal to the mean background at that specific angle minus the standard deviation at this angle.

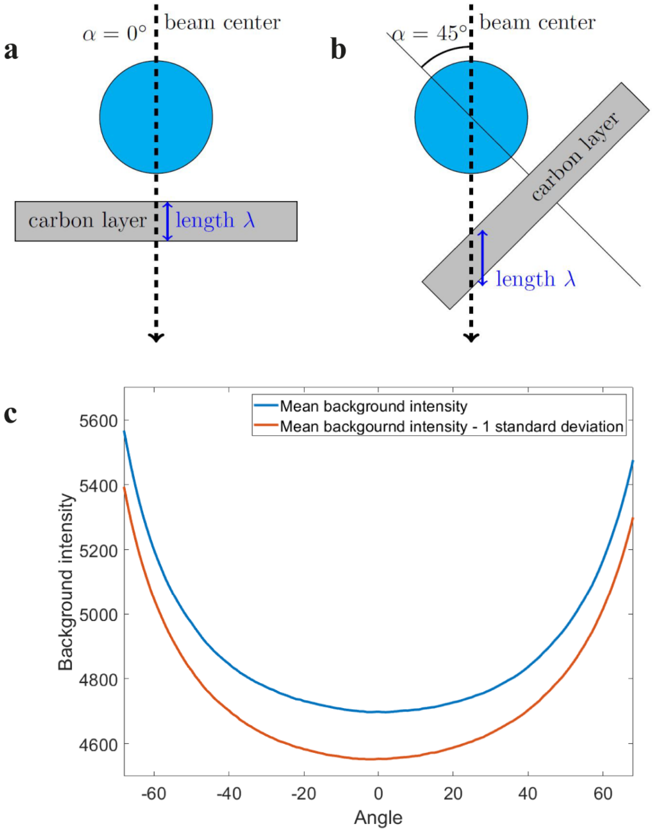

Figure A4.3: (a) Beam travelling through a sample and the underlying carbon layer at a tilt angle of 0 º. **(b)** Beam traveling through a sample and the underlying carbon layer at a tilt angle of 45º. The travel length λ through the carbon layer increases with increasing tilt angles. **(c)** Difference in background intensity caused by the carbon layer under various angles.

4.1.4 Charging correction

Charging occurs when the electrons of the beam interact with the silica sample. The imaged particle seems to have an increase in intensity on the left side of the particle, which is further on referred to as the charged side. The right side seems to be less affected and is referred to as the non-charged side.

A mean frame projection is created from all 137 projections by averaging using the center 90% percentiles values of each pixel. The fact that the particle projection is still asymmetric after averaging over all angles shows that charging is an effect of the beam and is unrelated to the porosity distribution of the particle. This asymmetry is further investigated by studying the radial average of the particle. The radial average is made by laying a raster of concentric circles on top of the image, starting from the chosen center. The spaces between the concentric rings are called radial bins. By collecting the intensity values in each bin and averaging over these values, an array of averaged intensity values for each radial bins is found. This array can then be displayed in a line plot where the radius of the radial bins is plotted against the averaged intensity of the bins. To investigate how the left side differs from the right side of the particle, two radial averages are made for the non-charged and charged side, respectively (**Figure A4.4**). From the radial average plot it is clear that the non-charged side has much lower radial average intensity values than the charged side. It is also visible that the radial average of the charged side has a maximum value at 215 pixels away from the center. This is, however, unphysical because the highest intensity should always be in the center at the position where the spherical particle is the thickest.

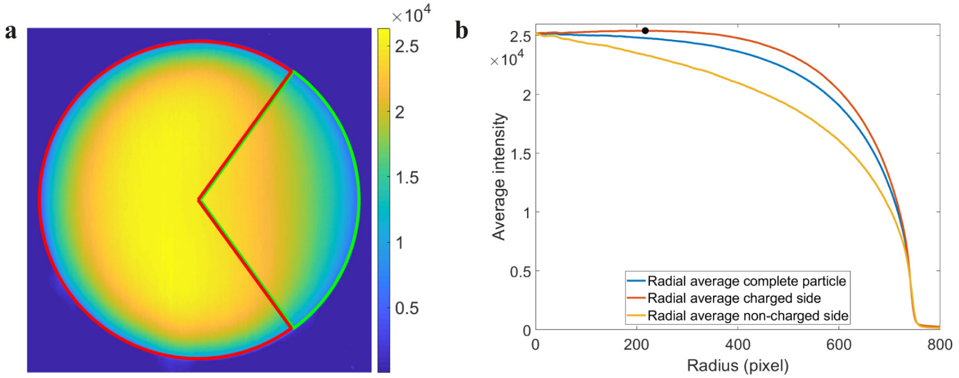

Figure A4.4: **(a)** Mean projection image of the particle. The particle is divided in a charged side (in red) and in a non-charged side (in green). **(b)** Radial average of the whole particle, charged and non-charged side. The black dot indicates the maximum intensity value of the charged side.

That there are two different relations between the thickness and intensity can also be seen in a thickness-intensity map. A thickness-intensity map is a matrix where the rows correspond to a thickness, the columns correspond to an intensity and the values inside the matrix give the amount of occurrences of this thickness-intensity combination in the projection image. The thickness-intensity map can be very useful to see which thickness-intensity relations are present and if a charging correction has been successful in correcting the charged area. To make a thickness-intensity map, an intensity image should be known and a theoretical thickness image should be known. The theoretical thickness image is an image of the thickness of a perfect sphere. In the alignment step the center $(x_C\,;\,y_C)$ and radius $\mathscr{R}$ of the particle in the projections have been found. The projections were then cropped so that the center of particle was in the middle and therefore $(x_C\,;\,y_C) = (0\,;\,0)$. Because the particle is known to be a sphere, the theoretical thickness $\mathscr{T}$ for a sphere with radius $\mathscr{R}$ can be calculated for every pixel $(x_C\,;\,y_C)$ in the projection:

$$\mathscr{T} = \begin{cases} 2\sqrt{\mathscr{R}^2 - x^2 - y^2}, & \text{if } x^2 + y^2 \leq \mathscr{R} \\ 0, & \text{if } x^2 + y^2 > \mathscr{R} \end{cases} \tag{A4.1}$$

For every pixel (x ; y) in the projection a theoretical thickness is known and a thickness image can be produced as can be seen in **Figure A4.5a**. In perfect circumstances the thickness-intensity map of a uniform sphere should only show one linear line, because the intensity increases linearly with the thickness, and the sphere would be radially symmetric. If the sphere would be porous, a line would still be visible, but there would be a distribution in intensity for every thickness value. From the thickness-intensity map of the imaged particle (**Figure A4.5b**) it can be seen that not one line, but two lines are visible. The reason for this is that there are two sides in the particle, a charged and a non-charged side. Each of these sides has a different thickness-intensity relation.

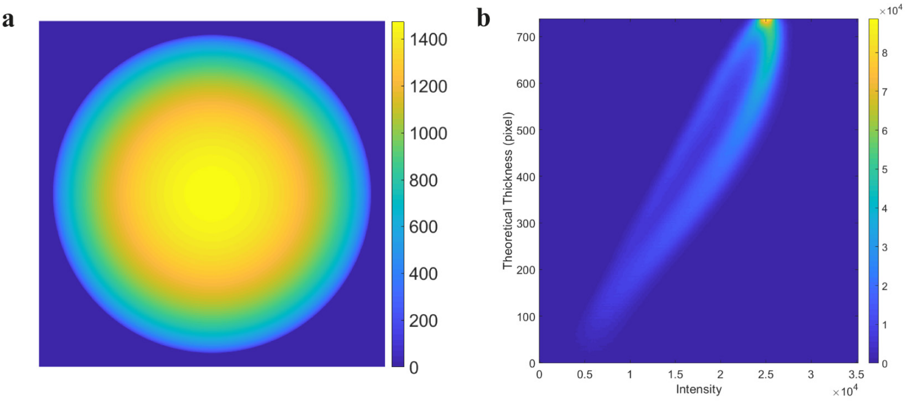

Figure A4.5: (a) Theoretical thickness image of a perfect sphere. **(b)** Thickness-intensity map of the imaged particle. Two relationships are visible, one for the charged side (right profile) and one for the non-charged side (left profile).

A correction for the charging effect is created using the non-charged area of the mean-projection image shown in Figure A4.5a. From the radial distribution of this area, a new image is made that is fully radially symmetric. A charging correction image is then found by dividing the radial symmetric image of the non-charged side by the mean projection image (**Figure A4.6a**):

$$f_{\text{charging}}(x,y)=\frac{\text{Radial symmetric image}(x,y)}{\text{Mean projection image}(x,y)} \tag{A4.2}$$

It may seem that this correction will also remove all local porosity variations, but the correction is based on the average over all projections, therefore deviations of the average are preserved. The intensity gradient in the image after charging is now radially symmetric, while local variations are still preserved (**Figure A4.6b**).

A second option to show the effectiveness of the charging correction is by making another thickness intensity map, as can be seen in **Figure A4.6c**. Now only one clear thickness-intensity relation is visible. There is still a small remainder of the charged-side thickness-intensity relation visible, but this relation is only a small fraction of what it was before. A third possibility to investigate whether the charging correction was successful is to make another radial average. The result is shown in **Figure A4.6d**. Now all lines fall together, and the maximum value is in the center. Therefore, this radial average shows that the charging correction was effective. The curve still differs from the radial average of a perfect sphere because the thickness intensity relation is still not linear.

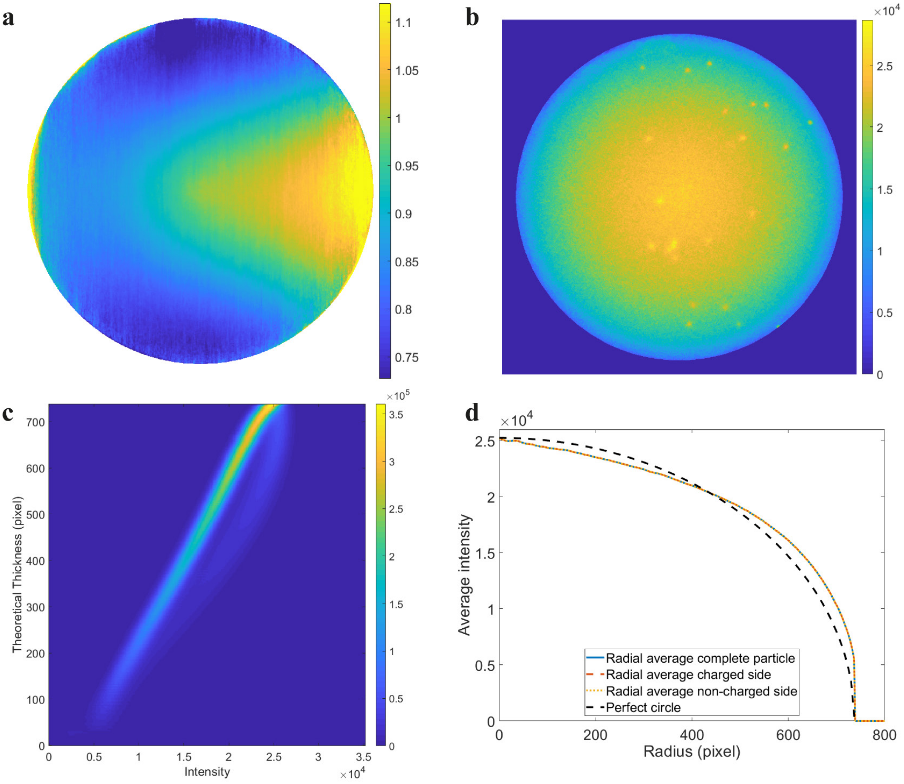

Figure A4.6: (a) Image of the charging correction, which consists of the ratio between the radial symmetric image based on the non-charged side and the mean projection image. **(b)** STEM micrograph at 0° tilt after correcting for the background and charge. **(c)** Thickness-intensity map after the charging correction. The majority of the map agrees with the non-charged thickness-intensity relationship. **(d)** Radial average of the projections after the charging correction compared to the radial average of a perfect sphere that is scaled to the maximum value of the projections.

4.1.5 Linearity correction

Besides charging, another cause for the inhomogeneity is the fact that the thickness-intensity relation is still not linear. Therefore, another correction is applied, similar to the correction in the previous section. In this step the correction for each pixel is defined by the image of a perfect sphere and the mean projection image:

$$f_{\text{linearity}}(x,y) = \frac{\text{Spherical thickness image}(x,y)}{\text{Mean projection image}(x,y)} \qquad \text{(A4.3)}$$

The thickness image that is used is the same image as shown in Figure A4.6a. When the linearity correction is applied, the intensity values now successfully correspond to the thickness of each point in the projection (**Figure A4.7a**). Local deviations are still preserved in the image because the correction was based on mean intensity image and not on a specific frame. In the thickness-intensity map in **Figure A4.7b** the relation between the thickness and the intensity also appears linear, in contrast to the thickness-intensity map in the previous section and the radial average is now similar to that of a perfect sphere as is displayed in **Figure A4.7c**.

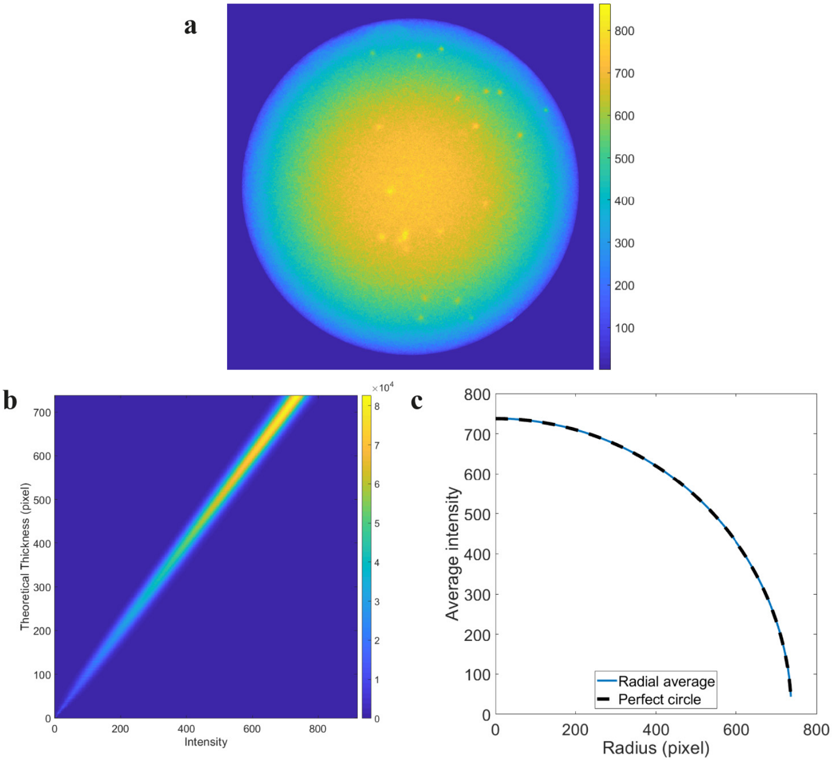

Figure A4.7: (a) STEM micrograph at 0° tilt after correcting for the background, charge and nonlinearity. **(b)** Thickness-intensity map after linear correction. The intensity now scales linearly with the thickness. **(c)** Radial average of the projections after linear correction. The profile now fits perfectly with the radial average of a perfect sphere.

4.1.6 Filtered back-projection and median filter

After the linearity correction, the particle is reconstructed in IMOD 4.9 using a weighted back projection algorithm with a linear density scaling of 1 and a low-pass radial filter (0.2 px^{-1} cut off with 0.05 px^{-1} fall off)[7]. The result of the filtered back-projection is a 3D matrix of 1601 × 1601 × 1601 voxels and a final pixel size of 1.432 nm·px^{-1}. A low voxel value constitutes a high probability of a pore and a high voxel value constitutes a high probability of silica voxel. However, seemingly random spikes appear in the matrix as well, which are considered noise. Noise can occur in the reconstruction when the sample is slightly moved in the projections, or because not enough projections were used in the reconstruction. The noise can be reduced by a median filter, which is similar to a Gaussian smoothing function in the way that is uses a window of the surrounding cells to modify the voxel value[8]. However, in a median filter every cell is replaced by the median values of the window of that cell. In this step a median filter with a window of 5 × 5 × 5 voxels are used. The center numerical cross section of the reconstruction after applying the median filter is shown in **Figure A4.8a**.

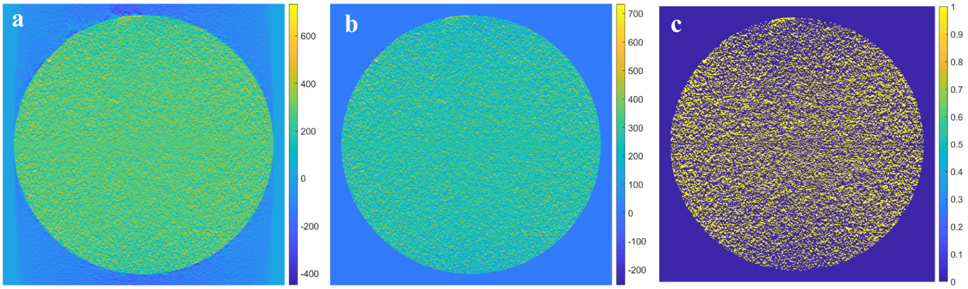

Figure A4.8: (a) Central numerical cross-section through the reconstruction after correcting for the background, charge and nonlinearity. The reconstruction has a total of 1601 × 1601 × 1601 voxels. High intensity values indicate silica, low intensity values indicate pores. **(b)** Central numerical cross-section after masking. A perfect spherical mask with a radius of 735 pixels is used. **(c)** Central numerical cross-section of the segmented reconstruction after applying all corrections. A global threshold of 294 is chosen in order to get a global porosity of 65%. The vaguely visible horizontal line is an artefact appearing along the direction of the rotation axis.

4.1.7 Spherical mask

Even though the particle is a sphere, values other than zero are also found outside the reconstructed object. The reason for this is that the reconstruction is not yet perfect. The reconstruction would improve if more than 137 projection and a wider range of angles were used[9]. However, it is known that the object is a near perfect sphere and therefore all the data outside the sphere in the reconstruction can be discarded. Therefore a perfect spherical mask is placed over the image. The mask is based on the distance r of a voxel to the center and the maximum radius of the sphere $\mathscr{R}_{\mathrm{max}}$. The value of $\mathscr{R}_{\mathrm{max}}$ is 738 pixels. Every voxel where the distance to the center r exceeds the maximum radius $\mathscr{R}_{\mathrm{max}}$ is set to zero. The result is shown in **Figure A4.8b**. All values inside the reconstruction are distributed between around −200 to 700.

4.1.8 Segmentation

The last step of the workflow is the segmentation step. In order to segment the particle, all values inside the 3D mask are collected. These values are then sorted from low to high in a distribution. Because nitrogen adsorption showed that 65.3% of the particle consists of pores, the 65.3 percentile in the distribution is taken as the global threshold. Every value below this threshold is then considered a pore, a zero in the reconstruction. Every value above the threshold is silica, a one in the reconstruction. The center numerical cross section of the new binary reconstruction is shown in **Figure A4.8c**. The porosity in this image seems to be uniformly distributed. A horizontal line is vaguely visible through the center of the figure, which is most likely an artefact created during the reconstruction by the rotation axis which is positioned in the same area.

In this context it is important to note that: depending on the total electron dose for data acquisition in combination with the employed reconstruction algorithm, tilt-range and increment of data acquisition, and the chosen segmentation threshold the size and shape of segmented features will vary[10-12].

4.1.9 Calculating the pore size distribution

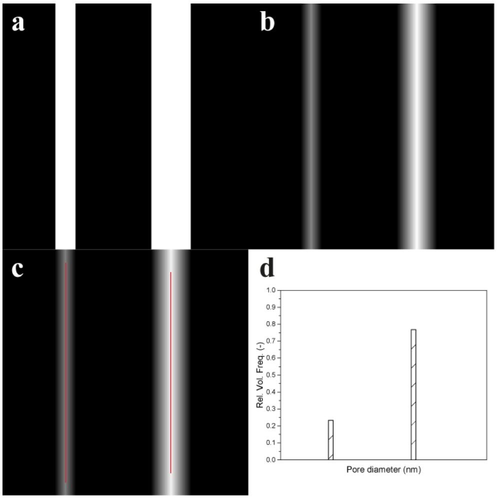

Figure A4.9: Schematic workflow for the calculation of the pore size distribution. **(a)** Binary image of two pores shown in white. **(b)** Corresponding distance transform. The intensity scales with the distance to the pore boundaries. **(c)** Distance transform overlaid with the corresponding skeleton. The skeleton does not extend all the way to the edge due to applied edge conditions. **(d)** Histogram of the corresponding pore size distribution.

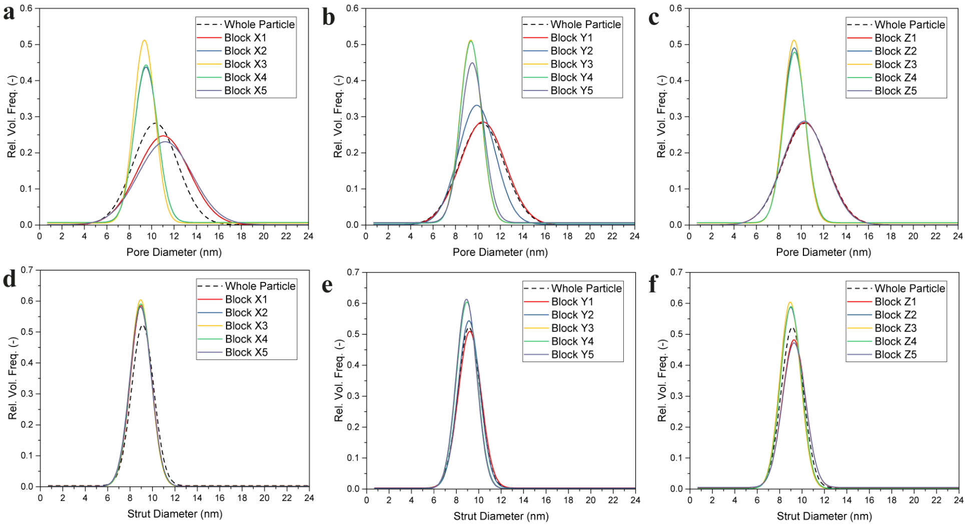

Figure A4.10: Comparison of the local pore size distribution along the **(a)** *x*-axis, **(b)** *y*-axis and **(c)** *z*-axis, respectively. The variations in the pore diameter indicate a subtle inhomogeneity throughout the particle. Comparison of the local strut size distribution along the **(d)** *x*-axis, **(e)** *y*-axis and **(f)** *z*-axis, respectively. The strut size remains relatively constant throughout the whole particle.

Appendix 4.2 Detailed description of the diffusion simulations

4.2.1 The diffusion equation

The tomographic reconstruction was used to compute the intraparticle diffusion constant via lattice Boltzmann simulations[13]. To this end, the lattice Boltzmann method was used to solve the diffusion equation inside the same sub-volumes as described in the main text but scaled down to 150 × 150 × 150 voxels:

$$\frac{\partial C}{\partial t} = \mathcal{D}_0 \Delta C \tag{A4.4}$$

where ΔC is a concentration gradient in pore network and $\mathcal{D}_0$ is the free diffusion coefficient in the pore network (2.3×10^{-9} $m^2 \cdot s^{-1}$). The equation was solved using zero flux boundary conditions on the material surface[14,15]:

$$-\mathcal{D}_0 \frac{\partial C}{\partial \hat{n}} = 0 \tag{A4.5}$$

where $\hat{n}$ is the outward-pointing unit normal vector, such that no diffusion takes place in the solid phase of the material. The top and bottom of the cube were set as the influx and outflux boundaries ($z = 0$ and $z = L$) and the concentration was set to given values (C_1 and C_2) to create a concentration gradient.

After the diffusion equation was solved to steady state, the effective diffusion coefficient could then be computed from the average flux J in the direction of the concentration gradient:

$$\overline{J_z} = \mathscr{D}_0 \overline{\frac{\partial C}{\partial z}} \tag{A4.6}$$

The effective diffusion constant then becomes:

$$\mathscr{D}_{\text{eff}} = -\frac{\overline{J_z} L}{C_2 - C_1} = k^* \mathscr{D}_0 \tag{A4.7}$$

where $C_2 - C_1$ is the concentration difference, L is the thickness of the volume and k^* is a dimensionless proportionality factor called the 'geometry factor', depending only on the geometry of the structure and not on the length scale or size of the object. However, it can be different in different directions so it has to be computed in all three dimensions. In **Figure A4.11** the effective diffusion is simulated in the x-, y- and z-direction in each of the five sub volumes along the x-axis of the particle. These results clearly show that the diffusion in the z-direction is different than in the x- and y-direction. This could indicate that the structure is anisotropic but it is probably the result of the missing wedge artefact[9], as shown in the next section.

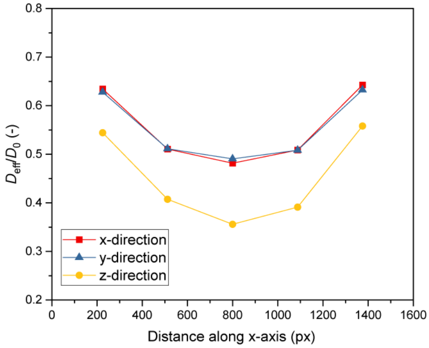

Figure A4.11: Effective diffusion in the five sub volumes along the x-axis of the particle, computed in the x-, y-, and z-direction. The diffusion constant in the z-direction is notably different than the diffusion constant in the other two directions, which is the result of the missing wedge artefact.

4.2.2 Missing wedge artefact

To account for the anisotropic resolution seen in Figure A4.11, tomography data was simulated from an isotropic structure with the same dimensions and porosity over the experimental angular range (± 68°) as well as over the full angular range (± 90°). To this end, a perfectly isotropic cube was created of 280 voxels (200 nm) using a diffusion limited cluster aggregation (DLCA) algorithm for aggregating particles[16]. The algorithm was run until all particles had aggregated. The particles were then allowed to "sinter" by smoothing the structure with a Gaussian filter ($\sigma = 2.8$) to get an average pore size of 10 nm and a threshold was chosen to achieve a porosity of 65%. Projections were then computed at angles from −68° to +68°, with steps of 1° and were used to reconstruct the 3D pore network. Reconstructions were constructed with and without the same processing steps as for the original tomogram, i.e., setting a threshold to match a porosity of 65% and applying a median filter to remove noise, prior to the segmentation of the data. Then we computed the center of mass, effective diffusion in all three coordinate directions, as well as the average pore size. The results are shown in **Table A4.1**.

Table A4.1: Computed parameters for the simulated isotropic cube and the corresponding reconstructions.

Simulation	**Isotropic cube**	**68° tilt pre-processing**	**68° tilt post-processing**	**90° Tilt pre-processing**
Center of mass (x,y,z) (nm)	99.75 99.98 99.88	99.31 99.35 99.34	99.13 99.41 98.30	99.45 99.52 98.97
$\mathscr{D}_{\text{eff}}/\mathscr{D}_0$ (x,y,z)	0.48 0.48 0.48	0.52 0.49 0.45	0.52 0.49 0.46	0.50 0.49 0.50
Avg. pore size (nm)	9.94	10.03	10.51	10.27

The results show that the simulated isotropic cube is indeed perfectly isotropic: the center of mass and effective diffusion constants have practically the same value in all three directions. The average pore size is 10 nm, which is consistent with the input value and consistent with the actual particle. The 68° tilt simulation pre- and post-processing has the same center of mass and almost the same average pore size but different values for $\mathscr{D}_{\text{eff}}/\mathscr{D}_0$ in the direction of the missing wedge artefact (z-direction) compared to the other directions, indicating that the imaging approach introduces anisotropy. There is no difference in the values for $\mathscr{D}_{\text{eff}}/\mathscr{D}_0$, indicating that the processing steps do not shift the location of the pore boundaries. There is a slight difference in the average pore size pre- and post-processing but this is likely a result of the relatively large smoothening effect of the media filter compared to the size of the dataset.

If we look at the 90° tilt simulation we can see that the center of mass and $\mathscr{D}_{\text{eff}}/\mathscr{D}_0$ have a very similar value in all three directions, indicating that no anisotropy is introduced by imaging. There is a slight deviation in the $\mathscr{D}_{\text{eff}}/\mathscr{D}_0$ values but this falls well within the margins of the lattice Boltzmann simulations. These results clearly show that the limited tilt-series that has been used for the tomographic reconstruction has a strong impact on the diffusion values calculated via lattice Boltzmann simulations in the direction of the missing wedge artefact (*z*-direction).

4.2.3 References

1. Gnanasekaran, K., de With, G. & Friedrich, H. Quantification and Optimization of ADF-STEM Image Contrast for Beam-Sensitive Materials. *R. Soc. Open Sci.* **5**, 171838 (2018).
2. Bals, S., Kilaas, R. & Kisielowski, C. Nonlinear Imaging using Annular Dark Field TEM. *Ultramicroscopy* **104**, 281–289 (2005).
3. van den Broek, W. *et al.* Correction of Non-Linear Thickness Effects in HAADF STEM Electron Tomography. *Ultramicroscopy* **116**, 8–12 (2012).
4. Zhong, Z. *et al.* Automatic Correction of Nonlinear Damping Effects in HAADF–STEM Tomography for Nanomaterials of Discrete Compositions. *Ultramicroscopy* **184**, 57–65 (2018).
5. Egerton, R. F. Radiation Damage to Organic and Inorganic Specimens in the TEM. *Micron* **119**, 72–87 (2019).
6. Egerton, R. F. Control of Radiation Damage in the TEM. *Ultramicroscopy* **127**, 100–108 (2013).
7. Kremer, J. R., Mastronarde, D. N. & McIntosh, J. R. Computer Visualization of Three-Dimensional Image Data Using IMOD. *J. Struct. Biol.* **116**, 71–76 (1996).
8. van der Heide, P., Xu, X. P., Marsh, B. J., Hanein, D. & Volkmann, N. Efficient Automatic Noise Reduction of Electron Tomographic Reconstructions based on Iterative Median Filtering. *J. Struct. Biol.* **158**, 196–204 (2007).
9. Arslan, I., Tong, J. R. & Midgley, P. A. Reducing the Missing Wedge: High-Resolution Dual Axis Tomography of Inorganic Materials. *Ultramicroscopy* **106**, 994–1000 (2006).
10. Chen, D. *et al.* The Properties of SIRT, TVM, and DART for 3D Imaging of Tubular Domains in Nanocomposite Thin-Films and Sections. *Ultramicroscopy* **147**, 137–148 (2014).
11. Friedrich, H. *et al.* A Quantitative Electron Tomography Study of Ruthenium Particles on the Interior and Exterior Surfaces of Carbon Nanotubes. *ChemSusChem* **4**, 957–963 (2011).
12. Wang, W. *et al.* Quantifying Morphology and Diffusion Properties of Mesoporous Carbon From High-Fidelity 3D Reconstructions. *Microsc. Microanal.* **25**, 891–902 (2019).
13. Gebäck, T., Marucci, M., Boissier, C., Arnehed, J. & Heintz, A. Investigation of the Effect of the Tortuous Pore Structure on Water Diffusion through a Polymer Film Using Lattice Boltzmann Simulations. *J. Phys. Chem. B* **119**, 5220–5227 (2015).
14. Ginzburg, I. Equilibrium-Type and Link-Type Lattice Boltzmann Models for Generic Advection and Anisotropic-Dispersion Equation. *Adv. Water Resour.* **28**, 1171–1195 (2005).
15. Gebäck, T. & Heintz, A. A Lattice Boltzmann Method for the Advection-Diffusion Equation with Neumann Boundary Conditions. *Commun. Comput. Phys.* **15**, 487–

505 (2014).

16. Lach-hab, M., González, A. E. & Blaisten-Barojas, E. Concentration Dependence of Structural and Dynamical Quantities in Colloidal Aggregation: Computer Simulations. *Phys. Rev. E - Stat. Physics, Plasmas, Fluids, Relat. Interdiscip. Top.* **54**, 5456–5462 (1996).

Chapter 5

Towards Monodisperse Microspheres using Microfluidic Processing

Abstract

Emulsion-templated materials are widely used in materials science. Although emulsions are powerful templates, a significant drawback is that they generally lead to very polydisperse materials. Here, a microfluidic processing route is reported to produce a wide size range of monodisperse emulsion droplets containing colloidal silica nanoparticle building blocks. These confined nanoparticles are subsequently assembled into mesoporous silica microspheres (MSMs). The formation mechanism as well as fundamental aspects, such as droplet kinetics, are investigated using time-resolved imaging techniques. This includes the comparison of imaging results quantified by image analysis with a theoretical mass-transfer model, which is based on the droplet number density, solvent characteristics and temperature. The results presented here provide key insights in the time-resolved formation of MSMs and can be used to optimize experimental procedures for MSM formation and potentially lead to a more direct route to monodisperse MSMs.

Part of this chapter is to be submitted as:

Fijneman, A. J. *et al.* Time-Resolved Investigation of Mesoporous Silica Microsphere Formation using In Situ Heating Optical Microscopy, in preparation.

5.1 General introduction

Emulsions are metastable dispersions of two or more immiscible liquids and are widely used in, e.g., food[1], personal care[2] and materials science[3]. Common applications include the use of emulsions as precursors[4], controlled-release systems[5] and as templates for the formation of spherical materials[6]. One example of emulsion-templated materials is provided by mesoporous silica microspheres (MSMs). MSMs are frequently used in high performance liquid chromatography (HPLC) and play an important role in the separation and analysis of a large variety of molecules based on differences in mass transfer properties[7–9]. In several industrially relevant processes, MSMs are synthesized via multiscale colloidal assembly of silica nanoparticles (sols) as building blocks within the confinement of emulsion droplets[10–13]. A significant drawback of emulsions, however, is that they generally lead to polydisperse particles. This is on account that emulsions are mainly produced by uncontrolled mixing and shaking, high-pressure homogenization or jet homogenization (e.g., spray-drying)[14].

In HPLC a fluid (the mobile phase or eluent) containing the analyte is passed through a fixed stationary bed (the stationary phase) and is separated into different fractions[7]. If the stationary bed is packed too dense, i.e., by using polydisperse particles, the back pressure can become too high for the system to handle. Hence, alternative preparation methods are required to produce monodisperse but variable sized MSMs. One way to create highly monodisperse MSMs of variable size is to use monodisperse emulsion droplets. Several technologies exist to produce monodisperse emulsion droplets including controlled-shear[15], membrane emulsification[16] and droplet microfluidics[17]. Microfluidic processing is the most powerful technology to accurately control the droplet size over a wide range (1 – 100 μm) with a low dispersity in size[17–20]. Due to technological limitations microfluidic processing is not yet suitable to produce emulsions on industrially desired volumes[21]. However, its ability to produce monodisperse droplets over a wide size range combined with its excellent reproducibility renders droplet microfluidics an ideal platform to study fundamental aspects, such as droplet kinetics, using time-resolved imaging techniques.

Previously, it has been shown that MSM formation is dependent on two main parameters: (1) the rate of sol particle gelation r_{gel} based on the size of the sol particles used as building blocks, the reaction temperature and ionic strength, and (2) the rate of emulsion droplet shrinkage r_{shrink} due to dewatering of the droplets, which is modulated by temperature, the composition of the oil phase and back pressure (see also Chapter 3)[22]. By manipulating the balance between external confinement, process conditions and intra droplet nanoparticle interactions, the porosity characteristics of the resulting MSMs can be tailored for different applications[10–13]. Although highly successful, insight into progression of droplet shrinkage and gelation is very limited due to a lack of time-resolved data. Time-resolved studies on the formation of MSMs have been performed using in situ small-angle X-ray scattering (SAXS)[23–25] and various theoretical models on the drying behavior of single droplets containing insoluble solid particles exist[26–31]. However, these studies lack spatially resolved information that give access to the interactions of the emulsion droplets and the surrounding solvent. Therefore, to remain as close to the protocols used in industrially relevant processes[10–13], a conventional optical microscope was outfitted with a heating and vacuum stage in order to study the droplet kinetics during MSM formation in real-time.

In this chapter, we describe a microfluidic processing route towards highly monodisperse MSMs with tunable porosity characteristics. Monodisperse emulsion droplets are generated over a wide range of droplet sizes and are used to investigate the effect of various assembly parameters on the formation of MSMs via dynamic time-resolved imaging. A theoretical mass-transfer model is developed and its results are compared to quantitative imaging data, showing an excellent match. With this strategy, the effects of various parameters on the underlying kinetics of colloidal assembly in confined spaces were investigated in real-time.

5.2 Microfluidic droplet generation

5.2.1 Flow induced droplet break-up

Microfluidic droplet generators can generally be categorized into three classes based on the way the droplets are produced: co-flowing devices, cross-flowing devices and flow-focusing devices[20,32]. In this work, flow-focusing devices are used to generate droplets. In a flow-focusing device the dispersed phase and continuous phase are simultaneously pushed through a small orifice (**Figure 5.1**). The dispersed phase is confined on both sides by the continuous phase and is forced to break up into droplets. The main advantage of this type of device is that the droplet size is easily controllable by the volumetric flowrate and the size of the orifice[33,34].

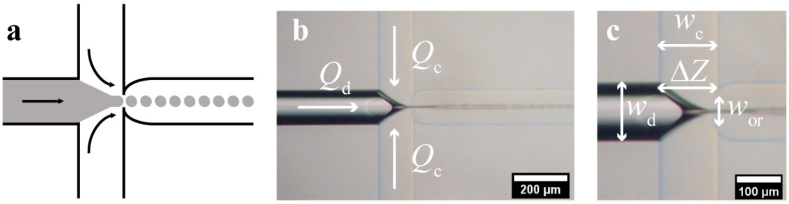

Figure 5.1: **(a)** Schematic illustration of a microfluidic flow-focusing device, highlighting the flow direction of the dispersed (grey) and continuous phase (white), respectively. **(b)** Image of the device. **(c)** Close-up image of the orifice region. Symbols described in the main text.

Flow induced droplet break-up is a physical phenomenon that can be described using a set of dimensionless numbers[32,35,36]. Arguably the most important one is the capillary number *Ca*, which represents the effect of viscous stress versus that of the interfacial tension. In a flow-focusing device the capillary number is given by[32]:

$$Ca = \frac{\eta_c w_d Q_c}{2\sigma \Delta Z}\left[\frac{1}{h_{or} w_{or}} - \frac{1}{2h_c w_c}\right] \tag{5.1}$$

where η_c is the viscosity of the continuous phase, w_d the width of the dispersed phase channel, Q_c the volumetric flow rate of the continuous phase, σ the interfacial tension, ΔZ the distance from the end of the dispersed phase channel to the entrance of the orifice, h_{or} the height of the orifice, w_{or} the width of the orifice, h_c the height of the continuous phase channel and w_c the width of the continuous phase channel (see also Figure 5.1c). Under standard operating conditions Ca generally ranges between 10^{-3} and 10[35].

Another important parameter is the Reynolds number Re, which represents the effect of inertia compared to the viscous stress[36]. Due to the small length scales of microfluidic chips and low flow rates Re is typically below 1, which is equivalent to fluid streams being laminar and, thus, easily controllable[35]. The Reynolds number and capillary number are related to each other by the Weber number $We = ReCa$, which relates the effect of inertia to the interfacial tension[32]. Finally, the ratio of the volumetric flow rates $\Phi = Q_d / Q_c$, wherein Q_d and Q_c are the volumetric flow rate of the dispersed phase and continuous phase, respectively and the viscosity ratio $\Lambda = \eta_d / \eta_c$, wherein η_d and η_c are the viscosity of the dispersed phase and continuous phase, respectively are also important in droplet break-up[36].

5.2.2 Five regimes of droplet break-up

Droplet break-up can only occur if the flow patterns are stable. If the total flow rate is too high or if the flow rate ratio is not well adjusted, no droplets are produced[37,38]. Under normal conditions five distinct regimes for droplet break-up exist. These are determined by the capillary number, ratio of the volumetric flow rate and viscosity ratio and will be briefly described below[18,39].

Regime 1 ("squeezing regime", **Figure 5.2a**) occurs at capillary numbers in the range of ($0.01 < Ca < 0.5$) and ratio volumetric flow rates in the range of ($0.4 < \Phi < 1.0$). Here, viscous shear forces are low and the interfacial tension is relatively large. In this regime the dispersed phase forms plug-like droplets, which completely block the orifice. This causes a buildup of pressure in the continuous phase. Eventually the pressure becomes so large that droplets are pinched off. These droplets are generally larger than the size of the orifice and monodisperse[40,41]. Regime 2 ("dripping regime", **Figure 5.2b**) occurs at comparable capillary numbers as the squeezing regime ($0.01 < Ca < 0.7$) but at a lower ratio of volumetric flow rate ($0.01 < \Phi < 0.4$). Here, the viscous forces start to dominate over the interfacial tension. In this regime the droplets break-up exactly at the orifice and before they have the chance to block the orifice. These droplets are roughly the same size as the orifice and are also highly monodisperse[42,43]. Regime 3 ("jetting regime", **Figure 5.2c**) occurs at capillary numbers in the range of ($0.5 < Ca < 2.0$) and ratio of volumetric flow rates ($0.05 < \Phi < 1.0$). Here, the dispersed phase forms an elongated liquid jet, which breaks up into droplets due to Rayleigh instability[44]. The droplets formed in this regime are generally polydisperse[45]. Regime 4 ("tip-streaming regime", **Figure 5.2d**) occurs at capillary numbers in the range of ($0.8 < Ca < 2.0$) and ratio of volumetric flow rates ($0.01 < \Phi < 0.05$). Under these conditions the dispersed phase is stretched out into an extremely thin jet with a conical-tip, which breaks up into droplets that are significantly smaller than the size of the orifice[36,46]. Regime 5 ("tip-multi-breaking regime", **Figure 5.2e**) is the rarest regime and only occurs at capillary numbers in the range of ($0.7 < Ca < 0.8$) and ratio of volumetric flow rates ($0.01 < \Phi < 0.05$). Under these conditions the conical tip of the jet is unsteady and periodically breaks of into multiple droplets due to oscillations of the tip. The droplets produced in this way are polydisperse and difficult to control[47,48]. In general, the dripping regime is the preferred mode because it gives the most monodisperse droplets over a wide size range.

All five regimes can occur regardless off the dimensions of the chip. If the ratio between Ca and Φ are scaled proportionally, the same break-up regime will occur. Specific to our application case, the fact that the dispersed phase contains silica nanoparticles does not matter as long as Λ is scaled proportionally. To illustrate the above behavior, the five break-up regimes are plotted as a function of Ca and Φ for droplets containing silica nanoparticles (5 wt%, 8 nm in diameter) and droplets without nanoparticles with $\Lambda = 0.05 \pm 0.01$ (**Figure 5.2f**). The different regimes can be clearly distinguished while occasionally there is some overlap of regimes due to the transition between modes.

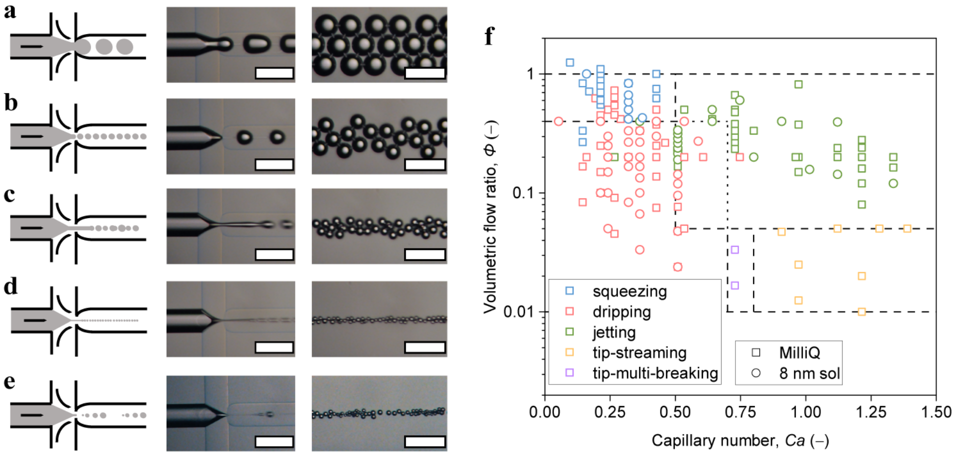

Figure 5.2: The five regimes of droplet break-up determined by a competition between the viscous forces, inertia and interfacial tension: **(a)** squeezing mode, **(b)** dripping mode, **(c)** jetting mode, **(d)** tip-streaming mode and **(e)** tip-multi-breaking mode. Scale-bar: 200 µm. **(f)** Overview of the five regimes with $\Lambda = 0.05 \pm 0.01$ for droplets with (circles) and without silica nanoparticles (squares).

5.2.3 Droplet size as a function of *Ca* and *Φ*

Similar to the droplet break-up regime, the size of the droplets is also a function of Ca, Φ and Λ. To control the droplet size over a wide range, four flow-focusing devices (chips) with different geometrical dimensions and orifices were used (see also **Table 5.1** in Materials and methods). Droplets produced with two of these chips (w_{or} = 105 µm and 72 µm, respectively) are shown in **Figure 5.3**.

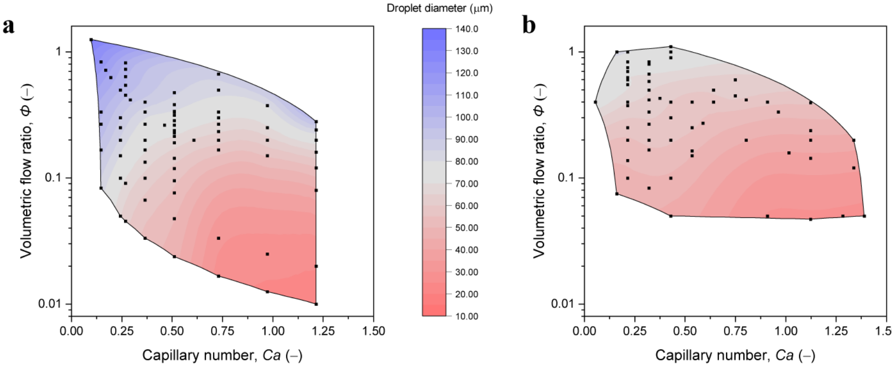

Figure 5.3: Droplet size as a function of *Ca* and *Φ* for different microchips. The viscosity ratio $\Lambda = 0.05 \pm 0.01$ in all cases. **(a)** w_{or} = 105 µm. **(b)** w_{or} = 72 µm.

Two trends are immediately clear. First, the larger the width of the orifice, the larger the range of droplets that can be produced. For w_{or} = 105 µm, the droplet size can be controlled from approximately 130 µm down to 20 µm. For w_{or} = 72 µm, the droplet size can be controlled from about 80 µm down to 30 µm. The range is limited by the width of the channels as well as the maximum flow rate that can be obtained within the chip. Second, the size of the droplets matches well with the different break-up regimes. As expected, the droplets are the largest in the squeezing regime and the smallest in the tip-streaming regime, regardless of the geometrical dimensions of the chip.

From Figure 5.3 it also becomes clear that predicting the droplet size is not straightforward. The main reason for this is that *Ca* and *Φ* are controlled indirectly by changing the ratio between Q_c and Q_d and these do not scale linearly. If Q_d is kept constant and Q_c is varied, the droplet size decreases exponentially with increasing *Ca* (**Figure 5.4a**). This is logical because the larger Q_c (and thus *Ca*), the thinner the dispersed phase jet that is produced. On the other hand, if Q_c (and thus *Ca*) is constant and Q_d is varied, both the packing density and size of the droplets can be controlled from a single stream of droplets at low Q_d to an almost complete hexagonal packing at high Q_d (**Figure 5.4b**).

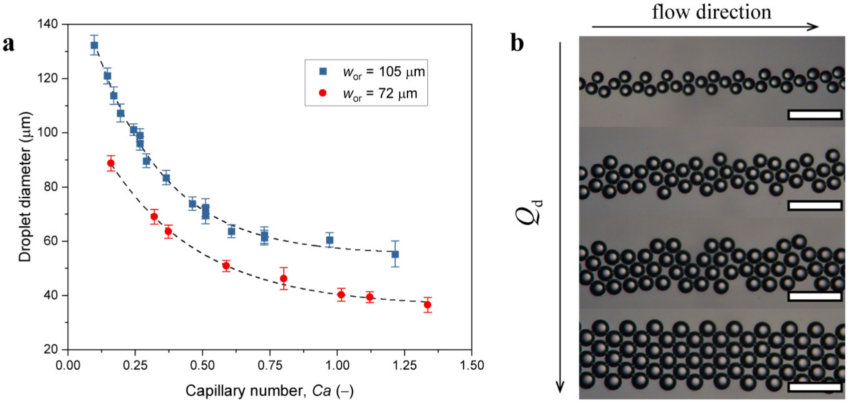

Figure 5.4: **(a)** Droplet size as a function of Ca at constant Q_d. In blue: $w_{or} = 105$ µm, $Q_d = 5$ µl·min^{-1}. In red: $w_{or} = 72$ µm, $Q_d = 3$ µl·min^{-1}. Q_c was varied from 3 to 25 µl·min^{-1}. The viscosity ratio was $\Lambda = 0.05 \pm 0.01$ in both cases. (**b**) Packing density as a function of Q_d for $w_{or} = 72$ µm, $Q_c = 6$ µl·min^{-1}. Q_d was varied from 0.5 to 5 µl·min^{-1}. The density increases from a single stream of droplets to hexagonal packing with increasing Q_d. Scale-bar: 200 µm.

5.3 Time-resolved MSM formation

In above sections the general principles of producing monodisperse emulsion droplets (with and without silica nanoparticles) are described. In the next sections the droplets with nanoparticles are turned into MSMs by controlled dewatering of the emulsion droplets (evaporation-driven assembly)[49,50] and the formation process is studied in detail.

When aqueous droplets containing insoluble solids such as, e.g., silica nanoparticles are dispersed in an immiscible liquid with a slight solubility for water and a temperature is applied, the droplets shrink due to diffusion of water into the immiscible phase[51,52]. This leads to an increase in solid concentration at the droplet surface and ultimately to the formation of a solid particle. In most industrially relevant processes used for the production of MSMs droplet shrinkage and nanoparticle gelation are intertwined, making it difficult to predict the effect of different parameters on the assembly behavior of silica nanoparticles in confined spaces[10–13]. For example, we have shown in Chapter 4 that MSMs produced via controlled drying can have local variations in porosity throughout the particles[53]. This could indicate that water evaporation does not occur homogeneous throughout the gelation process and that at some point during the process mass-transport is hindered, highlighting the need to study droplet drying kinetics in-real time throughout the MSM formation process.

To follow the MSM formation process in time, a conventional optical microscope was outfitted with a temperature-controlled heating and vacuum stage (**Figure 5.5a**). Samples were placed in the middle of two glass clover slides separated by a thin metal spacer ($d = 200$ µm, respectively 300 µm). Two configurations were used: “closed” and “open”, based on the type of spacer used (**Figure 5.5b**). In the “closed” system, the emulsion is not in contact with the environment inside the temperature stage and water cannot evaporate from the solvent.

This system is used to study the shrinkage behavior of pure liquid droplets as a function of temperature. In the "open" system, a vacuum can be applied, and water can freely evaporate from the solvent. This system is used to study the actual formation of MSMs.

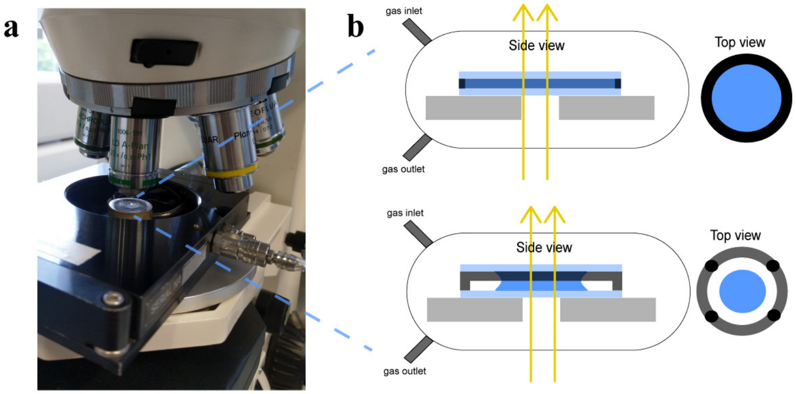

Figure 5.5: (a) Conventional optical microscope outfitted with a temperature-controlled heat and vacuum stage for the time-resolved imaging of MSM formation. **(b)** Schematic illustration of the set-up. Top: "closed" configuration. The emulsion is not in contact with the environment inside the temperature stage and no water can evaporate from the solvent. Bottom: "open" configuration. The emulsion is in contact with the environment inside the temperature stage and water can evaporate from the solvent. In the "open" configuration the temperature stage is sealed off with a lid.

5.3.1 Droplet shrinkage as a function of *T*

To investigate the fundamentals of droplet drying kinetics, pure water droplets without silica nanoparticles were dispersed in phenethyl alcohol (PEA) and imaged using the "closed" heating stage configuration. **Figure 5.6a** shows water droplets produced using a microfluidics platform with an average starting droplet radius of $a_0 = 23.5 \pm 1.6$ µm. The temperature profile was increased from $T_1 = 22.8$ °C to $T_2 = 40$ °C and $T_1 = 24$ °C to $T_2 = 50$ °C with a $\mathrm{d}T/\mathrm{d}t$ of 1 $°\mathrm{C \cdot min^{-1}}$, respectively. Images were taken every 20 seconds for a total of 25 and 33 minutes, respectively.

The center coordinates and radii of the shrinking droplets were measured using a Hough transform algorithm for the detection of circles in MATLAB[54]. The droplets move around slightly during heating of the system. Therefore, a script was developed to track the center coordinates of each droplet throughout the entire image stack. This was done by comparing the *x*,*y* position of the center of each droplet in each image to the position and radii of the droplets in the previous image. Based on the assumption that the droplets do not move around too much, the droplet are tracked if the *x*,*y* shift between images is smaller than the radius of the droplet (see Appendix section 5.1 and **Figure A5.1** for details).

Thereafter, 2D Voronoi diagrams were constructed for each image to evaluate local variations in the droplet number density. A Voronoi tessellation spatially partitions the image into convex cells, each containing a single droplet and the associated surroundings closer to that droplet than to any other droplet[55,56]. In order to avoid border effects[57], only those Voronoi cells that are fully located in the field of view are considered (**Figure 5.6b**). Since temporal spatial data in the z-direction is lacking, the area of each Voronoi cell was multiplied with a constant height equal to the thickness of the liquid layer given by the spacer height. To determine the amount of water the solvent can take up around each emulsion droplet, a volume fraction distribution was then constructed for each sample at $t = t_0$ (**Figure 5.6c**). The distribution is not symmetrical but skewed to the right. The median (50th percentile) volume fraction is slightly smaller for sample 1 ($T_2 = 40$ °C, $V_{W,0} / V_{tot} = 0.043$) than for sample 2 ($T_2 = 50$ °C, $V_{W,0} / V_{tot} = 0.048$). This difference is only related to the number of droplets in the field of view and not to the heating temperature. Furthermore, the width of the distribution, i.e., the spread in the local droplet number density (16th, respectively 64th percentile), also varies slightly between samples.

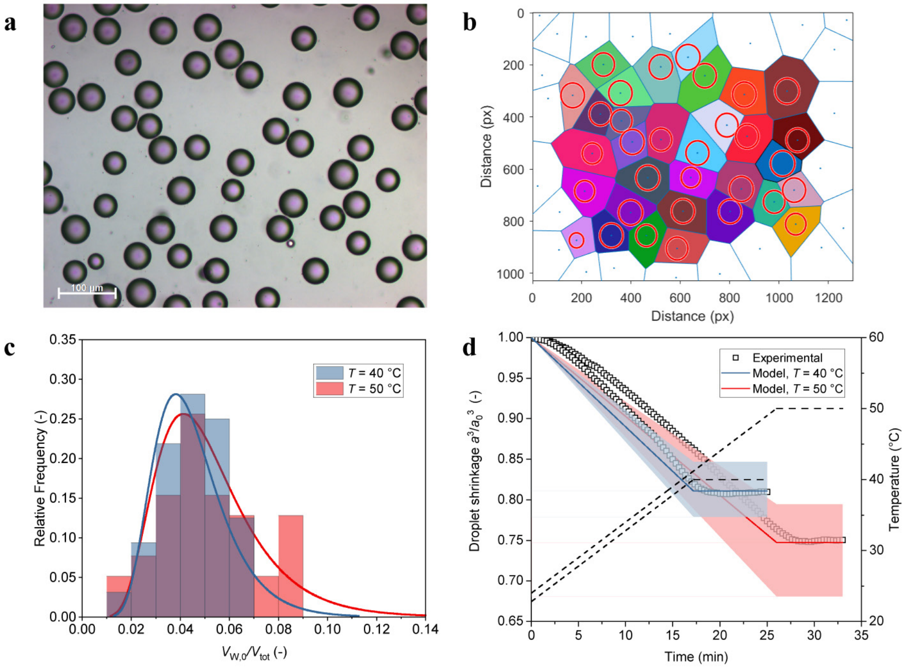

Figure 5.6: (a) Water droplets produced via the microfluidics set-up, with $a_0 = 23.5 \pm 1.6$ μm. **(b)** Voronoi diagram, indicating the diameters of the droplets in red. **(c)** Corresponding volume fraction distribution. **(d)** Droplet shrinkage as a function of temperature. $V_{W,0} / V_{tot} = 0.043$ with $0.857 < \chi < 1.233$ (sample 1) and $V_{W,0} / V_{tot} = 0.048$ with $0.794 < \chi < 1.227$ (sample 2). The temperature profile was increased from $T_1 = 22.8$ °C to $T_2 = 40$ °C (sample 1) and $T_1 = 24$ °C to 50 °C (sample 2) with a dT/dt of 1 °C·min^{-1}.

Figure 5.6d shows the droplet shrinkage as a function of temperature. The experimentally observed shrinkage shown here is the average droplet shrinkage over approximately 40 droplets. Two observations become immediately clear from the plotted data: 1) the droplets do not disappear completely, and 2) the average droplet shrinkage is higher for higher temperatures. The reason for 1) is that the system is closed and no water can evaporate from the solvent. The observed shrinkage is therefore only caused by an increase in water uptake of the solvent, which increases with increasing temperature[58]. After a certain time, in this case $t = 17.33$ min for $T = 40$ °C and $t = 26$ min for $T = 50$ °C, the final temperature is reached, and shrinkage stops because the solvent is saturated. Under different conditions, e.g., a dT/dt of 5 $°C{\cdot}min^{-1}$, this time will change accordingly. The total average shrinkage as well as the spread, however, remains the same regardless of the temperature ramp. Since the droplet number density is not identical in both samples, the full effect of temperature cannot be determined by only comparing the experimental data.

Therefore, a theoretical-mass transfer model was derived to describe droplet shrinkage that takes into account the physical properties of the system, i.e., local variations in the droplet number density (described by a so-called local evaporation coefficient χ and visualized in Figure 5.6d as the shaded areas around the solid lines), heating temperature and composition of the solvent phase. The model will be briefly introduced below. For detailed information with respect to the model derivation we refer to Appendix sections 5.2.1 – 5.2.4 and **Figures A5.2 – A5.4**.

5.3.2 Modelling droplet shrinkage

For simplicity, we only consider spherically symmetric droplets. At the droplet boundary a mass-conservation equation can be written, relating the change of volume of a droplet to the mass flux leaving the droplet[51,52].

$$\frac{\partial}{\partial t}(\rho_W V_d) = 4\pi a^2 \mathscr{D}_{W\to O} M_W \left.\frac{\partial C}{\partial r}\right|_{r=a} \tag{5.2}$$

where ρ_W is the density of the dispersed phase (water, subscript W), V_d is the droplet volume, a is the droplet radius, $\mathscr{D}_{W\to O}$ is the mass diffusion coefficient of the dispersed phase W in the continuous phase (oil, subscript O), which can be estimated using the Tyn and Calus method[59,60] (see Appendix 5.2.2 for details), M_W is the molar mass of the dispersed phase, C is the external concentration of water in the continuous phase and r is the distance from the droplet center.

The continuity equation for water in the continuous phase due to Fickian diffusion is given by:

$$\frac{\partial C}{\partial t} = \mathscr{D}_{W\to O} \frac{1}{r^2}\frac{\partial}{\partial r}\left(r^2 \frac{\partial C}{\partial r}\right) \tag{5.3}$$

Equations (5.2) and (5.3) must be solved simultaneously for boundary conditions at the interface $\left.C\right|_{r=a} = C_i$ and far away from the droplet $\left.C\right|_{r=\infty} = C_\infty$. Because the droplet radius changes as a function of time, this is known as a moving boundary problem, which are not easily solved[61]. A typical approach is to first solve equation (5.3) independently to steady-state. The outcome can then be inserted in equation (5.2), resulting in a nonlinear differential equation for *∂a/∂t*, which has to be solved numerically (see Appendix section 5.2.1 for details).

Assuming that the temperature is homogeneous throughout the system, i.e., the droplets plus the continuous phase, the water concentration at the droplet interface is governed by the temperature-corrected equilibrium solubility[52]:

$$C_\mathrm{i} = C_0 \exp\left[-\frac{\Delta_\mathrm{mix} H}{R}\left(\frac{1}{T} - \frac{1}{T_0}\right)\right] \tag{5.4}$$

where C_0 is the water solubility in the continuous phase at a reference temperature T_0, T_1 is the starting temperature, $\Delta_\mathrm{mix}H$ the enthalpy of mixing and R the universal gas constant.

In case the number of droplets is very small, the concentration of water far away from the droplets C_∞ does not change significantly with increasing temperature and can be assumed equal to the water solubility of the solvent at the reference temperature C_0[52]. However, in our application case there are many droplets that all shrink simultaneously during heating of the solvent. This means that the overall concentration of water in the solvent changes as a result of the shrinkage of the droplets and can no longer be assumed equal to C_0 but instead increases as the water solubility of the solvent increases with temperature. The total water concentration in the solvent can be written as a function of the starting concentration C_1 and the concentration as a result of the solved droplets (see Appendix section 5.2.1 for details):

$$C_\infty = C_1 + \frac{\chi \rho_\mathrm{W}}{M_\mathrm{W}}\left(1 + \frac{V_\mathrm{W,0} - V_\mathrm{tot}}{V_\mathrm{tot} - V_\mathrm{W,0}\left(\frac{a^3}{a_0^3}\right)}\right) \tag{5.5}$$

where C_1 is the concentration water at the starting temperature T_1, χ is a theoretically derived evaporation coefficient, $V_\mathrm{W,0}$ is the volume of the dispersed phase at $t = t_0$ and V_tot is the total volume of the system. The rest of the symbols have their usual meaning. The evaporation coefficient χ used here describes local variations in the droplet number density. Theoretically χ can vary between $0.323 < \chi < 1.474$ (see Appendix section 5.2.3 for details).

Equation (5.5) can be inserted in the steady-state solution of equation (5.3), resulting in a new nonlinear differential equation for *∂a/∂t*, which again has to be solved numerically. However, since in a typical experiment there are many droplets in close proximity of each other, the inter droplet distance is typically smaller than the diffusion length (see also Appendix section 5.2.4). Therefore, we can assume that at every point in time the concentration of water is the same everywhere in the solvent and replace equation (5.3) with:

$$C = C_\mathrm{i} = C_\infty \tag{5.6}$$

In this case an analytical solution can be derived for the droplet shrinkage as a function of the concentration water in the solvent (see Appendix section 5.2.1 for details):

$$a = a_0 \left[\frac{V_{\mathrm{tot}}}{V_{\mathrm{W},0}} + \left(\frac{V_{\mathrm{tot}}}{V_{\mathrm{W},0}} - 1 \right) \left(\frac{M_{\mathrm{W}}}{\chi \rho_{\mathrm{W}}} (C_{\mathrm{i}} - C_1) - 1 \right)^{-1} \right]^{1/3} \tag{5.7}$$

The water concentration at the droplet interface C_{i} has been defined above. Similarly, the starting concentration C_1 can be expressed as:

$$C_1 = C_0 \exp\left[-\frac{\Delta_{\mathrm{mix}} H}{R} \left(\frac{1}{T_1} - \frac{1}{T_0} \right) \right] \tag{5.8}$$

Inserting equation (5.4) and (5.8) into equation (5.7) results in an expression for the droplet shrinkage as a function of the water solubility and the temperature of the system:

$$a = a_0 \left[\frac{V_{\mathrm{tot}}}{V_{\mathrm{W},0}} + \left(\frac{V_{\mathrm{tot}}}{V_{\mathrm{W},0}} - 1 \right) \left[\frac{M_{\mathrm{W}}}{\chi \rho_{\mathrm{W}}} C_0 \left(\exp\left[-\frac{\Delta_{\mathrm{mix}} H}{R} \left(\frac{1}{T} - \frac{1}{T_0} \right) \right] - \exp\left[-\frac{\Delta_{\mathrm{mix}} H}{R} \left(\frac{1}{T_1} - \frac{1}{T_0} \right) \right] \right) - 1 \right]^{-1} \right]^{1/3} \tag{5.9}$$

For $V_{\mathrm{W},0} / V_{\mathrm{tot}} > 3$ vol%, the analytical solution matches closely to the numerical solution (**Figure A5.2**).

For simplicity the droplet temperature is assumed to be equal to temperature of the surrounding medium, which is controlled via the heating stage:

$$T(t) = \begin{cases} T_1 + (\dot{T}t)t, & t < (T_2 - T_1) / \dot{T}t \\ T_2, & t \geq (T_2 - T_1) / \dot{T}t \end{cases} \tag{5.10}$$

where T_1 is the starting temperature, T_2 the end temperature and $\dot{T} = \mathrm{d}T/\mathrm{d}t$ is the temperature ramp.

To determine whether C_{i} is indeed equal to C_∞, a Delaunay triangulation was performed to calculate the mean center distance between the droplets (**Figure A5.4a**)[56]. Since the diffusion length (121 µm) is larger than the inter droplet spacing (101 µm and 91 µm for sample 1 and 2, respectively), the concentration of dissolved water should be constant throughout the continuous phase. To confirm, C_∞ was plotted against C_{i} for both samples (**Figure A5.4b)**. A small deviation between the two concentrations can be seen during heating of the sample, but the final concentrations match well. The deviation is due to the mismatch in the actual droplet temperature compared to the measured temperature of the heating couple. There is a small time offset between the actual temperature of the medium compared to the temperature recorded by the thermal couple of the heating stage. Furthermore, the heat flux at the interface of the droplets and the surrounding solvent phase changes during heat-up of the sample due to shrinkage of the droplets. The heat flux can be calculated by writing an enthalpy conservation equation at the droplet interface similar to the mass-conservation equation described above[52], however, this is beyond the scope of this work.

5.3.3 Tuning droplet shrinkage

With an analytical equation for droplet shrinkage at hand, the effect of droplet number density on the droplet drying kinetics can now be investigated. To illustrate, the droplet shrinkage was plotted for water droplets in PEA with a radius of a_0 = 23.5 µm and a variable amount of water $V_{W,0} / V_{tot} = 0$ to 0.10 with $\chi = 1$ from T_1 = 22.8 °C to T_2 = 40 °C with a dT/dt of 1 °C·min^{-1}. (**Figure 5.7a**). At concentrations close to 0 vol% there is only one droplet that, under these conditions, takes approximately 12 minutes to be completely taken up in the surrounding solvent. When the initial water concentration exceeds 0.7 vol%, the droplets no longer disappear completely because at this concentration the amount of water in the droplets exceeds the maximum water uptake of the solvent[58]. The higher the initial water volume/weight fraction, the lower is the total droplet shrinkage. This is logical because the shrinkage is averaged over more droplets. It should be noted, however, that at low volume concentrations ($V_{W,0} / V_{tot}$ < 3 vol%) the analytical solution of the model cannot be used because the diffusion length is no longer larger than the inter droplet distance and therefore the concentration of water is no longer equal everywhere in the solvent.

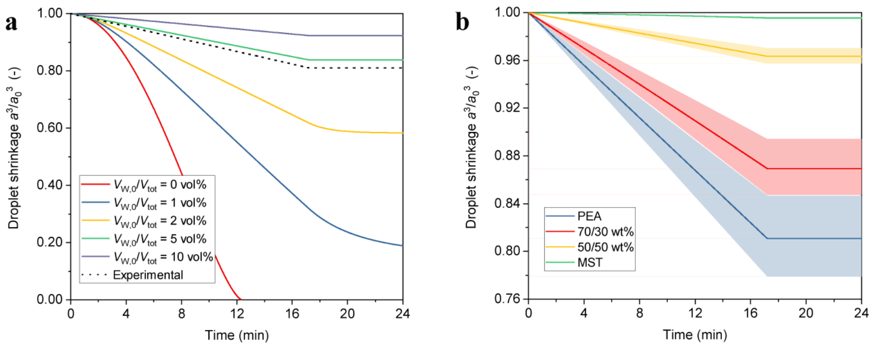

Figure 5.7: (a) Droplet shrinkage as a function of different initial water concentrations $V_{W,0} / V_{tot} = 0$ to 0.10 with $\chi = 1$. **(b)** Droplet shrinkage as a function of different solvents for $V_{W,0} / V_{tot} = 0.043$ with $0.857 < \chi < 1.233$. The temperature profile was increased in both cases from T_1 = 22.8 °C to T_2 = 40 °C with a dT/dt of 1 °C·min^{-1} and with an initial droplet radius of a_0 = 23.5 µm.

Droplet shrinkage can also be tuned by dispersing water droplets in different solvents, i.e., pure PEA, pure mesitylene (MST), 70/30 wt% PEA/MST and 50/50 wt% PEA/MST (**Figure 5.7b**). For each solvent, a fixed initial water concentration of $V_{W,0} / V_{tot} = 0.043$ was used and χ was varied between $0.857 < \chi < 1.233$. The values chosen for the physical properties are listed in **Table 5.2** (see Materials and methods). The droplet shrinkage is clearly the largest for water droplets dispersed in PEA, whereas there is almost no shrinkage for droplets dispersed in MST. MST is a non-polar solvent that has almost no affinity to water. Therefore, the water concentration in MST hardly increases with increasing temperature[62]. Mixtures of PEA/MST also show a reduced droplet shrinkage versus PEA. The droplet shrinkage is significantly reduced for mixtures with up to 50% MST, which is in agreement with prior experimental observations on the assembly of MSMs (see also Chapter 3)[22].

These results show that the shrinkage behavior of emulsion droplets at elevated temperatures can be accurately predicted with above model for the “closed” configuration.

5.3.4 MSM formation

Until now the general principles of droplet shrinkage without silica nanoparticles using the “closed” set-up are described. In the next sections droplet shrinkage with silica nanoparticles and their subsequent transition into MSMs using the “open” configuration is investigated. In the open system the shrinkage rate is no longer limited by the rate of saturation of the solvent. Instead, water can freely evaporate from the solvent and the shrinkage rate is controlled by applying a reduced pressure, as is typically done in industry[22].

Figure 5.8a shows the time-resolved transition of a water droplet with an initial radius of a_0 = 20.8 µm containing 5 wt% silica nanoparticles of 8 nm in diameter, dispersed in PEA, into a MSM. The temperature was varied from T_1 = 23 °C to T_2 = 80 °C with a dT/dt of 1 °C·min^{-1} and the pressure was reduced and kept constant at an absolute pressure of P = 200 mbar throughout the experiment. Images were taken every 30 seconds for a total of 70 minutes. The MSM formation process can be split into three stages: a standard droplet shrinkage stage (stage I), a fast shrinkage / transition stage (stage II) and a post-shrinkage stage (stage III) (**Figure 5.8b**).

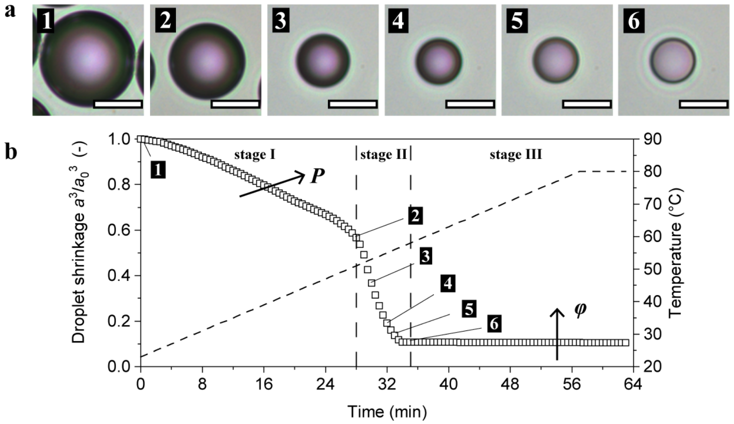

Figure 5.8: (a) Optical microscopy images of the transformation of a droplet filled with nanoparticles into a MSM. The six images represent the three stages of MSM formation described in the main text. Scale bar: 20 µm. **(b)** Graph showing droplet shrinkage versus time. The profile shows a gradual shrinkage stage (I) a rapid shrinkage / transition stage (II) and a post-shrinkage stages (III). The temperature profile was increased from T_1 = 23 °C to T_2 = 80 °C with a dT/dt of 1 °C·min^{-1} with a reduced pressure of P = 200 mbar and an initial droplet radius of a_0 = 20.4 µm.

In the first stage the droplets gradually shrink due to heating of the medium (image 1 and 2 in Figure 5.8a). The shrinkage rate is comparable to the shrinkage rate of pure water droplets described above. We hypothesize that during this stage particles are build up at the receding interface and form a loose gel network[31]. At the beginning of stage II the droplet radius decreases rapidly before any further shrinkage is completely hindered (image 3 and 4 in Figure 5.8a). This accelerated shrinkage has not been observed previously in case of pure water droplets and could indicate that the mechanically weak gel network is suddenly compressed, possibly due to a phase transition of the water inside the particle from liquid to gas. In addition to the rapid decrease in droplet diameter, the surface of the droplets transforms from "shiny" to "dull" (image 5 and 6 in Figure 5.8a). During stage III the particle no longer shrinks, indicating that a mechanical stable network has formed.

The shrinkage rate can be controlled by applying different reduced pressures. Experimentally, it was observed that the droplet shrinkage rate is higher under reduced pressure than under atmospheric pressure (**Figure A5.5**). This can be seen as a shift to the right of the curve in stage I and II. Furthermore, the total amount of shrinkage can be tuned by changing the silica volume fraction inside the droplets. Droplets with a higher initial volume fraction shrink less than droplets with a lower initial volume fraction. This can be seen as a change in the height of the plateau in stage III.

To investigate the transformation from liquid droplets into solid MSMs in more detail and, in particular the transition stage II, radially averaged intensity profiles were measured over time. The radial intensity profiles were made by laying a series of concentric rings (radial bins) on top of a droplet. The mean intensity value of each bin is then collected in an array, which is displayed in a line plot wherein the radius is plotted versus the intensity for each time step (see Appendix section 5.3.2 and **Figure A5.6** for details). The intensity profile summarizes the observed contrast changes that show both shrinkage of the emulsion droplet and the transformation into an MSM (**Figure 5.9a**). The three stages described earlier can easily be identified. A dip can be seen in the intensity of the particle core in stage II. This possibly indicates that the core is somewhat denser packed (lower porosity) than the surface of the particle due to rapid compression of the gel network, potentially explaining the local variations in porosity that were observed previously in the evaporation-driven assembly of MSMs[53]. Although this is difficult to judge based solely on 2D images as the core is also thicker than the rest of the particle. Radially averaged intensity profiles were also measured under identical conditions but at $P = 400$ mbar (**Figure A5.7**). At higher absolute pressure the duration of stage I is noticeably longer, indicating a slower overall evaporation rate compared to the $P = 200$ mbar case.

In addition to the radial intensity profiles an optical model was constructed, relating changes in the refraction and reflection of the light rays penetrating the sample to the composition of the particle interior (see Appendix section 5.3.3 and **Figures A5.8-A5.9** for details). Because there is a mismatch between the refractive index of the droplet / particle and the surrounding medium, some light rays that hit the edge of the droplet / particle are not collected by the objective lens of the microscope. The region were no light is collected is seen as a black outer rim[63]. The evolution of the outer rim thickness over time gives an indication of the changes happening in the droplet / particle interior

The evolution of the rim thickness is plotted over time in **Figure 5.9b**. At the start of MSM formation the mismatch in refractive index between the droplet and medium is the highest, hence, the thickness of the black outer rim is the largest (see also image 1 in Figure 5.8a). During stage I the rim thickness gradually decreases. This can be understood as the volume fraction of silica in the droplet gradually increases, reducing the mismatch in refractive index between the droplet and the medium[64,65]. In stage II the outer rim thickness rapidly decreases, which could be attributed to a sudden increase in the silica volume fraction due to the collapse of the gel network (see also image 3 in Figure 5.8a). At approximately $t = 32$ minutes the rim thickness remains constant for a few minutes (see also image 4 in Figure 5.8a). We speculate that at this point in time the water-filled interior of the particle is gradually exchanged for PEA. The refractive index value thereby approaches the refractive index value of the medium, which means that more light can be transmitted, ultimately resulting in a very thin outer rim (image 5 and 6 in Figure 5.8a).

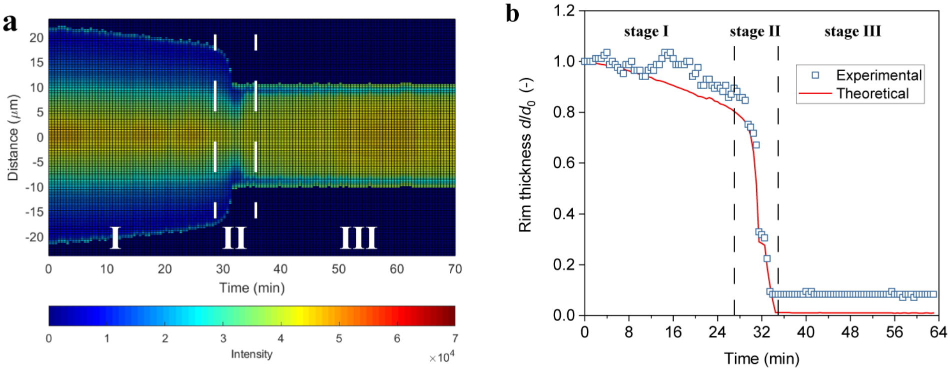

Figure 5.9: (a) Graph showing the radially averaged intensity profile versus time of the formation of a MSM. The profile shows the two shrinkage (I + II) and post-shrinkage (III) stages. The temperature profile was increased from $T_1 = 23$ °C to $T_2 = 80$ °C with a dT/dt of 1 °C·min^{-1} with a reduced pressure of $P = 200$ mbar and an initial droplet radius of $a_0 = 20.4$ μm. **(b)** Thickness of the dark outer rim determined experimentally as well as theoretically based on the way light rays are refracted and reflected by the particle.

These results provide some insight in the time-resolved formation of MSMs. The radial intensity profile maps and evolution of the rim thickness indicate when the MSMs are fully formed and what the effect is of various reaction conditions on the shrinkage and gelation rates. These results can be used to optimize the experimental procedure for MSM formation. Furthermore, a recent paper by Amstad et al.[66] demonstrated a microfluidic device capable of producing hundreds of liters of monodisperse droplets per hour. By integrating such device with the principles of controlled shrinkage shown here, it becomes possible to produce monodisperse MSMs on industrial relevant volumes.

5.4 Conclusions

In summary, we present a microfluidic processing route towards the synthesis of monodisperse MSMs with tunable porosity characteristics. The effect of various parameters on the kinetics of colloidal assembly in confined spaces were studied using in situ optical microscopy. In contrast with previous time-resolved studies on MSM formation, specific spatially resolved information was obtained between the emulsion droplets and the surrounding solvent. In addition, a theoretical mass-transfer model was introduced to describe droplet shrinkage based on the droplet number density and solvent characteristics. The model was compared to experimental imaging results which were quantified by image analysis with respect to droplet shrinkage and showed an excellent match. Furthermore, radial intensity profile maps were obtained to quantify the transformation of emulsion droplets into MSMs and to show the effect of different reaction conditions on the shrinkage and gelation rate. The results shown here are the first step towards full control and prediction over the size and porosity characteristics of MSMs, based on the initial emulsion droplet size and reaction conditions.

5.5 Materials and methods

Materials

Phenethyl alcohol (PEA, 99%) and mesitylene (MST, 97%) as the continuous phase and hydroxypropyl cellulose (HPC, average M 100.000 g·mol^{-1}) as a stabilizer and emulsifier were purchased from Acros Organics. The dispersed phase was a colloidal silica sol provided by Nouryon Pulp and Performance Chemicals AB, Sweden. It consists of colloidal silica nanoparticles of 8.2 ± 2.5 nm in water with a solid concentration of 14 wt%. The particle size was determined by cryoTEM (see Chapter 2 for details on the characterization procedure). All chemicals were filtered through a 0.22 μm filter prior to use.

Solvent characteristics

Interfacial tension was measured at 20 °C for the different solvent mixtures using the Wilhelmy-plate method on a Krüss K11 MK4 tensiometer. The platinum plate (19.9 × 10 × 0.2 mm) was cleaned and flame-dried before each measurement.

Viscosity measurements were performed at 20 °C on an Anton Paar Physica MCR 301 Rheometer with the concentric cylinder CC27 system (inner and outer diameter are 26.66 mm and 28.92 mm, respectively). Measurements were performed using different shear rates between 0.1 and 100 s^{-1}.

Transmission measurements were performed over a temperature range of 20 °C to 75 °C for different solvent mixtures in a fused silica cuvette on an Anton Paar Litesizer 500 with a 40 mW solid-state laser of 658 nm.

Microfluidic set-up

The microfluidic set-up used in this work was purchased from Micronit Microtechnologies (Enschede, Netherlands) and Fluigent (Jena, Germany). The microchips are made of borosilicate glass and are coated with a fluorinated polymer hydrophobic coating to form W/O emulsion droplets. Four chips with different geometrical dimensions were used, see **Table 5.1**. The continuous and dispersed phase were supplied to the microchips via flexible plastic tubing, which was regulated by two microfluidic pressure control modules (Fluigent Flow EZ, 7 bar). The modules were used to pressurize two plastic Falcon tubes containing the liquids such that the fluids began to flow into the microchip. Flow sensors were added to accurately control the flow rate in the system up to 1000 $\mu l \cdot min^{-1}$.

Optical microscopy images (1360 × 2048 pixels) of droplet formation were recorded with a Nikon D90 attached to a Zeiss Axiolab optical microscope. The shutter speed was set at 1/4000 and the f-number was fixed at 5.6.

The entire set-up was placed in a laminar flow cabinet (CaptAir Filterair 936) to prevent contamination.

Table 5.1: Dimensions of the four microchips used in this work.

	Chip A	**Chip B**	**Chip C**	**Chip D**
Dimensions (mm)	45 × 15	15 × 15	45 × 15	15 × 15
$w_c = w_d = \Delta Z$ (μm)	130	91	23	14
w_{outlet} (μm)	425	433	367	358
$h_c = h_d = h_{outlet}$ (μm)	125	83	17	8
w_{or} (μm)	105	72	14	7.2
h_{or} (μm)	75	50	10	5

Droplet kinetics

In situ optical microscopy of droplet shrinkage and gelation was performed with a Zeiss Axioplan 2 optical microscope outfitted with a Zeiss Axiocam and a Linkam THMS600 temperature stage. The temperature was controlled via a Linkam TMS94 controller.

Most image processing steps were done in MATLAB R2019a using in-house developed code. Additional information can be found in Appendix section 5.1.

Theoretical mass-transfer model

The differential equations were solved numerically using Mathematica 12.1 (Wolfram). Values for the physical parameters used in the model are listed in **Table 5.2**.

Table 5.2: Physical parameters used in the theoretical model.

	PEA	MST	70/30 wt% PEA/MST	50/50 wt% PEA/MST	unit
$\mathscr{D}_{W\to O}$	1.22×10^{-6}	2.21×10^{-5}	4.10×10^{-6}	7.66×10^{-6}	$cm^2\cdot s^{-1}$
M_w	122	120	121	121	$g\cdot mol^{-1}$
C_0	4.57	0.016	1.99	1.14	$mol\cdot L^{-1}$
$\Delta_{mix}H$	4300	22000	6600	3400	$J\cdot mol^{-1}$

5.6 References

1. McClements, D. J. *Food Emulsions: Principles, Practice, and Techniques*. (CRC Press, 2016). doi: 10.1201/9781420039436.
2. Brummer, R. *Rheology Essentials of Cosmetic and Food Emulsions*. (Springer-Verlag, 2006). doi:10.1007/3-540-29087-7.
3. Schramm, L. L. *Emulsions, Foams, and Suspensions: Fundamentals and Applications*. (Wiley, 2005). doi:10.1002/3527606750.
4. Chern, C.-S. *Principles and Applications of Emulsion Polymerization*. (John Wiley & Sons, Inc., 2008). doi:10.1002/9780470377949.
5. Bollhorst, T., Rezwan, K. & Maas, M. Colloidal Capsules: Nano- and Microcapsules with Colloidal Particle Shells. *Chem. Soc. Rev.* **46**, 2091–2126 (2017).
6. Gustafsson, H. & Holmberg, K. Emulsion-Based Synthesis of Porous Silica. *Adv. Colloid Interface Sci.* **247**, 426–434 (2017).
7. Snyder, L. R., Kirkland, J. J. & Dolan, J. W. *Introduction to Modern Liquid Chromatography. High-Performance Gradient Elution: The Practical Application of the Linear-Solvent-Strength Model* (John Wiley & Sons, Inc., 2009). doi:10.1002/9780470508183.
8. Gritti, F. & Guiochon, G. New Insights on Mass Transfer Kinetics in Chromatography. *AIChE J.* **57**, 333–345 (2011).
9. Gritti, F., Horvath, K. & Guiochon, G. How Changing the Particle Structure can speed up Protein Mass Transfer Kinetics in Liquid Chromatography. *J. Chromatogr. A* **1263**, 84–98 (2012).
10. Nyström, M., Herrmann, W., Larsson, B. (EKA Nobel AB) US 5256386 (1993).
11. Balducci, L., Ungarelli, R. (Enichem S.p.A.; Eniricerche S.p.A.) US 6103209 (2000).
12. Zhiping, J., Fisk, R. P., O’ Gara, J., Walter, T. H., Wyndham, K.D. (Waters Technologies Corporation) US 8778453 (2004).
13. Fijneman, A.J., Högblom, J., Sommerdijk, N.A.J.M., Friedrich, H. (Nouryon Chemicals International B.V.) filed EP 19177278.9 (2019).
14. Dickinson, E. Emulsions and Droplet Size Control. in *Controlled Particle, Droplet and Bubble Formation* 191–216 (Elsevier, 1994). doi:10.1016/B978-0-7506-1494-8.50012-2.

15. Schmitt, V., Leal-Calderon, F. & Bibette, J. Preparation of Monodisperse Particles and Emulsions by Controlled Shear. in *Topics in Current Chemistry: Colloid Chemistry II* 195–215 (2003).
16. Joscelyne, S. M. & Trägårdh, G. Membrane Emulsification - A Literature Review. *J. Memb. Sci.* **169**, 107–117 (2000).
17. Teh, S.-Y., Lin, R., Hung, L.-H. & Lee, A. P. Droplet Microfluidics. *Lab Chip* **8**, 198 (2008).
18. Zhu, P. & Wang, L. Passive and Active Droplet Generation with Microfluidics: a Review. *Lab Chip* **17**, 34–75 (2017).
19. Shang, L., Cheng, Y. & Zhao, Y. Emerging Droplet Microfluidics. *Chem. Rev.* **117**, 7964–8040 (2017).
20. Casadevall I Solvas, X. & Demello, A. Droplet Microfluidics: Recent Developments and Future Applications. *Chem. Commun.* **47**, 1936–1942 (2011).
21. Holtze, C. Large-Scale Droplet Production in Microfluidic Devices–an Industrial Perspective. *J. Phys. D. Appl. Phys.* **46**, 114008 (2013).
22. Fijneman, A. J. *et al.* Multiscale Colloidal Assembly of Silica Nanoparticles into Microspheres with Tunable Mesopores. *Adv. Funct. Mater.* **30**, 2002725 (2020).
23. Boissiere, C. *et al.* First In-Situ SAXS Studies of the Mesostructuration of Spherical Silica and Titania Particles during Spray-Drying Process. *Chem. Commun.* **3**, 2798–2799 (2003).
24. Sen, D. *et al.* Probing Evaporation Induced Assembly across a Drying Colloidal Droplet using In Situ Small-Angle X-Ray Scattering at the Synchrotron Source. *Soft Matter* **10**, 1621–7 (2014).
25. Bahadur, J. *et al.* Colloidal Nanoparticle Interaction Transition during Solvent Evaporation Investigated by In-Situ Small-Angle X-Ray Scattering. *Langmuir* **31**, 4612–4618 (2015).
26. Mezhericher, M., Levy, A. & Borde, I. Theoretical Drying Model of Single Droplets Containing Insoluble or Dissolved Solids. *Dry. Technol.* **25**, 1025–1032 (2007).
27. Sadek, C. *et al.* Drying of a Single Droplet to Investigate Process–Structure–Function Relationships: a review. *Dairy Sci. Technol.* **95**, 771–794 (2015).
28. Farid, M. A New Approach to Modelling of Single Droplet Drying. *Chem. Eng. Sci.* **58**, 2985–2993 (2003).
29. Liang, H., Shinohara, K., Minoshima, H. & Matsushima, K. Analysis of Constant Rate Period of Spray Drying of Slurry. *Chem. Eng. Sci.* **56**, 2205–2213 (2001).
30. Mezhericher, M., Levy, A. & Borde, I. Theoretical Models of Single Droplet Drying Kinetics: A Review. *Dry. Technol.* **28**, 278–293 (2010).
31. Handscomb, C. S., Kraft, M. & Bayly, A. E. A New Model for the Drying of Droplets Containing Suspended Solids. *Chem. Eng. Sci.* **64**, 628–637 (2009).
32. Christopher, G. F. & Anna, S. L. Microfluidic Methods for Generating Continuous Droplet Streams. *J. Phys. D. Appl. Phys.* **40**, R319–R336 (2007).
33. Anna, S. L., Bontoux, N. & Stone, H. A. Formation of Dispersions using ‘Flow Focusing’ in Microchannels. *Appl. Phys. Lett.* **82**, 364–366 (2003).
34. Nie, Z. *et al.* Emulsification in a Microfluidic Flow-Focusing Device: Effect of the Viscosities of the Liquids. *Microfluid. Nanofluidics* **5**, 585–594 (2008).
35. Kim, J. & Lee, C.-S. Microfluidic Approaches for Designing Multifunctional Polymeric Microparticles from Simple Emulsions to Complex Particles. in *Microfluidics: Fundamental, Devices and Applications* 375–404 (Wiley-VCH Verlag GmbH & Co. KGaA, 2018). doi:10.1002/9783527800643.ch12.

36. Anna, S. L. & Mayer, H. C. Microscale Tipstreaming in a Microfluidic Flow Focusing Device. *Phys. Fluids* **18**, 121512 (2006).

37. Dreyfus, R., Tabeling, P. & Willaime, H. Ordered and Disordered Patterns in Two-Phase Flows in Microchannels. *Phys. Rev. Lett.* **90**, 4 (2003).

38. Xu, J. H., Luo, G. S., Li, S. W. & Chen, G. G. Shear Force Induced Monodisperse Droplet Formation in a Microfluidic Device by Controlling Wetting Properties. *Lab Chip* **6**, 131–136 (2006).

39. Utada, A. S. *et al.* Dripping, Jetting, Drops, and Wetting: The Magic of Microfluidics. *MRS Bull.* **32**, 702–708 (2007).

40. Garstecki, P. *et al.* Formation of Monodisperse Bubbles in a Microfluidic Flow-Focusing Device. *Appl. Phys. Lett.* **85**, 2649–2651 (2004).

41. Gupta, A., Matharoo, H. S., Makkar, D. & Kumar, R. Droplet Formation via Squeezing Mechanism in a Microfluidic Flow-Focusing Device. *Comput. Fluids* **100**, 218–226 (2014).

42. Umbanhowar, P. B., Prasad, V. & Weitz, D. A. Monodisperse Emulsion Generation via Drop Break Off in a Coflowing Stream. *Langmuir* **16**, 347–351 (2000).

43. Fu, T., Wu, Y., Ma, Y. & Li, H. Z. Droplet Formation and Breakup Dynamics in Microfluidic Flow-Focusing Devices: From Dripping to Jetting. *Chem. Eng. Sci.* **84**, 207–217 (2012).

44. Powers, T. R., Zhang, D., Goldstein, R. E. & Stone, H. A. Propagation of a Topological Transition: The Rayleigh instability. *Phys. Fluids* **10**, 1052–1057 (1998).

45. Utada, A. S., Fernandez-Nieves, A., Stone, H. A. & Weitz, D. A. Dripping to Jetting Transitions in Coflowing Liquid Streams. *Phys. Rev. Lett.* **99**, 094502 (2007).

46. Suryo, R. & Basaran, O. A. Tip Streaming from a Liquid Drop Forming from a Tube in a Co-Flowing Outer Fluid. *Phys. Fluids* **18**, 082102 (2006).

47. Zhu, P., Kong, T., Kang, Z., Tian, X. & Wang, L. Tip-Multi-Breaking in Capillary Microfluidic Devices. *Sci. Rep.* **5**, 11102 (2015).

48. Gordillo, J. M., Sevilla, A. & Campo-Cortés, F. Global Stability of Stretched Jets: Conditions for the Generation of Monodisperse Micro-Emulsions using Coflows. *J. Fluid Mech.* **738**, 335–357 (2014).

49. Lee, S. Y., Gradon, L., Janeczko, S., Iskandar, F. & Okuyama, K. Formation of Highly Ordered Nanostructures by Drying Micrometer Colloidal Droplets. *ACS Nano* **4**, 4717–4724 (2010).

50. Lebedev-Stepanov, P. & Vlasov, K. Simulation of Self-Assembly in an Evaporating Droplet of Colloidal Solution by Dissipative Particle Dynamics. *Colloids Surfaces A Physicochem. Eng. Asp.* **432**, 132–138 (2013).

51. Ferrari, G., Meerdink, G. & Walstra, P. Drying Kinetics for a Single droplet of Skim-Milk. *J. Food Eng.* **10**, 215–230 (1989).

52. Jeffries, G. D. M., Kuo, J. S. & Chiu, D. T. Controlled Shrinkage and Re-expansion of a Single Aqueous Droplet inside an Optical Vortex Trap. *J. Phys. Chem. B* **111**, 2806–2812 (2007).

53. Fijneman, A. J. *et al.* Local Quantification of Mesoporous Silica Microspheres using Multiscale Electron Tomography and Lattice Boltzmann Simulations. *Microporous Mesoporous Mater.* **302**, 110243 (2020).

54. Yuen, H., Princen, J., Illingworth, J. & Kittler, J. Comparative Study of Hough Transform Methods for Circle Finding. *Image Vis. Comput.* **8**, 71–77 (1990).

55. Voronoi, G. Nouvelles Applications des Paramètres Continus à la Théorie des

Formes Quadratiques. Deuxième mémoire. Recherches sur les Parallélloèdres Primitifs. *J. für die reine und Angew. Math. (Crelles Journal)* **1908**, 198–287 (1908).
56. Okabe, A., Boots, B., Sugihara, K. & Nok Chiu, S. *Spatial Tessellations: Concepts and Applications of Voronoi Diagrams*. (Wiley-VCH Verlag GmbH & Co. KGaA, 2000). doi: 10.1002/9780470317013.
57. Gundersen, H. J. G. Notes on the Estimation of the Numerical Density of Arbitrary Profiles: the Edge Effect. *J. Microsc.* **111**, 219–223 (1977).
58. Goral, M. & Wisniewska-Goclowska, B. IUPAC-NIST Solubility Data Series. 82. Alcohols with Water–Revised and Updated: Part 5. C8–C17 Alcohols with Water. *J. Phys. Chem. Ref. Data* **36**, 685–731 (2007).
59. Tyn, M. T. & Calus, W. F. Diffusion Coefficients in Dilute Binary Liquid Mixtures. *J. Chem. Eng. Data* **20**, 106–109 (1975).
60. Tyn, M. T. & Calus, W. F. Temperature and Concentration Dependence of Mutual Diffusion Coefficients of some Binary Liquid Systems. *J. Chem. Eng. Data* **20**, 310–316 (1975).
61. Grinin, A. P., Shchekin, A. K., Kuni, F. M., Grinina, E. A. & Reiss, H. Study of Nonsteady Diffusional Growth of a Droplet in a Supersaturated Vapor: Treatment of the Moving Boundary and Material Balance. *J. Chem. Phys.* **121**, 387–393 (2004).
62. Goral, M. *et al.* IUPAC-NIST Solubility Data Series. 81. Hydrocarbons with Water and Seawater—Revised and Updated. Part 8. C9 Hydrocarbons with Water. *J. Phys. Chem. Ref. Data* **34**, 2299–2345 (2005).
63. Born, M. & Wolf, E. Geometrical Theory of Optical Imaging. in *Principles of Optics* 133–202 (Elsevier, 1980). doi: 10.1017/CBO9781139644181.
64. Heller, W. Remarks on Refractive Index Mixture Rules. *J. Phys. Chem.* **69**, 1123–1129 (1965).
65. McClymer, J. P. Precise Determination of the Refractive Index of Suspended Particles: Light Transmission as a Function of Refractive Index Mismatch. *Am. J. Phys.* **84**, 602–605 (2016).
66. Amstad, E. *et al.* Robust Scalable High Throughput Production of Monodisperse Drops. *Lab Chip* **16**, 4163–4172 (2016).

Appendices

Appendix 5.1 Droplet tracking

The center coordinates and radii of the shrinking droplets were measured using a Hough transform algorithm that detects circles in MATLAB[1]. A sensitivity factor of 0.80 and an edge threshold of 0.05 were used to detect most of the droplets without introducing false positives (**Figure A5.1a**). Because the droplets move around during heating, tracking of the position of individual droplets throughout the time series is needed (**Figure A5.1b**). Tracking was done by comparing the *x*,*y* position of the center of each droplet in each image to the position and radii of the droplets in the previous image. A droplet is tracked if the *x*,*y* offset between images is smaller than the radius of the droplet which applies to slow moving objects. By tracking the coordinates and radii throughout the time series data analysis becomes possible **(Figure A5.1c).** After correlation a moving mean with a window size of 10 was applied to repress noise (**Figure A5.1d**).

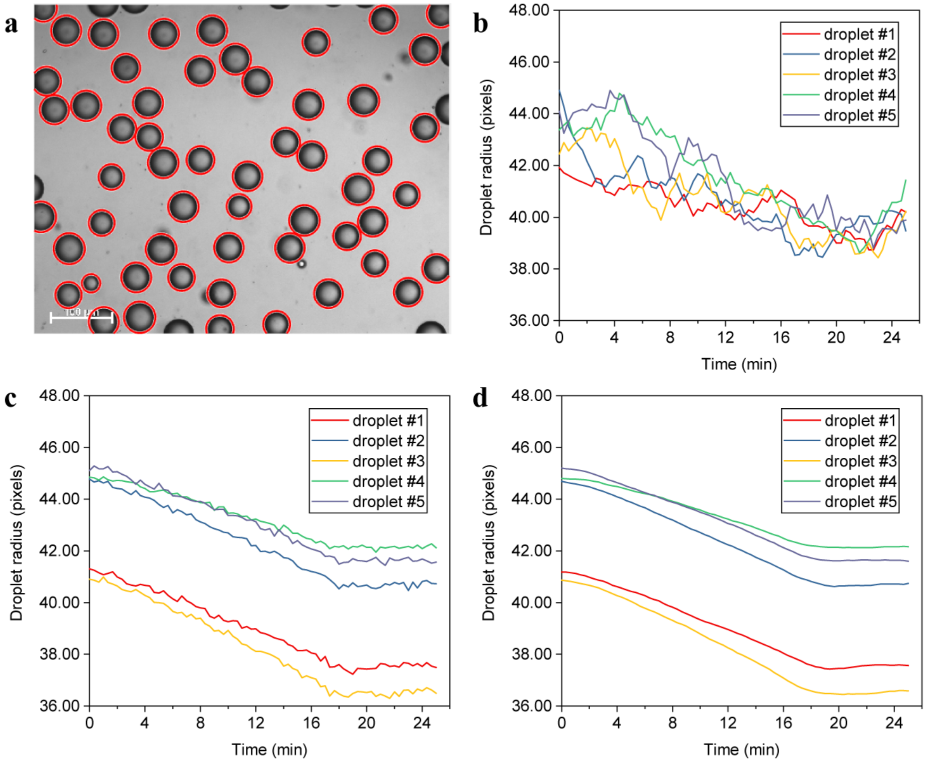

Figure A5.1: (a) Water droplets produced via the microfluidics set-up, with $a_0 = 23.5 \pm 1.6$ µm. The droplets are detected via a Hough transform algorithm. **(b)** Droplet radii throughout the time series before tracking. **(c)** Droplet radii throughout the time series after tracking. **(d)** Correlated droplet radii smoothened by a moving mean with a window size of 10.

Appendix 5.2 Theoretical mass-transfer model

5.2.1 Model derivation

Single droplet shrinkage

At the droplet boundary a mass-conservation equation can be written relating the change of volume of a droplet to the mass flux leaving the droplet[2,3].

$$\frac{\partial}{\partial t}(\rho_\mathrm{W} V_\mathrm{d}) = 4\pi a^2 \mathscr{D}_{\mathrm{W}\to\mathrm{O}} M_\mathrm{W} \left.\frac{\partial C}{\partial r}\right|_{r=a} \tag{A5.1}$$

where ρ_W is the density of the dispersed phase (water, subscript W), V_d is the droplet volume, a is the droplet radius, $\mathscr{D}_{\mathrm{W}\to\mathrm{O}}$ is the mass diffusion coefficient of the dispersed phase W in the continuous phase (oil, subscript O), which can be estimated using the Tyn and Calus method[4,5] (see Appendix 5.2.2 for details), M_W is the molar mass of the dispersed phase, C is the external concentration of water in the continuous phase and r is the distance from the droplet center.

Assuming spherical droplets, $V_\mathrm{d} = 4\pi a^3/3$, the change in droplet volume can then be described as a decrease of the droplet radius in time:

$$\frac{\partial a}{\partial t} = \frac{\mathscr{D}_{\mathrm{W}\to\mathrm{O}} M_\mathrm{W}}{\rho_\mathrm{W}} \left.\frac{\partial C}{\partial r}\right|_{r=a} \tag{A5.2}$$

The continuity equation for water in the continuous phase due to Fickian diffusion is given by:

$$\frac{\partial C}{\partial t} = \mathscr{D}_{\mathrm{W}\to\mathrm{O}} \frac{1}{r^2}\frac{\partial}{\partial r}\left(r^2 \frac{\partial C}{\partial r}\right) \tag{A5.3}$$

Equations (A5.2) and (A5.3) must be solved simultaneously for boundary conditions at the interface $C|_{r=a} = C_\mathrm{i}$ and far away from the droplet $C|_{r=\infty} = C_\infty$. The steady-state solution of equation (A5.3) is:

$$C = C_\infty + \frac{a}{r}\left(C_\mathrm{i} - C_\infty\right) \tag{A5.4}$$

where C_∞ is the water concentration far away from the droplet and C_i is the water concentration at the droplet interface. Taking the derivative and using $r = a$ yields:

$$\frac{\partial C}{\partial r} = -\frac{a}{r^2}\left(C_\mathrm{i} - C_\infty\right) = -\frac{1}{a}\left(C_\mathrm{i} - C_\infty\right) \tag{A5.5}$$

Inserting equation (A5.5) in equation (A5.2) results in:

$$\frac{\partial a}{\partial t} = -\frac{\mathscr{D}_{\mathrm{W}\to o} M_\mathrm{W}}{\rho_\mathrm{W} a}\left(C_\mathrm{i} - C_\infty\right) \tag{A5.6}$$

In case of a single dissolving droplet, C_∞ is equal to the water solubility C_0. The final equation can thus be written as:

$$\frac{\partial a}{\partial t} = -\frac{\mathscr{D}_{\mathrm{W}\to\mathrm{O}} M_\mathrm{W}}{\rho_\mathrm{W} a}\left(C_\mathrm{i} - C_0\right) \tag{A5.7}$$

Multiple droplet shrinkage

In case there are many droplets that all shrink simultaneously, the concentration of water far away from the droplets C_∞ changes as a result of the shrinkage of the droplets and is no longer equal to C_0.

The system consists of a dispersed phase (water, subscript W) and a continuous phase (oil, subscript O). We assume W can dissolve in O yielding an ideal solution, but O cannot dissolve in W:

$$V_{\text{tot}} = V_{\text{W}} + V_{\text{O}} = \left(V_{\text{WW}} + V_{\text{OW}}\right) + \left(V_{\text{OO}} + V_{\text{WO}}\right) = V_{\text{WW}} + V_{\text{OO}} + V_{\text{WO}} \tag{A5.8}$$

where V_{tot} is the total volume of the system, V_{WW} is the amount of water in the dispersed phase, V_{OW} is the amount of oil dissolved in the dispersed phase, which is negligible, V_{OO} is the amount of oil in the continuous phase and V_{WO} is the amount of water dissolved in the continuous phase, given as:

$$V_{\text{WO}} = V_{\text{WO,0}} + N(V_{\text{d,0}} - V_{\text{d,t}}) = V_{\text{WO,0}} + N\,{}^{4\pi}\!/_{3}\left(a_0^3 - a^3\right) \tag{A5.9}$$

where $V_{\text{WO,0}}$ is the initial amount of water dissolved in the continuous phase, $V_{\text{d,0}}$ is the volume of a single droplet at $t = t_0$, $V_{\text{d,t}}$ is the volume of a single droplet at $t = t_{\text{end}}$ and N the number of droplets. Here we assume that all droplets are spherically symmetrical and that the number of droplets is a function of V_{W} at $t = t_0$, i.e., $N = \dfrac{V_{\text{W,0}}}{{}^{4\pi}\!/_{3}\, a_0^3}$. Thus equation (A5.9) can be rearranged to:

$$V_{\text{WO}} = V_{\text{WO,0}} + V_{\text{W,0}}\left(1 - \frac{a^3}{a_0^3}\right) \tag{A5.10}$$

The total volume of the continuous phase is not constant but increases with an amount equal to the volume of solved droplets over time. The volume fraction of water in the solvent is thus:

$$\varphi = \frac{V_{\text{WO}}}{V_{\text{OO}} + V_{\text{WO}}} = \frac{V_{\text{WO}}}{V_{\text{tot}} - V_{\text{W}}} = \frac{V_{\text{WO,0}} + V_{\text{W,0}}\left(1 - \dfrac{a^3}{a_0^3}\right)}{V_{\text{tot}} - V_{\text{W,0}}\left(\dfrac{a^3}{a_0^3}\right)} = 1 + \frac{V_{\text{WO,0}} + V_{\text{W,0}} - V_{\text{tot}}}{V_{\text{tot}} - V_{\text{W,0}}\left(\dfrac{a^3}{a_0^3}\right)} \tag{A5.11}$$

The droplet number density is, however, not constant throughout the sample and thus the local volume fraction differs from the total volume fraction. The spread in droplet number density can be expressed via a so-called evaporation coefficient χ:

$$\chi = \varphi_{\text{local}} / \varphi \tag{A5.12}$$

Theoretically χ can vary between $0.323 < \chi < 1.474$ (see Appendix section 5.2.3 for details).

The total water concentration in the solvent can then be written as a function of the volume fraction as a result of the dissolved droplets:

$$C_{\infty} = C_{\mathrm{WO}} = \chi \frac{\varphi \rho_{\mathrm{W}}}{M_{\mathrm{W}}} = \frac{\chi \rho_{\mathrm{W}}}{M_{\mathrm{W}}} \left(1 + \frac{V_{\mathrm{WO,0}} + V_{\mathrm{W,0}} - V_{\mathrm{tot}}}{V_{\mathrm{tot}} - V_{\mathrm{W,0}} \left(\frac{a^3}{a_0^3} \right)} \right) \tag{A5.13}$$

The quantity $V_{\mathrm{WO,0}}$ is given as a function of the starting concentration C_1:

$$V_{\mathrm{WO,0}} = \frac{M_{\mathrm{W}}}{\chi \rho_{\mathrm{W}}} \left(V_{\mathrm{tot}} - V_{\mathrm{W,0}} \left(\frac{a^3}{a_0^3} \right) \right) C_1 \tag{A5.14}$$

Inserting equation (A5.14) in equation (A5.13) yields:

$$C_{\infty} = C_1 + \frac{\chi \rho_{\mathrm{W}}}{M_{\mathrm{W}}} \left(1 + \frac{V_{\mathrm{W,0}} - V_{\mathrm{tot}}}{V_{\mathrm{tot}} - V_{\mathrm{W,0}} \left(\frac{a^3}{a_0^3} \right)} \right) \tag{A5.15}$$

Equation (A5.15) can then be inserted into equation(A5.6), resulting in:

$$\frac{\mathrm{d}a}{\mathrm{d}t} = -\frac{\mathcal{D}_{\mathrm{W \to O}} M_{\mathrm{W}}}{\rho_{\mathrm{W}} a} \left(C_{\mathrm{i}} - C_1 \right) + \frac{\chi \mathcal{D}_{\mathrm{W \to O}}}{a} \left(1 + \frac{V_{\mathrm{W,0}} - V_{\mathrm{tot}}}{V_{\mathrm{tot}} - V_{\mathrm{W,0}} \left(\frac{a^3}{a_0^3} \right)} \right) \tag{A5.16}$$

However, in a typical experiment the diffusion length is larger than the inter droplet spacing (see also Appendix section 5.2.4). Therefore, we can assume that at every point in time the concentration water is equal everywhere in the solvent:

$$C = C_{\mathrm{i}} = C_{\infty} \tag{A5.17}$$

In this case an analytical solution can be derived for the droplet shrinkage as a function of the concentration water in the solvent:

$$a = a_0 \left[\frac{1 - \frac{V_{\mathrm{W,0}}}{V_{\mathrm{tot}}} + \left(\frac{M_{\mathrm{W}}}{\chi \rho_{\mathrm{W}}} \left(C_{\mathrm{i}} - C_1 \right) - 1 \right)}{\frac{V_{\mathrm{W,0}}}{V_{\mathrm{tot}}} \left(\frac{M_{\mathrm{W}}}{\chi \rho_{\mathrm{W}}} \left(C_{\mathrm{i}} - C_1 \right) - 1 \right)} \right]^{1/3} = a_0 \left[\frac{V_{\mathrm{tot}}}{V_{\mathrm{W,0}}} + \left(\frac{V_{\mathrm{tot}}}{V_{\mathrm{W,0}}} - 1 \right) \left(\frac{M_{\mathrm{W}}}{\chi \rho_{\mathrm{W}}} \left(C_{\mathrm{i}} - C_1 \right) - 1 \right)^{-1} \right]^{1/3} \tag{A5.18}$$

Assuming that the temperature is homogeneous throughout the system, i.e., the droplets plus the continuous phase, the water concentration at the droplet interface is governed by the temperature-corrected equilibrium solubility[3]:

$$C_{\mathrm{i}} = C_0 \exp\left[-\frac{\Delta_{\mathrm{mix}} H}{R} \left(\frac{1}{T} - \frac{1}{T_0} \right) \right] \tag{A5.19}$$

Similarly, the starting concentration C_1 can be expressed as:

$$C_1 = C_0 \exp\left[-\frac{\Delta_{\mathrm{mix}} H}{R} \left(\frac{1}{T_1} - \frac{1}{T_0} \right) \right] \tag{A5.20}$$

In these equations C_0 is the water solubility in the continuous phase at a reference temperature T_0, T_1 is the starting temperature, $\Delta_{\mathrm{mix}}H$ the enthalpy of mixing and R the universal gas constant.

Finally, inserting equation (A5.19) and (A5.20) into equation (A5.18) results in an expression for the droplet shrinkage as a function of the water solubility and the temperature of the system:

$$a = a_0 \left[\frac{V_{\mathrm{tot}}}{V_{\mathrm{W,0}}} + \left(\frac{V_{\mathrm{tot}}}{V_{\mathrm{W,0}}} - 1 \right) \left[\frac{M_{\mathrm{W}}}{\chi \rho_{\mathrm{W}}} C_0 \left(\exp\left[-\frac{\Delta_{\mathrm{mix}} H}{R} \left(\frac{1}{T} - \frac{1}{T_0} \right) \right] - \exp\left[-\frac{\Delta_{\mathrm{mix}} H}{R} \left(\frac{1}{T_1} - \frac{1}{T_0} \right) \right] \right) - 1 \right]^{-1} \right]^{1/3} \tag{A5.21}$$

For $V_{\mathrm{W,0}} / V_{\mathrm{tot}} > 3$ vol%, the analytical solution matches closely to the numerical solution (**Figure A5.2**). The numerical solution also suffers from the mismatch in the actual droplet temperature compared to the measured temperature of the heating couple, as discussed previously.

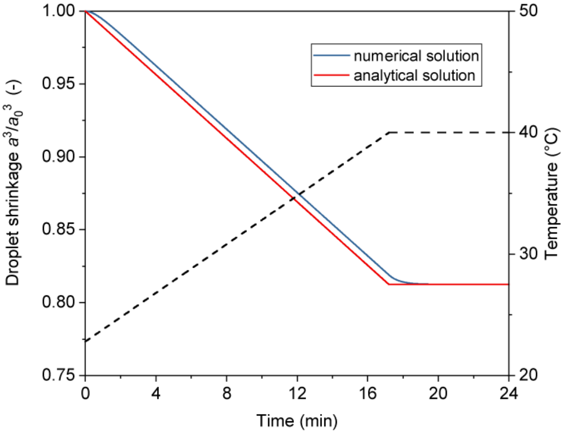

Figure A5.2: Comparison of the analytical solution of the mass-transfer model to the numerical solution. $V_{\mathrm{W,0}} / V_{\mathrm{tot}} = 0.043$ and $\chi = 1$. The temperature profile was increased from $T_1 = 22.8$ °C to $T_2 = 40$ °C with $\mathrm{d}T/\mathrm{d}t = 1$ °C·min^{-1}.

5.2.2 Diffusion equation

The diffusion coefficient can be estimated from the Tyn and Calus method[4,5]:

$$\mathscr{D}_{\mathrm{W}\rightarrow\mathrm{O}} = 8.93\times10^{-8}\left(\frac{\overline{V}_{\mathrm{m,W}}}{\overline{V}^{2}_{\mathrm{m,O}}}\right)^{1/6}\left(\frac{\mathscr{P}_{\mathrm{O}}}{\mathscr{P}_{\mathrm{W}}}\right)^{0.6}\frac{T}{\eta_{\mathrm{O}}} \qquad \text{(A5.22)}$$

$$\mathscr{P} = \overline{V}_{\mathrm{m}}\sigma^{1/4} \qquad \text{(A5.23)}$$

where $\overline{V}_{\mathrm{m,W}}$ (37.4 cm^3·mol^{-1}) and $\overline{V}_{\mathrm{m,O}}$ (150.46 cm^3·mol^{-1}) are the molar volume of the solute and solvent at the normal boiling point, $\mathscr{P}_{\mathrm{W}}$ (105.2 cm^3·g$^{1/4}$/(s$^{1/2}$·mol)) and $\mathscr{P}_{\mathrm{O}}$ (300.9 cm^3·g$^{1/4}$/(s$^{1/2}$·mol)) are parachors for the solute and solvent, η_{O} (13.84 cP) the viscosity of the solvent and σ (39.4 mN·m^{-1}) the surface tension at the temperature T.

5.2.3 Evaporation coefficient χ

To estimate the probabilities of more common values of χ we can randomly place spheres (droplets) in a volume V_{tot} and determine the probability that one of the spheres occupies the volume around a specific sphere.

First, the probability is calculated in case $\chi \leq 1$, indicating none of the other droplets can occupy the space around a droplet. To illustrate, a droplet is placed somewhere in the volume V_{tot}. The space occupied by this droplet is on average V_{tot} / N with $N = \dfrac{V_{\mathrm{W,0}}}{{}^{4\pi}\!/_{3}\, a_0^3}$. Thus, the volume that is unavailable for the next droplet is $V_{\mathrm{W,0}} / N$. The probability that a droplet i is not placed at random in the space around the first droplet (excluding the volume unavailable due to overlapping droplets) is:

$$\mathbb{P}_i = \frac{V_{\mathrm{tot}} - \xi\dfrac{V_{\mathrm{W,0}}}{N}i - \dfrac{V_{\mathrm{tot}}}{N} + \dfrac{Vw}{N}}{V_{\mathrm{tot}} - \xi\dfrac{V_{\mathrm{W,0}}}{N}i} = 1 - \frac{V_{\mathrm{tot}} - V_{\mathrm{W,0}}}{NV_{\mathrm{tot}} - \xi V_{\mathrm{W,0}}i} \qquad \text{(A5.24)}$$

where ξ is the volume excluding the droplets, which, assuming a maximum random packing fraction of 64%, $\xi = 100/64 = 1.56$. The other symbols have their usual meaning.

The probability that none of the droplets is placed in this space is:

$$\mathbb{P}_{\mathrm{tot}} = \mathbb{P}_{\chi\leq1} = \prod_{i=2}^{N}\left(1 - \frac{V_{\mathrm{tot}} - V_{\mathrm{W,0}}}{NV_{\mathrm{tot}} - \xi V_{\mathrm{W,0}}i}\right) = \frac{\left(N_{\mathrm{tot}}V_{\mathrm{tot}} - \xi V_{\mathrm{W,0}}\right)\left(\dfrac{V_{\mathrm{tot}} - N_{\mathrm{tot}}V_{\mathrm{tot}} + V_{\mathrm{W,0}}(-1+\xi)}{\xi V_{\mathrm{W,0}}}\right)_{N_{\mathrm{tot}}}}{\left((-1+N_{\mathrm{tot}})V_{\mathrm{tot}} - V_{\mathrm{W,0}}(-1+\xi)\right)\left(1 - \dfrac{N_{\mathrm{tot}}V_{\mathrm{tot}}}{\xi V_{\mathrm{W,0}}}\right)_{N_{\mathrm{tot}}}} \qquad \text{(A5.25)}$$

Similarly, the probability can be calculated in case $\chi \leq \chi_{\text{ref}}$.

$$\mathbb{P}_{\chi \leq \chi_{\text{ref}}} = \frac{\chi\left(N_{\text{tot}}V_{\text{tot}} - \xi V_{\text{W,0}}\right)\left(\frac{V_{\text{tot}} - \chi N_{\text{tot}}V_{\text{tot}} + \chi V_{\text{W,0}}\left(-1+\xi\right)}{\chi \xi V_{\text{W,0}}}\right)_{N_{\text{tot}}}}{\left(\left(-1+\chi N_{\text{tot}}\right)V_{\text{tot}} - \chi V_{\text{W,0}}\left(-1+\xi\right)\right)\left(1-\frac{N_{\text{tot}}V_{\text{tot}}}{\xi V_{\text{W,0}}}\right)_{N_{\text{tot}}}} \tag{A5.26}$$

The maximum value of $\chi_{\max}$ cannot exceed $V_{\text{tot}}/V_{\text{w,0}}$ since the amount of water cannot be higher than the total volume. Therefore, χ_{ref} ranges from 0 to $V_{\text{tot}}/V_{\text{w,0}}$. Now the probability distribution can be plotted and the probability for every χ can be estimated by taking the derivate of the distribution (**Figure A5.3**)

The integral of all probabilities should be 1. The χ-values for the first 16th and 84th percentile are therefore:

$$\chi_{16} = \int_0^{\chi} \frac{1}{\chi}\mathbb{P}_{\chi} \mathrm{d}_{\chi} \Big/ \int_0^{\chi_{\max}} \frac{1}{\chi}\mathbb{P}_{\chi} \mathrm{d}_{\chi} = 0.323 \tag{A5.27}$$

$$\chi_{84} = \int_0^{\chi} \frac{1}{\chi}\mathbb{P}_{\chi} \mathrm{d}_{\chi} \Big/ \int_0^{\chi_{\max}} \frac{1}{\chi}\mathbb{P}_{\chi} \mathrm{d}_{\chi} = 1.474 \tag{A5.28}$$

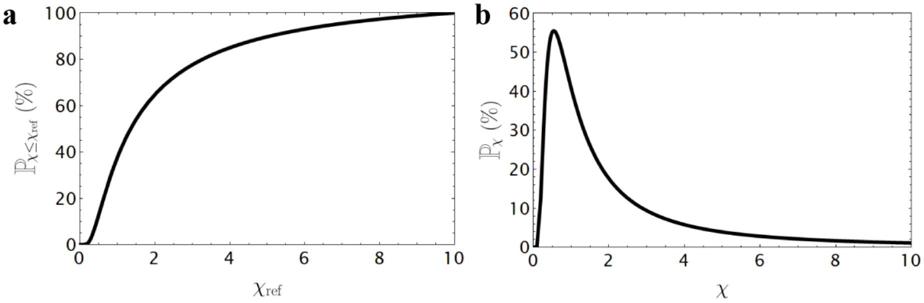

Figure A5.3 (a) Probability distribution for $\chi \leq \chi_{\text{ref}}$. **(b)** Probability density function for χ.

5.2.4 Inter droplet distance

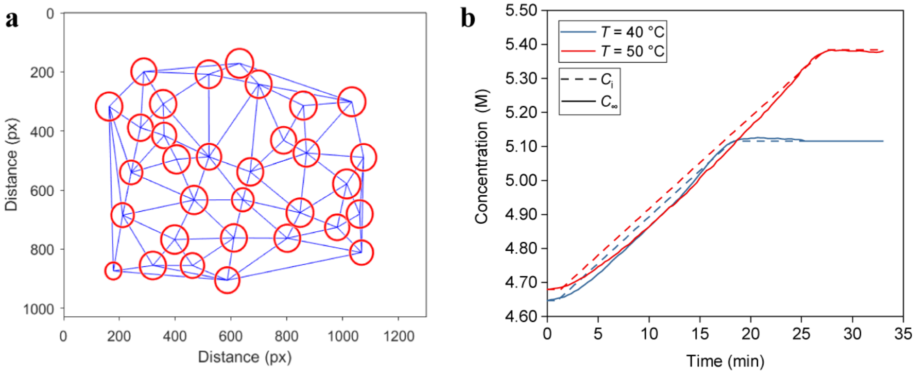

Figure A5.4: (a) Delaunay triangulation to determine the mean center distance between the droplets. **(b)** Concentration profile of water in the continuous phase at the droplet interface C_i and far away from the droplets C_∞.

Appendix 5.3 Time-resolved MSM formation

5.3.1 Effect of pressure

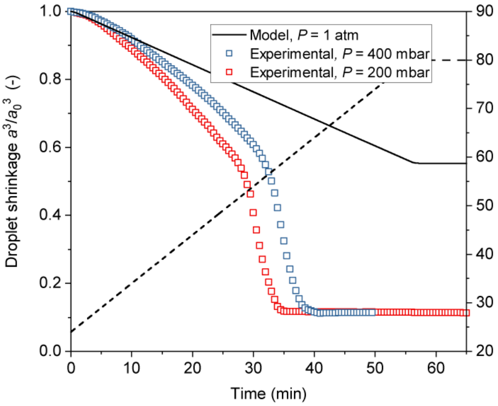

Figure A5.5: Effect of reduced pressure on the droplet shrinkage rate. The temperature profile was increased from T_1 = 24 °C to T_2 = 80 °C with a dT/dt of 1 °C·min^{-1} and an initial droplet radius of a_0 = 23 µm. The experimental data consist of droplets containing 5 wt% 8 nm in diameter silica nanoparticles, which form a MSM after approximately 35 minutes for P = 200 mbar and 40 minutes for P = 400 mbar, respectively. The droplet consists of pure water without nanoparticles.

5.3.2 Radial averaging

Radial averaging is an analysis technique to investigate the relation between the distance and intensity in an image. The radial average is made by laying a raster of concentric rings (radial bins) on top of a chosen center. The mean intensity value of each bin is then collected in an array, which is displayed in a line plot wherein the radius is plotted versus the intensity for each time step. A schematic illustration of the process is shown in **Figure A5.6**.

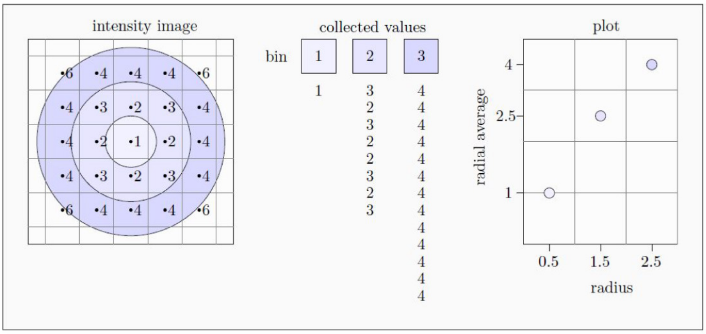

Figure A5.6 Schematic illustration of the radial averaging process.

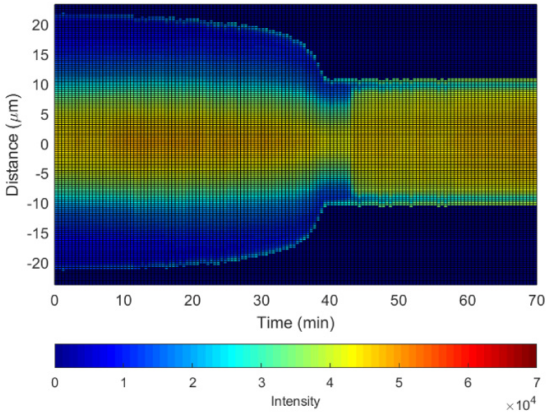

Figure A5.7: Graph showing the radially averaged intensity profile versus time of the formation of a MSM. The temperature profile was increased from $T_1 = 24$ °C to $T_2 = 80$ °C with a dT/dt of 1 °C·min^{-1} with a reduced pressure of $P = 400$ mbar and an initial droplet radius of $a_0 = 21.8$ µm.

5.3.3 Geometrical optics

In optical microscopy the interaction of a sample with an incoming light beam determines how light is passed through a sample and which outgoing light rays are captured by the objective lens[6]. The optical system has a numerical aperture, which determines over which range light rays can be captured by the lens:

$$\mathrm{NA} = n \sin \alpha \tag{A5.29}$$

where NA is the numerical aperture, *n* the refractive index of the medium in which the lens is working and α the maximal half-angle of the cone of light that can enter the lens. Here, NA = 0.4 and *n* is 1 (air), resulting in a half-angle of $\alpha = 23.5°$.

Once a light ray enters a sample, it can interact in multiple ways with the object (**Figure A5.8a**). Light rays that fall parallel to the normal line, i.e., the line orthogonal to the surface of the interface, do not experience any interaction with the sample and are fully transmitted (ray 1 in Figure A5.8a). When the incident angle between the light ray and the normal line is larger than zero, the light ray is both refracted and reflected (ray 2 and 3 in Figure A5.8a). Refraction is the change in direction when a light ray passes from one medium to another and can be calculated via Snell's law[6]:

$$\frac{n_1}{n_2} = \frac{\sin(\theta_2)}{\sin(\theta_1)} \tag{A5.30}$$

where θ_i is the angle relative to the normal line in a medium *i*. Only those light rays with an output angle below the half-angle of the objective are collected.

Reflection is the change in direction at the interface back into the same medium. Reflection for perpendicular incidence can be calculated via[6]:

$$\delta = \frac{(n_2 - n_1)^2}{(n_2 + n_1)^2} \tag{A5.31}$$

If light rays travel from an optical dense medium to an optical less dense medium, there is an incident angle above which total internal reflection occurs. This is called the critical angle (ray 4 in Figure A5.8a):

$$\theta_\mathrm{crit} = \sin^{-1}\left(\frac{n_2}{n_1}\right) \tag{A5.32}$$

Above the critical angle, no light rays are collected by the objective lens (ray 5 and 6 in Figure A5.8a).

The process is also visualized in **Figure A5.8b**. Refracted light rays with an output angle above the half-angle of the objective are not collected and neither are the light rays with an output angle above the critical angle. The region in between the refracted rays with an output angle higher than the half-angle and above the critical angle is seen as the outer black rim of the droplet / particle.

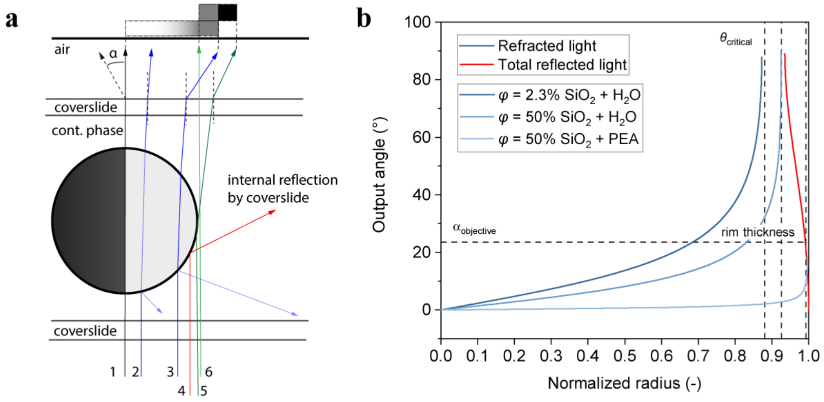

Figure A5.8: (a) Schematic illustration of the different interactions of light rays with a sample in an optical microscope. **(b)** Reconstruction of the interaction of the light rays. Refracted light rays with an output angle below the half-angle of the objective are collected. Totally reflected light rays are not collected by the lens. The region in between the refracted rays with an output angle higher than the half-angle and above the critical angle is seen as the outer black rim of the droplet, which changes during MSM formation.

During droplet shrinkage the volume fraction of silica increases and the refractive index changes. The refractive index of a mixture, such as a silica particle filled with water, can be estimated from so-called mixing-rules. The simplest of these rules is the Arago-Biot equation$^{7\text{-}9}$:

$$n_{\text{mix}} = \varphi_1 n_1 + \varphi_2 n_2 \tag{A5.33}$$

where n_{mix} is the refractive index of the mixture and φ_{i} and n_{i} the volume fraction and refractive index of component *i*, respectively. In our case, $n_{\text{water}} = 1.33$, $n_{\text{silica}} = 1.46$ and $n_{\text{PEA}} = 1.53$.

Following the Arago-Biot equation the refractive index of a water-filled particle becomes higher with an increasing volume fraction of silica (**Figure A5.9a**). This means a smaller mismatch in refractive index with the surrounding medium. Similarly, the critical angle above which total internal reflection occurs also increases with increasing silica volume fraction (**Figure A5.9b**). Hence, more refracted light rays can be captured by the objective lens during droplet shrinkage, which can be observed as a decrease in the thickness of the outer rim.

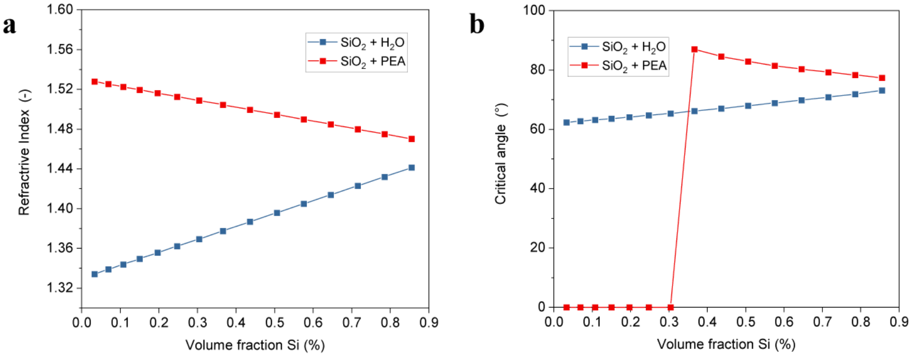

Figure A5.9: (a) Refractive index as a function of silica fraction for a water- and PEA-filled particle, respectively. **(b)** Critical angle as a function of silica fraction for a water- and PEA-filled particle, respectively.

5.3.4 References

1. Yuen, H., Princen, J., Illingworth, J. & Kittler, J. Comparative Study of Hough Transform Methods for Circle Finding. *Image Vis. Comput.* **8**, 71–77 (1990).
2. Ferrari, G., Meerdink, G. & Walstra, P. Drying Kinetics for a Single Droplet of Skim-Milk. *J. Food Eng.* **10**, 215–230 (1989).
3. Jeffries, G. D. M., Kuo, J. S. & Chiu, D. T. Controlled Shrinkage and Re-expansion of a Single Aqueous Droplet inside an Optical Vortex Trap. *J. Phys. Chem. B* **111**, 2806–2812 (2007).
4. Tyn, M. T. & Calus, W. F. Diffusion Coefficients in Dilute Binary Liquid Mixtures. *J. Chem. Eng. Data* **20**, 106–109 (1975).
5. Tyn, M. T. & Calus, W. F. Temperature and Concentration Dependence of Mutual Diffusion Coefficients of some Binary Liquid Systems. *J. Chem. Eng. Data* **20**, 310–316 (1975).
6. Born, M. & Wolf, E. Geometrical Theory of Optical Imaging. in *Principles of Optics* 133–202 (Elsevier, 1980). doi: 10.1017/CBO9781139644181.
7. Heller, W. Remarks on Refractive Index Mixture Rules. *J. Phys. Chem.* **69**, 1123–1129 (1965).
8. McClymer, J. P. Precise Determination of the Refractive Index of Suspended Particles: Light Transmission as a Function of Refractive Index Mismatch. *Am. J. Phys.* **84**, 602–605 (2016).
9. Wiederseiner, S., Andreini, N., Epely-Chauvin, G. & Ancey, C. Refractive-Index and Density Matching in Concentrated Particle Suspensions: a Review. *Exp. Fluids* **50**, 1183–1206 (2011).

Chapter 6

Towards the Fabrication of Microspheres with Hierarchical Morphologies

Abstract

Silica-based porous materials with well-defined porosity characteristics such as mesoporous silica microspheres (MSMs) play an important role in separation applications. Here, we report for the first time, the colloidal assembly of MSMs using fractal silica sols as building blocks, and we demonstrate their unique porosity characteristics using bulk characterization techniques such as nitrogen gas physisorption. Additionally, we describe experimental strategies for the synthesis of multilayered MSMs and hollow MSMs that have interesting potential separation applications that cannot be fulfilled using conventional MSMs. The results described here, although exploratory, highlight how the general principles of MSM synthesis can be extended to facilitate the manufacture of MSMs with hierarchical morphologies.

6.1 General Introduction

Porous materials with well-defined porosity characteristics are of great scientific, societal and industrial relevance for applications in insulation[1], catalysts[2], fuel cells[3] and separation[4]. One prominent example is mesoporous silica microspheres (MSMs), which are frequently used in high performance liquid chromatography (HPLC) for the separation and purification of molecules[5–7]. In this thesis the general principles for the synthesis of tailor-made isotropic MSMs from spherical building blocks have been discussed. This methodology can be further extended to fabricate MSMs with an additional order of complexity such as, e.g., MSMs assembled from non-spherical building blocks, multilayered microspheres or hollow microspheres (HMs).

To date, the majority of hierarchically ordered, porous materials are build-up from spherical building blocks, such as polymer latex beads or silica nanoparticles. Nonetheless, a large variety of non-spherical building blocks can also be used to fabricate materials that are ordered across multiple length scales, such as rods, polyhedral, patterned or branched particles[8–12]. However, the difficulty in synthesis of most of these exotic particles limits their widespread use in industrial applications. In the case of silica nanoparticles two types are manufactured industrially: spherical and anisotropic particles[13]. Due to their similar chemical nature both can readily be used as building blocks to synthesize MSMs with intentionally isotropic pore characteristics.

To achieve anisotropic pore characteristics in MSMs, multilayered microspheres have long been a topic of interest due to their unique properties for separation applications[14–19]. Microspheres with a solid core and porous shell, commonly known as core-shell microspheres (CSMs), are of particular interest in modern HPLC because the solid core provides higher mechanical stability while the porous shell allows for faster mass transfer kinetics due to shorter diffusion paths than conventional, fully porous MSMs[15,18]. CSMs with a porous core and a porous shell with different pore sizes, i.e., a pore gradient from the center to the exterior of the particles, can theoretically be used to separate molecules based on their size, similar to size exclusion chromatography[20]. Likewise, microspheres without a core, i.e., hollow microspheres or colloidosomes, have received a lot of interest due to their interesting potential applications for the loading and controlled release of (bio)macromolecules[21–24]. A schematic illustration of different MSMs is shown in **Scheme 6.1**.

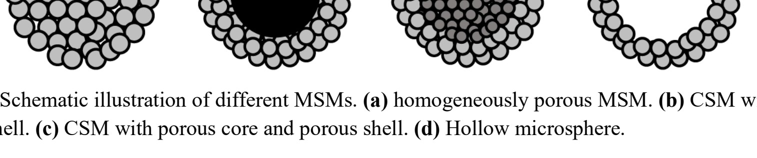

Scheme 6.1: Schematic illustration of different MSMs. **(a)** homogeneously porous MSM. **(b)** CSM with solid core and porous shell. **(c)** CSM with porous core and porous shell. **(d)** Hollow microsphere.

In this chapter, we extend on the general principles laid out throughout this thesis towards the synthesis of MSMs with complex morphologies. First, the effects of fractal silica sols as building blocks on the porosity characteristics of MSMs are investigated and compared to the results to conventional MSMs using standard bulk characterization techniques such as nitrogen physisorption and scanning electron microscopy (SEM). Subsequently, experimental strategies to fabricate both: CSMs and HMs are presented.

6.2 Fractal silica sols

6.2.1 Structural characterization of anisotropic sols

Nearly 30 years ago Yoshida already predicted that anisotropic silica sols would become important in future silica sol manufacturing processes to meet the rapidly changing needs of various fields of application[13]. Anisotropic silica sols have some unique properties compared to spherical silica sols. Due to their shape and relatively large specific surface area (SSA), they are especially useful as, e.g., binders in coatings[25], catalyst support[26] or viscosifying agents[26] but they can also be used for the fabrication of isotropic MSMs with unique porosity characteristics.

Anisotropic silica sols can be oriented in one-dimension (1D), i.e., rod-like sol particles and in three-dimensions (3D), i.e., branched- or fractal sol particles. Synthesizing anisotropic sols is difficult because there is no preferential orientation during nucleation or growth of a standard silica sol[26]. Directionality can be introduced by, e.g., the addition of salts during particle growth or by using a polymer as template. By adding Ca^{2+} ions to an active silicic acid sol, the growth can be directed in one direction to form 1D rod-like particles[25,27]. Alternatively, by adding a polymer such as polyethylene oxide to a solution of silica nanoparticles and subsequently consolidating the aggregates, 3D branched particles can be formed[26]. Depending on the concentration of SiO_2 and the viscosity of the sol, the degree of fractal aggregation (~1/*S*) can be estimated[28,29]:

$$S = \frac{Y}{1 - \left[(1-\varphi)\dfrac{\rho_{\mathrm{H_2O}}}{\rho_{\mathrm{sol}}} \right]} \tag{6.1}$$

where Y is the mass fraction of SiO_2 in the sol, ρ is the density and φ is the volume fraction of the dispersed phase, which can be estimated from the relative viscosity[28,29]:

$$\ln \eta_{\mathrm{R}} = \frac{2.5\varphi}{1-1.43\varphi} \tag{6.2}$$

The lower the '*S*-value', the higher the degree of fractal aggregation. Heavily branched sols generally have a higher viscosity and thus a lower *S*-value.

An alternative way to characterize fractal sols is by the mean cluster size or radius of gyration[30,31]:

$$R_g = \sqrt{\frac{1}{2N^2}\sum_{j=1}^{N}\sum_{i=1}^{N}\left|r_i - r_j\right|^2} \tag{6.3}$$

where N is the number of primary particles in the cluster and $|r_i - r_j|$ is the distance between primary particles i and j belonging to the same overall cluster.

An example of two fractal sols, named F1 and F2 in short, is shown in **Figure 6.1**. The image on the left displays sol F1 with viscosity of 16 mPa·s and an *S*-value of 35%. The image on the right displays sol F2 with a viscosity of 41 mPa·s and an *S*-value of 26%. Sol F2 clearly has a higher degree of fractal aggregation.

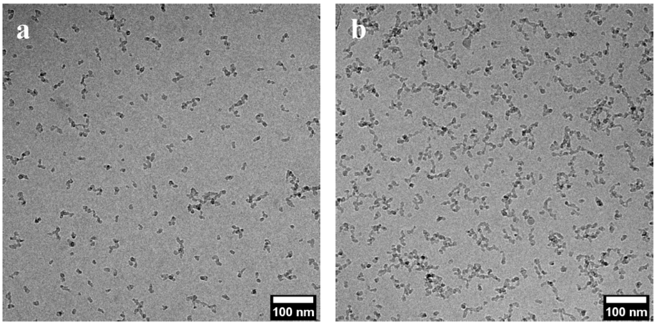

Figure 6.1: CryoTEM micrographs of dilute fractal nanoparticles (1 wt%). **(a)** silica sol F1 with a viscosity of 16 mPa·s and an *S*-value of 35%. **(b)** silica sol F2 with a viscosity of 41 mPa·s and an *S*-value of 26%.

6.2.2 Fractal sols as building blocks

Just like spherical nanoparticles, fractal nanoparticles can be used as building blocks to synthesize MSMs, following the same experimental protocol as described in detail in Chapter 3[32]. In brief, a water-in-oil (W/O) emulsion was prepared by adding fractal sol F2 to an external oil phase consisting of a mixture of phenethyl alcohol (PEA) and mesitylene (MST) with hydroxypropyl cellulose (HPC) as emulsifier under rapid stirring. After emulsification, gelation was induced by the addition of 100 µl of a 5 M ammonium acetate stock solution and by increasing the reaction temperature to 75 °C. After gelation the MSMs were removed from the oil phase via filtration and were subsequently dried and calcined to remove any organic residue. SEM images of a representative example are shown in **Figure 6.2**. The MSMs are perfectly spherical and have an external morphology that is very similar to MSMs made from spherical silica building blocks. Occasionally some individual MSMs form large aggregated structures, presumably due to the high reactivity of the fractal building blocks.

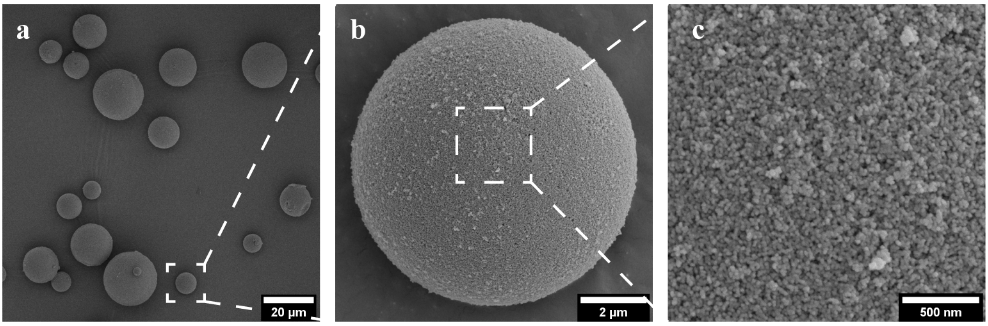

Figure 6.2: **(a)** Example of MSMs synthesized from fractal sol F2 after calcination. **(a)** Zoomed-in SEM image of a single MSM. **(b)** Zoomed-in SEM image of the surface of the MSM.

To evaluate the porosity characteristics, N_2 gas adsorption was performed and the results were compared to MSMs made from spherical 8 nm sized nanoparticles, as these are closest in size to the primary particles of the fractal sol (**Figure 6.3**). Both MSM species displayed IUPAC type IVa isotherms, which is characteristic for adsorption behavior inside mesoporous adsorbents[33]. The MSMs constructed from fractal sol particles can adsorb a significantly higher quantity of N_2 gas (1207 $cm^3 \cdot g^{-1}$) compared to MSMs constructed from spherical sol particles (594 $cm^3 \cdot g^{-1}$), indicating a significantly higher porosity (ϕ = 0.81 compared to ϕ = 0.67). Furthermore, the MSMs constructed from the fractal sol clearly have a larger average pore diameter, despite a significantly smaller specific surface area (280 $m^2 \cdot g^{-1}$ compared to 388 $m^2 \cdot g^{-1}$).

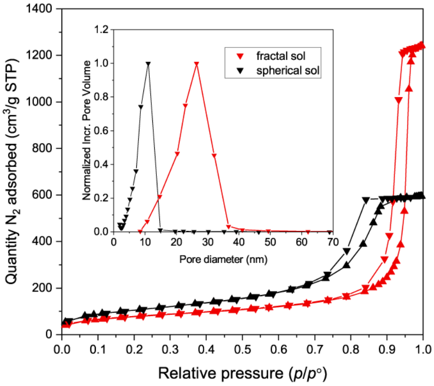

Figure 6.3: Representative N_2 adsorption/desorption isotherms of MSMs constructed from fractal sol F2 (in red, SSA = 280 $m^2 \cdot g^{-1}$, ϕ = 0.81) and MSMs constructed from spherical sol 2 (in black, SSA = 388 $m^2 \cdot g^{-1}$, ϕ = 0.67). Inset: PSDs for both MSM species, obtained from the respective desorption isotherms.

From an engineering point of view, it would be interesting to investigate how far the porosity of MSMs can be increased without compromising the structural integrity of the microspheres. Highly porous MSMs with large surface areas could, for example, be useful as catalyst supports[34]. Moreover, it would be interesting to investigate the role of inhomogeneity of the sol on the internal pore morphology using the tools described in Chapter 4. By embedding MSMs in sulfur and sectioning the microspheres using an ultramicrotome, ultra-thin cross-sections can be obtained that can be analyzed using TEM. Unlike polymer-based resins, sulfur can be sublimated under vacuum, yielding cross-sections free from any embedding medium[35,36]. For a successful application of sulfur embedding, see, e.g., Gnanasekaran et al.[36]. The MSMs can then be analyzed for local variations in, e.g., pore size and pore geometry[37].

Since fractal building blocks behave similar to spherical building blocks, fractal sols and spherical sols can be mixed in different ratios to co-assemble microspheres with unique properties. Blending a relatively large spherical sol with low surface area with a similar sized fractal sol with large surface area could yield MSMs with significantly larger SSAs than otherwise obtainable. A larger SSA means more active sites to functionalize with surface-active groups[38,39]. In chromatographic terms, MSMs with a larger SSA result in longer retention times, i.e., the time that an analyte is retained on a column[5]. Additionally, blending a small portion of fractal sol into a standard recipe could yield MSMs with the same properties but under milder reaction conditions. Due to the higher reactivity of the fractal sol, lower reaction temperatures or less salt is required to synthesize MSMs with the same porosity characteristics. This is similar to the fine tuning of MSMs via sol particle mixing introduced in Chapter 3. However, regardless of the size and shape of the building block used, the resulting MSMs are always isotropic. Therefore, in the next section, experimental strategies are discussed to obtain anisotropic MSMs.

6.3 Core-shell microspheres (CSMs)

Conventional, fully porous MSMs are used in HPLC instruments that operate in the range of 400 – 500 bar. Modern ultra-high pressure (UHPLC) instruments can operate under pressures as high as 1500 bar. Conventional MSMs generally have too low mechanical stability to handle the extreme mechanical load in UHPLC. Therefore, anisotropic MSMs such as CSMs with solid cores and porous shells are of interest due to their significant higher mechanical stability[40]. Most commercially available CSMs are synthesized via a layer-by-layer approach. The layer-by-layer approach is based upon electrostatic interactions to build alternating layers of positively charged polymers and negatively charged nanoparticles on top of core particles with a certain surface charge[41,42]. Although many variations to this method exist and several other procedures have been reported in literature to fabricate multilayered particles[43–46], the complexity and poor batch-to-batch reproducibility of most methods limits the widespread use of these materials in separation applications[17].

Here, we propose two potential routes for the assembly of CSMs based on the same overall experimental protocol established for isotropic MSMs (Scheme 6.2). Route (1) blends solid microspheres of pre-defined size or pre-assembled MSMs with a colloidal silica sol in a conventional water-in-oil emulsion system. Route (2) splits the conventional gelation process into two steps in order to add a second colloidal silica sol into the system. By controlling the gelation rate of the primary building blocks that form the core, as well as the size of the emulsion droplets and the gelation rate of the secondary building blocks that form the shell, it should, in theory, be possible to independently control the porosity characteristics of both parts and create multilayered MSMs exposing a gradient in pore characteristics. To date, we have successfully formed CSMs on multiple occasions, however, reproducibility and control over the nanoscale properties as shown in Chapter 3 is still lacking.

6.3.1 Microspheres as building blocks

In route 1 monodisperse solid microspheres or pre-assembled MSMs are used as building blocks to form CSMs. Two possible pathways are briefly discussed below: (i) blending pre-formed MSMs in the oil phase prior to forming an emulsion or (ii) blending solid microspheres with a colloidal silica sol prior to emulsification in the oil phase. A schematic illustration is shown in **Scheme 6.2**.

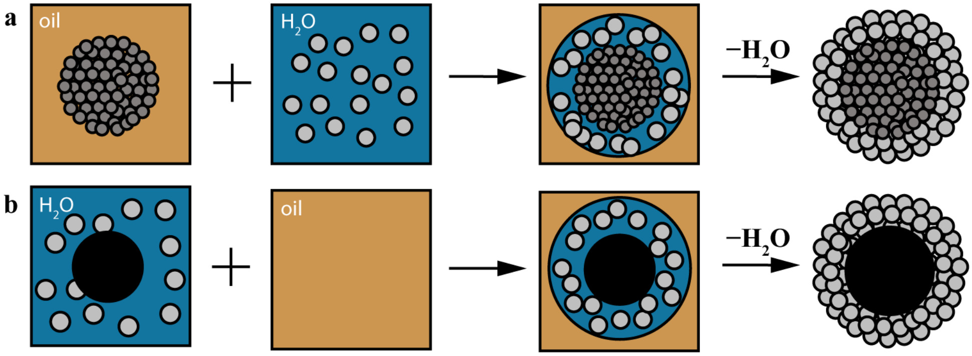

Scheme 6.2: Schematic illustration of route 1 to synthesize CSMs. **(a)** pathway i. **(b)** pathway ii. Orange indicates the oil phase. Blue indicates the water phase. Grey indicates silica nanoparticles. Dark grey indicates a porous MSM. Black indicates a solid microsphere. The steps are explained in the main text.

To illustrate pathway (i), a small amount of 5 µm monodisperse MSMs was dispersed in the oil phase prior to the addition of a silica sol. We hypothesized that the hygroscopic MSMs would attract the aqueous sol and form emulsion droplets around the dispersed MSMs. However, preliminary results showed this was not the case. It appeared to be energetically more favorable for the sol to form separate emulsion droplets rather than to interact with the MSMs. To improve the interaction, the surface of the MSMs was functionalized with a charged silane. However, this also did not result in a good interaction between the MSM and sol nanoparticles.

Alternatively, 2 µm monodisperse solid microspheres were blended directly into the sol prior to emulsification (pathway (ii)). Although this ensures a good interaction between the core microsphere and sol nanoparticles, the drawback is that upon emulsification there are several emulsion droplets containing multiple core particles. To have approximately one core particle per droplet, the droplets must be fragmented so that the droplet size is roughly equal to the size of one core particle. This can be done by fragmenting the crude emulsion droplets into smaller droplets using, e.g., a couette shear mixer[47,48]. A couette mixer consists of two concentric cylinders that are separated by a small gap. Under certain rheological and shear conditions it is possible to fragment a crude emulsion into an emulsion with a monodisperse size distribution[47,48]. Several attempts were made to fragment the emulsion droplets obtained in this work using an in-house designed couette mixer, however, none of these gave satisfactory results. The emulsion droplets were smaller after fragmentation and the number of droplets that contained only one core particle appeared to be higher than without shearing but the overall reproducibility was low.

If the droplets are not fragmented, the solid microspheres act as building blocks together with the silica nanoparticles and form large hybrid structures via a Pickering-type emulsion[49] (**Figure 6.4**). These structures appear to be hollow, with silica nanoparticles acting as a glue to hold the larger microspheres in place. Although unexpected, these large ≥ 100 µm sized microspheres could be potentially of interest in gas chromatography (GC) applications. GC columns are generally very long and large microspheres could reduce the pressure drop across the column[50].

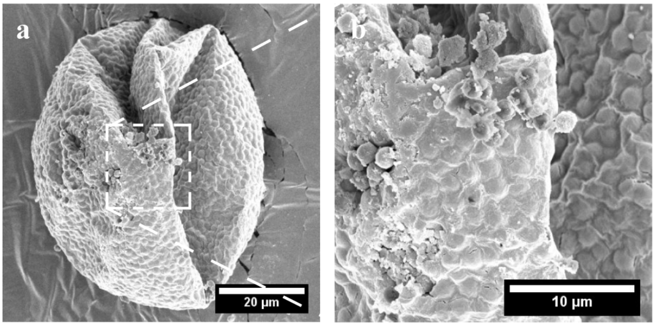

Figure 6.4: (a) SEM image of a large, hollow structure consisting of solid microspheres held together by layers of silica nanoparticles. **(b)** Zoomed-in SEM image of the surface of the structure.

6.3.2 Multi-gelation process

In the second route CSMs were formed by mixing two sol species. Due to the high stability of the emulsion droplets it was not possible to simply add two sols consecutively. Instead, the gelation process was split into two steps.

In the conventional experimental protocol, gelation is induced via the addition of salt and heat (gelation-driven assembly)[32]. Gelation is followed by water removal and the MSMs are filtered, dried and calcined. However, if after a first heating cycle and gelation of the first sol a second silica sol is added, emulsification and gelation can be induced a second time to form CSMs. A schematic illustration is shown in **Scheme 6.3**.

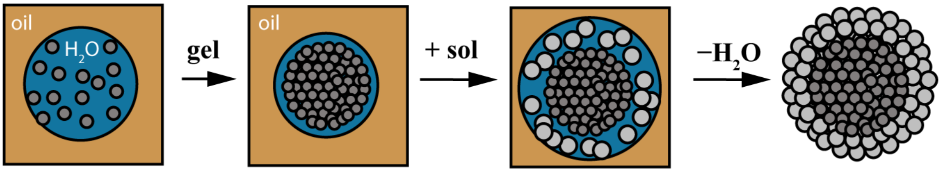

Scheme 6.3: Schematic illustration of route 2 to synthesize CSMs. Orange indicates the oil phase. Blue indicates the water phase. Grey indicates silica nanoparticles. The steps are explained in the main text.

To illustrate, CSMs were formed using two different silica sols as building blocks. First, core particles were formed via the emulsification and gelation-driven assembly of a silica sol consisting of 100 nm nanoparticles. At the end of the gelation process, the mixture was cooled down to room temperature and a second silica sol consisting of 8 nm nanoparticles was added. The mixture was then re-heated to induce a second gelation step, after which water was removed and the CSMs were filtered and dried. Two examples are shown in **Figure 6.5**. The CSMs clearly have two distinguishable layers but are also inherently flawed. The shell of the CSM in the first image is severely damaged and the shell of the CSM in the second image appears to be completely detached from the core. The core itself is relatively smooth, whereas the outer shell is heavily corrugated. It is unclear why this is the case. We speculate that the limited space of the nanoparticles in the outer layer and shorter diffusion path to the continuous phase plays an important role.

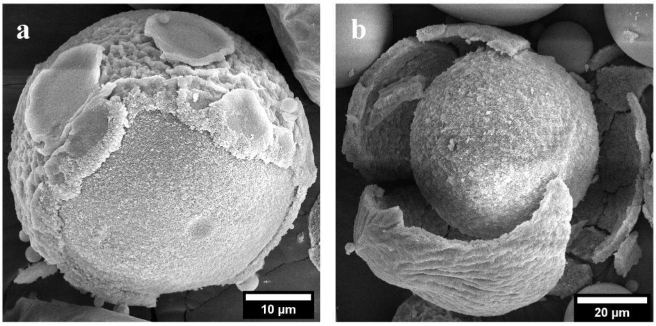

Figure 6.5: SEM images of CSMs formed via the multi-gelation protocol. The two layers have different morphology.

Although it is possible to form CSMs this way, the protocol is incredibly difficult to control, and the reproducibility is low. We expect that the droplet microfluidics system described in Chapter 5 can improve the reproducibility of synthesizing CSMs. For example, two flow-focusing microfluidic chips with different sized orifices can be placed in series to form controlled double emulsions[51]. By replacing one of the two aqueous silica sols by a silica sol dispersed in an organic solvent such as ethanol, monodisperse droplets of sol 1 may be formed in sol 2, which can be subsequently emulsified in the standard organic solvent. A schematic illustration is shown in **Scheme 6.4**.

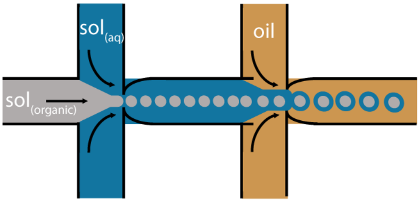

Scheme 6.4: Schematic illustration of a droplet microfluidic route towards CSMs. Grey indicates silica nanoparticles dispersed in an organic solvent. Blue indicates silica nanoparticles dispersed in water. Orange indicates the oil phase.

6.4 Hollow microspheres (HMs)

A special kind of CSMs are CSMs without a core, i.e., HMs. Many different experimental protocols have been reported to fabricate HMs such as templating routes using vesicles[52,53], solid particles[54,55] or emulsions[56–59]. Emulsions are ideal templates for the fabrication of spherical materials. However, due to their inherent thermodynamic instability they will ultimately phase separate after a certain period of time[60]. The emulsion system described throughout this thesis has a very high stability due to the use of HPC as emulsifier and stabilizer[61,62]. The HPC forms barrier around the emulsion droplets and prevents the droplets from coalescing[57]. Even after sedimentation the droplets remain intact for long periods of time (> 24 hours). This unique ability can be manipulated to synthesize HMs, as illustrated schematically in **Scheme 6.5**.

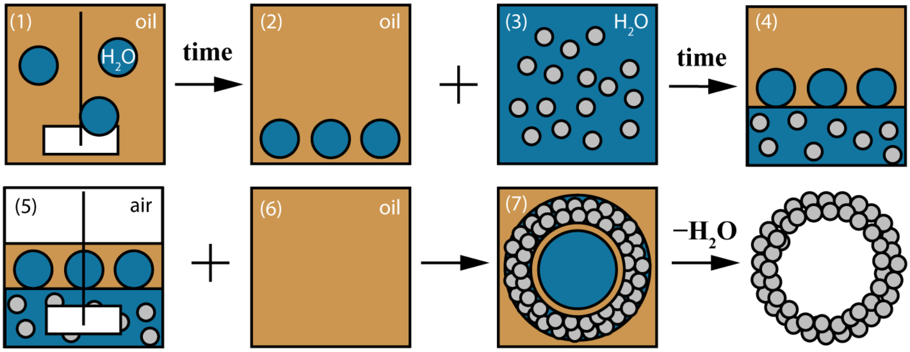

Scheme 6.5: Schematic illustration to synthesize HMs. Orange indicates the oil phase. Blue indicates the water phase. Grey indicates silica nanoparticles. The steps are explained in the main text.

In step 1, a mixed oil phase of PEA and MST with a density of $\rho_{\text{oil}} = 0.936\ \text{cm}^3\cdot\text{g}^{-1}$ was used to form a W/O emulsion consisting of Milli-Q droplets. After emulsification the mixture was allowed to sediment overnight. The water droplets sediment due to their slightly higher density ($\rho = 0.997\ \text{cm}^3\cdot\text{g}^{-1}$) than the oil phase (step 2). After sedimentation in step 3, a sol consisting of 14 wt%, 8 nm diameter nanoparticles (ρ = 1.079 cm^3·g^{-1}) was carefully added along the side of the beaker without disturbing the mixture. The sol is heavier than the other components and forms a layer below the sedimented water droplets (step 4). Although the sol and water droplets are both aqueous, they do not easily mix, most likely due to the strong barrier properties of the emulsifier. However, upon removing the excess oil layer and gentle mechanical stirring (step 5), a double W/O emulsion can be formed where water droplets are encapsulated by a thin layer of solvent and a layer of silica nanoparticles. Oil was then added again (step 6) and the sol was gelled using the same experimental protocol as established previously to form MSMs (step 7). Experimentally it was observed that if the oil layer is not removed in step 5 prior to gentle stirring, the sol layer preferentially forms independent emulsion droplets instead of the desired double emulsion droplets.

An example of the extracted and calcined reaction product is shown in **Figure 6.6**. Figure 6.6a shows a collection of large HMs with dented surfaces. This could be a result of shrinking of the interior water droplets during gelation. Since there are no silica nanoparticles in the core of the spheres, the final mechanical stability of the HMs is lower than for conventional MSMs. Figure 6.6b shows a relatively small HM with a smooth surface. The interior is clearly hollow with some smaller microspheres encapsulated by the larger microsphere. This is likely due to the unintentional formation of a triple emulsion due to mixing, although it is unclear if the small spheres are also hollow.

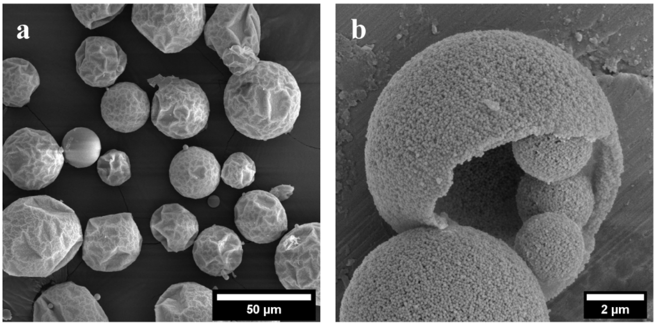

Figure 6.6: Examples of HMs formed via a sedimentation protocol. **(a)** SEM image of a collection of large, crumpled HMs. **(b)** SEM image of a damaged HM, clearly showing its hollow interior.

Like the formation of CSMs, this experimental protocol is incredibly difficult to control. The microspheres are clearly hollow but are not yet suitable for any potential application. We believe that the droplet microfluidic platform described in Chapter 5 can improve the reproducibility and ultimately lead to HMs with controlled morphology and tunable porosity characteristics of the silica shell. Similar to the formation of CSMs via droplet microfluidics, multiple chips with increasing sized orifices can be placed in series to form controlled multi-emulsions[51]. Three droplet generators in line are required to form a double W/O emulsion required to form HMs, as illustrated in **Scheme 6.6**.

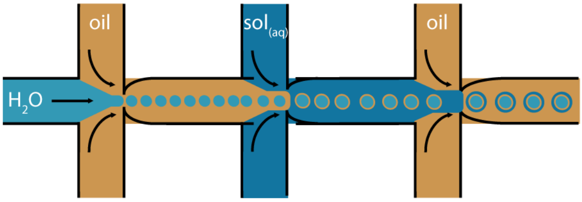

Scheme 6.6: Schematic illustration of a droplet microfluidic route towards HMs. Light blue indicates water. Orange indicates the oil phase and dark blue indicates silica nanoparticles dispersed in water.

6.5 Conclusions

In summary, we described three experimental strategies towards the synthesis of MSMs with complex morphologies. We demonstrated for the first time the use of fractal silica sols for the synthesis of MSMs and show how they affect the morphology and porosity characteristics of the microspheres. In contrast with conventionally used spherical silica sols, MSMs constructed from fractal sols have a significantly higher microsphere porosity, whilst the perfect spherical shape remains intact. Further characterization is required to elucidate the effect of the anisotropy of the sol on the formation of the porous network and to quantify any potential local differences in the pore distribution and tortuosity. Additionally, we describe strategies to synthesize CSMs and HMs. However, due to limited control over the emulsion droplet size and their behavior in bulk, batch-to-batch reproducibility is low and porosity characteristics such as the total pore size and porosity of the microspheres cannot yet be tailored. It is expected that the droplet microfluidics platform introduced in Chapter 5 can improve the reproducibility of the presented strategies by precise control over the formation of multi emulsions.

6.6 Materials and methods

Materials

The colloidal silica sols used in this work were provided by Nouryon Pulp and Performance Chemicals AB, Sweden and consist of colloidal silica nanoparticles (sol) of different sizes and concentrations in water (**Table 6.1**). All sols are ammonium stabilized, which means they have been brought to a pH of 8.5 – 10.5 by the addition of ammonia (25% w/w, Scharlau). The particle volume fraction of the sols was determined using X-ray fluorescence spectroscopy and the number mean particle diameter $D_P[1,0]$ and standard deviation (SD) were determined by cryoTEM (see Chapter 2 for details on the characterization procedure).

Table 6.1: Colloidal silica sols used to synthesize MSMs.

sol	SiO_2 wt%	number mean $D_P[1,0]$ ± SD (nm)	pH
1	12	4.2 ± 1.0	10.1
2	14	8.2 ± 2.5	9.2
3	30	17.5 ± 4.6	8.6
4	40	25.2 ± 5.8	9.1
5	22	95.4 ± 18.3	8.6
F1	12	4.2 ± 1.0	10.1
F2	14	8.2 ± 2.5	9.2

Phenethyl alcohol (PEA, 99%) and mesitylene (MST, 97%) as the oil phase and hydroxypropyl cellulose (HPC, average M 100.000 $g{\cdot}mol^{-1}$) as a stabilizer and emulsifier were purchased from Acros Organics. A 5 M stock solution of salt was prepared of ammonium acetate (Merck). All chemicals were used as received without further purification. The water used in this work was deionized by a Milli-Q Advantage A10 system (Merck Millipore) and had an electrical resistivity of 18.2 MΩ·cm at 25 °C.

Experimental protocol

Three different experimental protocols were carried out which are detailed below. For each procedure, a 5 wt% aqueous solution of hydroxypropyl cellulose (HPC) was used as emulsifier and stabilizing agent. It was prepared by dispersing HPC (5 g) in Milli-Q water (95 g) at 60 °C. The mixture was stirred continuously and allowed to cool to room temperature after one hour. Stirring was continued for 24 h. It was then filtered twice over 5 µm pore size filter paper (Munktell) and stored in a plastic container.

Procedure 1: synthesis of MSMs

An oil phase was prepared by mixing PEA (70 g), MST (30 g) and 5 wt% HPC (3.7 g) solution in a beaker at room temperature, and stirring at 300 RPM for one hour with an overhead mixer (IKA Yellow line OST Basic), after which the mixture was fully transparent.

Colloidal silica (10 g) and 5 M aqueous ammonium acetate solution (100 µl) were then added to above mixture under constant stirring (350 RPM) to form a W/O emulsion which had a white/milky appearance. After 60 minutes of stirring, the emulsion was poured in a round bottom flask that was subsequently attached to a rotary evaporator fitted with a water bath (Buchi R-200) and exposed to 75 °C at atmospheric pressure for 90 minutes. After gelling had occurred, rotary evaporation was continued for 90 minutes at a reduced pressure of 200 mbar, at which point almost all the water had been removed from the emulsion, resulting in an almost completely clear/transparent mixture. The temperature was then increased to 85 °C for a further 30 minutes, before being allowed to cool to room temperature. The resulting MSMs were separated by filtration over a Pyrex glass filter and dried at 90 °C for 16 hours. Finally, MSMs were calcined in air at 650 °C for 4 hours.

Procedure 2: synthesis of CSMs

Identical to procedure 1, except after gelling had occurred the mixture was poured back in a beaker and allowed to cool down to room temperature. After cooling down, a second silica sol (10 g) was added under constant stirring (350 RPM) to form emulsion droplets encapsulating the 'wet' MSMs. The mixture was then re-heated to 75 °C under a reduced pressure of 200 mbar for 90 minutes to remove water from the emulsion.

Procedure 3: synthesis of HMs

An oil phase was prepared by mixing PEA (50 g), MST (50 g) and 5 wt% HPC (2.2 g) solution in a beaker at room temperature, and stirring at 300 RPM for one hour with an overhead mixer (IKA Yellow line OST Basic), after which the mixture was fully transparent.

Milli-Q water (10 g) was then added to above mixture under constant stirring (350 RPM) to form a W/O emulsion which had a white/milky appearance. After 60 minutes of stirring, the emulsion was left to sediment overnight. After sedimentation, colloidal silica (10 g) was added slowly to above mixture without stirring, which immediately sank to the bottom of the beaker. The solvent top layer was then gradually removed via a peristaltic pump. After the solvent layer was removed, the mixture was gently stirred (100 RPM) to encapsulate the water droplets with a layer of sol. Afterwards, fresh solvent was gradually added, and gelation was induced via the same protocol as described in procedure 1.

Microsphere characterization

Specific surface areas, pore volumes and pore size distributions of the synthesized samples were determined from nitrogen sorption isotherms (Micromeritics TriStar 3000). The isotherms were measured at −196 °C. The specific surface area was calculated from the monolayer adsorbed gas quantity in the pressure interval $p/p°$ = 0.05-0.22 using the Brunauer-Emmett-Teller (BET) equation[63]. The pore volume and pore size distribution were calculated from the desorption isotherm using the Barrett–Joyner–Halenda (BJH) model[33,64]. Every sample displayed IUPAC type IVa isotherms, indicating adsorption behavior inside mesoporous adsorbents[33]. The microsphere porosity was calculated from the pore volume per gram microspheres and the density of amorphous silicon dioxide[65]:

$$\phi = \frac{V_{\text{pore}}}{\dfrac{1}{\rho_{\text{SiO}_2}} + V_{\text{pore}}} \tag{6.4}$$

where V_{pore} is the pore volume per gram particles and ρ_{SiO2} is the density of amorphous SiO_2, which we assume as 2.2 g·cm^{-3}.[66] While this value can be disputed, the effect of changing ρ_{SiO2} within reasonable boundaries is limited.

SEM images of select microspheres were obtained using a Quanta3D (Thermo Fisher Scientific) equipped with a field emission electron gun operating at 5 kV. The particles were deposited on a SEM-stub and sputter-coated with a 20 nm layer of gold (Emitech K550) to prevent charging.

CryoTEM micrographs were recorded with the TU/e CryoTitan electron microscope (Thermo Fisher Scientific) operating at 300 kV in bright-field TEM mode with an image sampling of 2048 × 2048 pixels (pixel size 0.387 nm·px^{-1}). The silica sols were diluted to approximately 1 wt% with Milli-Q water and applied on copper TEM grids (QUANTIFOIL® R 2/2, Cu 200 mesh - Quantifoil Micro Tools). The grids were surface plasma treated for 40 s using a Cressington 208 carbon coater prior to use. The samples were then vitrified by plunging them into liquid ethane using an automated vitrification robot (FEI Vitrobot Mark III).

6.7 References

1. Wicklein, B. *et al.* Thermally Insulating and Fire-Retardant Lightweight Anisotropic Foams based on Nanocellulose and Graphene Oxide. *Nat. Nanotechnol.* **10**, 277–283 (2015).
2. Taguchi, A. & Schüth, F. Ordered Mesoporous Materials in Catalysis. *Microporous Mesoporous Mater.* **77**, 1–45 (2005).
3. Vix-Guterl, C. *et al.* Electrochemical Energy Storage in Ordered Porous Carbon Materials. *Carbon N. Y.* **43**, 1293–1302 (2005).
4. Davis, M. E. Ordered Porous Materials for Emerging Applications. *Nature* **417**, 813–821 (2002).
5. Snyder, L. R., Kirkland, J. J. & Dolan, J. W. *Introduction to Modern Liquid Chromatography. High-Performance Gradient Elution: The Practical Application of the Linear-Solvent-Strength Model* (John Wiley & Sons, Inc., 2009). doi:10.1002/9780470508183.
6. Gritti, F. & Guiochon, G. New Insights on Mass Transfer Kinetics in Chromatography. *AIChE J.* **57**, 333–345 (2011).
7. Gritti, F., Horvath, K. & Guiochon, G. How Changing the Particle Structure can speed up Protein Mass Transfer Kinetics in Liquid Chromatography. *J. Chromatogr. A* **1263**, 84–98 (2012).
8. Glotzer, S. C. & Solomon, M. J. Anisotropy of Building Blocks and their Assembly into Complex Structures. *Nat. Mater.* **6**, 557–562 (2007).
9. Damasceno, P. F., Engel, M. & Glotzer, S. C. Predictive Self-Assembly of Polyhedra

into Complex Structures. *Science (80-.)*. **337**, 453–457 (2012).

10. Singh, G. *et al.* Self-Assembly of Magnetite Nanocubes into Helical Superstructures. *Science* **345**, 1149–1153 (2014).
11. Wang, D. *et al.* Interplay between Spherical Confinement and Particle Shape on the Self-Assembly of Rounded Cubes. *Nat. Commun.* **9**, 2228 (2018).
12. Sacanna, S. & Pine, D. J. Shape-Anisotropic Colloids: Building Blocks for Complex Assemblies. *Curr. Opin. Colloid Interface Sci.* **16**, 96–105 (2011).
13. Yoshida, A. Silica Nucleation, Polymerization, and Growth Preparation of Monodispersed Sols. in *The Colloid Chemistry of Silica* 51–66 (1994). doi:10.1021/ba-1994-0234.ch002.
14. Horvath, C. & Lipsky, S. R. Column Design in High Pressure Liquid Chromatography. *J. Chromatogr. Sci.* **7**, 109–116 (1969).
15. Guiochon, G. & Gritti, F. Shell Particles, Trials, Tribulations and Triumphs. *J. Chromatogr. A* **1218**, 1915–1938 (2011).
16. Kirkland, J. J., Schuster, S. A., Johnson, W. L. & Boyes, B. E. Fused-Core Particle Technology in High-Performance Liquid Chromatography : an Overview. *J. Pharm. Anal.* **3**, 303–312 (2013).
17. Hayes, R., Ahmed, A., Edge, T. & Zhang, H. Core-Shell Particles: Preparation, Fundamentals and Applications in High Performance Liquid Chromatography. *J. Chromatogr. A* **1357**, 36–52 (2014).
18. Tanaka, N. & McCalley, D. V. Core-Shell, Ultrasmall Particles, Monoliths, and Other Support Materials in High-Performance Liquid Chromatography. *Anal. Chem.* **88**, 279–298 (2016).
19. Wagner, B. M. *et al.* Superficially Porous Particles with 1000Å Pores for Large Biomolecule High Performance Liquid Chromatography and Polymer Size Exclusion Chromatography. *J. Chromatogr. A* **1489**, 75–85 (2017).
20. Collins, B. E., Dancil, K. P. S., Abbi, G. & Sailor, M. J. Determining Protein Size using an Electrochemically Machined Pore Gradient in Silicon. *Adv. Funct. Mater.* **12**, 187–191 (2002).
21. Botterhuis, N. E., Sun, Q., Magusin, P. C. M. M., Van Santen, R. A. & Sommerdijk, N. A. J. M. Hollow Silica Spheres with an Ordered Pore Structure and their Application in Controlled Release Studies. *Chem. - A Eur. J.* **12**, 1448–1456 (2006).
22. Dinsmore, A. D. *et al.* Colloidosomes: Selectively Permeable Capsules Composed of Colloidal Particles. *Science* **298**, 1006–1009 (2002).
23. Thompson, K. L., Williams, M. & Armes, S. P. Colloidosomes: Synthesis, Properties and Applications. *J. Colloid Interface Sci.* **447**, 217–228 (2015).
24. Bollhorst, T., Rezwan, K. & Maas, M. Colloidal Capsules: Nano- and Microcapsules with Colloidal Particle Shells. *Chem. Soc. Rev.* **46**, 2091–2126 (2017).
25. Watanabe, Y., Ando, M., Tanimoto, K., Tsutomu, K. & Kawashima, M. (Nissan Chemical Industries Ltd.) US 5221497 (1993).
26. Ventelon, L., Hernandez, J., Lafuma, F., Chassenieux, C. & Perreur, C. (Rhodia Chimie) US 7884153 (2011).
27. Yoshida, A., Watanabe, Y., Andoo, M. & Tanimoto, K. A Method for Preparing New Elongated-Shaped Silica Sols. *Bull. Chem. Soc. Jpn.* **64**, 1682–1683 (1991).
28. Iler, R. K. & Dalton, R. L. Degree of Hydration of Particles of Colloidal Silica in Aqueous Solution. *J. Phys. Chem.* **60**, 955–957 (1956).
29. Mooney, M. The Viscosity of a Concentrated Suspension of Spherical Particles. *J. Colloid Sci.* **6**, 162–170 (1951).

30. Khan, M. N., Auerbach, S. M. & Monson, P. A. Lattice Model for Silica Polymerization: Monte Carlo Simulations of the Transition between Gel and Nanoparticle Phases. *J. Phys. Chem. B* **118**, 10989–10999 (2014).
31. Häbel, H. *et al.* From Static Micrographs to Particle Aggregation Dynamics in Three Dimensions. *J. Microsc.* **262**, 102–111 (2016).
32. Fijneman, A. J. *et al.* Multiscale Colloidal Assembly of Silica Nanoparticles into Microspheres with Tunable Mesopores. *Adv. Funct. Mater.* **30**, 2002725 (2020).
33. Thommes, M. *et al.* Physisorption of Gases, with Special Reference to the Evaluation of Surface Area and Pore Size Distribution (IUPAC Technical Report). *Pure Appl. Chem.* **87**, 1051–1069 (2015).
34. Cai, Y., Chen, Y., Hong, X., Liu, Z. & Yuan, W. Porous Microsphere and its Applications. *Int. J. Nanomedicine* **8**, 1111–1120 (2013).
35. Hugo, R. C. & Cady, S. L. Preparation of Geological and Biological TEM Specimens by Embedding in Sulfur. *Micros. Today* **12**, 28–31 (2004).
36. Gnanasekaran, K., Grimaldi, C., With, G. & Friedrich, H. A Unified View on Nanoscale Packing, Connectivity, and Conductivity of CNT Networks. *Adv. Funct. Mater.* **29**, 1807901 (2019).
37. Fijneman, A. J. *et al.* Local Quantification of Mesoporous Silica Microspheres using Multiscale Electron Tomography and Lattice Boltzmann Simulations. *Microporous Mesoporous Mater.* **302**, 110243 (2020).
38. Berthod, A. Silica: Backbone Material of Liquid Chromatographic Column Packings. *J. Chromatogr. A* **549**, 1–28 (1991).
39. Nawrocki, J. The Silanol Group and its Role in Liquid Chromatography. *J. Chromatogr. A* **779**, 29–71 (1997).
40. Lamotte, S., Kromidas, S. & Steiner, F. Comparison and Selection of Modern HPLC Columns. in *The HPLC Expert* 203–242 (Wiley-VCH Verlag GmbH & Co. KGaA, 2016). doi:10.1002/9783527677610.ch4.
41. Decher, G. & Hong, J.-D. Buildup of Ultrathin Multilayer Films by a Self-Assembly Process, Consecutive Adsorption of Anionic and Cationic Bipolar Amphiphiles on Charged Surfaces. *Makromol. Chemie. Macromol. Symp.* **46**, 321–327 (1991).
42. Decher, G. Fuzzy Nanoassemblies: Toward Layered Polymeric Multicomposites. *Science* **277**, 1232–1237 (1997).
43. Schneider, G. & Decher, G. From Functional Core/Shell Nanoparticles Prepared via Layer-by-Layer Deposition to Empty Nanospheres. *Nano Lett.* **4**, 1833–1839 (2004).
44. Tong, W., Song, X. & Gao, C. Layer-by-layer assembly of microcapsules and their biomedical applications. *Chem. Soc. Rev.* **41**, 6103–6124 (2012).
45. Chen, W. *et al.* Synthesis and Optimization of Wide Pore Superficially Porous Particles by a One-Step Coating Process for Separation of Proteins and Monoclonal Antibodies. *J. Chromatogr. A* **1414**, 147–157 (2015).
46. Shenoy, D. B., Antipov, A. A., Sukhorukov, G. B. & Möhwald, H. Layer-by-Layer Engineering of Biocompatible, Decomposable Core-Shell Structures. *Biomacromolecules* **4**, 265–272 (2003).
47. Mabille, C. *et al.* Rheological and Shearing Conditions for the Preparation of Monodisperse Emulsions. *Langmuir* **16**, 422–429 (2000).
48. Schmitt, V., Leal-Calderon, F. & Bibette, J. Preparation of Monodisperse Particles and Emulsions by Controlled Shear. in *Topics in Current Chemistry: Colloid Chemistry II* 195–215 (2003). doi:10.1007/3-540-36412-9_8.
49. Aveyard, R., Binks, B. P. & Clint, J. H. Emulsions Stabilised Solely by Colloidal

Particles. *Adv. Colloid Interface Sci.* **100–102**, 503–546 (2003).

50. McNair, H. M., Miller, J. M. & Snow, N. H. *Basic Gas Chromatography*. (Wiley, 2009). doi:10.1002/9781119450795.
51. Shah, R. K. *et al.* Designer Emulsions using Microfluidics. *Mater. Today* **11**, 18–27 (2008).
52. Kim, S. S. Ultrastable Mesostructured Silica Vesicles. *Science* **282**, 1302–1305 (1998).
53. Hubert, D. H. W. *et al.* Vesicle-Directed Growth of Silica. *Adv. Mater.* **12**, 1286–1290 (2000).
54. Caruso, F., Caruso, R. A. & Möhwald, H. Production of Hollow Microspheres from Nanostructured Composite Particles. *Chem. Mater.* **11**, 3309–3314 (1999).
55. Chen, J.-F., Ding, H.-M., Wang, J.-X. & Shao, L. Preparation and Characterization of Porous Hollow Silica Nanoparticles for Drug Delivery Application. *Biomaterials* **25**, 723–727 (2004).
56. Underhill, R. S. *et al.* Oil-Filled Silica Nanocapsules for Lipophilic Drug Uptake: Implications for Drug Detoxification Therapy. *Chem. Mater.* **14**, 4919–4925 (2002).
57. Park, J. H., Oh, C., Shin, S. Il, Moon, S. K. & Oh, S. G. Preparation of Hollow Silica Microspheres in W/O Emulsions with Polymers. *J. Colloid Interface Sci.* **266**, 107–114 (2003).
58. Teng, Z., Han, Y., Li, J., Yan, F. & Yang, W. Preparation of Hollow Mesoporous Silica Spheres by a Sol-Gel/Emulsion Approach. *Microporous Mesoporous Mater.* **127**, 67–72 (2010).
59. Li, D. *et al.* Synthesis of Uniform-Size Hollow Silica Microspheres through Interfacial Polymerization in Monodisperse Water-in-Oil Droplets. *ACS Appl. Mater. Interfaces* **2**, 2711–2714 (2010).
60. Tadros, T. F. Emulsion Formation, Stability, and Rheology. in *Emulsion Formation and Stability* 1–76 (Wiley-VCH Verlag GmbH & Co. KGaA, 2013). doi:10.1002/9783527647941.
61. Wüstenberg, T. Hydroxypropylcellulose. in *Cellulose and Cellulose Derivatives in the Food Industry* 319–342 (Wiley-VCH Verlag GmbH & Co. KGaA, 2014). doi:10.1002/9783527682935.ch07.
62. Dickinson, E. Hydrocolloids as Emulsifiers and Emulsion Stabilizers. *Food Hydrocoll.* **23**, 1473–1482 (2009).
63. Brunauer, S., Emmett, P. H. & Teller, E. Adsorption of Gases in Multimolecular Layers. *J. Am. Chem. Soc.* **60**, 309–319 (1938).
64. Barrett, E. P., Joyner, L. G. & Halenda, P. P. The Determination of Pore Volume and Area Distributions in Porous Substances. I. Computations from Nitrogen Isotherms. *J. Am. Chem. Soc.* **73**, 373–380 (1951).
65. Lowell, S., Shields, J. E., Thomas, M. A. & Thommes, M. Other Surface Area Methods. in *Characterization of Porous Solids and Powders: Surface Area, Pore Size and Density* (ed. Lowell, S.) 82–93 (Springer, 2004). doi:10.1007/978-1-4020-2303-3_6.
66. Iler, R. K. *The Chemistry of Silica*. (John Wiley & Sons, Inc., 1979). ISBN: 047102404X.

Summary and Outlook

Rational Design of Porous Silica-Based Materials via Multiscale Colloidal Assembly

The work described in this thesis provides useful insight in the underlying mechanisms of colloidal assembly in spherical confinement and specifically on the formation of mesoporous silica microspheres (MSMs). Although MSMs have existed for many years, their formation remains a particularly relevant topic since MSMs are widely used in the pharmaceutical industry and life sciences for the separation and purification of molecules[1]. MSMs are industrially produced on a multi-tonne scale but the range of properties, such as for pore size and porosity, that can be achieved is limited. This makes it difficult for the industry to adapt to the ever-changing needs of the pharmaceutical market. In most industrially relevant processes used today, a generic type of MSM with standard porosity characteristics is produced, which subsequently receives multiple time-consuming post-treatment steps to modify its properties to the size and shape of the molecules of interest[2–4]. In this work, we have outlined novel strategies to directly produce a wide range of tailor-made MSMs with independent control over surface area, pore size and overall porosity, without the need for additional steps. This was achieved by a systematic investigation of the entire MSM formation process, including theoretical studies on nanoparticle gelation, modeling droplet kinetics under different reaction conditions, the synthesis of a large variety of different MSMs as well as the multiscale characterization of MSMs from the macroscopic scale down to the nanometer scale.

Like many silica-based materials, the formation of MSMs proceeds via colloidal assembly of silica nanoparticles. The nanoparticles used as building blocks directly influence the internal (size of the pores and struts) and external morphology (specific surface area) of the MSMs produced. Therefore, in Chapter 2, we used an extended version of the classical DLVO theory as a theoretical framework to quantitatively describe the stability of the silica sols used throughout this work. Furthermore, we described nanoparticle aggregation as a function of salt concentration and have shown that the rate of destabilization is related to the particle size and particle volume fraction. The insights in nanoparticle aggregation behavior have been used as the basis for all experiments performed throughout the remainder of the thesis.

The general principles of MSM formation are established in Chapter 3, where we introduced a strategy to the design of perfectly spherical MSMs with precisely tunable porosity characteristics across multiple length scales that is both highly reproducible and scaleable[5]. We used a combination of evaporation-driven and gelation-driven assembly methods to fabricate MSMs with tailor-made properties over a much wider range than has been shown so far in literature. The different MSMs were characterized by a combination of scanning electron microscopy and physical adsorption measurements and were classified based on their total surface area, pore volume, average pore sizes and width of their pore size distributions. Each MSM displayed a significantly narrower pore distribution than can be obtained when additional post-treatment steps are used. This is important for the pharmaceutical market, since the width of the pore size distribution determines the resolution and efficiency that can be obtained in HPLC[6].

One of the main challenges that was addressed throughout this work was the characterization of the micrometer sized MSMs down to the nanometer scale pore level. This is not straightforward because most techniques either do not have the required resolution to resolve nanometer-sized pores or cannot deal with thick samples, which then require cross-sectioning by microtomy[7,8]. In Chapter 4 we developed a method to obtain quantitative insight into the pore network of commercial MSMs using a combination of low convergence angle scanning transmission electron microscopy tomography with image analysis and lattice Boltzmann simulations[9]. We have shown an excellent match between bulk and single-particle properties, indicating an extraordinary homogeneity from particle to particle. Furthermore, our analysis revealed local intraparticle differences in porosity and pore sizes that were not known before and that could have a profound impact on the mass-transport behavior through individual MSMs[10].

To further elucidate the MSM formation process, we presented a microfluidic processing route in combination with in-situ optical microscopy in Chapter 5. We studied the effect of various parameters on the kinetics of emulsion droplet shrinkage and colloidal assembly in confined spaces and corroborated the results with a theoretical mass-transfer model that is based on the droplet number density, solvent characteristics and temperature. Moreover, radial intensity profile maps were obtained to quantify the transformation of emulsion droplets into MSMs and to show the effect of different reaction conditions on the shrinkage and gelation behavior in confined spaces. The results described in this chapter provides novel insights in the MSM formation process, such as evidence that indicates a sudden collapse of droplets during MSM formation that could potentially explain the local variations in porosity as observed previously.

With the knowledge obtained throughout this thesis, we have described some exploratory results in Chapter 6 that highlight how the general principles of MSM formation can be extended to fabricate MSMS with truly hierarchical morphologies. We have presented experimental strategies to synthesize anisotropic MSMs, such as core-shell microspheres and hollow microspheres using multi emulsions, that have unique potential applications that cannot be fulfilled with standard isotropic MSMs. However, due to limited control over the emulsion droplet size and behavior in bulk, reproducibility remains low. Furthermore, we synthesized MSMs from non-spherical fractal silica sols and showed that these MSMs have significantly higher microsphere porosities than MSMs synthesized from conventionally used spherical sols.

In conclusion, the work presented in this thesis provides the tools required for the microstructural design of the next generation of tailor-made silica microspheres for use in separation applications, catalysis and beyond. It is now possible to tune pore size and porosity independently for a wide variety of molecules of interest and combined with microfluidics create monodisperse MSM in a "one step process", resulting in custom materials that could improve resolution and efficiency of HPLC.

Although a great deal of insight on the MSM formation process has been obtained in this work, parts of the mechanism remain unclear. In future experiments it would be interesting to have an even more in depth look at the MSM formation process using a combination of microfluidic processing and, e.g., liquid-phase scanning electron microscopy or liquid-phase transmission electron microscopy in order to visualize the gelation of silica nanoparticles in real time. In addition, it would be interesting to investigate the effect of the polydispersity of the silica sols used as building blocks on the width of the pore size distribution. We expect that the width of the pore distribution could be decreased significantly if more monodisperse nanoparticles are used to fabricate MSMs, which will further improve the functional properties of the material. Special attention should also be paid to the fractal sols described in Chapter 6. We expect that these non-spherical sols will play a key role in the future design of novel MSMs that require extra-high porosities. Furthermore, it would be worthwhile to look at ways to scaleup the microfluidic processing route to produce monodisperse MSMs on a somewhat larger scale.

The next step in MSM formation is total control over the entire process, i.e., to predict particle properties, such as the size and porosity characteristics of the MSMs, based solely on the initial droplet size and reaction conditions. In this work we have shown that we can predict the porosity characteristics over a large range based on the reaction conditions, as well as how different parameters affect the shrinkage behavior of emulsion droplets in different solvent mixtures. However, many details are still unclear and further research on the process and resulting MSM properties is required. Ultimately, the goal is to combine everything in a simple, powerful toolbox to design tailor-made silica-based materials with hierarchical porosity for specific applications in separation, catalysis and beyond.

References

1. Unger, K. K., Ditz, R., Machtejevas, E. & Skudas, R. Liquid Chromatography-its Development and Key Role in Life Science Applications. *Angew. Chemie* **49**, 2300–2312 (2010).
2. M. Nyström, W. Herrmann, B. Larsson (EKA Nobel AB) US 5256386 (1993).
3. L. Balducci, R. Ungarelli (Enichem S.p.A.; Eniricerche S.p.A.) US 6103209 (2000).
4. J. Zhiping, R. P. Fisk, J. O' Gara, T. H. Walter, K. D. Wyndham (Waters Technologies Corporation) US 8778453 (2004).
5. Fijneman, A. J. *et al.* Multiscale Colloidal Assembly of Silica Nanoparticles into Microspheres with Tunable Mesopores. *Adv. Funct. Mater.* **30**, 2002725 (2020).
6. Snyder, L. R., Kirkland, J. J. & Dolan, J. W. *Introduction to Modern Liquid Chromatography. High-Performance Gradient Elution: The Practical Application of the Linear-Solvent-Strength Model* (John Wiley & Sons, Inc., 2009).

doi:10.1002/9780470508183.

7. Johnson, T. F. *et al.* Three Dimensional Characterisation of Chromatography Bead Internal Structure using X-ray Computed Tomography and Focused Ion Beam Microscopy. *J. Chromatogr. A* **1566**, 79–88 (2018).
8. Maire, E. *et al.* On the Application of X-ray Microtomography in the Field of Materials Science. *Adv. Eng. Mater.* **3**, 539 (2001).
9. Fijneman, A. J. *et al.* Local Quantification of Mesoporous Silica Microspheres using Multiscale Electron Tomography and Lattice Boltzmann Simulations. *Microporous Mesoporous Mater.* **302**, 110243 (2020).
10. Gritti, F. & Guiochon, G. New Insights on Mass Transfer Kinetics in Chromatography. *AIChE J.* **57**, 333–345 (2011).

List of Publications

Patents

- Fijneman, A. J. *et al.*, Porous Silica Particles (Nouryon Chemicals International B.V.) filed EP 19177278.9 (2019).

Publications

- Fijneman, A. J. *et al.* Multiscale Colloidal Assembly of Silica Nanoparticles into Microspheres with Tunable Mesopores. *Adv. Funct. Mater.* **30**, 2002725 (2020).
- Fijneman, A. J. *et al.* Local Quantification of Mesoporous Silica Microspheres using Multiscale Electron Tomography and Lattice Boltzmann Simulations. *Microporous Mesoporous Mater.* **302**, 110243 (2020).
- Fijneman, A. J. *et al.* Time-Resolved Investigation of Mesoporous Silica Microsphere Formation using In Situ Heating Optical Microscopy (in preparation).
- Rosas-Arbelaez, W., Fijneman, A. J. *et al.* Hierarchical Micro-/Mesoporous Zeolite Microspheres Prepared by Colloidal Assembly of Zeolite Nanoparticles (submitted).

Not related to this thesis

- Li, L., Fijneman, A.J. *et al.* Directed Nucleation and Growth by Balancing Local Supersaturation and Substrate/Nucleus Lattice Mismatch. *Proc. Natl. Acad. Sci.* **115**, 3575–3580 (2018).
- Tao, J., Fijneman, A.J. *et al.* Control of Calcium Phosphate Nucleation and Transformation through Interactions of Enamelin and Amelogenin Exhibits the “Goldilocks Effect.” *Cryst. Growth Des.* **18**, 7391–7400 (2018).

Curriculum Vitae

Remco Fijneman was born on November 8th 1991 in Tilburg, the Netherlands. After finishing his secondary education, he studied Chemistry and Chemical Engineering at Eindhoven University of Technology (TU/e) where he obtained his master's degree (MSc) with a specialization in Molecular Systems and Materials Chemistry in 2016. His graduation research was carried out under the supervision of prof. Nico Sommerdijk in the Laboratory of Materials and Interface Chemistry. During his university studies he did two international internships, first at the Harvard John. A Paulson School of Engineering and Applied Sciences (USA) in the group of prof. Joanna Aizenberg and later at the Pacific Northwest National Laboratory (USA) in the group of prof. James de Yoreo. In September 2016 he started his PhD project in the Horizon 2020 Marie Curie innovative training network "MULTIMAT" under the supervision of prof. Bert de With and dr. Heiner Friedrich. From 2016 to 2019 he performed his doctoral research on-site at Nouryon Pulp and Performance Chemicals in Bohus, Sweden. In 2019 he returned to the Netherlands to complete his PhD work at the Laboratory of Physical Chemistry at TU/e. The most important findings of his PhD are described in this thesis.

Acknowledgements

It's hard to believe that my PhD journey is already over. It feels like only yesterday that I got on a plane to Sweden to start my adventure. Although the course of my project was far from normal, I never once regretted signing up for the challenge. I've made some great new friends along the way, met many fantastic people, learned a lot about the Swedish culture, I have grown as a person, both professionally and personally and I am extremely proud of the work in front of you (seriously, you should read it!). Obviously, I could not have done it without the help of many people.

First of all, I would like to thank my promotor Bert de With for taking over the supervision of the project and making it possible for me to successfully finish my research at TU/e in time. Bert, despite not being involved since the very beginning, you put in a great amount of effort to understand everything related to the project. The (scientific) discussions we had were not only fun but also extremely helpful and really shaped my thesis. I am very grateful for your time and effort on correcting the different chapters of the thesis. Thanks again and hopefully you will enjoy your second retirement.

Secondly, I would like to thank my daily supervisors Heiner Friedrich and Joakim Högblom. Heiner, although most of our discussions were via Skype, your ideas, scientific input, knowledge on data analysis and critical review of the manuscripts were extremely valuable for the direction of the thesis. I am amazed how well you understood the ins and outs of the whole process even though you have never actually seen it in person. Thank you for the cool microscopy and tomography experiments, your patience, the drinks at the F.O.R.T. and everything else. You are a great researcher.

Joakim, equal thanks has to be given to you. Thank you for the daily supervision during my time at Nouryon. I am extremely lucky that you wanted to be part of my project. Without your knowledge and infinite ideas (except the napalm, that was not very successful…) and especially your never ending enthusiasm, I don't think we would have accomplished this much. I had a lot of fun working with you and am grateful for the time (and beers) that we shared. It's a shame that we cannot celebrate the defense in person but I am sure we will meet again one day.

Next, I would like to thank Magnus Palmlöf and Michael Persson. Magnus, thank you for all your support during my time at Nouryon. You helped me a lot with all the administrative tasks, housing, taxes, translating papers from Swedish to English and so much more. I am grateful for the time and energy that you put in the MULTIMAT project and to make my time at Nouryon as pleasant as possible. It was truly a pleasure!

Michael, many thanks to you as well. Your scientific input was very valuable during our monthly meetings. Thanks as well for introducing me to various people in your large network both within and beyond Nouryon and giving me to opportunity to present my results on many occasions.

I would also like to thank my second promotor, Catarina Esteves. Catarina, thank you for being part of my committee. Although we did not have many scientific conversations together I certainly enjoyed the ones that we had.

Further, I would like to express my gratitude towards the remaining members of my defense committee, Krister Holmberg and Fausto Gallucci. Thank you for your critical evaluation of my PhD thesis. I would also like to extend my thanks to Emiel Hensen for chairing the ceremony.

Many thanks as well to my original promotor Nico Sommerdijk. Nico, we have known each other already since you were my mentor during my Bachelor studies. Thank you for giving me the opportunity to join the MULTIMAT project and to carry out my research in your group (albeit from 1000 km distance) and your supervision the first years of the project.

Thanks as well to Remco Tuinier for giving me the opportunity to finish my research in your group. Although my time in SPC was short, I felt immediately welcome and thoroughly enjoyed my time in the group.

Tobias Gebäck, thank you for the nice collaborative work on the lattice Boltzmann simulations. I learned a lot from you and wish you the very best in your future work.

Richard Oldroyd, for drafting up our patent application and giving me a short overview of the ins and outs of the patent world. It was really interesting!

Olof, David, João and Patrik, thanks for all your help during my secondment at Insplorion. It's a shame we couldn't get my system compatible with the sensor technology but nevertheless it was a nice experience!

Fredrik, Börje, Peter, thanks for all the help and support in the lab at Nouryon and for sharing some wonderful stories!

Ingeborg, Anne, Pauline, Ton and Paul, thank you for your help and support with various techniques. You made it possible for me to do many cool experiments.

Pleunie, Imanda, thank you so much for helping out with all the administrative tasks, even though the university did not always understand when I started with my PhD.

My PhD research was funded by the European Union Horizon 2020 Marie Curie innovative training network MULTIMAT. Special thanks to Elizabeth McKenzie for being an amazing project manager. You handled MULTIMAT like a boss.

A great deal of gratitude also goes out to my awesome colleagues and friends, both in Sweden and in the Netherlands.

Emma, Matilda, Fang, Jagoda, Daniel, Sigrún, Ayda, Almedina, Hanna, Emelie, Lisa, Josefin, Mark, Andreas, Jesper, Daniel, Oskar, Andréa, Bram, Sylvain, Pontus and Andrej, thanks so much for all the good times we had in Sweden! At first I was afraid it would be difficult to make new friends but that quickly changed when I met all of you. I had so much fun hanging out with all of you. All the times we went to Yaki-Da, the kräftskiva, Midsummer, the Polish wedding, BOOST, Out of Office After Work and of course the countless fika breaks. Thank you so much for making my time in Sweden so fun!

Alice, my friend at Swedish class. It was good to have somebody to talk to in broken Swedish without feeling bad about it.

Walter, my MULTIMAT buddy, thanks for always making time to hang out. How many times did we go out for drinks, watch a movie and just have a good time? We had a lot of fun together and I am happy we also got a great paper in the end!

All my other MULTIMAT buddies: Paula, Deniz, Hanglong, Pierre, Luis, Gerardo, Pallabi, Massimiliano, Peter, Xufeng and Xiaobin. It was great fun to hang out with all of you during the various courses, trips and activities. It's a shame we couldn't meet up more often!

My paranymphs Stijn and Gilles. Stijn, we got to know each other really well in just a short time. Thanks for the laughs, the video calls, working out together and of course for your tremendous help with the theoretical model! Gilles, it feels like I have known you already forever. We shared a lot of good times together and hopefully that will never change.

Jason, it was really fun to work with you the past year. Although the direction of the project changed several times and the equipment didn't always work as intended, we really accomplished some great results and learned lots of interesting new things. Thanks!

Maurits and Arthur, without your amazing MATLAB skills I would still be struggling with a lot of the code and my thesis would lack a lot of content.

Mark, my office mate. Thanks for listening to my endless rants.

Zino and Rick thanks for all the laughs over the years. I had a lot of fun spending time with both of you, enjoying coffee or a beer and to complain about anything and everything.

Machi, kampai!

Laura, my colleagues in Sweden were very impressed by all the 3D models that you printed out for me!

Bernette, Demi, Mohammad S., Mohammad M., Ayberk, Sai, Lisette, Michiel, Zaf, Christian, Stefan, Joeri, Mila, Siyu, Jeroen, Timo, Vincent, Jasper, Nazila, Naomi, Marieke, Alvaro, thanks for all the good times in SMG/SPC!

Wouter, Patricia, Jasper and Klaas, thanks for the "alternative ONCS" during himmelsfärd! I cherished the bottle of Jäger until my very last day in Sweden (not really).

Lisa, it was great to meet-up with you and share more than a few glasses of wine when you lived in Stockholm. Thanks for the good times!

Rianne, thanks for coming to see me in Sweden. It was a lot fun to show you around in Göteborg!

Sven, for inviting me to celebrate midsummer in Spain. It was short but a lot of fun!

Bart, if you would have told me four years ago that we would go to the SSC every week to work out I would have laughed in your face. Nevertheless, I am glad that we did. It was fun!

Bompa, Gijs, Gilles, Huisman, Sandy and Tom, de gillers van tafel 13. You are by far the craziest but also the best group of friends somebody could wish for. Thank you for all the amazing times we shared. Proost en op de volgende!

Pap, mam, Maikel, bedankt voor alle steun en het vertrouwen de afgelopen jaren. Het was niet altijd even makkelijk, maar ik wist dat ik altijd op jullie kon rekenen.

/Remco